North Atlantic Current in model and observations: Transport variability, flow paths and hydrography

Tilia-Manuela Breckenfelder

Universität Bremen, 2017

North Atlantic Current in model and observations: Transport variability, flow paths and hydrography

Vom Fachbereich für Physik und Elektrotechnik der

Universität Bremen genehmigte Dissertation

zur Erlangung des akademischen Grades

Doktor der Naturwissenschaften (Dr. rer. nat.)

von

Dipl.-Phys. Tilia-Manuela Breckenfelder

aus Tettnang

1. Gutachterin: Prof. Dr. Monika Rhein
2. Gutachter: Prof. Dr. Paul G. Myers

Abstract

The North Atlantic Current (NAC) is subject to variability on multiannual to decadal time scales, influencing the transport of volume, heat and freshwater from the subtropical to the eastern subpolar North Atlantic (NA). Current observational time series are either too short or too episodic to comprehensively study the processes involved, therefore models are used to complement the observations. For this study, moored and ship-based observations from three sections along the NAC pathway, satellite altimetry data and $1/20°$ hindcast VIKING20 model configuration (1960-2008) output are used. They are investigated and compared to describe hydrography, flow field and transport time series. The flow into and out of the NA is monitored at 47°N, the flow from the western into the eastern basin of the NA is captured by a section at the western flank of the Mid-Atlantic Ridge (MAR), and the distribution in the eastern basin of the NA is observed at the OVIDE line. These three sections thus provide an extensive picture of the flow.

Overall, the model results agree with the observed NAC mean transports at the three sections within the standard deviations, but exhibit in general higher temperature and salinity values. Furthermore, the general circulation of the subpolar NA as exhibited in satellite altimetry data is qualitatively well captured by the model. The two main differences are: The simulated Northwest Corner (NWC) reaches further into the Labrador Sea by around $2°$; at the MAR the simulated NAC is more focused to the Charlie-Gibbs-Fracture Zone and follows mainly the northern path into the eastern basin in contrast to the observations.

To extend the study of the NAC and more generally of the NA, the influence of the North Atlantic Oscillation (NAO) on the flow, temperature, and salinity distributions are investigated in the model. The NA-wide five year composites, calculated for the five strongest/weakest NAO years and the five strongest transitions from one NAO state into the other, reveal stronger velocities, different pathways across the MAR area and a northward shift of the NWC during positive NAO years in comparison to negative NAO years. Furthermore, warm and saline water is confined and carried along by the strong NAC flow during positive NAO years and therefore warmer and saline water reaches further north into the subpolar gyre region during negative NAO years.

In summary, this study extends the knowledge about the NAC and about the performance of the VIKING20 model configuration in comparison with observations. To increase the knowledge of the NA circulation, further model studies should be performed with extended temporal overlap with observations. Furthermore, with the described discrepancies of the current model configuration, updated models should be devised.

Contents

Abbreviations

ADCP	Acoustic Doppler Current Profiler
AGRIF	Adaptive Grid Refinement in FORTRAN
AMOC	Atlantic Meridional Overturning Circulation
Argo	Global array of temperature/salinity profiling floats
AVISO	Archiving, Validation and Interpretation of Satellite Oceanographic data
CGFZ	Charlie Gibbs Fracture Zone
CNES	Centre National d'Études Spatiales
CORE.v2	Coordinate Ocean-ice Reference Experiments II
CTD	Conductivity, Temperature, Depth
DJFM	December, January, February, March
Duacs	Data Unification and Altimeter Combination System
DWBC	Deep Western Boundary Current
EB	European Basin
ENAC	Eastern North Atlantic Current
FFZ	Faraday Fracture Zone
FP	Flemish Pass
GOCE	Gravity field and steady-state Ocean Circulation Explorer

GRACE	Gravity Recovery And Climate Experiment
IB	Iberian Basin
ICB	Iceland Basin
IS	Irish Shelf
ISOW	Iceland-Scotland Overflow Water
lADCP	lowered Acoustic Doppler Current Profiler
LIM2	Louvain-la-Neuve Ice Model
LSW	Labrador Sea Water
MADT	Map of Absolute Dynamic Topography
MAR	Mid-Atlantic Ridge
MDT	Mean Dynamic Topography
MFZ	Maxwell Fracture Zone
MIT/gcm	Massachusetts Institute of Technology General Circulation Model
MOW	Mediterranean Overflow Water
NA	North Atlantic
NAC	North Atlantic Current
NAO	North Atlantic Oscillation
NBR	Newfoundland Basin Recirculation
NEMO	Nucleus for European Modelling of the Ocean
NFB	Newfoundland Basin flow
nm	nautical mile ($1\,\text{nm} = 1.852\,\text{km}$)
NWC	Northwest Corner
OGCM	Ocean General Circulation Model

OVIDE	Observatoire de la Variabilité Interannuelle à Décennale
PIES	Pressure-equipped Inverted Echo Sounders
RAPID	Rapid Climate Change program
SF	Subpolar Front
SPG	Subpolar Gyre
Ssalto	Ssalto multimission ground segment
SSH	Sea Surface Height
SST	Sea Surface Temperature
Sv	Sverdrup ($1\,\mathrm{Sv} = 10^6\,\mathrm{m^3s^{-1}}$)
SWF	Southward flow
ULSW	Upper Labrador Sea Water
WBC	Western Boundary Current
WNAC	Western North Atlantic Current
WOA	World Ocean Atlas
WOCE	World Ocean Circulation Experiment

1. Introduction

The subpolar North Atlantic (NA) is characterized by considerable variability in water mass transformation and transports on intraseasonal to multidecadal time scales, with some of the variability connected to atmospheric modes like the North Atlantic Oscillation (NAO) (e.g. *Curry and McCartney*, 2001; *Häkkinen and Rhines*, 2004; *Brauch and Gerdes*, 2005; *Kieke et al.*, 2007; *Hauser et al.*, 2015; *Delworth and Zeng*, 2016). The transport of warm and salty water in the upper ocean from the subtropics into the Newfoundland basin (Figure 1.1) is carried by the northward extension of the Gulf Stream and dubbed the North Atlantic Current (NAC). Part of the NAC recirculates to the south in the interior of the Newfoundland basin (e.g. *Mertens et al.*, 2014). A fraction of the NAC transport continues north to the southern Labrador Sea where it retroflects to the east forming the Northwest Corner (NWC) (*Rossby*, 1996). Ultimately, the NAC crosses the Mid-Atlantic Ridge (MAR) into the eastern basin, forming the southern rim of the cyclonic Subpolar Gyre (SPG), the main circulation feature in this region. In the Newfoundland Basin and at the MAR, the velocity field in the NAC is deep reaching (*Rhein et al.*, 2011; *Mertens et al.*, 2014; *Roessler et al.*, 2015) and is influenced by the presence of fracture zones (Figure 1.1), mainly the Charlie Gibbs Fracture Zone (CGFZ), Faraday Fracture Zone (FFZ) and Maxwell Fracture Zone (MFZ) (e.g. *Bower and von Appen*, 2008).

The buoyancy loss of the NAC by the cooling along its northward pathway contributes to the formation of Labrador Sea Water (LSW) in the Labrador Sea (*Talley and McCartney*, 1982), connecting the warm upper branch and the cold lower branch of the Atlantic Meridional Overturning Circulation (AMOC). Based on projections from climate models, it is expected that global warming will cause significant changes in the circulation as well as the temperature and salinity properties of water masses formed there. This in turn will lead to changes in heat and
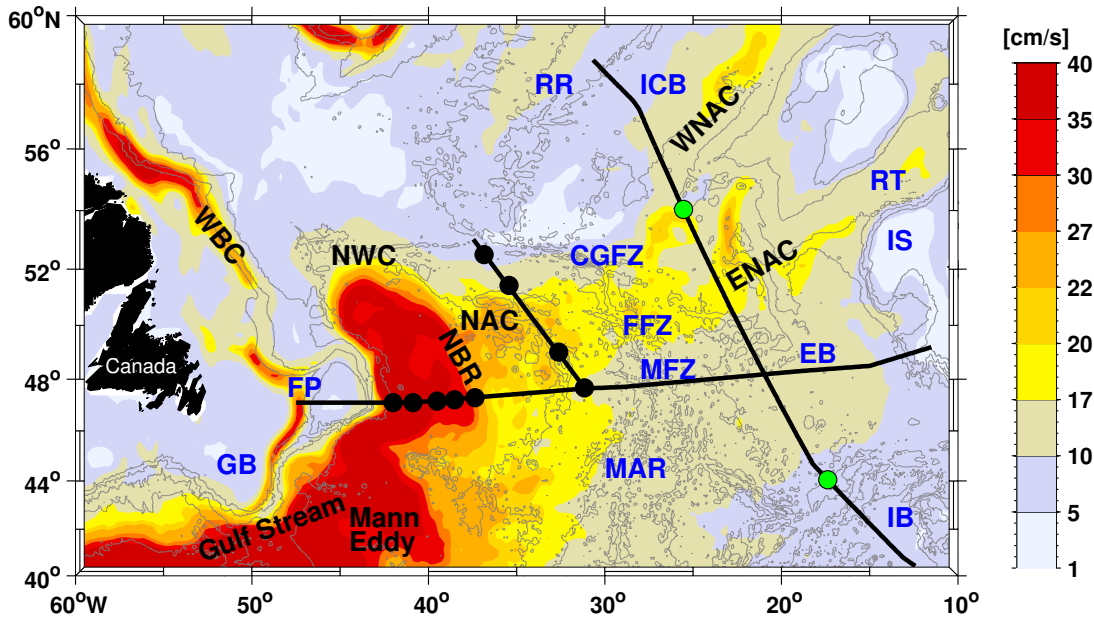
Figure 1.1.: Map of the subpolar North Atlantic with the mean sea surface speed from gridded geostrophic velocity provided by AVISO and bottom topography from ETOPO2 database (*Etopo2*, 2001), indicated by grey lines with a depth interval of 1000 m between 5000 m depth and the surface. Abbreviations: North Atlantic Current (NAC), Western Boundary Current (WBC), Northwest Corner (NWC), western NAC (WNAC), eastern NAC (ENAC), Newfoundland Basin Recirculation (NBR), Charlie-Gibbs Fracture Zone (CGFZ), Faraday Fracture Zone (FFZ), Maxwell Fracture Zone (MFZ), Mid-Atlantic Ridge (MAR), Iceland Basin (ICB), European Basin (EB), Iberian Basin (IB), Grand Banks (GB), Flemish Pass (FP), Reykjanes Ridge (RR), Rockall Trough (RT), and Irish Shelf (IS). The positions of the PIES at the 47°N and the MAR sections are marked by the black dots. The PIES divide the MAR section in a northern, a central and a southern segment. North of the northernmost PIES at the MAR the extended section used in the model to take the more northern pathway of the NAC into account is shown by the thick black line across the PIES positions. The 47°N section is marked by the black line and the black line from 40°N to 58°N is the OVIDE section. The green dots indicate the geographical separation of the OVIDE line in Iceland Basin, European Basin and Iberian Basin following *Mercier et al.* (2015).

freshwater fluxes, which could have consequences for the future climate and sea level in Western Europe (*IPCC*, 2013).

Although the importance of the NAC as part of the climate-relevant meridional overturning of the Atlantic is widely known, continuous measurements of the mean NAC transports and its variability away from the western boundary are rare and too short to study decadal fluctuations. In *Rhein et al.* (2011) the first continuous two-year long (2006-2008) NAC transport time series at the MAR calculated from an array of bottom mounted Pressure-equipped Inverted Echo Sounders (PIES) instruments was published. *Roessler et al.* (2015) used the correlation between the PIES derived transport time series (2006-2010) at the MAR and the sea level anomalies from altimetry to extend the transport time series to the time period of altimeter data from 1992 to 2013. They argue that the annually averaged time series is close to the absolute transports, although they assume a zero transport at a reference level of 3400 dbar. The 21-year mean was 27.4 Sverdrup ($1\,\mathrm{Sv} = 10^6\,\mathrm{m^3 s^{-1}}$) (with a standard deviation of 4.7 Sv), consisting of 60 % warm water with subtropical (about 16 Sv, densities $< 27.68\,\mathrm{kg/m^3}$), and 40 % with subpolar origin. No long-term trend was found, but substantial variability on time scales of 120 days (meanders, eddies) and 4-9 years, with the latter partly explained by the NAO index.

Lherminier et al. (2010); *Mercier et al.* (2015); *García-Ibáñez et al.* (2015) and *Daniault et al.* (2016a) analyzed repeated hydrographic and velocity (from vessel mounted Acoustic Doppler Current Profiler (ADCP)) sections from Greenland to Portugal in the Observatoire de la Variabilité Interannuelle à Décennale (OVIDE) program. These hydrographic measurements were carried out between 1997 and 2012. The authors calculated the full depth absolute circulation using an inverse model constrained by the ADCP data and by an overall mass balance. They found large transport variability over the whole water column. The mean NAC transport above the $\sigma_1 = 32.1\,\mathrm{kg/m^3}$ isopycnal (which is around 250 m above the $\sigma_\theta = 27.68\,\mathrm{kg/m^3}$ at the Reykjanes Ridge but converges to a similar depth in the Iberian Basin) was 16 Sv, and equally split between the Eastern North Atlantic Current (ENAC) and Western North Atlantic Current (WNAC) branch of the NAC (*Lherminier et al.*, 2010). These numbers are similar to the mean NAC transport of 15.5 Sv (densities $< 27.55\,\mathrm{kg/m^3}$), that *Sarafanov et al.* (2012) calculated from repeated hydrographic sections at 59.5°N, measured annually between 2002 and 2008. Both estimates from repeated hydrography are comparable to the mean continuously measured NAC transport (1992 – 2013) of subtropical water crossing

the MAR (*Roessler et al.*, 2015).

The geographical limits of a section influence the mean transport value across the section in the eastern NA (*Daniault et al.*, 2016a). *Daniault et al.* (2016a) analyzed 6 OVIDE repeat sections from 2002 to 2012 and instead of separating the flow into ENAC and WNAC, they defined a northern, a central and a southern branch of the NAC with fixed boundaries. They found a total top to bottom flow of 11 Sv, 14.2 Sv, and 16.6 Sv, respectively. The transport for all branches for densities smaller than $\sigma_1 = 32.15 \, \mathrm{kg/m^3}$ was 27.2 Sv, with 58 % (15.8 Sv) of the transport in the southern NAC branch, and only 12 % in the northern branch. They reported a similar mean transport as found at the MAR section (*Roessler et al.*, 2015), when projecting the section limits from the MAR section onto the OVIDE line and referencing the flow to 3400 dbar.

1.1. The North Atlantic Oscillation

The North Atlantic Oscillation is described as the dominant mode of the atmospheric variability in the North Atlantic region (*Visbeck et al.*, 2003). It is closely related to the Arctic Oscillation and can be defined by the first empirical orthogonal function of climate variability for the Atlantic (*Talley et al.*, 2011). The NAO is found to be significantly correlated with surface air temperature and Sea Surface Temperature (SST) across wide regions of the North Atlantic and neighboring regions (*Hurrell and Deser*, 2009). The NAO can be quantified by a dimensionless index calculated from the pressure difference between the Azores high and the Iceland low, describing the alternation of atmospheric mass between these two pressure systems. The simultaneously strengthening and weakening of these two pressure systems is often defined by the normalized pressure difference between Ponta Delgada, Azores and Stykkisholmur/Reykjavik, Iceland and calculated for the wintertime (December, January, February, March (DJFM)) (Figure 1.2) (*Hurrell*, 1995). The NAO time series exhibits seasonal to multidecadal variations, but is roughly decadal (*Talley et al.*, 2011). From the 1950s to 1960s a negative NAO was dominating, afterwards until the 1990s the positive NAO dominated. In the early 2000s negative NAO years are exhibited followed by positive NAO years until today, interrupted in 2010 by a strong negative NAO year.
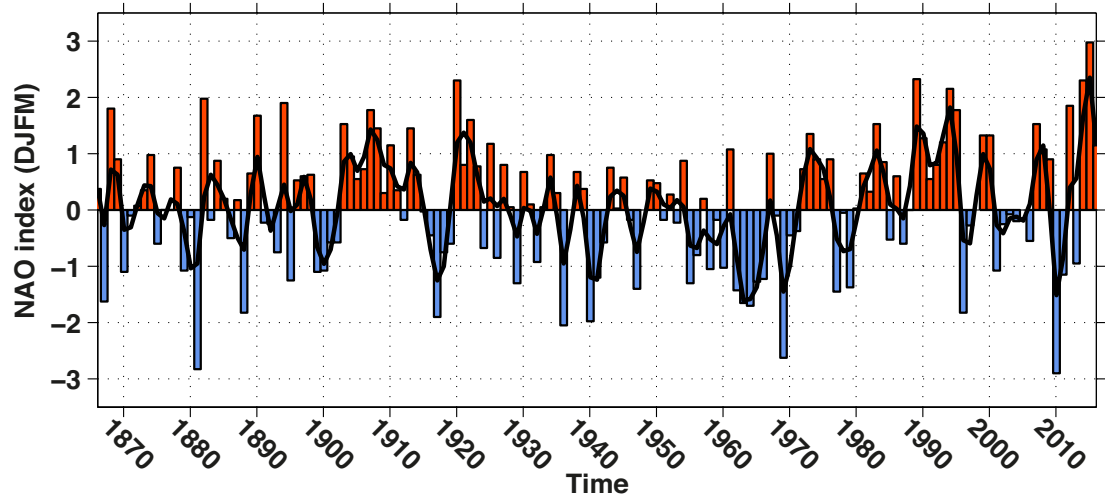
Figure 1.2.: North Atlantic Oscillation index from December to March calculated by the normalized pressure difference between Azores high and Iceland low (*Hurrell*, 1995)[1]. The red bars indicate positive and the blue bars negative NAO years. The black line is the filtered index by three year low pass filter.

During positive NAO years the Icelandic low exhibits anomalously low pressure, while higher pressures than normal are found at the Azores high (*Hurrell*, 1995). The number and intensity of storms are increased over the NA (*Hurrell and Deser*, 2009). The higher pressure difference leads to stronger westerlies towards Europe (*Hurrell*, 1995) and shifts their pathway further north (*Talley et al.*, 2011). The stronger westerlies change the surface behavior of the NA by Ekman drift (Figure 1.3) (e.g. *Chaudhuri et al.*, 2011) and leads to a strengthening of the SPG during positive NAO years (e.g. *Curry and McCartney*, 2001; *Bersch*, 2002; *Häkkinen and Rhines*, 2004; *Bersch et al.*, 2007; *Lohmann et al.*, 2009). *Roessler et al.* (2015) report more transport crossing the MAR during positive NAO years towards the northeast. Furthermore, a expansion and zonal shift of the SPG towards the east is reported during positive NAO years (Figure 1.3) (e.g. *Bersch*, 2002; *Curry and McCartney*, 2001; *Chaudhuri et al.*, 2011; *Stendardo et al.*, 2015).

The NAO further influences the temperature and salinity of the NA (e.g *Eden and Willebrand*, 2001; *Bersch et al.*, 2007; *Frankignoul et al.*, 2009; *Herbaut and*

---

[1]NAO data are taken from `https://climatedataguide.ucar.edu/climate-data/hurrell-north-atlantic-oscillation-nao-index-station-based`
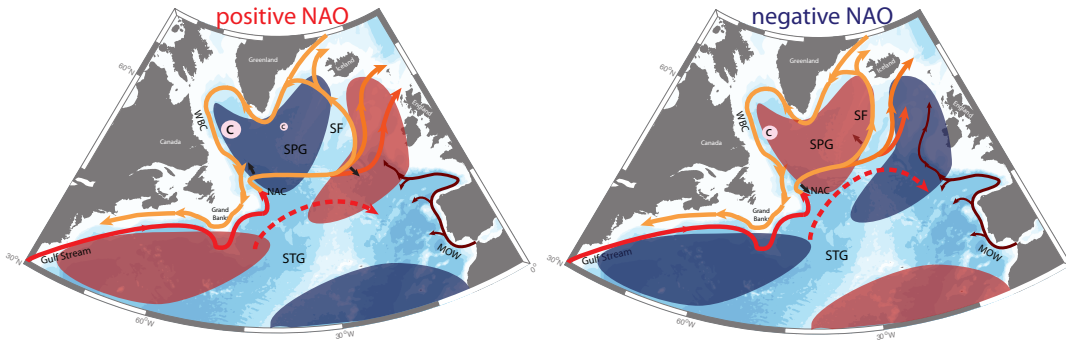
Figure 1.3.: Schematic ocean response to the positive and negative NAO phases. The SPG is illustrated by the orange arrows. The subpolar Front (SF) is the northernmost NAC branch at the eastern side of the SPG, the other branches are represented in light orange and dark orange. The Suptropical Gyre (STG) is illustrated by the dashed red arrow and the Mediterranean Overflow Water (MOW) by the purple arrows. Stronger (weaker) deep convection is indicated by larger (smaller) pink circles. The movements of the SF are indicated by black arrows.
The red and blue patches represent positive and negative temperature anomalies in response to the NAO phases, respectively. Taken from *Stendardo* (2011).

Houssais, 2009; *Reverdin*, 2010). During positive NAO years heat is extracted from the SPG (*Delworth and Zeng*, 2016) leading to a cold SPG (*Talley et al.*, 2011) and an increased deep-water formation (*Delworth and Zeng*, 2016). Furthermore, during positive NAO years LSW production is found to be strong and anomalously cool (*Talley et al.*, 2011). During negative NAO years warmer and more saline water reaches further north into the NA (*Eden and Willebrand*, 2001). During this time the SPG is contracted and the preferred pathway of the NAC is into the Iceland basin and not into the Rockall Trough (*Bersch*, 2002). This westward shift of the SPG allows a northward penetration of the Mediterranean Overflow Water (MOW) into the Rockall Trough (*Lozier and Stewart*, 2008) and in addition the northward advance of subtropical water (*Bersch et al.*, 2007). Conversely, during positive NAO years the northward flow of the MOW is blocked by the eastward shift of the SPG (*Lozier and Stewart*, 2008), and the salinity in the Rockall Trough decreases (*Burkholder and Lozier*, 2011).

1.2. Goals and Outline

There are only a few studies that compare model output with observations in detail. The goal of this work is to extend the knowledge about the NAC and the NA in model and observations and to obtain new insights about seasonal to decadal variability and pathways of the NAC. The focus is on a detailed look at the accuracy of some of the features of the VIKING20 model configuration in comparison with observations in the NA. This is done over the entire NA and across different sections along the pathway of the NAC, from velocity, transport, temperature and salinity distributions. The flow into and out of the NA is monitored at 47°N, the flow from the western into the eastern basin of the NA is captured by a section at the western flank of the Mid-Atlantic Ridge, and the distribution in the eastern basin of the NA is observed at the OVIDE line. These three sections thus provide an extensive picture of the flow.

At 47°N *Mertens et al.* (2014) already described that the main vertical and horizontal circulation features, the strength of the NAC inflow into the Newfoundland basin, and the Newfoundland Basin Recirculation (NBR) were well simulated by the VIKING20 model configuration. They used the model to discuss the relation between the variability found in the deep western boundary current, the NAC, and the NAC recirculation. In this study the analysis of the 47°N section is extended to 2016 and the simulated transport time series is compared to an observational transport time series from 1993 to 2008. Furthermore, the entire 47°N section, from Flemish Pass to the Irish Shelf is investigated and compared.

To extend the study of the NAC and more generally of the NA, the influence of the NAO on the distribution of flow, salinity, and temperature are investigated in the model. Furthermore, the influence of the NAO on the pathway of the NAC is studied.

After the data and methods chapter (chapter 2) the model output is compared with observations in chapter 3. The analysis starts with a general comparison of the circulation in the NA before focusing on the vertical hydrographic and velocity distributions at three sections along the NAC pathway. At these sections the mean transport and the corresponding variability, the mean temperature and salinity and their evolution are investigated and compared between model and observations.

Based on the agreement between model and observations the influence of the North Atlantic Oscillation on the NA and the NAC in the model is investigated in chapter 4. After the discussion and conclusion chapter 5 the thesis ends with a summary and outlook in chapter 6.

2. Data and Methods

In this study observational data such as ship board hydrographic measurements, satellite altimetry and PIES data are compared to the high resolution VIKING20 ocean model configuration. Here the model configuration and the observational data sources are described, as well as the methods to obtain observed and simulated transport time series. The comparison focuses on three sections along the pathway of the NAC, one across 47°N, one at the western flank of the MAR and one in the eastern basin of the NA. Across these three sections different observational data are available and therefore used in this study.

2.1. VIKING20 model configuration

The VIKING20 model configuration[1] is based on the Nucleas for European Modelling of the Ocean (NEMO) ocean (*Madec*, 2008) and Louvain-la-Neuve Ice Model (LIM2) sea ice (*Fichefet and Maqueda*, 1997) model, developed in the DRAKKAR framework (*DRAKKAR*, 2007). This configuration uses a local grid refinement technique (Adaptive Grid Refinement in FORTRAN (AGRIF), *Debreu et al.* (2008)), which allows a high-resolution nest to be coupled into a coarser grid via a two-way nesting scheme (*Behrens*, 2013; *Böning et al.*, 2016). In the case of the VIKING20 configuration, the coarser grid is a global tri-polar ORCA025 grid with a nominal 1/4° horizontal resolution (*Barnier et al.*, 2006). Embedded in this grid is a high-resolution nest covering the North Atlantic between 32°N and 80°N, with grid sizes of 1/20° (Figure 2.1). The vertical grid of this configuration uses 46 vertical levels, with a 6 m thick surface layer, and increasing with depths up to layer thickness of 250 m at around 1000 m. A partial cell approach

---

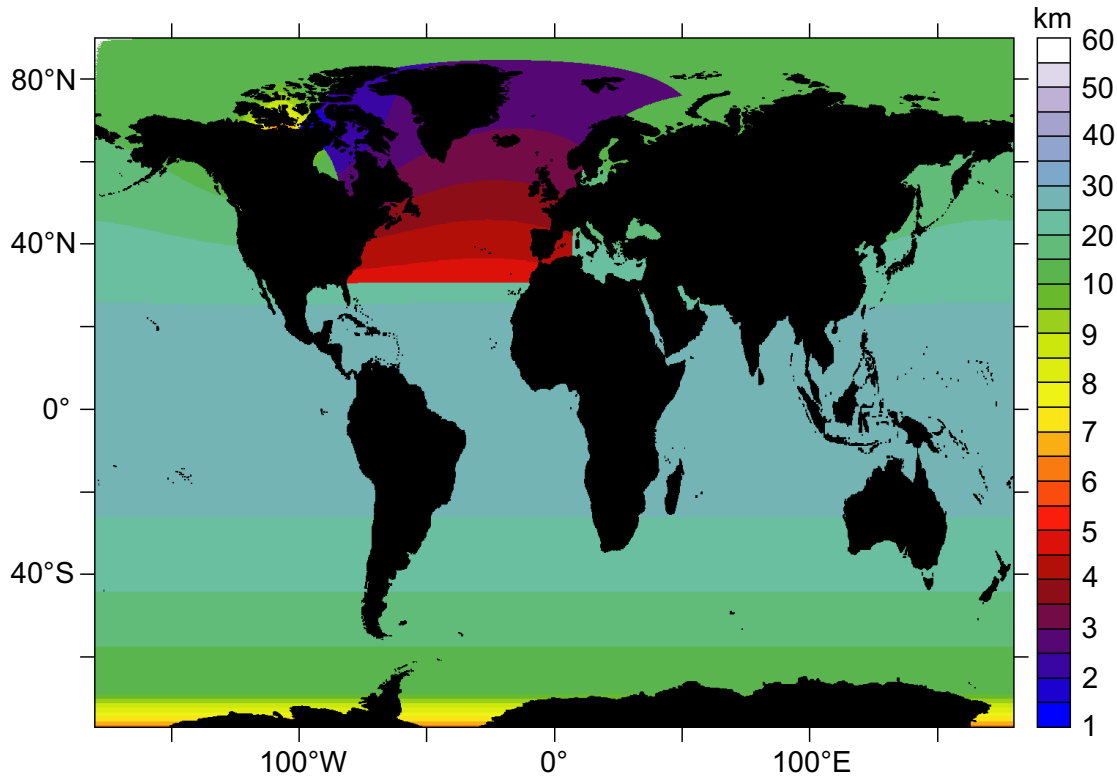[1]The VIKING20 model configuration run was done by E. Behrens

Figure 2.1.: Horizontal resolution of the VIKING20 model configuration (*Behrens*, 2013)

is implemented to improve the near topographically-steered circulation (*Barnier et al.*, 2006). In this study 5-day averaged model fields are used for the period 1960-2008, which was forced with interannually varying atmospheric conditions based on Coordinate Ocean-ice Reference Experiments II (CORE.v2) reanalysis product (*Large and Yeager*, 2009). The simulation was started from rest with initial condition based on Levitus (*Levitus*, 1998) and followed by a 30-year long spin-up simulation before the reference hindcast has been started in 1948.

Studies like *Fischer et al.* (2014), *Mertens et al.* (2014), and *Böning et al.* (2016) have shown a good performance of this simulation against observations in the subpolar North Atlantic. In *Fischer et al.* (2014) the variability of the Deep Western Boundary Current (DWBC) transport from Denmark Strait to the tail of the Grand Banks was investigated using seven observational sections in comparison to the VIKING20 model in order to relate the local observations to the large scale perspective. They reported that the DWBC in the model has its maximum vari-

ance at intra seasonal periods and the best agreement between the modeled and observed spectra is found for the Flemish Cap section at 47°N.

Along this 47°N section between Flemish Cap and 36°W *Mertens et al.* (2014) studied the strength of the NAC inflow into the Newfoundland basin, the NAC recirculation and the DWBC from seven cruises and moored data in comparison to the VIKING20 model. Adding additional freshwater near Greenland to simulate the increase of melt water from the West Greenland shelf was found to be influencing the surface salinity in the central Labrador Sea, but so far no significant impact on the AMOC in the VIKING20 model configuration was found (*Böning et al.*, 2016). The study also showed that decadal freshwater content anomalies in the subpolar NA, which have been observed by *Curry and Mauritzen* (2005) and *Boyer et al.* (2007), can be successfully simulated.

The model was initialized with the World Ocean Atlas (WOA) 1998 (*Levitus*, 1998) salinity climatology (Figure 2.2a), derived from data for the years 1900-1997. This climatology and the mean VIKING20 salinity distribution (1960-2008) in 100 m depths are comparable. However, owing to the resolution the salinity distribution in the model (0.05 ° resolution) is more detailed compared to the coarse climatology (1 ° resolution). Observed salinities in the central and northern Labrador Sea (Figure 2.2a) are fresher than found in the model (Figure 2.2b). This is even enhanced when compared to the WOA 2013 (*Zweng et al.*, 2013) climatology (Figure 2.2c), which is the average of six "decadal" climatologies for the following time periods: 1955-1964, 1965-1974, 1975-1984, 1985-1994, 1995-2004, and 2005-2012 (*Zweng et al.*, 2013). The NWC in the model evolved nicely from the WOA 1998 climatology NWC to a similar NWC as in the WOA 2013, which comprises the entire model time period.

The northwestern extension of the NWC in the model is reflected by high salinity signatures along the western flank of the Labrador Sea, with salinities > 35.4 stretching to 54°N (Figure 2.2b), while in the WOA 2013 data, this salinity does not reach farther than about 49°N (Figure 2.2c). The salinity structures in the Eastern Atlantic also show similar patterns. In the observations south of about 49°N, the observed horizontal gradients are more or less meridional (Figure 2.2 a,c), while in the model, the zonal gradients dominate (Figure 2.2b). This leads to lower salinities in that region. North of 49°N, both, model and observations exhibit
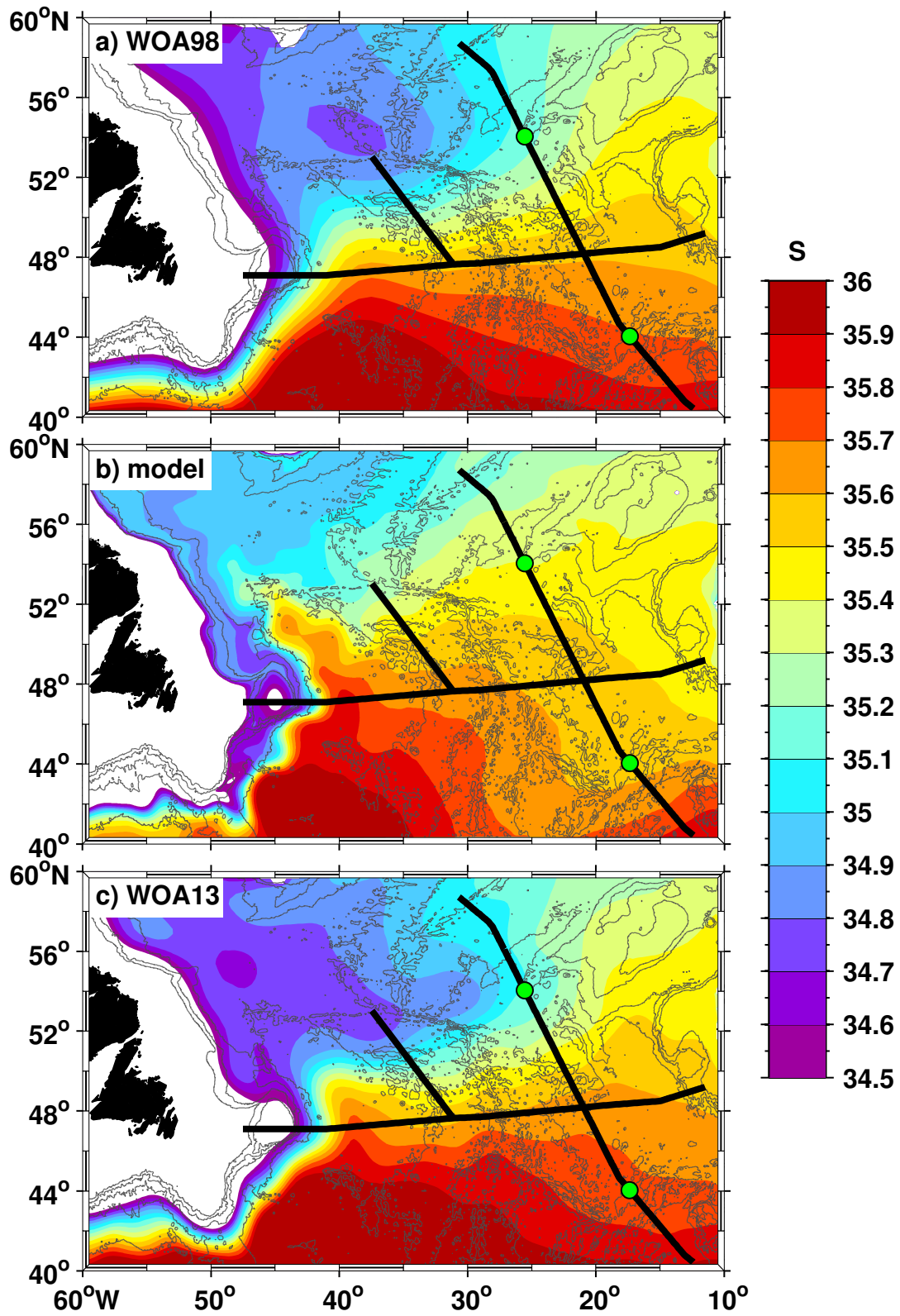
Figure 2.2.: Salinity distribution in 100 m depth from a) WOA 1998 climatology, b) the VIKING20 model mean from 1960-2008 and c) the WOA 2013 climatology. The three sections are marked.

zonal gradients, but the salinities are higher in the model than in the observations. As an example the meridional salinity difference between 41°N and 57°N at 30°W in the eastern Atlantic is around 0.4 in the model and 1.0 in the observations. The higher salinities in the VIKING20 configuration are found to be related to the improvements in the NAC compared to two coarser model configurations (*Behrens*, 2013). The salinity in the Labrador Sea rises by the increased inflow of warmer and saltier Irminger Water, which accompanied the improvement of the NAC.

2.2. Observational data

2.2.1. Absolute geostrophic surface velocity

The absolute geostrophic surface velocity used here is provided by Ssalto multimission ground segment (Ssalto)/Data Unification and Altimeter Combination System (Duacs) and distributed by Archiving, Validation and Interpretation of Satellite Oceanographic data (AVISO) with support from Centre National d'Études Spatiales (CNES)[2]. It is computed from the daily Map of Absolute Dynamic Topography (MADT) and has a spatial resolution of $1/4°\text{x}1/4°$ on a Cartesian grid. The MADT is inferred from the sea level anomaly and the Mean Dynamic Topography (MDT), both are referenced over a twenty-year period (1993-2012). The MDT is a combination of seven years of Gravity Recovery And Climate Experiment (GRACE), two years of Gravity field and steady-state Ocean Circulation Explorer (GOCE) data and in situ measurements.

2.2.2. Hydrographic data

The hydrographic data across the 47°N section and along the MAR were taken during the summer months on various ship cruises. Across the MAR eight repeated sections were taken between July 2008 and May 2016 (Table 2.1). At the 47°N section data from 14 ship cruises were taken between July 2003 and May 2016 (Table 2.2). Only the Maria S. Merian cruises MSM28 and MSM53 and the Meteor cruise M85/1 occupied the entire section from 47°-11°W (Figure A.1 and Figure

---
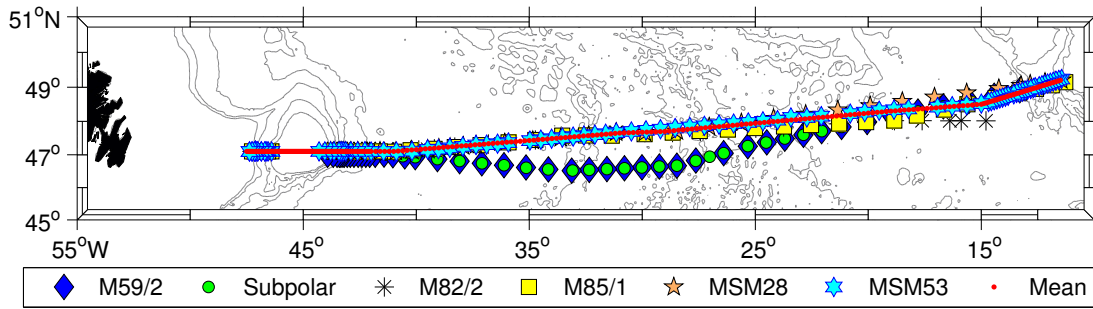
[2]`www.aviso.altimetry.fr/duacs/`

Figure 2.3.: CTD and lADCP measurement positions from some cruises along the 47°N section (Table 2.2). The red points show the mean track on which the individual sections were interpolated. The section starts in the west at the Flemish Pass, crossing the Flemish Cap and the MAR and ends in the east at Goban Spur at the Irish shelf break.

A.2). The mean section on which the individual sections were interpolated and merged to one section is therefore orientated on these cruise tracks (Figure 2.3). The Meteor cruise M59/2 in 2003 and the Subpolar cruise with the french vessel Thalassa in 2005 started around 44/43°W and ended around 13°W but followed in between a more southern track. This track was also occupied in the years 2007 and 2008 with the Maria S. Merian cruises MSM5/1 and MSM9/1. From 2009 onward the cruise tracks followed the more northern section, but individual cruise

Table 2.1.: Cruises along the MAR section

Cruise	Ship	Month/Year	Stations
MSM9/1	Maria S. Merian	07-08/2008	18
M82/2	Meteor	08-09/2010	19
M85/1	Meteor	06-08/2011	20
MSM21/2	Maria S. Merian	06-07/2012	18
MSM28	Maria S. Merian	05-06/2013	22
MSM38	Maria S. Merian	05-06/2014	20
MSM43	Maria S. Merian	05-06/2015	17
MSM53	Maria S. Merian	03-05/2016	20

Table 2.2.: Cruises along the 47°N section

Cruise	Ship	Month/Year	Longitude	Stations
M59/2	Meteor	07-08/2003	44° - 13°W	47
Subpolar	Thalassa	06-07/2005	43° - 13°W	38
MSM5/1	Maria S. Merian	04-05/2007	44° - 41°W	13
MSM9/1	Maria S. Merian	07-08/2008	44° - 29°W	28
MSM12/3	Maria S. Merian	07-08/2009	47° - 31°W	26
M82/2	Meteor	08-09/2010	47° - 15°W	47
M85/1	Meteor	06-08/2011	47° - 11°W	46
MSM21/2	Maria S. Merian	06-07/2012	47° - 31°W	31
MSM27	Maria S. Merian	04-05/2013	47° - 43°W	16
MSM28	Maria S. Merian	05-06/2013	47° - 11°W	40
MSM38	Maria S. Merian	05-06/2014	47° - 29°W	52
MSM42	Maria S. Merian	05-05/2015	47° - 45°W	16
MSM43	Maria S. Merian	05-06/2015	44° - 31°W	24
MSM53	Maria S. Merian	03-05/2016	47° - 11°W	102

tracks started and ended on different positions (Table 2.2, Figures A.1,A.2).
The obtained shipboard hydrographic data were interpolated onto a regular grid
with 10 m vertical resolution. The horizontal spacing differs along the 47°N section
and the section along the MAR. At 47°N the mean track starts in the Flemish Pass
with a resolution of around 2 nautical mile (1 nm = 1.852 km) (nm) and decreases
to around 8 nm in the interior of the basin. In the eastern part of the section the
horizontal resolution increases to 4 nm at the Irish shelf. Individual cruise tracks
show different horizontal resolution (Figures A.1, A.2). The stations spacing along
the MAR array was around 20 nm (Figure A.9).

The velocity measurements were done by lowering two Teledyne-RD Workhorse
Monitor lowered Acoustic Doppler Current Profilers (lADCPs) operating on
300 kHz. The instruments worked in a synchronized mode at a ping rate of 1 Hz
and 10 m depth bins, one ADCP was upward and one downward looking. The

Table 2.3.: Cruises along the OVIDE line

Cruise	Ship	Month/Year	Reference
OVIDE 2002	Thalassa	06-07/2002	*Lherminier et al.* (2007)
OVIDE 2004	Thalassa	06-07/2004	*Lherminier et al.* (2010)
OVIDE 2006	Maria S. Merian	05-06/2006	*Gourcuff et al.* (2011)
OVIDE 2008	Thalassa	06-07/2008	*Mercier et al.* (2015)
OVIDE 2010	Thalassa	06-07/2010	*Mercier et al.* (2015)

obtained velocity profiles were treated as described by *Visbeck* (2002) and in addition a tidal model (TPXO7.2 tidal model (*Egbert and Erofeeva*, 2002)[3]) was used to detide the velocity data. The maximum tidel velocity along the 47°N section was found slightly inshore of 43°W from which it decreases further offshore, which was already described by *Mertens et al.* (2014) and *Schneider et al.* (2015). Across the MAR section the maximum tidal influence was found to be 3 cm/s. This value was found on various locations during the observation period.

To measure salinity, temperature and pressure a Sea-Bird Electronics SBE 911plus Conductivity, Temperature, Depth (CTD) sensor was used on each cruise and lowered along with the ADCPs. Salinity was calibrated by comparing the CTD measurements to water samples from Niskin bottles, lowered along with the instruments. The root mean square error between calibrated CTD salinity and bottle salinity was between 0.0015 and 0.003. The uncertainty for the salinity is 0.002-0.003 (*Rhein et al.*, 2011). The uncertainty of the temperature measurement from the SBE 911plus is around 0.002-0.003°C, the initial accuracy of the temperature sensor is 0.001°C with a typical stability of 0.0002°C per month (*Sea-Bird Electronics*, 2016). The initial accuracy of the pressure sensor is about 1 m and it has a typical stability of 1.4 m per year (*Sea-Bird Electronics*, 2016).

The OVIDE data set in the eastern basin of the NA comprises five repeated measurements for every second year between 2002 and 2010 (Table 2.3) and was provided by Pascale Lherminier and published in *Mercier et al.* (2015). Along

---

[3]http://volkov.oce.orst.edu/tides/TPXO7.2.html

the OVIDE line about ninety hydrographic stations were taken each cruise. The station spacing was between 25 nm and less than 12 nm, depending on topographic features (*Mercier et al.*, 2015).

2.2.3. Pressure-equipped Inverted Echo Sounders (PIES)

The Pressure-equipped Inverted Echo Sounders (PIES) instruments are deployed along the MAR (Table 2.4) and 47°N (Table 2.5) sections (Figure 2.4). The deployment along the MAR section started in 2006 with four PIES instruments and is still ongoing. Here PIES data until 2010 are taken into account. During this time period three different instruments were deployed at the BP12 position (BP stands for "Bremen PIES") (*Roessler et al.*, 2015). The mean depth and position of these three instruments are used in the model (Table 2.4) and shown in the overview of the PIES instrument positions (Figure 2.4). The geographical positions of the PIES instruments are at the western flank of the MAR, below the crest of the ridge and near a crossing point of the ground track of the TOPEX/Poseidon/Jason-1/Jason-2 satellites (*Roessler et al.*, 2015). Furthermore the positions were based on the observed flow field inferred from drifters (*Reverdin et al.*, 2003; *Brambilla*

Table 2.4.: PIES overview along the MAR section. This data were used by *Roessler et al.* (2015) to calculate the observed transport time series along this section. During this time period three different instruments were deployed at the BP12 position. Here the mean depth and position of these three instruments as a reference for the section in the model is given. Due to instrument lost there are no data at the BP12 position from 08/2008 until 11/2009. For more details see *Roessler et al.* (2015), their Figure 8 and Table 1.

PIES	Deployment period	Depth [m]	Position
BP12	08/2006-08/2010	3996	47°40.17'N / 31°09.43'W
BP13	08/2006-08/2010	3948	49°00.86'N / 32°36.87'W
BP14	08/2006-11/2009	3602	51°25.64'N / 35°26.29'W
BP15	08/2006-08/2010	3437	52°30.56'N / 36°51.10'W

Table 2.5.: PIES overview along the 47°N section

PIES	Deployment period	Depth [m]	Position
BP27	06/2014-04/2016	4486	47°05.84'N / 40°52.53'W
BP28	05/2013-04/2016	4578	47°09.68'N / 39°30.06'W
BP29	05/2013-04/2016	4607	47°12.52'N / 38°31.09'W
BP30	05/2013-04/2016	4546	47°17.52'N / 37°21.47'W
BP31	05/2014-04/2016	4236	47°05.84'N / 41°59.94'W

and Talley, 2006) to cover the flow of the NAC into the eastern subpolar North Atlantic (*Rhein et al.*, 2011).

At 47°N the PIES deployment of the instruments taken into account to calculate the transport considered here started in 2013. The five PIES are located in the western basin of the NA near the continental shelf to capture the flow of the NAC into the NA and the NBR, as well as partly the Western Boundary Current (WBC) towards the south. The southernmost PIES at the MAR section (BP12) is deployed along the 47°N section and is therefore used in combination with the
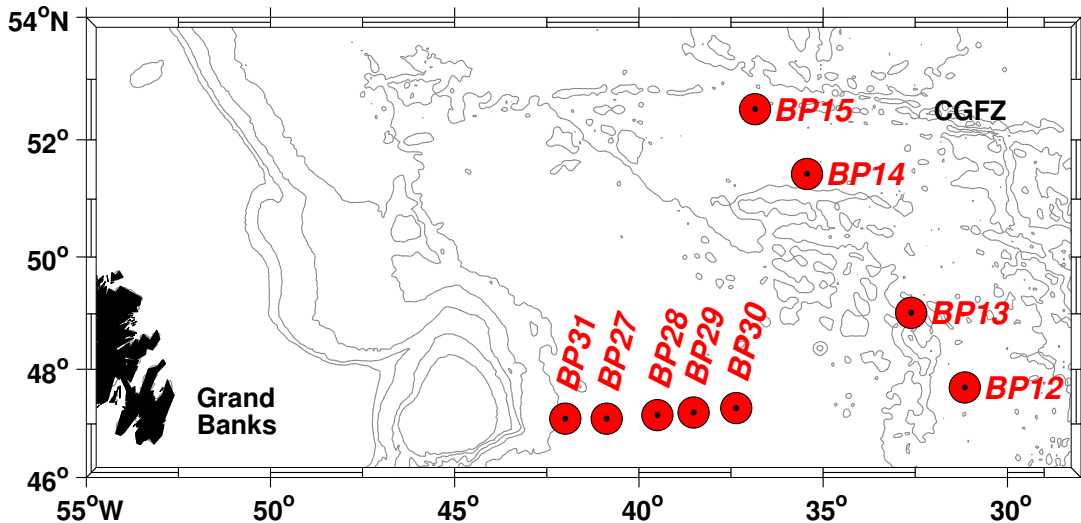

Figure 2.4.: PIES instrument locations along the 47°N and the MAR sections.

PIES instruments in the western basin.

The PIES instruments are mounted to a tripod and deployed from ships in a free fall procedure. After the deployment the position of the PIES instrument at the sea floor is measured in a trilateral technique from the ship. The PIES instrument measures the round trip travel time of an acoustic signal from the bottom to the surface and the pressure at the sea floor (*Watts and Rossby*, 1977; *Chaplin and Watts*, 1984). The instrument works with 24 pings per hour at a frequency of 12 kHz (*University of Rhode Island*, 2015). The travel time is converted with use of Global array of temperature/salinity profiling floats (Argo) and shipboard CTD profiles to profiles of temperature, salinity, density, and specific volume anomaly. The uncertainty of the mean travel times are 0.14 milliseconds (*Roessler et al.*, 2015).

2.3. Transport calculation

Along the path of the NAC at the three different sections transport measurements are compared with the model output. Along the 47°N and the MAR sections the deployed PIES instruments were used in combination with satellite altimetry data to obtain transport time series. At the OVIDE line the observed transport calculations are based on five repeated cruise tracks between 2002 and 2010.

2.3.1. Transport time series from PIES instruments

PIES instruments are deployed along the MAR (Table 2.4) and the 47°N (Table 2.5) sections. The observed transport time series along the MAR section is taken from *Roessler et al.* (2015) and the observed transport across the 47°N section is provided personally by A. Roessler[4].

---

[4]Observed transport across the 47°N section is provided by A. Roessler and is part of a joint paper in preparation

Transport at the MAR section

Across the MAR section the observed baroclinic transport time series from 1993 until 2008 is calculated from a combination of along-track Sea Surface Height (SSH) measurements (updated delayed time Sea Level Anomaly (SLA) product from AVISO) and PIES data (*Roessler et al.*, 2015). The PIES instrument measures the round trip travel time of an acoustic signal from the bottom to the surface and the pressure at the sea floor (*Watts and Rossby*, 1977; *Chaplin and Watts*, 1984). *Roessler et al.* (2015) defined the baroclinic transport component of the geostrohpic transport as the component resulting from temperature and salinity fields, following e.g. *Guinehut et al.* (2006) and *Meijers et al.* (2011).

Argo and shipboard CTD profiles are used to calculate a transfer function to convert travel times to profiles of temperature, salinity, density, and specific volume anomaly. Based on these reconstructed time series, the geostrophic velocity distribution and transport time series are calculated relative to a reference level. *Roessler et al.* (2015) referenced the transports to the deepest common depth of the PIES (3400 dbar), which is located well below the ridge crest of the MAR. Owing to the unknown drift of the pressure sensors, only the barotropic transport fluctuations can be analyzed. Their contribution to the standard deviation of the mean 4-year transport time series exceeds the contribution from the baroclinic transport component by around one third. *Roessler et al.* (2015) used the correlation between the altimeter derived surface velocities and the baroclinic transports calculated from the PIES data to extend the 4-year transport time series to the time period of the altimeter measurements (1993 – 2013). The barotropic transport fluctuations were found not to be correlated with the satellite altimetry data (*Roessler et al.*, 2015), therefore only the baroclinic transport component could be extended over the whole satellite time period. Following earlier studies (e.g. *Stramma et al.*, 2004; *Rhein et al.*, 2011) *Roessler et al.* (2015) chose the isopycnal $\sigma_\theta = 27.68 \, \text{kg/m}^3$ to separate the warm subtropical water of the NAC above from the deep water layers below that depth and found 60 % of the transport above this isopycnal. In this study the same percentage is used to separate the observational transport at the PIES array at the MAR into a subtropical and deep water component. The geographical positions of the PIES divide the section into three segments, roughly representative of the flow through Maxwell (southern segment),

Faraday (central segment) and Charlie Gibbs (northern segment) fracture zones.

Transport at the 47°N section

The observed transport time series across the 47°N section are calculated from PIES instruments in combination with Argo and shipboard CTD profiles.[5]. Along this section due to strong velocities near the sea floor no level of no motion could be identified. Therefore the velocity profiles were referenced to MADT product of AVISO. The mean offset was calculated based on daily measurement differences between the mean absolute geostrophic surface velocity from AVISO and the PIES velocity profiles over the deployment period of the PIES. This procedure changes only the mean and makes the transport absolute. The correlation (correlation coefficients between 0.81 and 0.86) between the up to three year long absolute PIES transports and the altimeter derived surface velocities are used to extend the transport time series to the time period of the altimeter measurements (1993 - 2016).

The geographical positions of the PIES instruments along the 47°N section (Figure 2.5) divide the section into different subsections in which different dominating currents are flowing. The NAC is the northward transport between the PIES instrument 30 and 31 (Figure 2.5). The southward flow between the two westernmost PIES is part of the southward flowing WBC, which reaches further west above the continental slope until the Flemish Cap (*Mertens et al.*, 2014). The part captured by the PIES instruments is here called Southward flow (SWF). Further east between PIES 27 and 30 the southward flow is the NBR, which was investigated from shipboard measurements at around the same location by *Mertens et al.* (2014). Further east until the MAR (between PIES location 30 and 12) the net transport across the section is here called Newfoundland Basin flow (NFB).

---

[5]A. Roessler provided the observed transports across the 47°N, they are part of a joint paper in preparation.
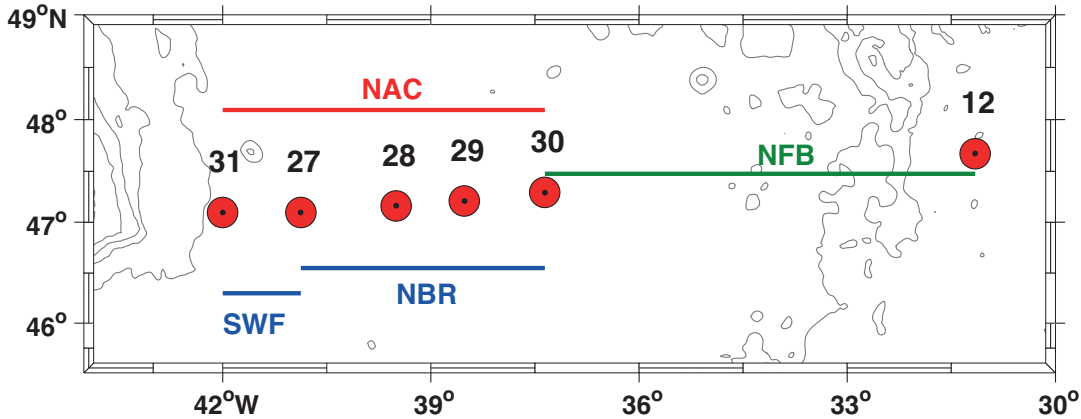
Figure 2.5.: PIES instrument locations along the 47°N section. The longitudinal range of different currents crossing the section are marked. The NAC (red) is defined as the northward flow between PIES 31 and 30. Southward flow (SWF) and NBR (blue) are both flowing towards the south and the net flow between PIES 30 and 12 is the NFB flow (green).

2.3.2. Transport calculation along the OVIDE line from Portugal until Reykjanes Ridge

The absolute transports across the OVIDE line were calculated from a combination of the CTD data and ship-mounted ADCP data by using an inverse model based on the least squares formalism (*Lherminier et al.*, 2010; *Mercier et al.*, 2015)[6]. For the transport calculations the eastern OVIDE section is divided into the subsections Iceland (58°N-54°N), European (54°N-44°N), and Iberian (44°N -41°N) following *Mercier et al.* (2015). The geographical positions of the two NAC branches (Figure 1.1) at the OVIDE line differ between model and observations. The observed WNAC branch is found between 53°30'N and 57°N, while in the model the WNAC is shifted towards the north and reaches to 57°30'N. The ENAC in the observations is defined to flow between 46°N and 53°30'N, while in the model, the pathway is located between 47°30'N and 53°30'N. As stated before, the same isopycnal ($\sigma_\theta = 27.68 \, \text{kg/m}^3$) was used to separate the upper from the deep ocean.

---

[6]The OVIDE data were provided by P. Lherminier and are published in *Mercier et al.* (2015). The data are available at `www.seanoe.org` (*Mercier et al.* (2016); *Daniault et al.* (2016b))

2.3.3. Transport calculation in the model

The VIKING20 model configuration is calculated on a horizontal tri-polar grid, with one pole in the south and two poles in the north, one over Siberia and the other one over Canada to avoid singularities at the geographic North Pole (*Behrens*, 2013). The output data are horizontally discretized on an Arakawa C-grid (Figure 2.6), i.e. the u-velocity components are located at the left and right grid faces, the v-velocity components at the centers of the upper and lower grid faces and temperature and salinity are located on the grid center (*Arakawa and Lamb*, 1977).

In order to compare the output with the observations the simulated data have to be rotated/transformated[7] on the longitude, latitude geographic coordinate system. To do so the simulated velocity components (u_s and v_s) are calculated onto
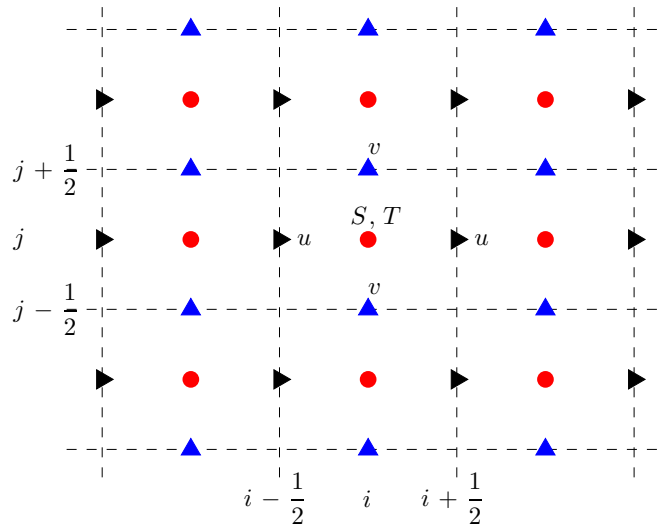

Figure 2.6.: Horizontal schema of Arakawa C-grid. u (black) and v (blue) mark the velocity component position and S, T (red) the temperature, salinity location. i, j are the indices of the grid points in the x and y directions, respectively.

---

[7]Coordinate transformation are described e.g. by *Nolting* (2011)

the grid center:

$$ut = 0.5 \cdot (u_s(i - 0.5, j) + u_s(i + 0.5, j))$$
$$vt = 0.5 \cdot (v_s(i, j - 0.5) + v_s(i, j + 0.5))$$

i, j are the indices of the grid points in the x and y directions, respectively. The rotation on the geographic coordinate system is done by using the angle ϕ between the simulated and the geographic coordinate systems:

$$u(lon, lat) = ut \cdot cos(\phi) - vt \cdot sin(\phi)$$
$$v(lon, lat) = ut \cdot sin(\phi) + vt \cdot cos(\phi)$$

To investigate the simulation output on the three sections considered in this study, the data are bilinear interpolated[8] onto the required geographical position $P = (x, y)$ (Figure 2.7). First the four neighboring points $I_{ij} = (x_i, y_j)$ used in the bilinear interpolation are linearly interpolated into the x-direction, the subscripts
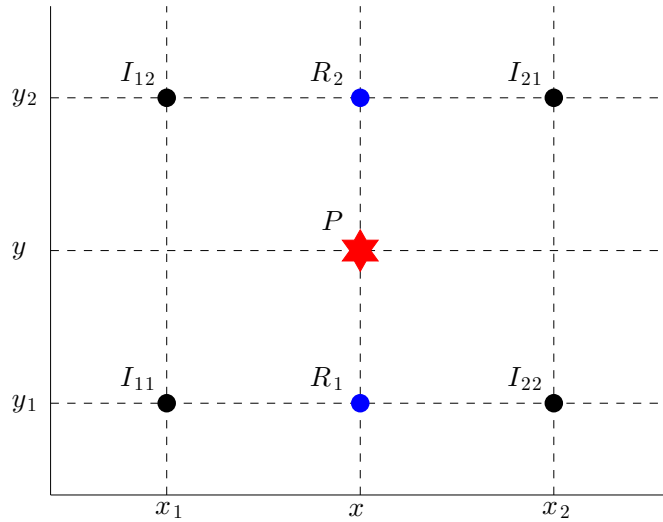

Figure 2.7.: Schema of bilinear interpolation. I_{ij} (black) are the four neighboring points, which are used to interpolate onto the required geographical position P (red). R_i (blue) are support points.

---

[8]Bilinear interpolation is described e.g. by *Acharya and Tsai* (2007)

1 and 2 stands exemplarily for the indices i and j:

$$R_1 = \frac{x_2 - x}{x_2 - x_1} \cdot I_{11} + \frac{x - x_1}{x_2 - x_1} \cdot I_{21}$$

$$R_2 = \frac{x_2 - x}{x_2 - x_1} \cdot I_{12} + \frac{x - x_1}{x_2 - x_1} \cdot I_{22}$$

where $R_j = (x, y_j)$ are support points. From these support points the further interpolation is done in the y-direction onto the required position P:

$$
\begin{aligned}
P &= \frac{y_2 - y}{y_2 - y_1} \cdot R_1 + \frac{y - y_1}{y_2 - y_1} \cdot R_2 \\
&= \frac{(x_2 - x)(y_2 - y)}{(x_2 - x_1)(y_2 - y_1)} \cdot I_{11} + \frac{(x - x_1)(y_2 - y)}{(x_2 - x_1)(y_2 - y_1)} \cdot I_{21} \\
&\quad + \frac{(x_2 - x)(y - y_1)}{(x_2 - x_1)(y_2 - y_1)} \cdot I_{12} + \frac{(x - x_1)(y - y_1)}{(x_2 - x_1)(y_2 - y_1)} \cdot I_{22} \\
&= \frac{1}{(x_2 - x_1)(y_2 - y_1)} \cdot [x_2 - x \quad x - x_1] \cdot \begin{bmatrix} I_{11} & I_{12} \\ I_{21} & I_{22} \end{bmatrix} \cdot \begin{bmatrix} y_2 - y \\ y - y_1 \end{bmatrix}
\end{aligned}
$$

This interpolation has to be performed for each variable and onto all three sections.

The observed transport from the PIES instruments are defined as perpendicular to the section. Therefore, the transformed and interpolated simulated velocities $\vec{v}$ are projected along the normal of the section $\vec{n}$. The projected velocity magnitude $|\vec{v}_n'|$ along the normal can be calculated by:

$$|\vec{v}_n'| = \vec{v} \cdot \hat{n}$$

In order to correctly project the velocities one has to incorporate that a degree in longitude in the geographical coordinate system has to be scaled by cosine of the latitude.

The simulated absolute volume transports across the sections are obtained by multiplying each velocity magnitude $|\vec{v}_n'|$ with the corresponding grid area and than take the sums over the entire section and from the surface until the required depth level.

The observed 21-year NAC transport time series at the western flank of the MAR

is referenced to 3400 dbar and only includes the baroclinic transport component, which is calculated from the density field. To calculate this baroclinic transport *Roessler et al.* (2015) used the specific volume anomaly δ to obtain geostrophic velocities at the PIES positions along the MAR. The simulated baroclinic transport is calculated from the simulated salinity and temperature fields. Therefore, the mean relative velocities (geostrophic velocity) v_g between the two end points A, B of the section are calculated by (e.g. equation 8.9A, p.73 *Pond and Pickard*, 1989):

$$
\begin{aligned}
v_g &= \frac{1}{L2\Omega sin\phi} \cdot \left[\int_{p_1}^{p_2} \delta_B dp - \int_{p_1}^{p_2} \delta_A dp \right] \\
&= \frac{1}{L2\Omega sin\phi} \cdot [\Delta\Phi_B - \Delta\Phi_A]
\end{aligned}
$$

with the Coriolis parameter $2\Omega sin\phi$, including the angular velocity of the Earth's rotation Ω and latitude ϕ. L is the distance between A and B, p_i are isobaric surfaces between A and B at different depths, δ_i is the specific volume anomaly and $\Delta\Phi_i$ the geopotential anomaly at A and B. The simulated baroclinic transport is calculated by vertically integrating the geostrophic velocities between A and B and multiplying with the respective distance L.

At the MAR the simulated section starts at the southernmost PIES position (47°40'N/31°09'W) and ends at around 53°N/37°27'W, i.e. 0.5° further north than the northernmost PIES position (52°30'N/36°51'W, Table 2.4). This extension takes into account the more northward flow path in the model (Figure 3.1). An extension of the section towards the southeast did not increase the northeastward mean transport across the section. As in the observations, the modeled transports are separated in the three segments (northern, central and southern segment), with an additional model segment from 52°30'N to 53°N (extended segment).

At the 47°N and OVIDE sections the simulated transport sections are at the same geographical positions as the observed. Here the observed transports are absolute transports and no simulated baroclinic transports are calculated. Along the 47°N section the simulated transports are separated as in the observations in NAC, SWF, NBR and NFB defined by the PIES positions (Figure 2.5). Additionally, the entire WBC was calculated as defined by *Mertens et al.* (2014), as well as the transport through the Flemish Cap and the flow in the eastern basin of the NA. At the OVIDE line the simulated transports are separated according to the

observations into Iceland, European and Iberian basins following *Mercier et al.* (2015) and into WNAC and ENAC branches of the NAC. The WNAC branch is defined further north in the simulation than in the observations by around half a degree and the simulated ENAC is more concentrated than the observed one, it starts around 1.5° further north but ends at the same geographical position as the observations.

Along all three sections the water column is separated into the subtropical water mass above the $\sigma_\theta = 27.68\,\mathrm{kg/m^3}$ isopycnal and into the deep ocean below this density, as in the observations. The simulated and observed annual mean transports are affected by the large variability on time scales of several months to years. For a better comparison we follow *Roessler et al.* (2015) who calculated the annual means with the center around the end of January. This time interval was chosen to match the time period of the winter NAO index.

3. The North Atlantic Current in model and observations

The circulation system in the NA is analyzed from observational data in comparison with a high resolution model output. To further understand the properties of the NAC different sections along its pathway from the Newfoundland basin into the eastern basin of the NA are investigated. The investigation is based on three observational sections, one at 47°N in the Newfoundland basin, one along the Mid-Atlantic Ridge and one further east between Portugal and Greenland. At these sections hydrographic properties, velocity and transport estimates are investigated and compared between observations and the model output.

3.1. Circulation and mean transport of the North Atlantic Current

The most distinct feature in the subpolar NA is the NAC, which flows from the southwest into the eastern Atlantic, via the NWC and across the MAR. The path of the NAC is clearly visible in the mean (1993-2008) near surface velocity (100 m depth) of the model (Figure 3.1a), and in the mean surface velocity field calculated from the altimeter observations for the same time period (Figure 3.1b). Along the NAC path transports from model and observations are compared on several locations and presented in Figure 3.2. The modeled transports (Figure 3.2a) are the absolute mean transports for the time period 1993 – 2008, the same period where observations are available. The observations at 47°N in the Newfoundland Basin (2003-2011 (*Mertens et al.*, 2014)) and at the OVIDE line in the eastern Atlantic (2002, 2004, 2006, 2008, and 2010 (*Mercier et al.*, 2015)) are based on
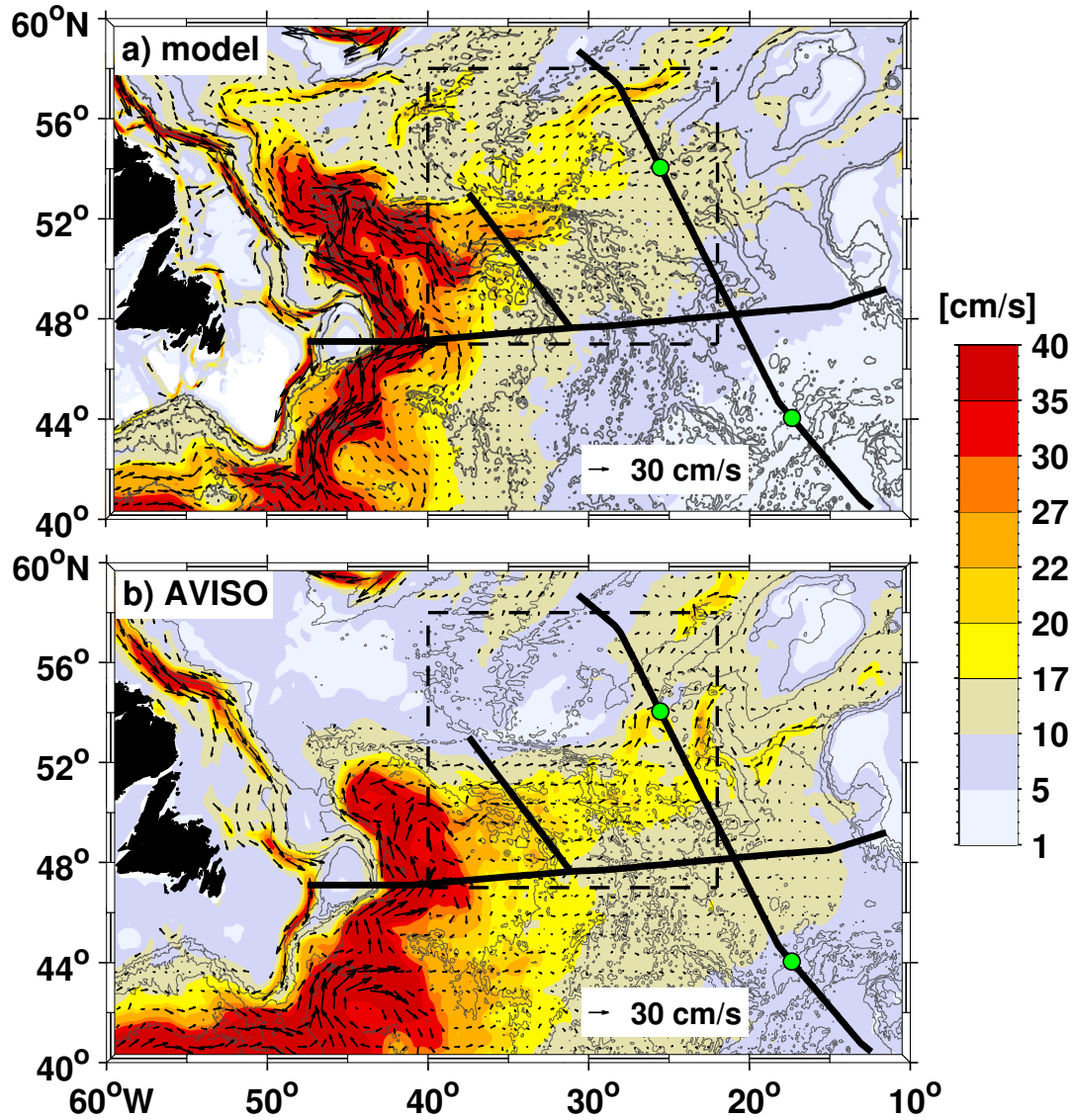
Figure 3.1.: a) Mean velocity at 100 m depth from the model, 1993- 2008. The colors are displaying the magnitude of the velocity vectors with a resolution of 1/20°. The arrows indicate the direction of velocities > 10 cm/s. The region within the dashed black lines is displayed in more detail in Figure 3.3. The 47°N, the MAR and the OVIDE sections are also shown. The bottom topography is taken from the model. b) The same as a) but for the observed absolute surface geostrophic velocity from AVISO averaged from 1993 to 2008, resolution 1/4°. Bottom topography is taken from ETOPO2 database (*Etopo2*, 2001). In both figures grey lines indicate the topography with a depth interval of 1000 m between 5000 m depth and the surface. For clarity the velocity vectors are displayed with a reduced resolution.
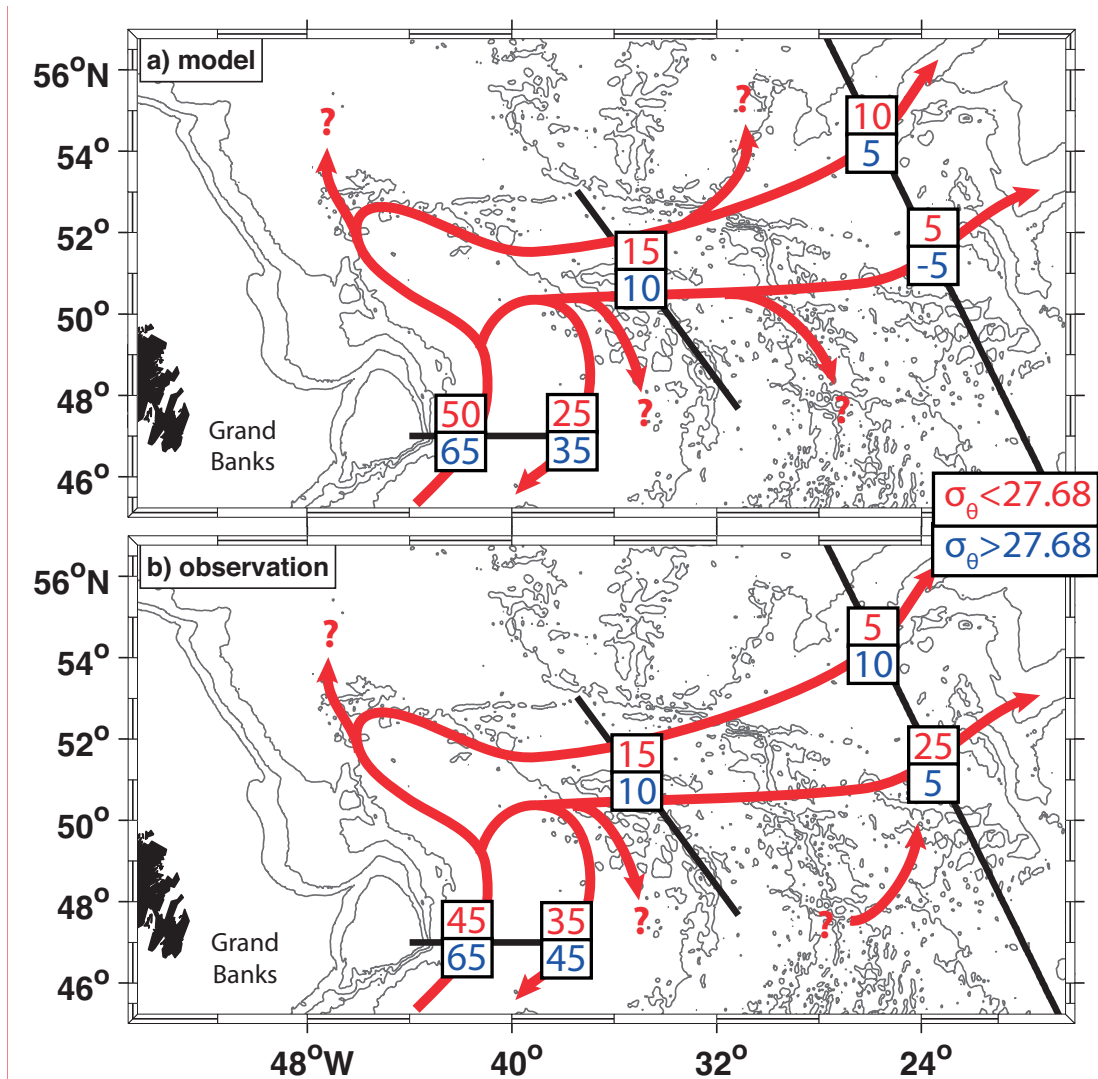
Figure 3.2.: NAC circulation cartoon (not water masses) with a) absolute mean transports from the model from 1993 until 2008 and b) observed transports. The calculation of the mean transports focuses on the two observational sections, studied here and the inflow of the NAC into the NA at 47°N. The question marks indicate possible pathways influencing the means compared here. The observed NAC and NBR transports at 47°N are taken from *Mertens et al.* (2014), and are the means of six lADCP repeats taken between 2003 and 2011. The observed transport at the PIES array is the mean from 1993 until 2008, the separation into the two density ranges are done after *Roessler et al.* (2015). Observed western and eastern NAC transports at the OVIDE line are calculated from the OVIDE data, five lADCP repeats taken between 2002 and 2010 (*Mercier et al.*, 2015). Red numbers: NAC transport with $\sigma_\theta < 27.68 \, \mathrm{kg/m^3}$, blue: transport of water with $\sigma_\theta > 27.68 \, \mathrm{kg/m^3}$ (after *Mertens et al.* (2014)). The transport numbers are rounded to 5 Sv. Figure is taken from *Breckenfelder et al.* (2017).

several repeated hydrographic and lADCP sections, so the mean transport has large uncertainties and the numbers are rounded. A more detailed comparison with continuous time series at the MAR and across the 47°N sections, as well as a discussion about the circulation and the transport at the OVIDE line follows in section 3.3.

The high velocities at the continental slope off Canada and Greenland highlight the WBC that transports cold and fresh water to the south. The Mann Eddy (∼42°N, 45°W) and the Newfoundland Basin recirculation (NBR, *Mertens et al.* (2014)) centered at 47°N, 39°W are clearly visible in the model and observational velocity distributions (Figure 3.2).

At 47°N, the observed and simulated northward inflow of the NAC occurs close to the WBC and show in terms of volume transport similar strengths. These confirm the findings of *Mertens et al.* (2014), which described and compared the observed transports to a mean VIKING20 transport calculated over 47 years. They reported that the NAC carries in both cases a similar amount of transport northward and the recirculation in the Newfoundland basin seems weaker in the model. North of 45°N, the NAC flows in close contact with the WBC east of Flemish Cap to about 54°N in the model (Figure 3.2a), and 51°N in the observations (Figure 3.2b). In the southern Labrador Sea, the observations depict two main pathways where the NAC retroflects to the east at about 48.5°N and 51.5°N, the latter defining the observed location of the NWC. In the model (Figure 3.2a), the NAC reaches further into the Labrador Sea to about 54°N before turning east. Part of the modeled mean flow seems to proceed farther north than the observations suggest. A realistic simulation of the NAC in the Newfoundland Basin has been, and continues to be, a key challenge of ocean and climate modeling. The prime model factor that influences this regional behavior is the horizontal resolution: while the common problem of coarse ocean/climate models is a southward displacement of the NAC (associated with a cold and fresh bias in the Newfoundland Basin), a typical feature of eddying models has been a northward shift of that path (*Marzocchi et al.*, 2015), hinting at the importance of the mesoscale current-topography interaction along the continental slope. It is conceivable that the dynamics near the boundary are also affected by the parameterization of subgrid-scale mixing: however, to our knowledge these possible dependencies have not been examined yet (owing certainly in part to the high costs of conducting systematic model sen-

sitivity experiments at resolutions of 1/10° or higher). One interesting hint in this regard has been given by *Smith et al.* (2000): in their 1/10° simulation they noted a northward displacement of the NWC which partly could be remedied in a (albeit very short) sensitivity experiment with somewhat increased mixing coefficients.

The mean transport crossing the MAR is similar in the observations and in the model, about 25 Sv cross the MAR towards the eastern Atlantic, with 15 Sv of subtropical origin. The mean (1993-2008) observed flow field in the vicinity of the PIES array at the MAR (Figure 3.3b) shows predominant zonal velocities to the east in a broad path with the highest velocities between 48°N and 51°N, i.e. the central segment of the PIES array. Some of the NAC in the model also follows this path, although the dominant pathway there is farther north between 51°N and 53°N, exhibiting velocities that exceed 30 cm/s (Figure 3.3a). In the model the NAC clearly prefers the flow through the CGFZ, while in the observations, the
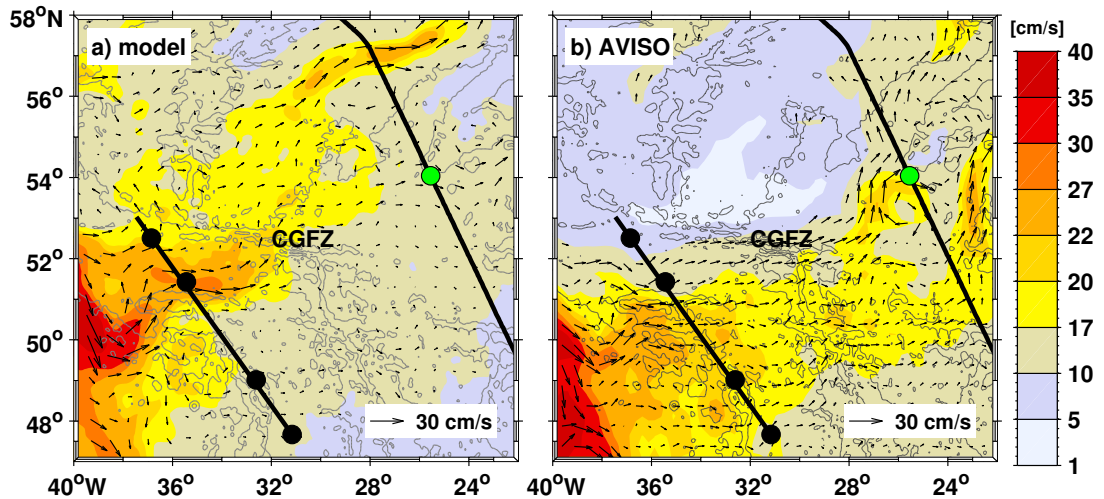

Figure 3.3.: Velocity field as in Figure 3.1, but zoomed into the marked area. The black lines show the location of the PIES array at the MAR, including the model extension and the location of the OVIDE line. Black dots are the location of the PIES. The green dot indicates the geographical separation of the OVIDE line in Iceland Basin and European Basin following (*Mercier et al.*, 2015). The Charlie Gibbs Fracture Zone (CGFZ) is marked. a) Mean modeled velocities at 100 m depth (1993 – 2008). b) Mean geostrophic velocity at the sea surface from AVISO (1993 - 2008).

NAC is mainly found farther south. The preference for the CGFZ could be due to the more northern NWC in the Labrador Sea. The more northern pathway of the NAC is at least partly responsible for the higher salinities found in the eastern Atlantic north of 49°N (Figure 2.2b, mean modeled salinity distribution from 1960-2008) in the model. Furthermore, this northern NAC is fresher compared to the branch south of the CGFZ.

In the eastern Atlantic, the observations (Figure 3.1b, Figure 3.3b) show two main NAC pathways, with the more northwestern branch (dubbed WNAC by *Lherminier et al.* (2010)) following the western flank of the Iceland basin, and the more southeastern branch (ENAC) at the Rockall Trough. In the observations the ENAC (25 Sv) carries most of the water with $\sigma_\theta < 27.68\,\mathrm{kg/m^3}$ (Figure 3.2b), while in the model, the WNAC transport is more pronounced (10 Sv) compared to the ENAC (5 Sv). This more pronounced WNAC in the model could be a consequence of the more northward NAC pathways compared to the observed flow field. The biggest discrepancy however is the observed larger ENAC transport of 25 Sv, which is larger than the modeled transports of WNAC and ENAC together. Choosing adapted boundaries for the two NAC branches instead of fixed (*Lherminier et al.*, 2010) or separating the NAC flow in three branches instead of two (*Daniault et al.*, 2016a) modifies the observed transports of the NAC branches and makes them more comparable with the model results (*Lherminier et al.*, 2010) with 8 Sv for each, WNAC and ENAC) or increases the discrepancies further (*Daniault et al.*, 2016a).

Overall, the simulated main circulation features of the NA are comparable with observations, such as the here presented altimetry data, observed transport measurements and other observational studies using e.g. floats at several density levels to investigate the circulation in the NA (e.g. *Lavender et al.*, 2000; *Bower et al.*, 2002; *Pérez-Brunius et al.*, 2004). In the model the velocity field reveals stronger horizontal gradients compared to altimeter data, owing to the higher resolution of the model (1/20° versus 1/4°). The effect of different spatial resolution and temporal averaging on the flow field have been discussed already by (*Fratantoni*, 2001), who compared satellite tracked drifter trajectories and drifter derived eddy kinetic energy with values calculated from satellite altimetry. The most remarkable differences between the VIKING20 model and observations are the shift of the NWC further into the Labrador Sea and the more northward pathways of the NAC, leading to the preference for the CGFZ and the WNAC in the model.

3.2. Vertical hydrographic and velocity distributions

The model configuration simulated the mean velocity and salinity distribution over the North Atlantic well. In this section the vertical structure is compared. It is started with a section across the 47°N latitude. The section starts at the Flemish Cap and ends before the coast of the Iberian Island at around 10°W. The next section is along the western side of the MAR. In the eastern Atlantic the comparison is focused on the OVIDE line between Portugal and the Reykjanes Ridge.

3.2.1. Hydrography and velocity across the 47°N section

The hydrography and velocity along the 47°N section was taken during 14 cruises between 2003 and 2016. Here the mean profiles are compared to the simulated summer mean (March-September) for the last 13 model years (1996-2008). The individual profiles for each cruise are shown in the appendix A in Figures A.3, A.4, A.5, A.6 , A.7, A.8.

Velocities across the section from model and observations are comparable in magnitude and distribution (Figure 3.4). The main velocity features such as the deep reaching northward flowing NAC around the positions of the PIES instruments with the numbers 31 and 28 and the southward directed NBR further east are simulated well. Overall, the simulated velocity distribution seems to be more batrotropic through out the water column than the observations.

Looking into more detail, the southward flow in the western and central part of Flemish Pass, between Grand Banks and Flemish Cap, and the recirculation across the eastern slope described by *Schneider et al.* (2015), are seen in both distributions and exhibit similar velocities. Above the Flemish Cap, the flow direction changes from northward to southward directed mean velocity. The southward velocity is the WBC, which exhibits a slope and a rise core in the observations (e.g. *Mertens et al.*, 2014; *Schneider et al.*, 2015). These two cores are also visible in the 47 year mean of meridional velocity from VIKING20 model data, which were compared to observed mean velocity distribution calculated from six hydrographic sections
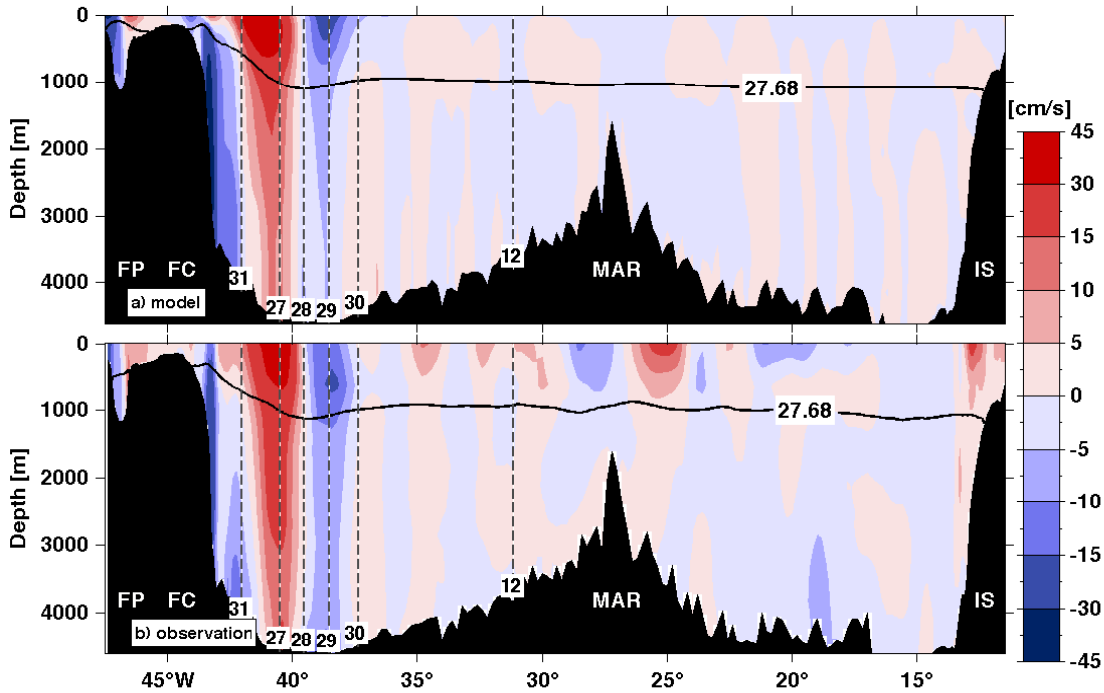
Figure 3.4.: Mean velocity along the 47°N section calculated from the simulated summer mean over the last 13 model years (1996-2008) (a), and composite of 14 repeat lADCP sections between 2003 and 2016 (Table 2.2) (b). The position and the name of the PIES instruments (Table 2.5) are marked by the vertical lines. Flemish Pass (FP), Flemish Cap (FC), MAR, and the Irish Shelf (IS) are marked. Northward flowing velocity is displayed in red. The isopycnals $\sigma_\theta = 27.68\,\text{kg/m}^3$, which are used to separate the subpolar flow from the deep ocean are displayed. For clarity the observed velocities are treated vertically with a sliding average filter of 600 m length to eliminate the influence of internal waves, which are not present in the model. The modeled sections show the topography from the VIKING20 model, and the observed sections the ETOPO5 topography (*National Geophysical Data Center*, 1988).

between 44°W and 36°W (*Mertens et al.*, 2014). In contrast to this the here considered simulated mean velocity distribution calculated for the last 13 model years in the months March-September exhibit a more uniform current with only one core.

Above and east to the WBC the NAC flows towards the north in the observations and in the model. The NAC starts in the mean at around 43°W until 39°W at

the sea surface and reaches down to the bottom of the sea. The flow is surface intensified and exhibits similar velocities in model and observation. Further east both distributions show the deep reaching, surface intensified NBR flow towards the south between the PIES number 28 and 30. East of the position of the PIES number 30 the velocity distributions exhibit alternating flow pattern, which reach often through the entire water column. In the observation the flow above the MAR is more surface intensified than in the simulation. The observed velocities in the east above the slope of Goban Spur at the Irish shelf break is towards the south and exhibit velocities up to -10 cm/s. In this area the simulated velocities are smaller and northward directed above the Goban Spur.

The observed high velocities towards the south at the sea floor at around 19°W with velocities up to -8 cm/s are also observable in the individual profiles of the cruises (Figures A.7, A.8). Southward flowing velocities at this location are found during the M58/2, Subpolar, M85/2, M85/1, MSM28, and MSM53 cruises, but during individual cruises they are not so prominent as in the mean section. The velocities around this feature are in the same range of magnitude during individual sections, but alter their directions during individual cruises and therefore cancel each other out during the calculation of the mean section.

Overall the simulated mean section is more saline (Figure 3.5a) and warmer (Figure 3.6a), as the observations (Figure 3.5b, Figure 3.6b), except in the eastern basin in the deep ocean. Here the observations exhibit salinities up to 34.90 and temperatures above $2\,°C$, where as the modeled salinities are up to 34.89 and the temperatures are below $2\,°C$. The freshest and the coldest water is found in the western part of the section at the slope of the Grand Banks, here the observations exhibit temperatures up to $-1\,°C$ and the model below $1.5\,°C$. This fresh and cold signal reaches in the observations across the Flemish Pass and the Flemish Cap further east. In the simulation it is bounded to the slope of the Grand Banks. Further east above the Flemish Pass and the Flemish Cap the simulation is warmer and less saline above the $\sigma_\theta = 27.68\,\mathrm{kg/m^3}$ isopycnal than below this isopycnal. The warmest and saltiest signals are found at the surface around 40°W, at the boundary between the northward flowing NAC and the southward directed NBR (Figure 3.4). In the observations the rise part of the WBC is warmer (more than $1\,°C$) and saltier (around 0.01) than the slope part, due to interactions with the NAC (Figure 3.5, 3.6; *Mertens et al.* (2014); *Schneider et al.* (2015)).
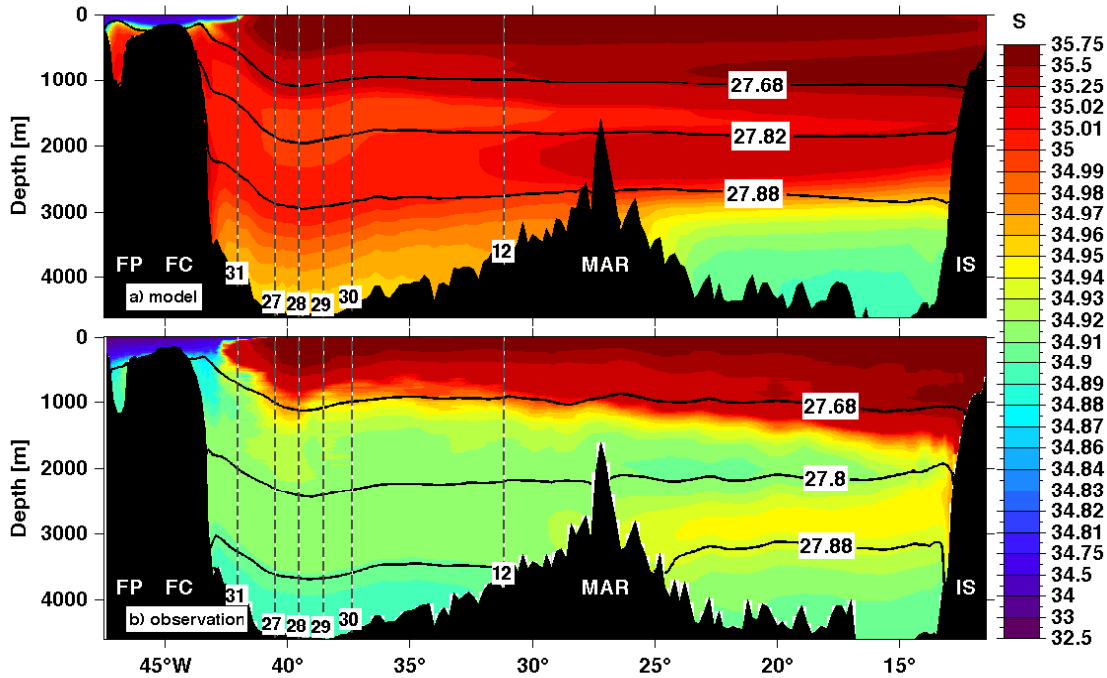
Figure 3.5.: Same as Figure 3.4, but for the mean salinity over the last 13 model years (1996-2008) (a), and composite of 14 repeat CTD sections between 2003 and 2016 (Table 2.2) (b). Additionally, the isopycnals $\sigma_\theta = [27.8, 27.88]\,\text{kg/m}^3$, which are used to separate the LSW and the ISOW are displayed. To encompass the LSW salinity minimum the isopycnal was changed to $\sigma_\theta = 27.82\,\text{kg/m}^3$ in the simulation.

The temperature distributions from model and observations in the western basin of the NA show similar temperatures. In the eastern basin, the simulated warm water reaches further down than in the observations. These warm waters in the simulation are more saline than the observations. The latter shows a salinity minimum (34.90) in the eastern basin at around 2000 m. This relative salinity minimum is between $\sigma_\theta = [27.68 - 27.8]\,\text{kg/m}^3$ and is part of the Labrador Sea Water (Figure 3.5). *Sy* (1988) already described from hydrographic data taken during a Meteor cruise in 1984 that such a salinity minimum can be pursued from the CGFZ until 45°N. Furthermore, below the LSW layer they described a relative salinity maximum, which they identified as Iceland-Scotland Overflow Water (ISOW), also referred to as Northeast Atlantic Deep Water (e.g. *Våge et al.*, 2011; *Kieke and Yashayaev*, 2015). *Fleischmann et al.* (2001) reported the occurrence of the ISOW at the eastern flank of the MAR at 48°N from tracer data taken during
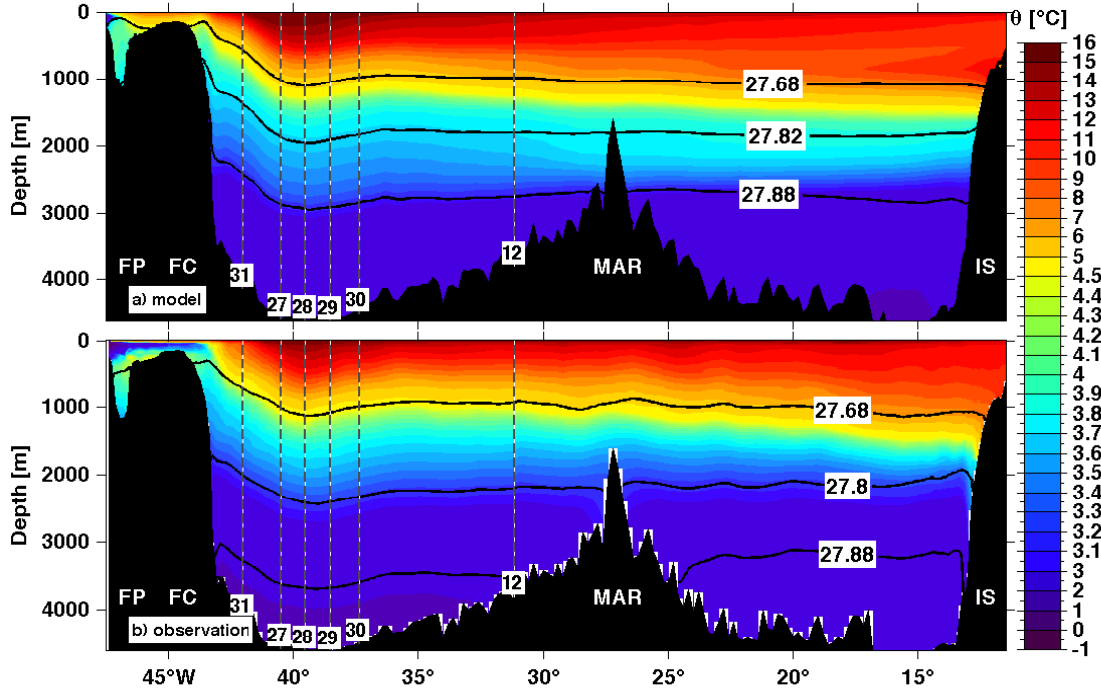
Figure 3.6.: Same as Figure 3.5, but for the mean potential temperature over the last 13 model years (1996-2008) (a), and composite of 14 repeat CTD sections between 2003 and 2016 (Table 2.2) (b).

a Meteor cruise in 1994. They furthermore described in combination with other tracer measurements taken between 1981 and 1994 that the ISOW flows partly passed the CGFZ southward along the topography of the MAR. The ISOW mass is found between $\sigma_\theta = [27.8 - 27.88]\,\mathrm{kg/m^3}$ (e.g. *Dickson and Brown*, 1994; *Våge et al.*, 2011). At the 47°N section the ISOW is observed between the MAR and the slope of the Irish shelf starting at around 3000 m and rising to around 2000 m in the eastern part of the section with salinities around 34.95 (Figure 3.5b). Such a high salinity signal is also found in the simulation in the expected density layers. The simulated ISOW is more saline (35) and exhibits a more horizontal distribution, which does not reach so far down at the MAR as in the observations.

Due to the higher salinity the density of the deep ocean in the simulation is denser and therefore the simulated isopycnals used here to distinguish between LSW and ISOW are further up in the water column than in the observations. To encompass the LSW salinity minimum the lower boundary of the simulated LSW layer was changed to $\sigma_\theta = 27.82\,\mathrm{kg/m^3}$ in the simulation. The lower bound of the

ISOW was not changed, because the $\sigma_\theta = 27.88 \, \text{kg/m}^3$ isopycnal in the simulation is found below the corresponding salinity maximum.

Above $\sigma_\theta = 27.68 \, \text{kg/m}^3$ the high salinity signals in the observation and simulation is Mediterranean Outflow Water (MOW) (Figure 3.5), which leaves the Mediterranean Sea through the Strait of Gibraltar. This water mass is defined $\sigma_\theta = [27.50 - 27.66] \, \text{kg/m}^3$ (*Lozier and Stewart*, 2008; *Stendardo et al.*, 2015) and reaches further west in the simulation than in the observations.

The salinity and temperature differences in the upper 1000 m along the section almost compensate each other regarding density, so that the depth of the isopycnal $\sigma_\theta = 27.68 \, \text{kg/m}^3$ chosen to separate the warm, subtropical NAC water above from the deep water below is nearly the same between observations and model (Figures 3.4, 3.5, 3.6). Starting at the Flemish Cap the isopycnal decreases from around 500 m to below 1000 m at around the position of the PIES number 28. Farther east the isopycnal is nearly horizontal and at around 1000 m depth in the observations and in the model. In the Flemish Pass the observed $\sigma_\theta = 27.68 \, \text{kg/m}^3$ isopycnal increases from west to east, as already described by *Schneider et al.* (2015). Their comparison with a Massachusetts Institute of Technology General Circulation Model (MIT/gcm) model showed, that the model is warmer and saltier and the simulated isopycnal lay below the observed and has a stronger slope. In the VIKING20 simulation the $\sigma_\theta = 27.68 \, \text{kg/m}^3$ isopycnal is found above the observations, due to the higher salinities in the simulation.

3.2.2. Hydrography and velocity across the MAR array

The velocity and hydrographic distributions at the PIES array along the MAR from model and observational data are comparable in magnitude and distribution. The observations are the mean distributions of eight repeated CTD and LADCP sections between July 2008 and May 2016 (Table 2.1). The model on the other hand is the summer mean (March - September) for the last eight model years of this simulation (2001-2008). The modeled distribution is in general more saline (Figure 3.7a) and warmer (by about 0.5 °C below 1000 m depth and 1 °C above) (Figure 3.8a) than observed (Figure 3.7b and Figure 3.8c). As already discussed in the horizontal distributions at 100 m depth, the VIKING20 warm and saline
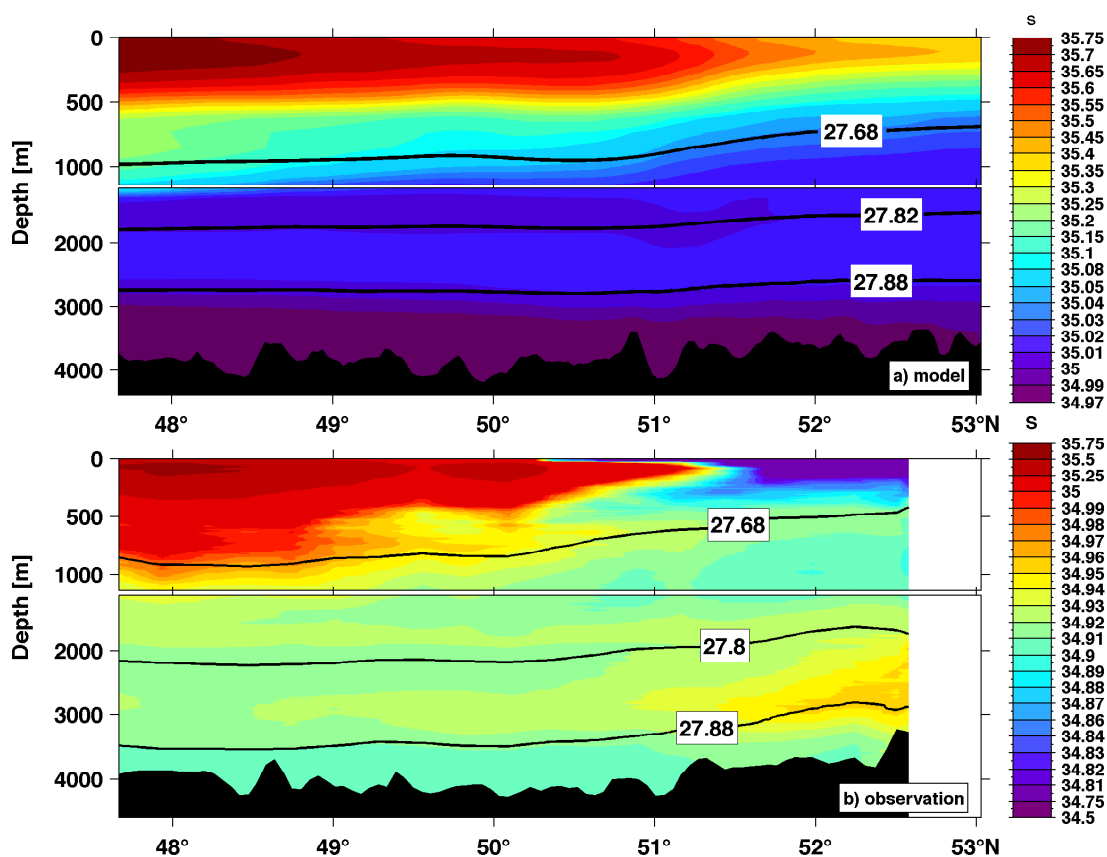
Figure 3.7.: Mean salinity along the MAR array calculated from the last eight model years 2001-2008 (a), and composite of eight repeat CTD sections between 2008 and 2016 (b). Note the different salinity color scales for the model and the observations, which were chosen for visibility reasons. The upper 1000 m are vertically stretched to better display the different salinity distribution. The isopycnals $\sigma_\theta = 27.68 \, \mathrm{kg/m^3}$, which are used to separate the subpolar flow from the deep ocean are displayed. Additionally, the isopycnals $\sigma_\theta = [27.8, 27.88] \mathrm{kg/m^3}$, which are used to separate the LSW and the ISOW are displayed. In the simulation the $\sigma_\theta = 27.82 \, \mathrm{kg/m^3}$ isopycnal is used as the lower LSW boundary. The modeled sections show the topography from the VIKING20 model, and the observed sections the ETOPO5 topography (*National Geophysical Data Center*, 1988).

surface water reaches farther to the north than in the observations, but in both, model and observations, the saltiest and warmest water is found in the central and southern part of the section. The observed subpolar water north of 51°30'N
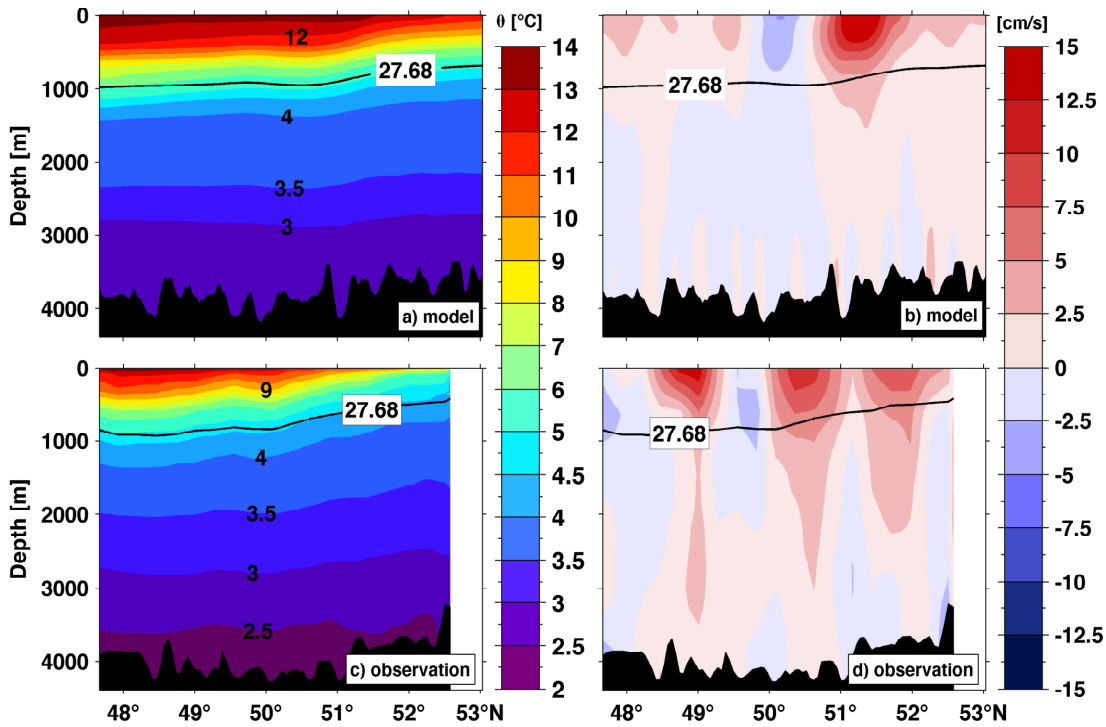
Figure 3.8.: Same as Figure 3.7 but for the mean potential temperature (a,c) and velocity (b,d) sections along the MAR section calculated from the last eight model years 2001-2008 (a,b), and composite of eight repeat CTD and lADCP sections between 2008 and 2016 (c,d). The velocity distributions are defined perpendicular to the PIES array and the velocities towards the northeast are displayed in red. Due to visibility reasons only the isopycnals $\sigma_\theta = 27.68\,\mathrm{kg/m^3}$ are displayed. For clarity the observed velocities are treated vertically with a sliding average filter of 600 m length to eliminate the influence of internal waves, which are not present in the model.

is by about 0.8 fresher than in the model, so that the horizontal gradients in the observations are sharper than in the model despite the higher spatial resolution of the latter. In the deep ocean, both distributions include the Labrador Sea Water below the $\sigma_\theta = 27.68\,\mathrm{kg/m^3}$ isopycnal, the model is warmer and more saline compared to the observations. The latter shows a stronger relative minimum at around 1000 m in the northern part of the section with salinities around 34.9 and the layer reaches down to around 2000 m depth. In the simulation the layer of the LSW is smaller and only reaches down to around 1800 m, here a relative salinity

minimum is visible, with salinites of around 35. To better encompass the LSW layer the lower bound is again changed to $\sigma_\theta = 27.82\,\mathrm{kg/m^3}$ in the simulations.

The high salinities observed north of the subpolar front (at 52°N) around 3000 m (Figure 3.7b) are a feature of the Iceland-Scotland Overflow water (ISOW) that flows mainly through the CGFZ from the eastern into the western Atlantic (e.g. *Dickson and Brown*, 1994; *Saunders*, 1994). The relative maximum salinity signal of this water mass is not found in the modeled section investigated here (Figure 3.7a). The ISOW in the model crosses the MAR farther north between 58°N and 60°N and around 30°W (Figure A.17). Part of the difference in the deep ocean is owed to the different vertical resolution of the model (up to several 100 m) and in the observations (1 m) and to the overall denser simulation.

In the upper 1000 m, salinity and temperature differences almost compensate each other regarding density, so that the depth of the isopycnal $\sigma_\theta = 27.68\,\mathrm{kg/m^3}$, chosen to separate the warm, subtropical NAC water above from the deep water below is nearly the same between observations and model (Figure 3.7 and Figure 3.8). The isopycnal rises from around 1000 m in the southern part of the section to around 600 m in the model and around 500 m in the observations. The relative steep slope of the isopycnal south of 52°N in the model and south of 51°N in the observation indicate the subpolar front, respectively. In both distributions a second branch of the subpolar front can be observed, at around 49°30'N in the model and at around 49°N in the observations. In general, modeled and observed velocities are in the same order of magnitude and their vertical and horizontal structures are similar (Figure 3.8b,d). In both cases, the mean velocity distribution is surface-intensified, but mostly reaches down to the bottom, producing horizontally alternating coherent jets over the whole water column. The strongest velocity signal in observation and model reaches up to 16 cm/s and is found above the isopycnal $\sigma_\theta = 27.68\,\mathrm{kg/m^3}$, and at the subpolar front, in the model at around 51°20'N, and in the observation further south at around 50°40'N (Figure 3.8b,d). The strongest southwest flowing velocity exceeds -7 cm/s in the observations. In the model however the summer mean velocity only reaches up to -5 cm/s.

3.2.3. Hydrography and velocity across the OVIDE line

The OVIDE data were taken every second year between 2002 and 2010 during the summer months. These are compared with simulated composite data calculated for the summer months (May until July) in the years 2000, 2002, 2004, 2006, and 2008. Overall, the velocity and hydrographic distributions at the OVIDE line from observational data and simulated model output are comparable in magnitude and distribution. In the simulation the warmer surface water reaches further north as in the observations (Figure 3.9), which is in agreement with the MAR sections (Figure 3.8). Below the $\sigma_\theta = 27.68 \, \text{kg/m}^3$ isopycnal in the deep ocean the simulated and observed temperature are in the same range of magnitude, above 3000 m the simulation is warmer by about half a degree. Furthermore, east of the Reykjanes Ridge centered at around 2000 m the simulation is warmer and more saline as the observations (Figure 3.10). This relative maximum in salinity is a signature of the ISOW in the model, which is further up in the water column than the observational one. *Daniault et al.* (2016a) described the ISOW directly above the slope of the ridge, which is seen reaching down to 3000 m between around 56°N and the northern end of the here considered section. Above the ISOW and reaching further east until around 44°N the relative minimum of the LSW is observed with salinities of around 34.9. In the simulation this relative minimum is smaller, more saline with salinities of around 35, it is again further up in the water column, and does not reach so far east. Here again the lower bound of the LSW layer was changed to $\sigma_\theta = 27.82 \, \text{kg/m}^3$ in the simulation.

The signal of the Mediterranean Water is simulated and observed in the east of the section at around 1000 m, seen as well in *Daniault et al.* (2016a), which analysed the same OVIDE data used here but with additional data taken in 2012. The simulated warm and saline Mediterranean water reaches further west than in the observation. The observed salinity maximum above the top of the Reykjanes Ridge at the sea surface is identified by *Daniault et al.* (2016a) as a signal of the Subpolar Mode Water, which is formed by deep winter convection in the subpolar North Atlantic (e.g. *McCartney and Talley*, 1982; *Brambilla and Talley*, 2008). In the simulation this signal is not clearly differentiated from the warm and saline surface layer over the entire section. In the Iberian basin at the sea floor *Daniault et al.* (2016a) described the Lower North East Atlantic Deep Water, with temperature
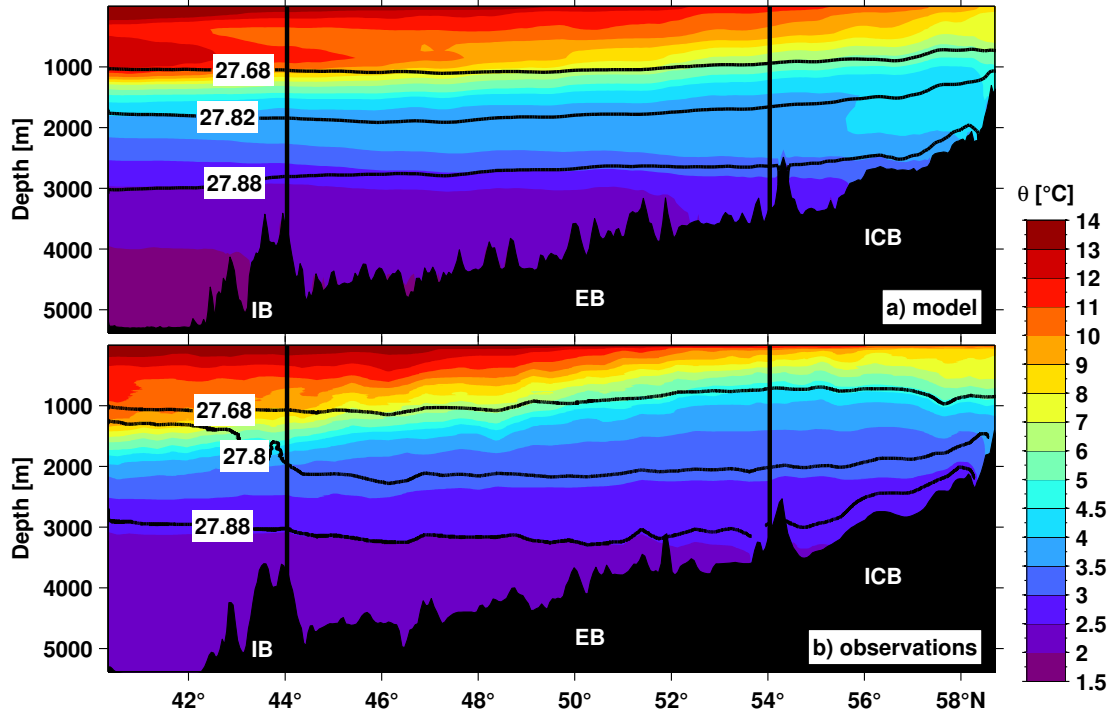
Figure 3.9.: Mean potential temperature at the OVIDE line in model a) and observation (*Mercier et al.*, 2015) b). The modeled temperature is the mean from every second year between the years 2000 and 2008. The black lines mark the separation in the Iberian (IB), European (EB) and Iceland (ICB) basins for the transport calculations (Table 3.5). The isopycnals $\sigma_\theta = 27.68\,\mathrm{kg/m^3}$, which are used to separate the subpolar flow from the deep ocean are displayed. Additionally, the isopycnals $\sigma_\theta = [27.8, 27.88\,]\mathrm{kg/m^3}$, which are used to separate the LSW and the ISOW are displayed. In the simulation the $\sigma_\theta = 27.82\,\mathrm{kg/m^3}$ is exhibit as the lower boundary of the LSW layer. The modeled sections show the topography from the VIKING20 model, and the observed sections the ETOPO5 topography (*National Geophysical Data Center*, 1988).

above $2\,°\mathrm{C}$ in the observations and below $2\,°\mathrm{C}$ in the simulation.

The salinity and temperature differences in the upper $1000\,\mathrm{m}$ almost compensate each other regarding density so that the depth of the isopycnal $\sigma_\theta = 27.68\,\mathrm{kg/m^3}$ is nearly the same in observation and model, like at the 47°N and along the MAR sections. The isopycnal starts at around $1000\,\mathrm{m}$ in the eastern part of the section and rises only slightly until the Reykjanes Ridge. The mean observed and simulated velocity distributions across the OVIDE line show features with similar
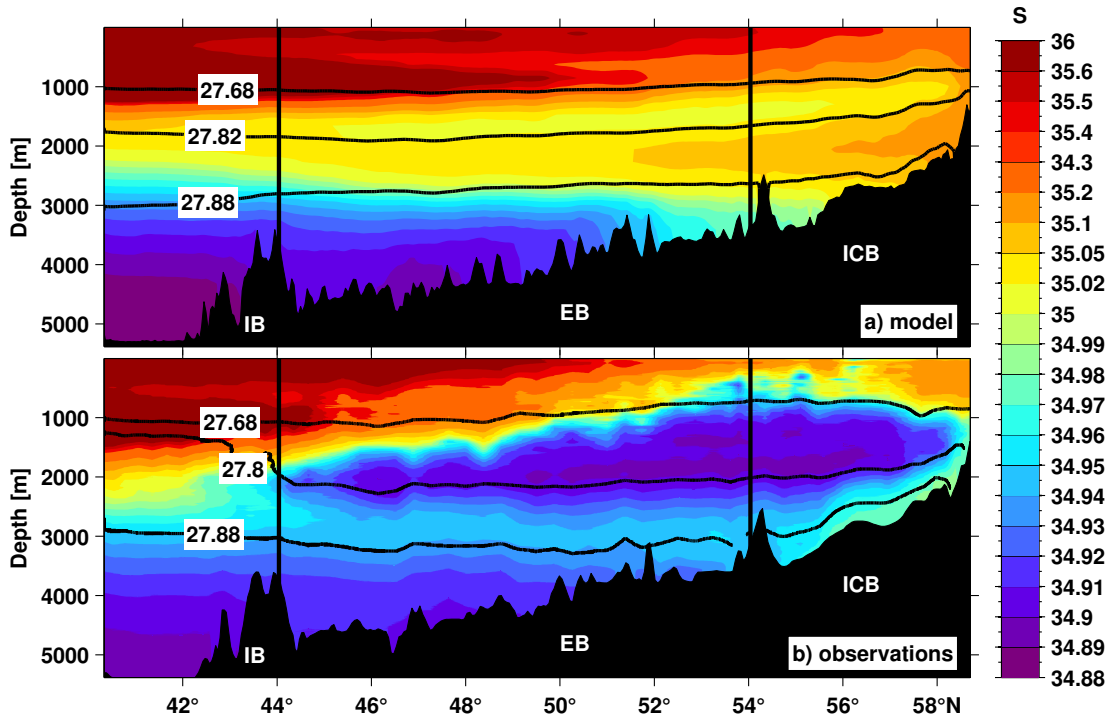
Figure 3.10.: Same as Figure 3.9 but for mean salinity at the OVIDE line in model a) and observation (*Mercier et al.*, 2015) b).

horizontal and vertical extensions and are in the same order of magnitude (Figure 3.11). Both distributions show surface intensified flow, which mostly reaches down to the bottom, producing horizontally alternating coherent jets over the whole water column. Such a behavior was already observed and simulated at the 47°N and along the MAR sections. At the OVIDE section south of 53°N the modeled velocities are generally weaker than the observed ones. The model shows two alternating strong velocity bands between 56°N and 58°N with velocities up to 14 cm/s towards the northeast and −6 cm/s towards the southwest, also visible in the horizontal distributions at 100 m depth (Figure 3.1a). This feature is also present in the observations, but weaker and with smaller velocities (Figure 3.11b). The strongest mean velocity towards the northeast in the observation is found around 47°N with around 15 cm/s. This strong velocity band marks the southern extension of the eastern branch of the NAC (ENAC) in the observations, which reaches until around 54°N. The modeled ENAC starts farther north than the observations, at around 47°30'N, but ends around the same latitude. Here the WNAC starts
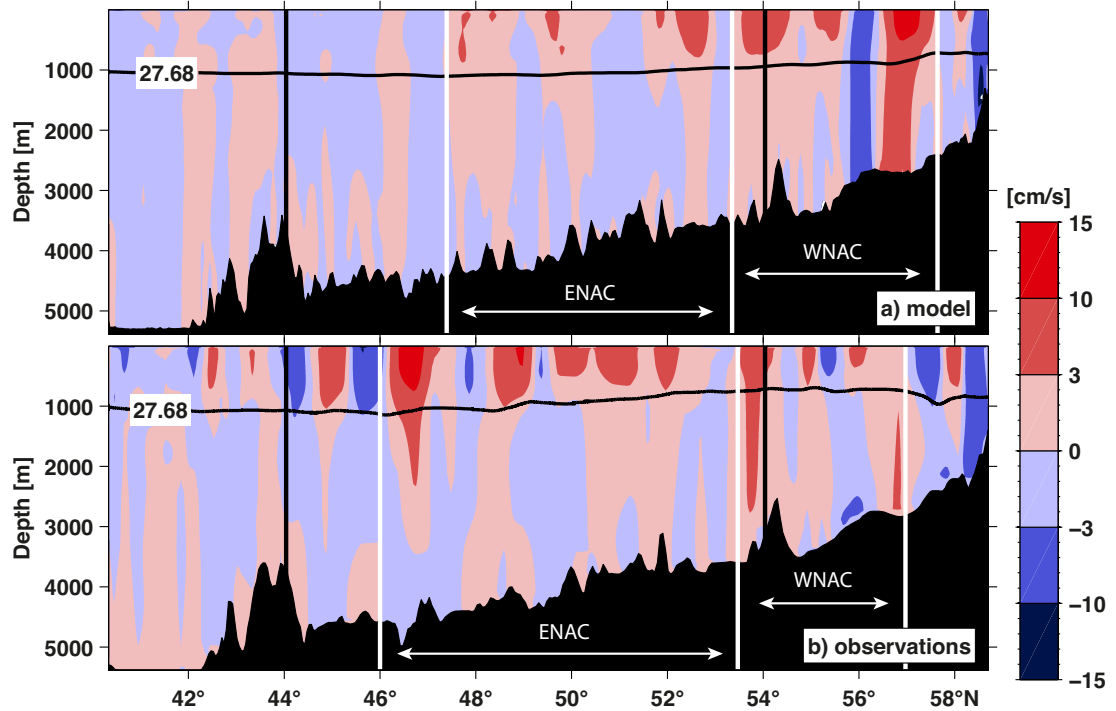
Figure 3.11.: Same as Figure 3.9 but for the mean velocity at the OVIDE line in model a) and observation (*Mercier et al.*, 2015) b). The velocity distribution are defined perpendicular to the section and the velocities towards the northeast are displayed in red. The white lines separate the flow into the western branch of the NAC (WNAC) and the eastern branch of the NAC (ENAC) in the model and the observations, respectively. Due to visibility reasons only the isopycnals $\sigma_\theta = 27.68 \, \text{kg/m}^3$, which are used to separate the subpolar flow from the deep ocean are displayed.

in both distributions but extending further north in the simulation. The branches are defined by the maximum mean transport towards the northeast.

3.3. Transports of the North Atlantic Current

Across the 47°N and the MAR sections the comparison between observational transport and simulated transport is analyzed in detail. In both cases the transport time series are from 1993 until 2008, which is the overlapping time period of the different data sources are compared. The observational transport time series are calculated from PIES measurements and along track altimetry data. The transport time series along the MAR section is taken from *Roessler et al.* (2015) and the time series along the 47°N is provided by A. Roessler[1]. Along the OVIDE section the simulated transports are compared to absolute observed transports, which were calculated from a combination of CTD and ship-mounted ADCP data and are provided by P. Lherminier[2].

3.3.1. Transport across the 47°N section

Along the 47°N section the model output is investigated and compared by dividing the section into subsections defined by the position of the PIES instruments (Figure 2.5, Table 2.5). The southward flow between PIES BP27 (40°52'W) and BP31 (41°59'W) is called the SWF and is part of the southward flowing WBC, which extend further west until around 44°W. The northward flow between the positions of PIES BP30 (37°21'W) and BP31 marks the NAC. The NBR is defined as the southward directed flow between the PIES BP27 and BP30. From BP30 further east until BP12 at the MAR the net flow is called the Newfoundland Basin (NFB) transport. From the easternmost PIES until the Irish shelf another subsection across the 47°N section is defined and in the western part of the section above the Flemish Pass. The Flemish Pass subsection is defined between 47°24'W and 46°24'W following *Schneider et al.* (2015). The mean transports across these subsections are found in table 3.1 along with observational mean transport values. The observation of the WBC ($-37.3\,\mathrm{Sv}$) is taken from (*Mertens et al.*, 2014) and derived from hydrographic measurements taken during six ship cruises between 2003 and 2011. The observational value did not change by taking further data

---

[1] The observed transports across the 47°N section are provided by A. Roessler and are part of a joint paper in preparation. Due to copy right reasons the observational time series are not shown.

[2] The OVIDE data were provided by P. Lherminier and are published in *Mercier et al.* (2015)

Table 3.1.: Absolute observed and simulated mean transports across the 47°N section and the subsections defined by the geographical positions of the PIES instruments (Table 2.5). The simulated transports corresponding standard deviations calculated from the 5-day means are given as well. In the eastern part, no observed transport estimates are available. The WBC observations are basd on six repeated lADCP measurements from 2003 to 2011 and taken from *Mertens et al.* (2014). The Flemish Pass observations are based on six shipboard measurements from 2009 to 2014 and provided by L. Schneider, 2017.

Subsection of 47°N section	Modeled transport [Sv]		Observed transport [Sv]
period	1960-2008	1993-2008	1993-2008
Flemish Pass	-5.1 ± 2.0	-4.9 ± 2.1	-5.4 ± 1.0
WBC ↓	-59.9 ± 23.4	-65.8 ± 24.6	-37.3 ± 7.4
SWF ↓	-12.6 ± 18.2	-12.6 ± 18.7	-47.1 ± 32.7
NAC ↑	113,5 ± 38.3	122.5 ± 38.6	165.6 ± 45.1
NBR ↓	-51.4 ± 30.6	-54.4 ± 30.2	-90.7 ± 31.2
NFB	1.2 ± 22.8	2.0 ± 22.7	-11.5 ± 22.6
eastern	-6.5 ± 8.6	-6.1 ± 8.4	
entire	0.1 ± 1.9	0.1 ± 1.9	

from more cruises into account [3]. The observations in the Flemish Pass are from six shipboard measurements between 2009 and 2014 [4]. These observations are only taken during summer months and are only snapshots. The other observational mean transports are calculated from a continuing transport time series from 1993 to 2008 from PIES instruments in combination with satellite altimetry. Overall the simulated and observed mean transports in the different subsections agree within the standard deviations.

The mean simulated (122.5 Sv with a standard deviation of 38.6 Sv) and observed (165.6 Sv with a standard deviation of 45.1 Sv) northward transports in the NAC

---

[3]C. Mertens, pers. com. 2017
[4]L. Schneider, submitted PhD-thesis April 2017, pers. com. 2017

subsection are comparable within the standard deviations from 1993 to 2008 (Table 3.1). The simulated mean transport slightly decreases to 113.5 Sv when taking the entire model time period into account. The simulated mean NAC is deep reaching and around 64 % are found below the $\sigma_\theta = 27.68 \, \mathrm{kg/m^3}$ isopycnal, which is in agreement with observations from six repeated lADCP sections (*Mertens et al.*, 2014). The seasonal cycle is around 12 % of the simulated mean transport of the NAC section from 1960 to 2008. This reduces to around 6 % for the time period where observations are available from 1993 to 2008, but in both cases the maximum of the seasonal cycle is found in August and the minimum in May. Furthermore, no significant seasonal cycles are found in the two corresponding spectra. The observed seasonal cycle is around 22 % of the absolute top to bottom mean transport of the NAC section and exhibits its maximum in December and its minimum in August. This seasonal cycle is found to be significant in respect to the corresponding 95 % confidence level of the red noise spectrum. The northward directed NAC transport decreases from 1993 to 2008 by 23.8 Sv in the simulation and by 7.1 Sv in the observations (Table 3.2). Over the entire model time period from 1960 to 2008 the simulated NAC transport exhibits an increase of 31 Sv (Figure 3.12). The minimum annual mean transport (below 70 Sv) are found in the 1960s, from which the annual transport increases until 1995, where the annual maximum of around 160 Sv is reached. In the 2000s the top to bottom annual mean transport in the NAC subsection of the 47°N section alternates. The simulated and observed top to bottom annual mean transports in the NAC subsection from 1993 to 2008 behave comparable, with a correlation coefficient of $r = 0.4$ ($p = 0.1$).

At the other three subsections (SWF, NBR, and NFB) where observational transport time series are available the observed and simulated annual means (Figure 3.13) are not significantly correlated to each other. However, the amplitudes are comparable and the mean transports from 1993 to 2008 are in the same order of magnitude (Table 3.1). The mean top to bottom net flow across the NFB subsection however is northward directed in the simulation and southward in the observations. The NBR and NFB subsection mean transports decrease slightly taking the entire model time period into account. The simulated and observed mean transports across the three sections are influenced by the seasonal cycle, but non of the spectra exhibit a significant seasonal cycle in respect to the corresponding red noise spectrum. Across the NBR subsection e.g. the observed seasonal

Table 3.2.: Cumulated trends for observed and simulated absolute transports across the 47°N section and the subsections defined by the geographical positions of the PIES instruments (Table 2.5). The * marks the non-significant trends. The significance is calculated using a two-sided t-test with a 95 % confidence level and the error of the trend is calculated from the 95 % confidence bounds for the corresponding time period.

Subsection of 47°N section	Modeled transport trend [Sv]		Observed transport trend [Sv]
period	1960-2008	1993-2008	1993-2008
Flemish Pass	1.1 ± 0.3	1.4 ± 0.5	
WBC ↓	-17.7 ± 3.0	16.5 ± 5.5	
SWF ↓	-2.5 ± 2.3	7.0 ± 3.7	-2.2 ± 4.8*
NAC ↑	31.2 ± 4.9	-23.8 ± 8.7	-7.1 ± 4.6
NBR ↓	-15.8 ± 4.0	0.3 ± 7.0*	8.9 ± 3.2
NFB	4.4 ± 3.0	7.9 ± 5.2	1.0 ± 2.3*
eastern	0.4 ± 1.1*	0.5 ± 1.9*	
entire	0.26 ± 0.24	0.2 ± 0.4*	

mean is around 22 % of the mean from 1993 to 2008 and the simulated one around 10 %. The influence of the seasonal cycle increases for the entire model time period to 20 % of the mean transport. The simulated maxima are found during winter (December, February) and the minima in August and September from 1993 to 2008 and 1960 to 2008, respectively. The observed extrema are reversed, the maximum is found in September and the minimum in December.

SWF and NBR transports are deep reaching in the simulation and around 86 % and 61 % of the mean flow is found below the $\sigma_\theta = 27.68 \, \text{kg/m}^3$ isopycnal, respectively. This is in agreement with an observed NBR flow towards the south taken from six repeated lADCP sections with around 56 % of the flow found in the deep ocean (*Mertens et al.*, 2014). Across the NFB subsection the simulated net mean flow in the subtropical water mass is towards the south and in the deep ocean towards the north, these two flow directions eliminate each other regarding the mean
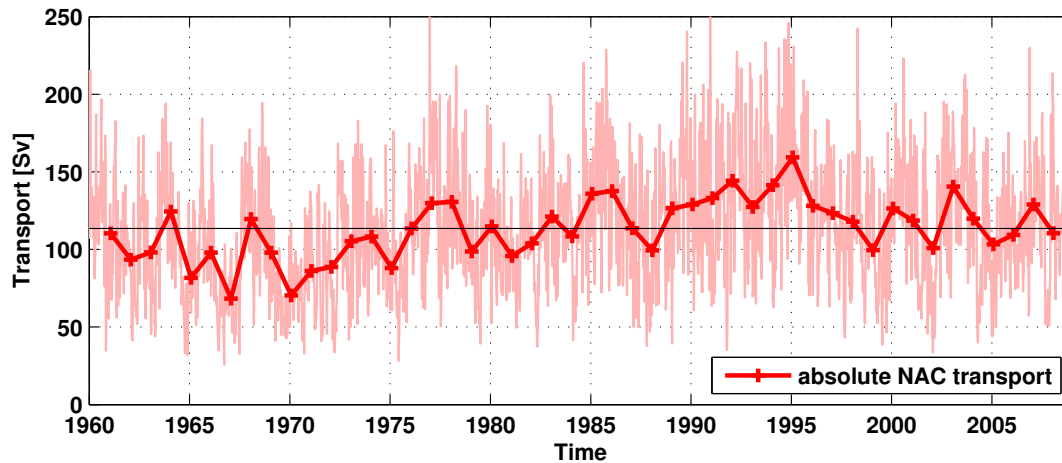
Figure 3.12.: Absolute top to bottom transport from the VIKING20 model config-
uration from 1960 to 2008 across the NAC subsection along the 47°N
section. The bold line and markers are annual means and the thin
line display the 5-day mean of the model. The mean value over the
entire time period is exhibit by the black line.

top to bottom transport. Over the entire model time period the top to bottom net
transport across the NFB subsection increases by 4.4 Sv, which is even enhanced to
7.9 Sv for the time period where observations are available (Table 3.2). Across the
NFB subsection the observed increase is not significant. The observations exhibit
a significant increase in the NBR subsection by 8.9 Sv from 1993 to 2008, but the
corresponding simulated transport time series does not show a significant increase.
The simulation even decreases by 15.8 Sv over the entire model time period across
the NBR subsection.

It is found that in the individual subsections investigated across the 47°N section
the main part of the simulated mean flow is below the $\sigma_\theta = 27.68 \, \text{kg/m}^3$ isopycnal
in the deep ocean. In the Flemish Pass e.g. the simulated net flow is found
to be -5.1 Sv towards the south and around 81% is found to be in the deep
ocean. A similar top to bottom southward flow of -5.4 Sv is reported from six
shipboard measurements between 2009 and 2014, but with around 61% above the
$\sigma_\theta = 27.68 \, \text{kg/m}^3$ isopycnal[5]. This discrepancy was expected from the density
distributions represented by the $\sigma_\theta = 27.68 \, \text{kg/m}^3$ isopycnals in the Flemish Pass

---

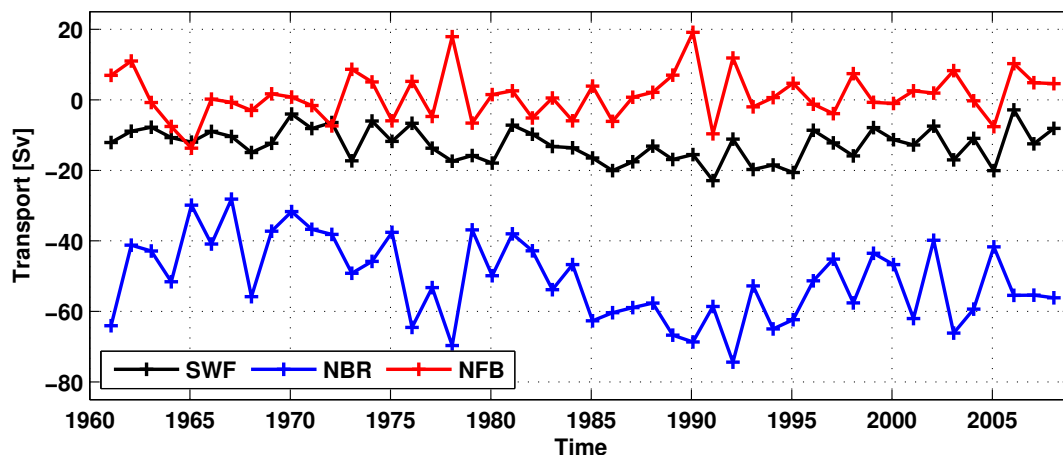[5]L. Schneider, submitted PhD-thesis April 2017, pers. com. 2017

Figure 3.13.: Absolute top to bottom annual mean transport from the VIKING20 model configuration from 1960 to 2008 across the SWF (black), NBR (blue), and NFB (red) subsections along the 47°N section.

(cf. Figure 3.4).

Even though simulated transports across the individual subsections at the 47°N section exhibit a preference towards the deep ocean, this is canceled out considering the entire section. Here, around 18.2 Sv with a standard deviation of 6.6 Sv is flowing towards the north in the upper ocean, which is balanced by a southward flow of around −17.6 Sv with a standard deviation of 7.4 Sv in the deep ocean from 1960 to 2008. During this time period only a small mean transport of around 0.1 Sv towards the north is simulated and a transport increase by 0.26 Sv.

Along the 47°N section the model simulates the mean transports within the standard deviations of the observations. The simulated transport time series along the four subsections SWF, NAC, NBR, NFB, where observational transport time series are available exhibit similar amplitudes but their temporal variability are not significantly correlated with the observations.

3.3.2. Transport across the MAR array

At the MAR section, a continuous observed transport time series is compared to the absolute and baroclinic transport time series from 1993 until 2008 (Table 3.3 and Figure 3.14). The mean transports from observations and the model are comparable within the error margins. The mean baroclinic transport in the model referenced to 3400 m depth is 24.6 Sv with a standard deviation of 7.1 Sv. The observed transport of 27.4 Sv with a standard deviation of 4.7 Sv is about 10 % higher than the simulated one, but has a lower standard deviation. Compared to observations, the transport in the upper layer is more dominating in the model (70 %) than in the observations (60 %), caused by a more intensified upper ocean flow. The contribution of the VIKING20 barotropic and ageostrophic components to the mean model transport amounts to about 7 %, increasing the mean to 26.4 Sv with a standard deviation of 8.7 Sv. When including the standard deviations of the velocity fluctuations in the reference level (*Rhein et al.*, 2011), the observed

Table 3.3.: Mean absolute and baroclinic transport components from the model and observed mean transports across the PIES array at the MAR and the subsections defined by the geographical positions of the PIES instruments. The transports corresponding standard deviations calculated from the 5-day means are given as well. The extended subsection takes the northward shift of the NAC in the model into account. The sum of the three observed segments (26.1 Sv) does not necessarily agree with the transport of the total array which is calculated independently (27.4 Sv) (*Roessler et al.*, 2015).

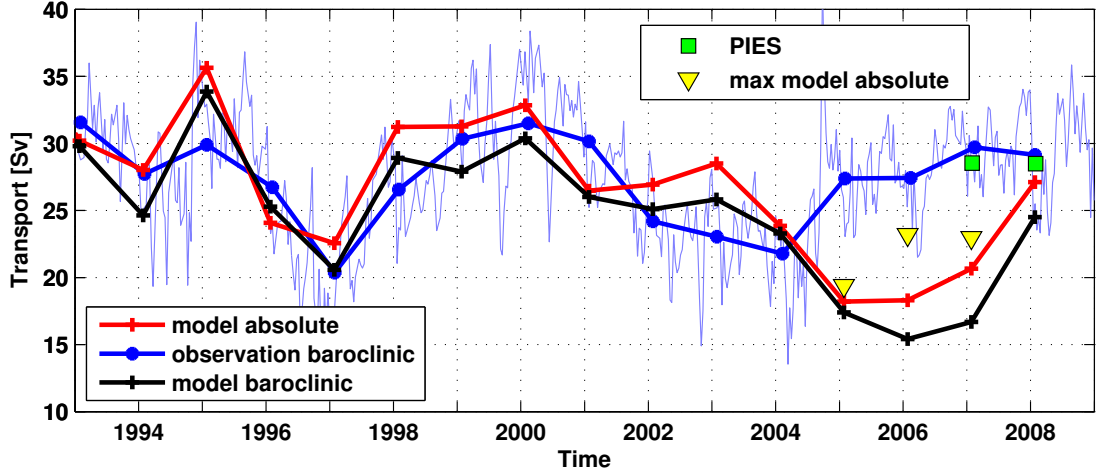| Subsection of MAR array	Modeled absolute transport [Sv]		Modeled baroclinic transport [Sv]		Observed transport [Sv]
period	1960-2008	1993-2008	1960-2008	1993-2008	1993-2008
southern	4.5 ± 9.0	3.5 ± 9.1	5.1 ± 8.5	3.9 ± 8.4	8.6 ± 7.7
central	8.2 ± 12.5	8.0 ± 11.1	8.4 ± 9.4	8.6 ± 10.0	12.2 ± 7.0
northern	10.0 ± 10.5	11.7 ± 12.3	8.6 ± 9.4	9.9 ± 11.0	5.3 ± 3.0
extended	3.6 ± 6.5	3.1 ± 7.5	2.3 ± 6.2	2.1 ± 7.1	
entire	26.2 ± 8.8	26.4 ± 8.7	24.5 ± 7.1	24.6 ± 7.1	27.4 ± 4.7

Figure 3.14.: Absolute (red), and baroclinic (black) transport from the VIKING20 model and observed baroclinic (blue) transport time series from 1993-2008 at the PIES array along the MAR. The bold lines and markers are annual means and the thin line displays the 10-day values of the altimeter observations. The green squares mark the in-situ measurements from the PIES instruments (*Roessler et al.*, 2015). The yellow triangles indicate the maximum annual transport across the section as discussed in section 5.1. The section is extended further north until the maximum transport for that year is found.

standard deviation increases to 8.6 Sv, and is very close to the modeled one. The higher absolute transport might indicate that also in the real ocean, the barotropic and ageostrophic flow components contribute to the annual means and therefore *Roessler et al.* (2015) slightly underestimate their observed NAC transport. However, this increased transport lies still in the same range of magnitude.

Figure 3.14 and Figure 3.15 show the time series of the NAC transports referenced to 3400 m depth from observations and model and also the simulated absolute transports. The annual mean absolute transport is always higher than the baroclinic transport, except for the year 1996. From 1993 to 2004, the observed and simulated baroclinic time series are similar and highly correlated (correlation coefficient of 0.7), while for the years afterwards, the observed transports increase almost linearly until 2008, while the simulated transports reach a minimum of nearly 15 Sv in 2006. In the following time period, the modeled transport rises rapidly and comes close to the observed transport at the end of 2008 (Figure 3.14).
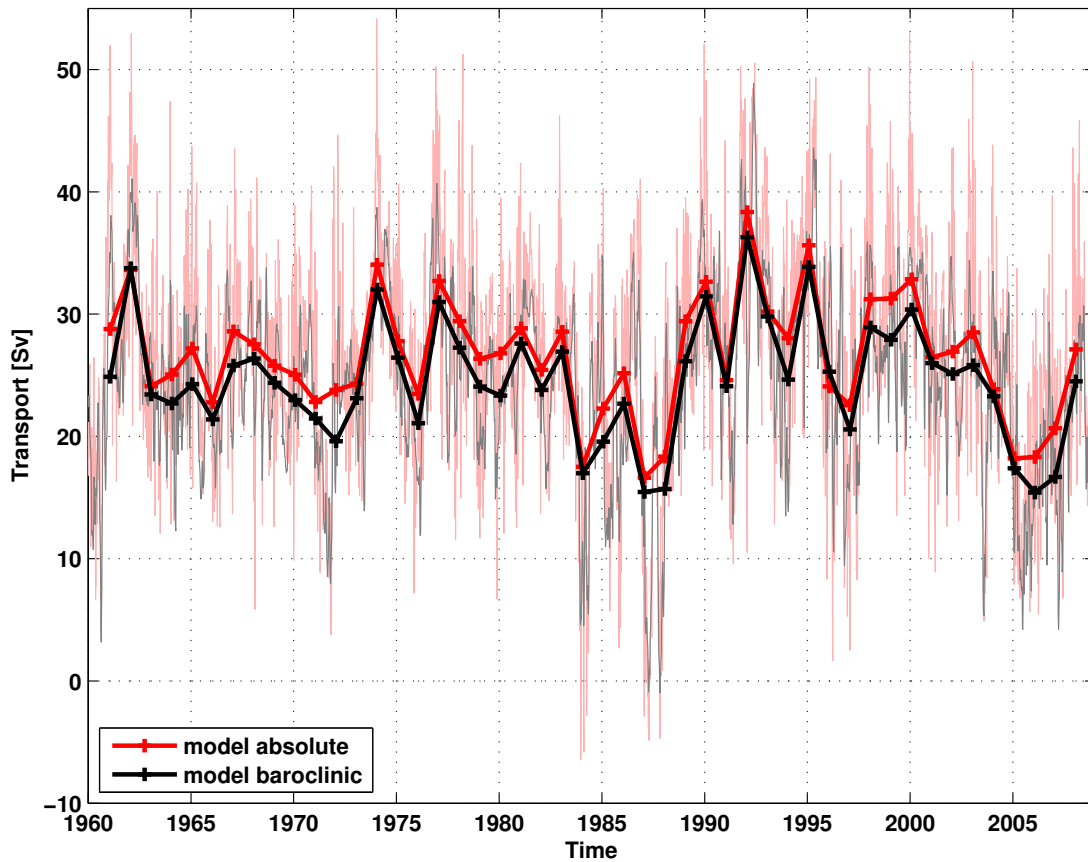
Figure 3.15.: Absolute (red) and baroclinic (black) transport from the VIKING20 model from 1960 to 2008 at the location of the PIES array along the MAR. The bold lines and markers are annual means and the thin lines display the 5-day mean of the model (red and black).

This different behavior of observed and modeled transport will be discussed in section 5.1. The total (baroclinic and barotropic) transport estimates from the PIES instruments alone for the years 2007 and 2008 are close to the observational transports, as expected since the latter is based on a correlation between the altimetry derived 4-year along-track SSH measurements and PIES derived baroclinic data (Figure 3.14). The influence of the barotropic fluctuations on the annual means is small due to their short time scales (*Roessler et al.*, 2015).

The absolute and baroclinic transports and their variability change only slightly when taking the entire model time period (1960-2008) into account (Table 3.3, Figure 3.15). The longer time series shows that the minimum in 2006 is not so

uncommon. Similar minima are found in 1972, 1984, and 1987-88. The largest annual mean transports occurred in 1992 and in 1995 with values above 34 Sv.

Independent of the time period and transport component, the extended model segment north of 52°30'N contributes about $9 - 10\,\%$ of the mean (Figure 3.16, Table 3.3). Overall 57 % of the absolute mean transport and 49 % of the baroclinic transport are located in the northern and extended segments. The strongest mean transport in the model is found in the northern segment. In the observations only 20 % of the mean transport is found in that segment. The strongest observed mean flow toward the northeast is in the central segment (47 %) (Table 3.3).

As pointed out by *Roessler et al.* (2015) no significant trend in the NAC transport time series was observed. Individual segments, however, had opposing trends,
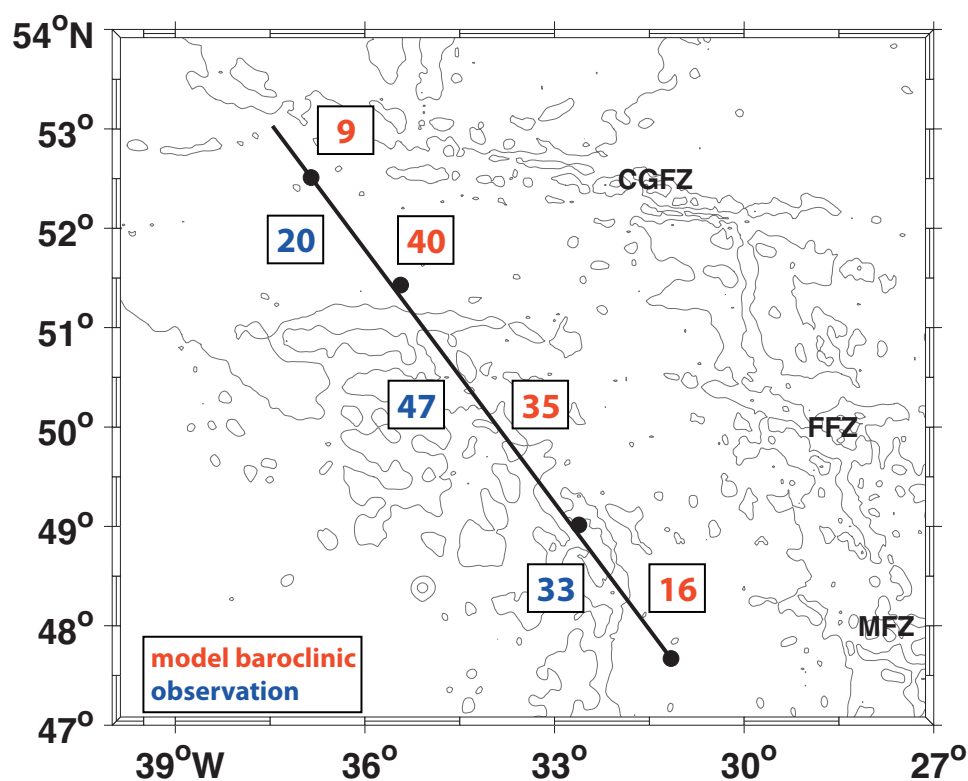
Figure 3.16.: Mean fractions (%) of modeled baroclinic (red) and observed (blue) mean transport relative to 3400 dbar calculated from 1993 to 2008 at the MAR section. The positions of the PIES are indicated by the black dots *Roessler et al.* (2015).

Table 3.4.: Cumulated trends for the modeled absolute, modeled baroclinic and observed transport components for different time periods at the MAR section. The * marks the non-significant trends. The significance is calculated using a two-sided t-test with a 95 % confidence level and the error of the trend is calculated from the 95 % confidence bounds for the corresponding time period.

Subsection of MAR array	Modeled absolute transport trend [Sv]		Modeled baroclinic transport trend [Sv]		Observed transport trend [Sv]
period	1960-2008	1993-2008	1960-2008	1993-2008	1993-2008
southern	0.003 $\pm$ 1.2*	2.3 $\pm$ 2.1	-0.7 $\pm$ 1.1*	1.7 $\pm$ 1.9	-1.7 $\pm$ 2.5*
central	-3.4 $\pm$ 1.4	-6.0 $\pm$ 2.5	-2.7 $\pm$ 1.2	-5.7 $\pm$ 2.3	3.8 $\pm$ 2.2
northern	5.6 $\pm$ 1.4	-2.9 $\pm$ 2.8	4.5 $\pm$ 1.2	-2.9 $\pm$ 2.5	-2.3 $\pm$ 0.1
extended	-2.4 $\pm$ 0.9	-2.0 $\pm$ 1.7	-1.8 $\pm$ 0.8	-2.7 $\pm$ 1.6	
entire	-0.3 $\pm$ 1.1*	-8.6 $\pm$ 1.9	-0.7 $\pm$ 0.9*	-9.7 $\pm$ 1.5	-0.8 $\pm$ 1.4*

leading to a more focused NAC in the central subsection and decreasing transports in the southern and northern segments (Table 3.4). This is in contrast to the negative trend in the VIKING20 NAC for the time period 1993 to 2008, caused by the transport decrease between 2005 and 2007 that was not found in the observations. Over the longer 1960-2008 period, no significant trend was found for the absolute nor for the baroclinic NAC transports in the VIKING20 model, but individual segments behave differently (Table 3.4). While in the observations, the NAC flow gets more focused with time in the central segment, the simulated transports in the central subsection decreased significantly by either around 3 Sv (1960-2008) or 6 Sv (1993-2008). The flow through the extended model segment weakened by about 2 Sv in all time periods. For the years 1960-2008, the weaker flow in the central and the extended subsection is compensated by an intensified flow in the northern subsection, with no significant trends in the southern segment. In 1993-2008, the model exhibits weaker transports in all segments but the southern subsection (Table 3.4).

The seasonal cycles for the transport from observations and modeled absolute and baroclinic transports are shown in Figure 3.17. The observed seasonal cycle has its maximum transport (1.5 Sv) in November and its minimum in March (-1.2 Sv).
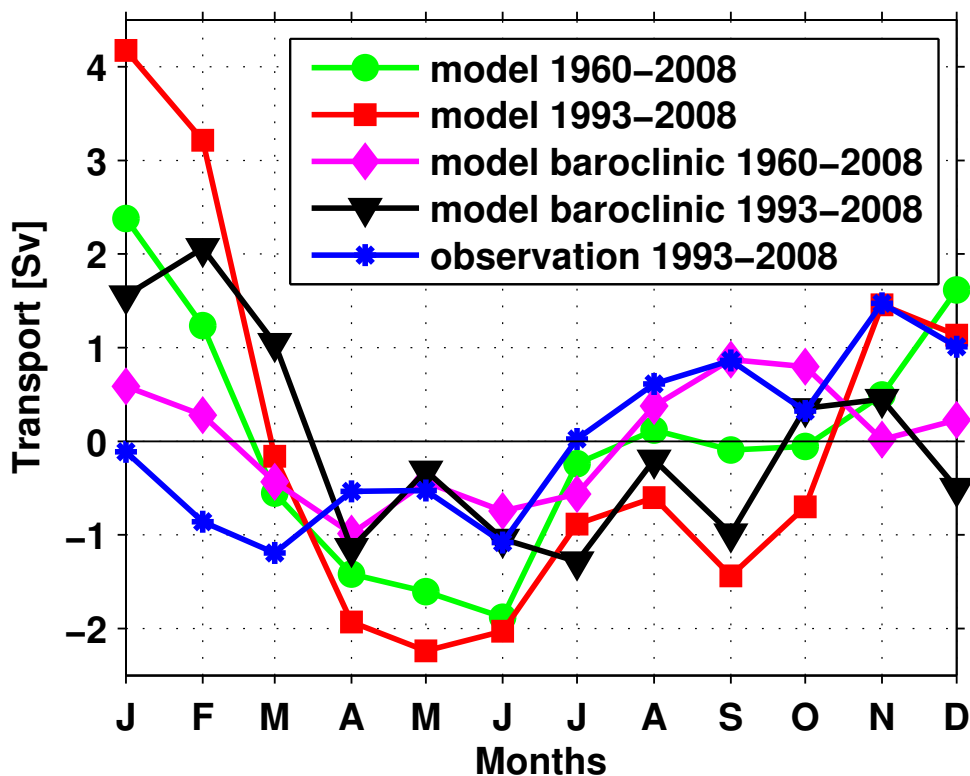
Figure 3.17.: Seasonal cycles at the MAR section for the absolute transport from 1960-2008 (green) and from 1993-2008 (red) and the baroclinic transport from 1960-2008 (pink) and for 1993-2008 (black) from the model. The observations from 1993-2008 are displayed in blue.

This cycle is about 10 % of the mean transport, comparable to the simulated baroclinic transport for the observational period (14 %). The seasonal cycle for the absolute transport in the model is larger for both periods: 24 % for 1993-2008, and 16 % for 1960-2008, and the extreme transports are shifted by about 1 - 2 months compared to observations: the maximum is found in December-January and the minimum in May – July (Figure 3.17). Although the seasonal cycles are clearly observable neither the power spectrum of the altimetry transport nor of the modeled transports show significant seasonal peaks with respect to the corresponding 95 % confidence levels of the red noise spectrum for the time period 1993-2008 (Figure 3.18). The observed significant peak at around 120 days is found to be caused by eddies and meanders (*Roessler et al.*, 2015). In the
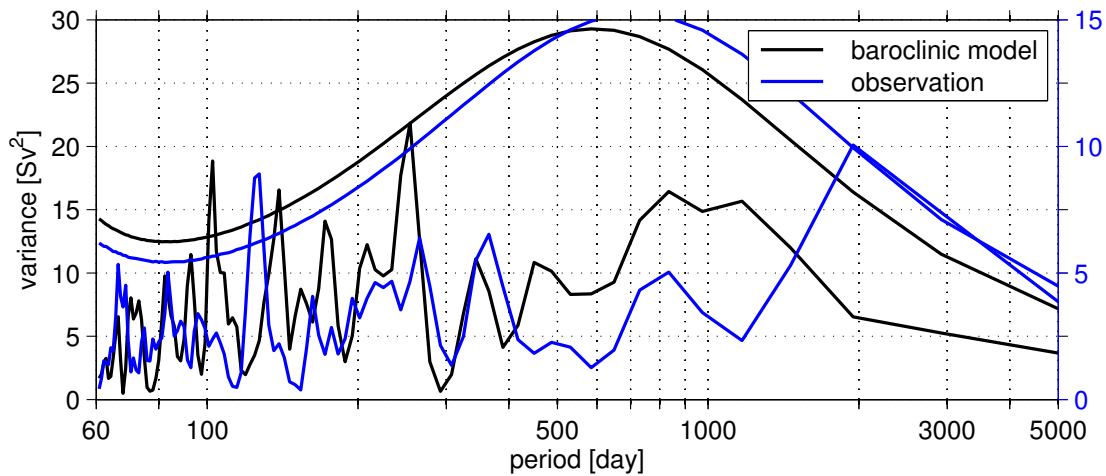
Figure 3.18.: Variance conserving power spectra of the simulated baroclinic transport component (black) and the altimetry derived observational transport time series (blue) at the MAR section. The respective 95 % confidence levels are illustrated in the corresponding colors. Note the different scales for the simulation and the observation. In order to eliminate the influence of the very short time periods monthly data of the transport time series were used.

simulated baroclinic transport component two significant peaks around this time are found, at 100 days and around 140 days. Furthermore, between 200 and 300 days one nearly significant peak is visible. *Roessler et al.* (2015) found the most prominent peak in the observations at around 1500-3300 days (4-9 years), which they relate to the NAO index. In the shorter time period considered here, this peak is just significant in the observations. The simulation does not show this peak in the baroclinic and absolute transport components between 1993 and 2008. For the time period 1960-2008, however, the simulated absolute transport component exhibits a significant peak at around 3 years.

3.3.3. Transport across the OVIDE line

Across the OVIDE section the observed data were taken every second year between 2002 and 2010 during the summer months. These data are compared with transports from the model calculated for every second summer (May until July) for the last eight model years (2000-2008).

The strongest velocity band in the observations is found around 54°N, belonging to the western branch of the NAC (WNAC) carrying 12.7 Sv with a standard deviation of 10.5 Sv (Table 3.5). Starting around the same latitude but extending further north the modeled WNAC is found with a transport of 17.8 Sv and a standard deviation of 5.1 Sv. The broad velocity band between 46°N and 53°30'N in the observation represents the ENAC with a transport of 28.8 Sv and a standard deviation of 7.4 Sv. The modeled ENAC (Figure 3.11a) starts further north at 47°30'N and carries 7.9 Sv with a standard deviation of 3.6 Sv towards the east (Table 3.5).

The simulated ENAC and WNAC transport time series are significantly anti-

Table 3.5.: Five year mean transport from model and observations across the OVIDE line for different subsections along the line. The top to bottom water column is divided by the $\sigma_\theta = 27.68 \, \text{kg/m}^3$ isopycnal into subtropical and deep sea water masses. The standard deviations are given. The observed ENAC is defined between 46°N and 53°30'N, where the observed WNAC starts and ends at 57°N. The simulated WNAC starts 0.5° further north at 57°30'N and ends around the same position as the observed one. The simulated ENAC is found between 47°30'N and around 53°30'N (Figure 3.11). The last three entries show the mean transport and the corresponding standard deviation over the entire model time period for the whole water column and the divided water masses for the WNAC, ENAC and, for the entire section.

Subsection of OVIDE line	Entire water column		Subtropical water ($\sigma_\theta < 27.68 \, \text{kg/m}^3$)		Deep sea ($\sigma_\theta > 27.68 \, \text{kg/m}^3$)	
	Model	Observation	Model	Observation	Model	Observation
ICB 54° - 58.7°N	7.0 ± 4.2	-5.3 ± 9.9	7.9 ± 3.0	-3.3 ± 3.7	-0.8 ± 1.7	-2.0 ± 6.2
EB 44° - 54°N	5.7 ± 3.2	23.6 ± 11.4	7.3 ± 2.8	20.1 ± 5.7	-1.5 ± 1.4	3.5 ± 6.6
IB 40.4° - 44°N	-2.1 ± 2.2	-3.7 ± 6.6	-1.5 ± 1.3	-2.5 ± 5.0	-0.6 ± 1.2	-1.2 ± 1.7
WNAC	17.8 ± 5.1	12.7 ± 10.5	12.4 ± 2.2	4.3 ± 4.3	5.5 ± 3.2	8.5 ± 6.9
ENAC	7.9 ± 3.6	26.8 ± 7.4	9.2 ± 3.2	23.2 ± 4.3	-1.3 ± 0.9	3.7 ± 4.4
entire section	10.5 ± 2.7	14.3 ± 8.9	13.5 ± 1.3	14.3 ± 2.3	-3.0 ± 2.7	-0.03 ± 7.20
WNAC 1960-2008	15.8 ± 7.9		10.5 ± 4.5		5.3 ± 4.2	
ENAC 1960-2008	5.6 ± 8.2		8.2 ± 4.6		-3.2 ± 4.3	
entire 1960-2008	13.9 ± 7.8		15.5 ± 3.6		-1.6 ± 5.5	

correlated with a correlation coefficient of -0.6 from 1960 to 2008, and the observations in the 2000s also show this anti-correlation pattern (Figure 3.19). Further north near 60°N such an anti-correlated behavior is found from satellite altimetry data in the poleward flow west and east of the Reykjanes Ridge and in two subbranches east of the Ridge (*Chafik et al.*, 2014). Over the whole time period, the ENAC in the model weakens by $-2.9 \pm 3.0\,\text{Sv}$, while the WNAC transport increases significantly by $6.6 \pm 3.4\,\text{Sv}$.

The mean top to bottom transport across the entire OVIDE section from 1960 to 2008 is $13.9\,\text{Sv}$ with a standard deviation of $7.8\,\text{Sv}$ (Table 3.5). This is in the
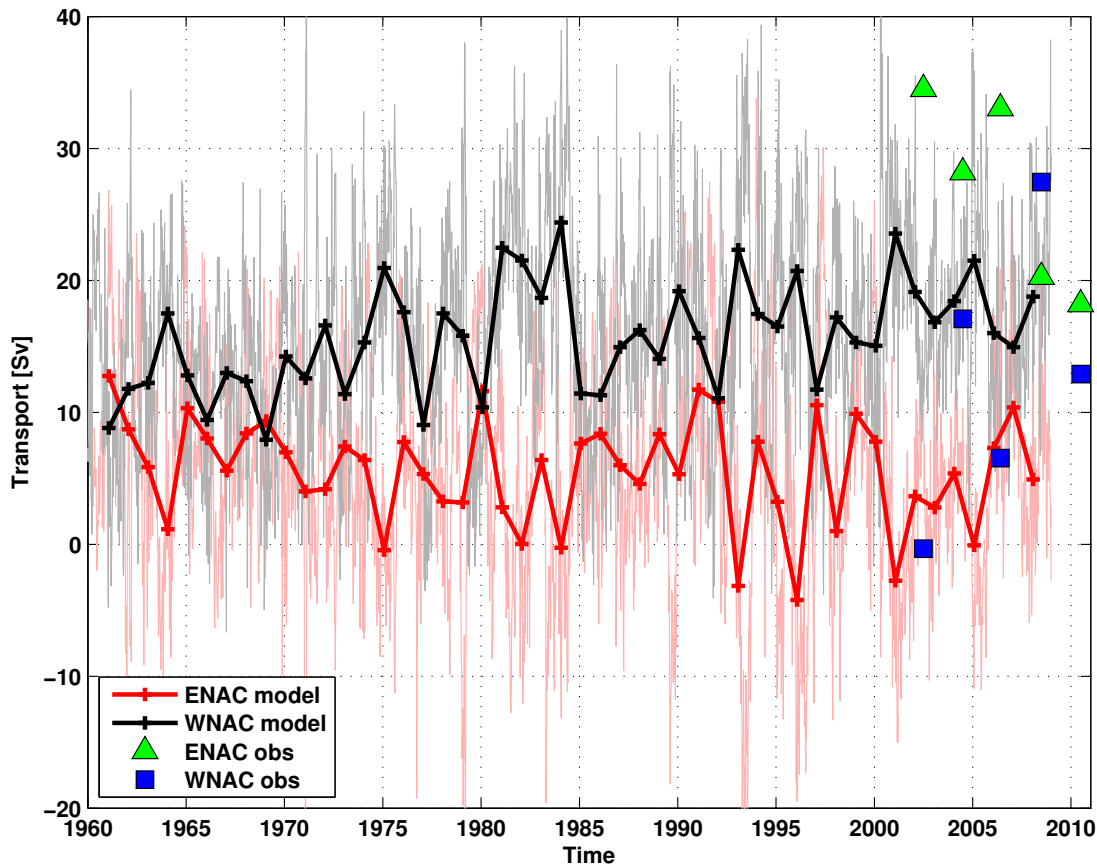
Figure 3.19.: WNAC (black) and ENAC (red) from the VIKING20 model from 1960 to 2008 at the OVIDE line. The bold lines and markers are annual means and the thin lines display the 5 day mean of the model (red and black). The observed WNAC (blue square) and ENAC (green triangle) are marked as well (*Mercier et al.*, 2015).

same range as the observed mean transport of 14.3 Sv with a standard deviation of 8.9 Sv. The simulated transport calculated for every second summer for the last eight model years is around 27 % smaller, but is still within the standard deviation. The smaller transport during the last model years could be caused by the same mechanism than the simulated minimum transport at the MAR section during these years. In the observations, most of the eastward transport was found in the European basin (following *Mercier et al.* (2015)), encompassing the two NAC branches (23.6 Sv). In the model, the flow through that segment is much weaker (5.7 Sv), and the eastward transports are more focused at the Iceland basin (7.0 Sv), while in the observations, the flow in that basin is reversed (-5.3 Sv). The flow in the Iberian Basin is westwards and comparable in model and observations (Table 3.5).

Overall, the simulated and observed flow at the OVIDE section is found to be surface intensified. The simulated subtropical water ($\sigma_\theta < 27.68$ kg/m^3) mass over the entire section and the ENAC as well as in the Iceland and European basins exhibit higher mean transports than over the entire water column. These flows show southwestward directed mean transports in the deep ocean, which eliminate the strong northeastward flow in the upper ocean from 1993 to 2008 (Table 3.5). In the observations the flow direction in the upper and deep ocean in the different basins are in the same directions except for the entire section, where a small southwest directed flow is found in the deep ocean.

3.4. Temperature and salinity evolution

The long-term variability of the hydrographic properties is investigated along all three sections from observations and model. The observational data are CTD data, which were taken during different cruises, but mostly during summer. In section 3.2 the mean hydrographic section between model and observations was compared. Here the focus is on the time evolution of the temperature and salinity and their variability. The trends of the simulated salinity are analyzed, although their realism has to be questioned since the VIKING20 model configuration is suffering from a spurious drift in the freshwater content of the subpolar North Atlantic of unknown origin [6].

3.4.1. Temperature and salinity across the 47°N section

The simulated temperature and salinity across the 47°N section is compared to data taken during 14 cruises between 2003 and 2016 (Table 2.2). The section is divided into different subsections as described in section 3.3.1. For the WBC, SWF and NBR only temperature and salinity values are taken into account for which the corresponding meridional velocity was southward directed. For the NAC the northward directed meridional velocity in the subsection was relevant. In the NFB, eastern, and Flemish Pass subsections as well as over the entire section no flow direction was considered. Overall the simulated mean temperature (March - September 1996-2008) over the entire water column are in the same order of magnitude as the observations. Only the mean temperature values in the NFB section and across the entire section are not within the standard deviation of the mean observational data (Table 3.6). Over the entire section the simulated mean temperature from 1996 to 2008 is $5.0\,°C$, which is around $0.6\,°C$ higher than the observations with $4.3\,°C$. Considering only cruises which are conducted further into the east than 41°W (not MSM5/1 MSM27 and MSM42), the observed mean value over the entire section increases to $4.5\,°C$ with a standard deviation of $0.2\,°C$

Dividing the water column by the $\sigma_\theta = 27.68\,\mathrm{kg/m^3}$ isopycnal the simulated mean temperature values in the upper and deep ocean are comparable with the

---

[6]C. Böning, pers. com. 2017

Table 3.6.: Mean observed and simulated potential temperature and their corresponding standard deviations across the 47°N section. The section is divided into the subsections defined by the geographical positions of the PIES instruments (Table 2.5). For SWF, NBR and WBC only temperature values are taken into account to calculate the mean temperature for which the corresponding velocity vector is defined towards the south, marked with ↓. For the NAC, the velocity vectors are defined towards the north, this is marked by ↑. The observations from 2003 to 2016 are compared to simulated mean values calculated from the summer mean from 1996 to 2008 and to the total mean over the entire model time period (1960 to 2008). For the latter period the simulated cumulated trends are exhibit as well. The * marks the non-significant trend. The significance is calculated using a two-sided t-test with a 95 % confidence level and the error of the trend is calculated from the 95 % confidence bounds for the corresponding time period.

Subsection of 47°N section	Entire water column		Subtropical water ($\sigma_\theta < 27.68\,\mathrm{kg/m^3}$)		Deep sea ($\sigma_\theta > 27.68\,\mathrm{kg/m^3}$)	
	Model	Observation	Model	Observation	Model	Observation
Flemish Pass	4.1 ± 0.3	3.7 ± 0.4	5.3 ± 1.1	3.5 ± 0.7	3.85 ± 0.16	3.90 ± 0.07
WBC ↓	3.9 ± 0.2	3.4 ± 0.5	7.2 ± 1.2	5.5 ± 1.3	3.18 ± 0.10	3.00 ± 0.27
SWF ↓	3.4 ± 2.2	3.5 ± 0.1	9.6 ± 3.9	7.1 ± 2.0	2.81 ± 0.38	2.63 ± 0.38
NAC ↑	4.7 ± 0.3	4.4 ± 0.4	11.0 ± 0.5	9.2 ± 0.7	3.18 ± 0.07	3.01 ± 0.20
NBR ↓	5.3 ± 0.8	5.0 ± 2.0	11.2 ± 0.5	10.2 ± 1.3	3.23 ± 0.15	2.85 ± 0.23
NFB	4.9 ± 0.1	4.4 ± 0.1	10.5 ± 0.3	9.2 ± 0.4	3.28 ± 0.03	3.00 ± 0.05
eastern	5.3 ± 0.1	4.9 ± 0.2	10.5 ± 0.2	8.2 ± 0.7	3.28 ± 0.02	3.17 ± 0.06
entire	5.0 ± 0.1	4.3 ± 0.5	10.4 ± 0.2	8.1 ± 2.2	3.37 ± 0.03	3.16 ± 0.33
	Model 1960-2008		Model 1960-2008		Model 1960-2008	
	mean	trend	mean	trend	mean	trend
Flemish Pass	3.9 ± 0.3	0.13 ± 0.05	4.7 ± 1.2	0.32 ± 0.15	3.71 ± 0.22	0.084 ± 0.029
WBC ↓	3.5 ± 0.2	0.07 ± 0.03	7.1 ± 1.4	0.30 ± 0.18	3.14 ± 0.10	0.039 ± 0.013
SWF ↓	3.4 ± 2.0	0.25 ± 0.25	9.3 ± 3.3	$-0.11 \pm 0.43*$	2.81 ± 0.41	0.106 ± 0.052
NAC ↑	4.6 ± 0.3	0.32 ± 0.04	10.8 ± 0.6	0.95 ± 0.07	3.16 ± 0.40	0.024 ± 0.009
NBR ↓	5.2 ± 0.9	0.40 ± 0.11	11.0 ± 0.7	0.86 ± 0.08	3.21 ± 0.14	0.060 ± 0.018
NFB	4.9 ± 0.1	0.20 ± 0.01	10.3 ± 0.4	0.48 ± 0.04	3.28 ± 0.04	0.026 ± 0.005
eastern	5.2 ± 0.1	0.08 ± 0.01	10.3 ± 0.2	0.22 ± 0.03	3.29 ± 0.02	0.014 ± 0.003
entire	5.0 ± 0.1	0.15 ± 0.01	10.3 ± 0.3	0.38 ± 0.03	3.27 ± 0.02	0.022 ± 0.003

observations within the standard deviations across the entire section. Individual subsections behave differently. In the subtropical water mass ($\sigma_\theta < 27.68\,\mathrm{kg/m^3}$) only the mean temperature from observation and simulation in the SWF and NBR subsections are comparable within the standard deviations. The simulated NAC in the upper ocean with $11.0\,°\mathrm{C}$ and a standard deviation of $0.5\,°\mathrm{C}$ is around $1.8\,°\mathrm{C}$ warmer than the observations $9.2\,°\mathrm{C}$ with a standard deviation of $0.7\,°\mathrm{C}$. In the deep ocean the simulated and observed NAC mean temperature are similar within the standard deviation. Here only the mean temperatures in the NBR, NFB and the eastern subsections are not comparable within the standard deviations.

Taking the entire model time period into account the mean temperature value in the upper and deep ocean changes only slightly in all subsections. However, the temperature across the entire section and in the individual subsections increase over the entire time period. The trends are not equally distributed along the section and different subsections show different trends. The strongest increase in the entire water column is found in the NBR subsection with a cumulated trend of $0.4\,°\mathrm{C}$ from 1960 to 2008. The NAC shows the strongest increase with $0.95\,°\mathrm{C}$ over the entire model time period in the subtropical water mass and in the deep ocean the SWF subsection increases strongest by $0.11\,°\mathrm{C}$. In the Flemish Pass the temperature increased below the $\sigma_\theta = 27.68\,\mathrm{kg/m^3}$ isopycnal by $0.08\,°\mathrm{C}$ over the entire model time period, which is smaller than the $0.3\,°\mathrm{C/decade}$ found by *Schneider et al.* (2015) for the Upper Labrador Sea Water (ULSW) and Deep LSW water masses defined below $\sigma_\theta = 27.68\,\mathrm{kg/m^3}$ from ship board measurements between 1993 and 2013. They compared their ULSW observations with the monthly output of a MIT/gcm model and saw similar trends in both data during the overlapping time period (1993-2009). Taking their entire model time period into account (1960-2009) it is seen that this positive trend started in the 1990s and is part of a multidecadal cycle and the simulated ULSW increased by around $0.2\,°\mathrm{C}$ from 1960 to 2009. This increase is still one magnitude higher than the simulation of the VIKING20 configuration considered here, this might be due to the different horizontal, vertical and temporal resolutions of the models.

The mean temperature anomaly over the NAC subsection shows that before the 1990s the temperature was below the mean temperature and increased afterwards (Figure 3.20). In 2003 the observed temperature anomaly starts around $0.2\,°\mathrm{C}$ below the simulated temperature anomaly. This is reversed in 2007, where the
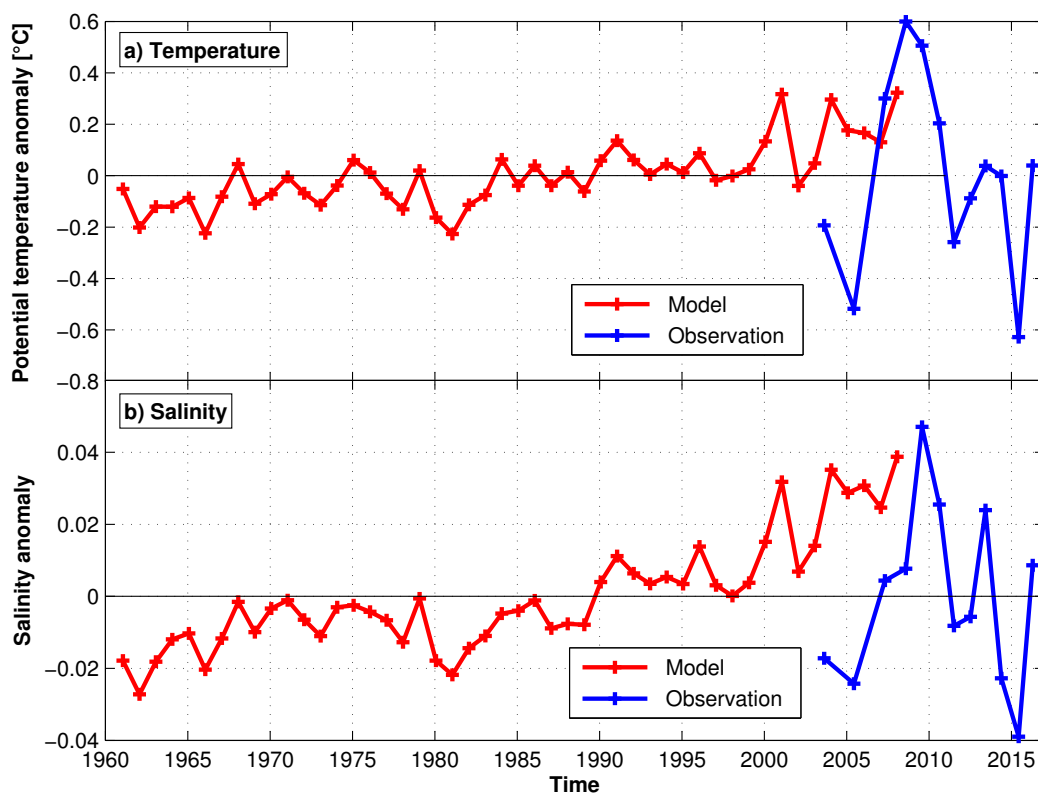
Figure 3.20.: Top to bottom annual temperature a) and salinity b) anomaly evolution from model and observations across the NAC subsection at the 47°N section.

simulation is around $0.2\,°C$ below the observation. The difference even increases in 2008 to around $0.3\,°C$. Overall the observations show higher variability as the simulated temperature and seem to increase by around $0.2\,°C$ from 2003 to 2016. This trend is larger than the simulated one of $0.32\,°C$ (1960-2008). The amplitude of the simulated annual mean temperature anomaly increased since the 1990s. Taking only the last 12 model years into account the simulated temperature would increase by around $0.3\,°C$ from 1997 to 2008, which would be larger than the increase in the observations. Furthermore, the observations are taken during the summer months (March - August) and are only snapshots, where as the simulation are annual means. The seasonal influence on the simulated temperature values of the NAC subsection is around $4.5\,\%$ of the mean. In the upper ocean the seasonal

cycle contributes to the mean temperature of the NAC subsection by around 9 %
and in the deep ocean by around 1 %. The maximum of the seasonal cycle of
the NAC subsection is found in October and the minimum in April. In the other
subsections and across the entire 47°N section the influence of the seasonal cycle
on the mean temperatures through the entire water column are from 18 % in the
SWF to 2 % in the eastern part of the section. The maximum of the seasonal
cycles are found between July and October and the minimum between February
and May. Considering the subtropical water mass the strongest seasonal cycle
is found in the Flemish Pass, where it is around 48 % of the mean temperature.
The maximum seasonal cycle in the Flemish Pass is found in September and the
minimum in March. The influence in the other subsections and across the entire
sections are smaller and their maxima are found between July and October and
their minima between March and April.

The simulated (summer 1996 to 2008) and observed mean salinity across the
entire 47°N section and through the entire water column are comparable within
the standard deviations (Table 3.7). The simulated and observed mean salinities
in the subsections are not in the same order of magnitude except for the SWF and
NBR subsections. In the subtropical water mass only the WBC, the SWF and the
NBR subsections are comparable within the standard deviation. The simulated
NAC e.g. is by around 0.4 more saline than the observation. The simulated mean
salinity values in the deep ocean are general more saline than the observations
except for the WBC and the eastern subsections, where the two different salinity
mean values are comparable within the standard deviations. Overall the differences
between the simulated and observed mean salinity decrease in all subsections and
for the entire water column as well as for the upper and deep ocean, by taking the
entire model period into account. However, like the temperature the salinity across
the entire section and the individual subsections increase over the entire model
time period, with individual trends. The strongest increase in the entire water
column is found like in the temperature in the NBR subsection with a cumulated
trend of 0.06 from 1960 to 2008. This section also shows the strongest increase
(0.14) in the subtropical water mass, whereas the Flemish Pass again exhibits the
strongest increase (0.04) in the deep ocean. This increase is again smaller than
the 0.03/decade in the observed ULSW (1993-2013), but it is in the same range
of magnitude as the simulated increase in ULSW salinity of around 0.05 from the

Table 3.7.: Same as Table 3.6 but for observed and simulated salinity.

Subsection of 47°N section	Entire water column		Subtropical water ($\sigma_\theta < 27.68\,\text{kg/m}^3$)		Deep sea ($\sigma_\theta > 27.68\,\text{kg/m}^3$)	
	Model	Observation	Model	Observation	Model	Observation
Flemish Pass	34.92 ± 0.05	34.61 ± 0.10	34.60 ± 0.14	34.41 ± 0.13	34.996 ± 0.028	34.896 ± 0.008
WBC ↓	34.99 ± 0.02	34.89 ± 0.03	34.88 ± 0.14	34.81 ± 0.16	35.000 ± 0.010	34.906 ± 0.008
SWF ↓	35.01 ± 0.13	34.95 ± 0.12	35.13 ± 0.36	35.01 ± 0.20	34.984 ± 0.011	34.916 ± 0.010
NAC ↑	35.08 ± 0.02	34.99 ± 0.02	35.42 ± 0.06	35.03 ± 0.09	34.992 ± 0.007	34.916 ± 0.008
NBR ↓	35.12 ± 0.06	35.06 ± 0.16	35.49 ± 0.05	35.37 ± 0.15	34.990 ± 0.008	34.913 ± 0.007
NFB	35.10 ± 0.01	34.99 ± 0.01	35.44 ± 0.03	35.25 ± 0.06	34.996 ± 0.005	34.916 ± 0.005
eastern	35.15 ± 0.01	35.04 ± 0.03	35.54 ± 0.02	35.33 ± 0.09	34.944 ± 0.011	34.932 ± 0.010
entire	35.12 ± 0.01	34.92 ± 0.21	35.49 ± 0.02	35.12 ± 0.32	34.997 ± 0.005	34.920 ± 0.009
	Model 1960-2008		Model 1960-2008		Model 1960-2008	
	mean	trend	mean	trend	mean	trend
Flemish Pass	34.87 ± 0.06	0.041 ± 0.007	34.53 ± 0.15	-0.037 ± 0.020	34.963 ± 0.030	0.0399 ± 0.0036
WBC ↓	34.98 ± 0.02	0.017 ± 0.002	34.84 ± 0.17	$0.009 \pm 0.022^*$	34.988 ± 0.010	0.0177 ± 0.0011
SWF ↓	35.00 ± 0.12	0.033 ± 0.015	35.10 ± 0.34	-0.058 ± 0.044	34.975 ± 0.013	0.0203 ± 0.0015
NAC ↑	35.06 ± 0.02	0.044 ± 0.003	35.36 ± 0.07	0.124 ± 0.008	34.984 ± 0.008	0.0173 ± 0.0008
NBR ↓	35.10 ± 0.07	0.057 ± 0.007	35.44 ± 0.07	0.137 ± 0.008	34.982 ± 0.012	0.0187 ± 0.0013
NFB	35.08 ± 0.02	0.040 ± 0.001	35.39 ± 0.04	0.092 ± 0.004	34.989 ± 0.007	0.0190 ± 0.0007
eastern	35.14 ± 0.01	0.024 ± 0.001	35.51 ± 0.03	0.045 ± 0.004	34.939 ± 0.013	0.0104 ± 0.0016
entire	35.11 ± 0.01	0.031 ± 0.001	35.45 ± 0.03	0.064 ± 0.004	34.991 ± 0.006	0.0169 ± 0.0004

MIT/gcm model from 1960 to 2009 (*Schneider et al.*, 2015).

The simulated and observed salinity anomaly of the NAC subsection (Figure 3.20b) show a similar behavior as the simulated and observed temperature anomaly along the same subsection (Figure 3.20a). In 2003 the observed salinity anomaly starts around 0.03 below the simulated salinity anomaly. In contrast to the observed temperature anomaly (Figure 3.20a) the observed salinity anomaly is not above the simulated salinity anomaly in the years 2007 and 2008. The observed variability is again stronger than the simulated one. The observed salinity increases from 2003 to 2016 by around 0.03. The simulated NAC increases over the entire model time period by around 0.04, which is again smaller than the observed increase. As already seen from the temperature anomaly the amplitude of the simulated annual mean salinity anomaly increased since the 1990s. Taking there-

fore only the last 12 model years into account the simulated salinity increased by around 0.04 from 1997 to 2008, which is as already seen in the temperature comparison larger than the increase found in the observations. The seasonal influence on the simulated salinity values of the NAC subsection is 0.03 % of the mean. In the upper ocean the seasonal cycle contributes to the mean salinity of the NAC subsection by around 9 % and in the deep ocean the influence is smaller than 0.1 %. In the upper ocean the maximum of the seasonal cycle of the NAC subsection is found in October and the minimum in April. In the other subsections and across the entire 47°N section the influence of the seasonal cycle on the mean salinities through the entire water column and in the deep ocean is smaller than 0.1 % of the mean. In contrast, in the upper ocean the strongest influence on the mean salinity is found in the Flemish Pass, with 48 % of the mean. The weakest seasonal cycle influence is found across the entire section (5 %), the NFB (5 %), and eastern (4 %) subsections. The maximum of the seasonal cycles in the different subsections in the upper ocean are found between July and October and the minimum in March or April.

3.4.2. Temperature and salinity across the MAR array

Across the MAR section the simulated temperature and salinity is compared to observational data taken during 8 cruises between 2008 and 2016. The simulated summer mean temperature across the entire MAR section is from 2001 to 2008 4.8 °C, which is around 1 °C higher than the observations with 3.9 °C (Table 3.8). In the upper ocean (above $\sigma_\theta > 27.68\,\text{kg/m}^3$) the mean simulation is around 2.3 °C warmer, where as in the deep ocean only around 0.4 °C. The differences between the simulated and observed mean temperatures are decreasing slightly by taking the entire model time period into account. Here the mean simulated temperature over the entire section is around 4.6 °C with a standard deviation of 0.2 °C. This decrease is also illustrated by the simulated temperature trend accumulated to 0.24 °C over the entire model time period. The trend is not equally distributed along the section, therefore different subsections show different trends. In the deep ocean even negative trends are observed in the extended and northern subsections of the MAR section. The mean temperature anomaly over the entire sections shows that during the 1980s the temperature was below the mean temperature

Table 3.8.: Mean observed and simulated potential temperature across the MAR section and their corresponding standard deviations. The section is divided into the subsections defined by the positions of the PIES and the water column is divided into subtropical water and deep sea. The observations from 2008 to 2016 are directly compared to simulated mean values calculated from the summer mean from 2001 to 2008 and to the total mean over the entire model time period (1960 to 2008). For the latter period the simulated cumulated trends are exhibit as well.

Subsection of MAR array	Entire water column		Subtropical water ($\sigma_\theta < 27.68\,\mathrm{kg/m^3}$)		Deep sea ($\sigma_\theta > 27.68\,\mathrm{kg/m^3}$)	
	Model	Observation	Model	Observation	Model	Observation
southern	5.1 ± 0.2	4.4 ± 0.2	10.3 ± 0.4	8.7 ± 0.7	3.37 ± 0.03	3.10 ± 0.03
central	4.8 ± 0.2	3.9 ± 0.2	9.9 ± 0.4	7.5 ± 0.8	3.33 ± 0.04	3.08 ± 0.03
northern	4.5 ± 0.3	3.5 ± 0.1	8.9 ± 0.5	5.7 ± 0.5	3.40 ± 0.05	3.11 ± 0.04
extended	4.3 ± 0.3		8.5 ± 0.7		3.37 ± 0.06	
entire	4.8 ± 0.2	3.9 ± 0.1	9.7 ± 0.4	7.6 ± 0.7	3.36 ± 0.04	3.09 ± 0.03
	Model 1960-2008		Model 1960-2008		Model 1960-2008	
	mean	trend	mean	trend	mean	trend
southern	5.0 ± 0.2	0.14 ± 0.02	10.1 ± 0.4	0.37 ± 0.05	3.36 ± 0.04	0.008 ± 0.005
central	4.6 ± 0.2	0.39 ± 0.02	9.5 ± 0.5	0.90 ± 0.06	3.31 ± 0.04	0.018 ± 0.005
northern	4.4 ± 0.3	0.11 ± 0.03	8.7 ± 0.6	0.58 ± 0.08	3.37 ± 0.06	-0.027 ± 0.007
extended	4.1 ± 0.2	0.10 ± 0.03	8.1 ± 0.7	0.51 ± 0.09	3.33 ± 0.06	-0.024 ± 0.008
entire	4.6 ± 0.2	0.24 ± 0.02	9.4 ± 0.4	0.66 ± 0.05	3.33 ± 0.04	0.003 ± 0.005*

and increased in the 1990s (Figure 3.21a). In 2008 the observed temperature anomaly starts around 0.1 °C below the simulated temperature anomaly. Overall the observed temperature seems to exhibit a negative trend, but this is in the same range as the transitions seen in the simulation for example in the 1970s and 1980s and furthermore only 8 observational data points are available. Therefore, this negative trend could be just a phase in a long term variability. However, the temperature decreases from 4.2 °C to 3.9 °C in 2016, which is around 6 % of the mean temperature. Furthermore, the observations are taken during the summer months (April - August) and are only snapshots, where as the simulation are annual means. The seasonal influence on the simulated temperature values are found to
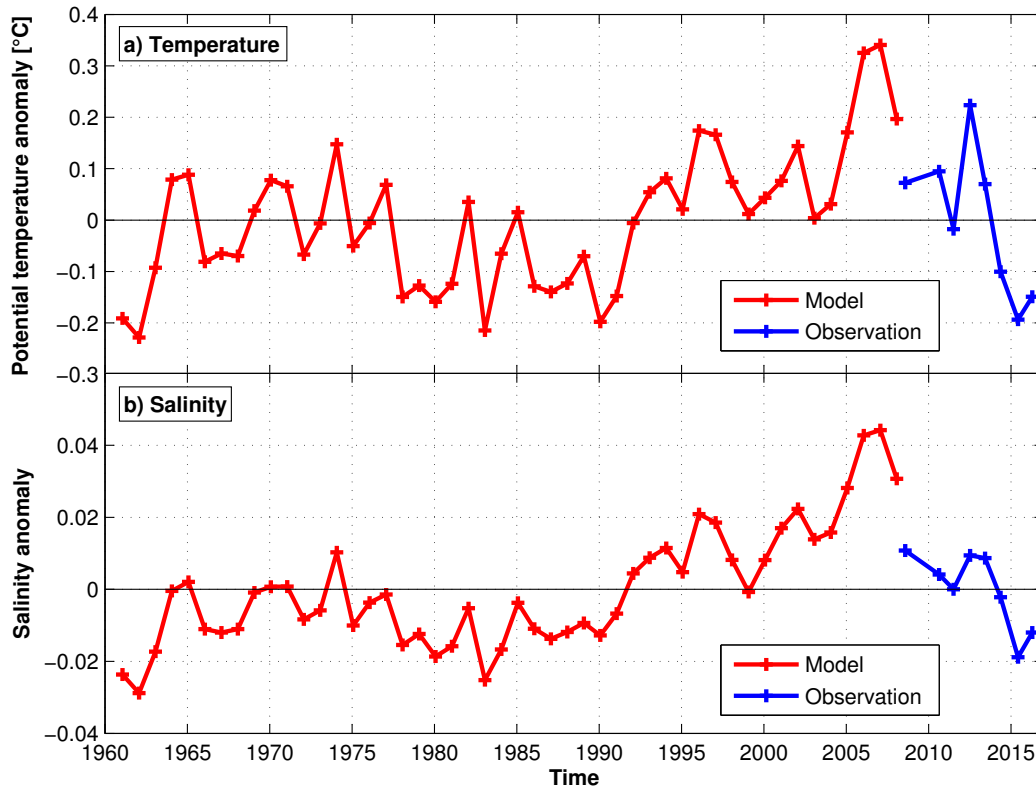
Figure 3.21.: Annual temperature and salinity anomaly evolution from model and observations across the entire MAR section over the whole water column.

be around 2% of the mean over the entire section and through the whole water column. In the upper ocean the seasonal cycle contributes to the mean temperature by around 7 %. The maximum of the seasonal cycle is found in October and the minimum in April. Individual subsections show different maximum, in the central subsection it is found in November and in the southern part in September.

The simulated mean salinity from 2001 to 2008 is around 0.15 higher than the observed mean salinity between 2008 and 2016 (Table 3.9). The difference between the simulated and observed mean salinity decreases by taking the entire model period into account, here the simulated mean salinity over the entire section and the whole water column is 35.06 with a standard deviation of 0.02. The simulated and observed salinity anomaly (Figure 3.21b) shows the same behavior as the simulated

Table 3.9.: Same as Table 3.8 but for salinity.

Subsection of MAR array	Entire water column		Subtropical water ($\sigma_\theta < 27.68\,\mathrm{kg/m^3}$)		Deep sea ($\sigma_\theta > 27.68\,\mathrm{kg/m^3}$)	
	Model	Observation	Model	Observation	Model	Observation
southern	35.11 ± 0.01	34.98 ± 0.02	35.44 ± 0.03	35.18 ± 0.09	35.005 ± 0.005	34.920 ± 0.003
central	35.09 ± 0.01	34.94 ± 0.01	35.38 ± 0.03	35.02 ± 0.08	35.004 ± 0.006	34.919 ± 0.003
northern	35.06 ± 0.02	34.91 ± 0.01	35.25 ± 0.06	34.84 ± 0.03	35.007 ± 0.007	34.926 ± 0.005
extended	35.05 ± 0.02		35.21 ± 0.07		35.008 ± 0.008	
entire	35.08 ± 0.01	34.94 ± 0.01	35.36 ± 0.03	35.04 ± 0.06	35.005 ± 0.006	34.921 ± 0.003
	Model 1960-2008		Model 1960-2008		Model 1960-2008	
	mean	trend	mean	trend	mean	trend
southern	35.09 ± 0.02	0.038 ± 0.002	35.38 ± 0.05	0.086 ± 0.006	34.995 ± 0.008	0.019 ± 0.001
central	35.06 ± 0.02	0.055 ± 0.002	35.29 ± 0.07	0.152 ± 0.007	34.993 ± 0.007	0.017 ± 0.001
northern	35.03 ± 0.02	0.029 ± 0.003	35.18 ± 0.07	0.090 ± 0.009	34.995 ± 0.008	0.013 ± 0.001
extended	35.02 ± 0.02	0.027 ± 0.002	35.11 ± 0.07	0.085 ± 0.009	34.996 ± 0.008	0.012 ± 0.001
entire	35.06 ± 0.02	0.043 ± 0.002	35.28 ± 0.05	0.118 ± 0.006	34.994 ± 0.007	0.016 ± 0.001

and observed temperature anomaly (Figure 3.21a). In contrast to the simulated mean temperature the seasonal cycle of the simulated mean salinity has its maximum in May and its minimum in September. The central subsection exhibits the maximum already in April and in the northern subsection the minimum is shifted to August. The southern part even exhibits the minimum in November. The seasonal cycle of the salinity over the entire section explains only $0.01\,\%$ of the mean salinity value.

In contrast to the observations over the whole water column and the upper ocean the deep ocean shows in all subsections and over the entire section an increase in temperature and salinity. The temperature increases from $3.23\,°\mathrm{C}$ to $3.29\,°\mathrm{C}$ and the salinity from 34.916 to 34.920 from 2008 to 2016. The maximum salinity and temperature is observed in 2012 (Figure 3.21). In the southern subsection through the entire water column mean temperature up to $5\,°\mathrm{C}$ and mean salinities reaching 35.02 are observed. The subtropical water during this cruise was nearly $10\,°\mathrm{C}$ warm and 35.3 saline.

3.4.3. Temperature and salinity across the OVIDE line

The observational CTD data along the OVIDE line are taken every other year between 2002 and 2010. These are compared to simulated temperature (Table 3.10) and salinity (Table 3.11) mean values calculated from every other year between 2000 and 2008 during the summer (May - July) and to mean values calculated over the entire model time period.

Table 3.10.: Mean observed and simulated potential temperature and their corresponding standard deviations across the OVIDE line. The section is divided into different subsections by topographic features and into WNAC and ENAC. The top to bottom water column is divided into subtropical and deep sea water masses. The every second year observations from 2002 to 2010 are compared to simulated mean values calculated from the summer mean from 2000 to 2008 (every other year) and to the total mean over the entire model time period (1960 to 2008). For the latter period the simulated cumulated trends are exhibit as well. The * marks the non-significant trend.

Subsection of OVIDE line	Entire water column		Subtropical water ($\sigma_\theta < 27.68\,\mathrm{kg/m^3}$)		Deep sea ($\sigma_\theta > 27.68\,\mathrm{kg/m^3}$)	
	Model	Observation	Model	Observation	Model	Observation
ICB 54° - 58.7°N	5.22 ± 0.12	4.00 ± 0.07	8.3 ± 0.3	6.3 ± 0.1	3.95 ± 0.04	3.31 ± 0.07
EB 44° - 54°N	5.07 ± 0.07	4.35 ± 0.03	10.4 ± 0.2	8.0 ± 0.1	3.31 ± 0.04	3.18 ± 0.03
IB 40.4° - 44°N	5.07 ± 0.03	4.89 ± 0.07	12.2 ± 0.1	10.7 ± 0.1	3.14 ± 0.02	3.10 ± 0.04
WNAC	5.15 ± 0.13	4.59 ± 0.08	8.6 ± 0.3	6.8 ± 0.1	3.80 ± 0.04	3.53 ± 0.07
ENAC	5.08 ± 0.08	4.24 ± 0.06	10.1 ± 0.1	7.6 ± 0.2	3.35 ± 0.04	3.21 ± 0.04
entire section	5.09 ± 0.06	4.45 ± 0.03	10.4 ± 0.2	8.5 ± 0.1	3.36 ± 0.03	3.18 ± 0.03
	Model 1960-2008		Model 1960-2008		Model 1960-2008	
	mean	trend	mean	trend	mean	trend
ICB 54° - 58.7°N	5.1 ± 0.2	0.17 ± 0.02	7.9 ± 0.5	0.38 ± 0.06	3.94 ± 0.05	$-0.003 \pm 0.006^*$
EB 44° - 54°N	5.0 ± 0.1	0.20 ± 0.01	10.1 ± 0.3	0.36 ± 0.03	3.29 ± 0.03	0.031 ± 0.003
IB 40.4° - 44°N	5.0 ± 0.1	$0.003 \pm 0.007^*$	12.0 ± 0.2	0.41 ± 0.03	3.17 ± 0.04	-0.104 ± 0.003
WNAC	5.0 ± 0.1	0.23 ± 0.02	8.2 ± 0.5	0.44 ± 0.06	3.79 ± 0.05	0.016 ± 0.006
ENAC	5.0 ± 0.1	0.24 ± 0.01	9.7 ± 0.3	0.41 ± 0.03	3.34 ± 0.03	0.020 ± 0.004
entire section	5.0 ± 0.1	0.14 ± 0.01	10.1 ± 0.3	0.36 ± 0.03	3.36 ± 0.02	-0.017 ± 0.003

The simulated summer mean temperature across the entire OVIDE section considered here and through the whole water column is 5.09 °C, which is around 0.6 °C warmer compared to the observation with a mean temperature of 4.45 °C (Table 3.10). In the upper ocean the mean simulation is around 1.9 °C warmer, where as in the deep ocean only around 0.2 °C. Dividing the section into Iceland, European and Iberian basins and considering the WNAC and ENAC subsections it is seen that the model overall is warmer and more saline than the observations (Table 3.11). This is found in the entire water column and in the upper and deep ocean, except for the deep ocean in the Iberian basin, where the simulation and the observations are comparable within the standard deviations. Taking the entire model time period into account the simulated mean temperature and salinity decreases slightly, but is still larger than the observations. The decrease in salinity and temperature is also illustrated by the simulated temperature and salinity trends. The accumulated temperature trend over the entire model time period across the entire section is around 0.1 °C and the corresponding salinity trend is around 0.03. The trend is not equally distributed along the section, individual subsections ex-

Table 3.11.: Same as Table 3.10 but for observed and simulated salinity.

Subsection of OVIDE line	Entire water column		Subtropical water ($\sigma_\theta < 27.68\,\mathrm{kg/m^3}$)		Deep sea ($\sigma_\theta > 27.68\,\mathrm{kg/m^3}$)	
	Model	Observation	Model	Observation	Model	Observation
ICB 54° - 58.7°N	35.127 ± 0.014	34.942 ± 0.008	35.27 ± 0.03	35.01 ± 0.01	35.062 ± 0.007	34.920 ± 0.009
EB 44° - 54°N	35.148 ± 0.012	34.982 ± 0.005	35.56 ± 0.03	35.15 ± 0.02	35.007 ± 0.006	34.929 ± 0.003
IB 40.4° - 44°N	35.220 ± 0.006	35.094 ± 0.012	35.98 ± 0.02	35.53 ± 0.02	35.008 ± 0.003	34.959 ± 0.008
WNAC	35.121 ± 0.013	34.979 ± 0.007	35.31 ± 0.03	35.06 ± 0.01	35.047 ± 0.006	34.940 ± 0.008
ENAC	35.135 ± 0.012	34.962 ± 0.006	35.49 ± 0.03	35.08 ± 0.03	35.006 ± 0.006	34.926 ± 0.003
entire section	35.165 ± 0.010	35.009 ± 0.004	35.61 ± 0.03	35.24 ± 0.01	35.016 ± 0.005	34.936 ± 0.005
	Model 1960-2008		Model 1960-2008		Model 1960-2008	
	mean	trend	mean	trend	mean	trend
ICB 54° - 58.7°N	35.10 ± 0.02	0.041 ± 0.002	35.21 ± 0.05	0.083 ± 0.006	35.050 ± 0.010	0.019 ± 0.001
EB 44° - 54°N	35.12 ± 0.01	0.043 ± 0.001	35.50 ± 0.04	0.088 ± 0.004	34.998 ± 0.007	0.020 ± 0.001
IB 40.4° - 44°N	35.21 ± 0.01	0.015 ± 0.001	35.92 ± 0.04	0.097 ± 0.004	35.010 ± 0.006	-0.012 ± 0.001
WNAC	35.09 ± 0.02	0.047 ± 0.002	35.24 ± 0.05	0.091 ± 0.006	35.035 ± 0.010	0.023 ± 0.001
ENAC	35.11 ± 0.02	0.050 ± 0.001	35.42 ± 0.04	0.103 ± 0.004	34.997 ± 0.007	0.021 ± 0.001
entire section	35.14 ± 0.01	0.034 ± 0.001	35.55 ± 0.04	0.085 ± 0.004	35.010 ± 0.004	0.010 ± 0.001

hibit different trends. In the deep ocean even negative trends are observed in the Iberian and Iceland basins. The strongest temperature and salinity trends over the entire water column are found in the WNAC and ENAC subsections. The WNAC, with mean temperature of $5.15\,°C$ and mean salinity of 35.121 (summer mean 2000 - 2008), increases over the entire model time period by around $0.2\,°C$ and 0.05. This increase is also found for the simulated temperature and salinity of the ENAC. The mean temperature and salinity of the ENAC is $5.08\,°C$ and 35.135, respectively. $2.4\,\%$ of the mean temperature of the ENAC is explained by the seasonal cycle, which has its minimum in April and its maximum in September. The seasonal influence on the mean temperature of the WNAC is around $3.5\,\%$, with the minimum in March and the maximum in September. The seasonal cycle of the temperature across the entire OVIDE section and over the entire water column is around $2.5\,\%$ of the mean, where the minimum is found in April and the maximum in September. The strongest seasonal cycle, with the minimum in March and the maximum in September is found in the Iceland Basin with $3.8\,\%$ of the mean. The influence of the seasonal cycle on the salinity over the entire section and on the WNAC and ENAC is smaller than $1\,\%$.

The temperature anomaly of the ENAC shows that in the 1970s and 1980s the temperature was slightly below the mean temperature and increased in the 1990s (Figure 3.22a). The temperature time series of the WNAC exhibits in comparison to the temperature time series of the ENAC a stronger variation around the mean value. During the 1960s the WNAC temperature was above the mean value, followed by a time period below the mean value until around 1995. The temperature time series of the WNAC shows a strong increase in temperature starting in the late 1980s. The salinity time series of the ENAC and WNAC (Figure 3.22b) behave similar than the corresponding temperature time series, but the differences between the two time series are larger in the temperature. In 2002 the observed ENAC temperature anomaly starts around $0.1\,°C$ below the simulated ENAC and increased slightly by $0.06\,°C$ until 2010. The salinity in contrast decreases during the observations. The ENAC reached its maximum temperature and salinity in the year 2004 with $4.3\,°C$ and 34.94. The maximum temperature in the observed WNAC was found in 2006 and was around $4.9\,°C$, where as the maximum salinity was found 2010 with 35. As in the ENAC the WNAC observed temperature and salinity anomaly is below the simulated one. The temperature of the WNAC
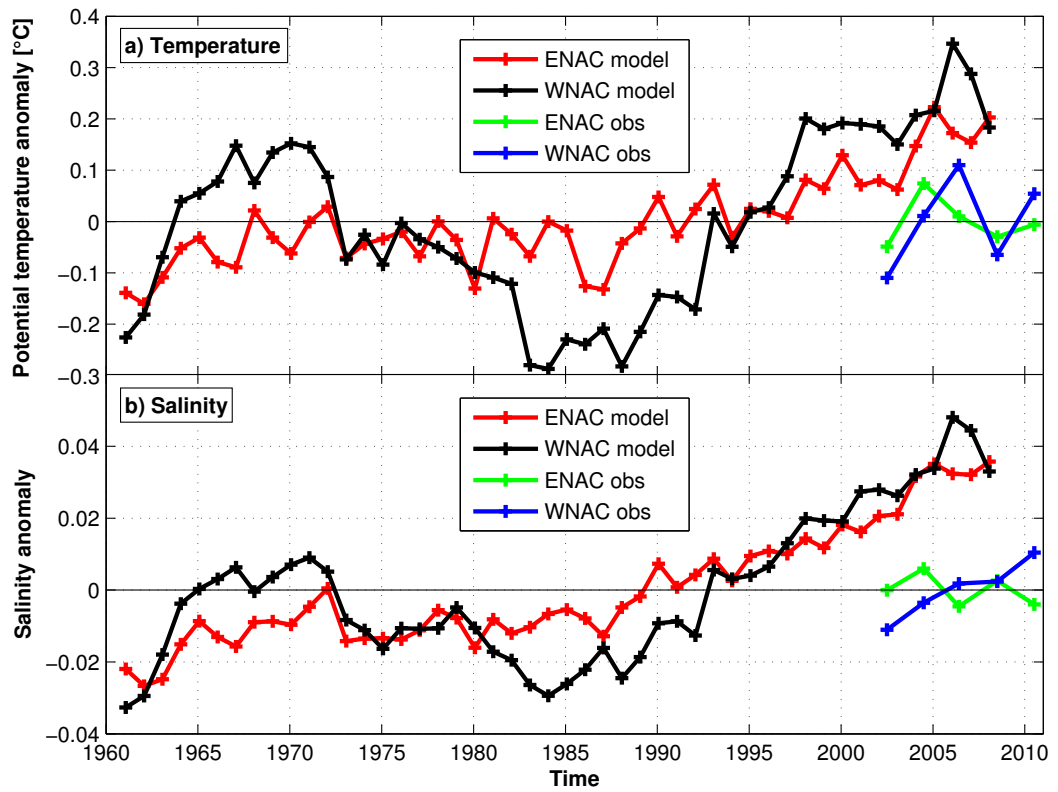
Figure 3.22.: Annual temperature and salinity anomaly evolution of the WNAC and ENAC across the OVIDE line over the entire water column from model and observations.

increased from 2002 to 2010 by around $0.2\,^\circ$C.

4. Influence of the North Atlantic Oscillation on the North Atlantic and the North Atlantic Current

The influence of the atmospheric mode of the North Atlantic Oscillation on the North Atlantic and the North Atlantic Current is investigated by using velocity, transport, temperature, and salinity composites for the five highest and five lowest NAO years. In a second step the direct feedback of the NAO on the NA and NAC is investigated by studying transitions from one NAO state to the other. The NAO winter (DJFM) index is defined as the normalized pressure difference between Ponta Delgada, Azores and Stykkisholmur/Reykjavik, Iceland (*Hurrell*, 1995).

Roessler et al. (2015) found that the spectrum of the 21 year observational transport time series at the PIES array along the MAR section shows a significant $4 - 9$ year peak, and is significantly cross-correlated with the NAO. The cross-correlation is calculated between annual means of the transport time series and the NAO winter index (Figure 4.1). This approach eliminates partly the effect of meanders and eddies. The monthly influence on the transport is calculated by changing the center of the annual mean transport in each step by one month. The probability tests the hypothesis of no correlation by using a t-statistic with n-2 degrees of freedom, a p-value less than 0.05 indicates a significant correlation. The NAO winter (DJFM) index for observations and model have been computed from the difference of normalized sea level pressures between Ponta Delgada, Azores and Stykkisholmur/Reykjavik, Iceland (*Hurrell*, 1995), for the modeled NAO the CORE.v2 sea level pressure was used (*Scholz et al.*, 2014).
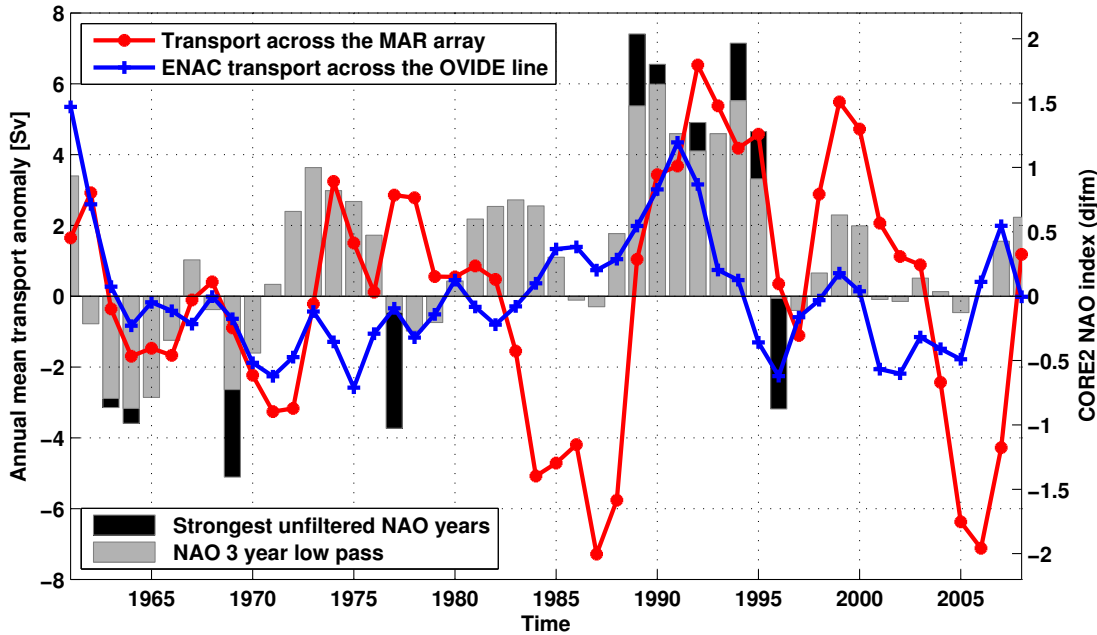
Figure 4.1.: Annual mean transport anomaly across the PIES array at the MAR (red) and the ENAC across the OVIDE line (blue) and winter CORE.v2 NAO (gray). For clarity the time series are treated with a 3-year low pass filter. The black bars mark the five strongest/weakest NAO years, which where used to calculate the composites in section 4.1 and show the strength of the unfiltered NAO index for that year.

Along the 47°N section in the Newfoundland basin the influence of the NAO index on the transports of different flows are various (Table 4.1). The northward flowing NAC transport is found to be significantly correlated with the NAO in model and observations. However, the simulated NAC transport is only significantly correlated to the NAO over the entire model time period from 1960 to 2008 and not from 1993 to 2008, in which observations are available and found to be significantly correlated to the NAO index. The correlation coefficient and the range of the significant correlations are similar in observations and model. None of the simulated transports across the 47°N section show a significant correlation with the NAO index from 1993 to 2008, this could be due to the influence of other natural variability during those years at this section and furthermore, the NAO index exhibits after strong positive NAO years in the 1990s only moderate index values in the early 2000s. The observations, however exhibits a significant anti-correlation

Table 4.1.: Cross-correlation between NAO index and transports at the 47°N section. The maximum significant correlation coefficient r is given with it corresponding lag time (in months). Positive lags indicate that the transport follows the NAO index. The range of the significant correlation is displayed in months. No significant correlations are marked with an x. The correlation is calculated between annual means of the transport time series and the NAO winter index. The monthly influence on the correlation is calculated by changing the center of the annual mean transport in each step by one month. The cross-correlation from 1960 to 2008 was calculated with a maximum lag of 72 months and the cross-correlation from 1993 to 2008 with a maximum lag of 24 months. The observations were provided by A. Roessler.

| Transport at 47°N | Model | | | | | | Observation | | |
| | 1960-2008 | | | 1993-2008 | | | 1993-2008 | | |
	max. r	Lag	Range	max. r	Lag	Range	max. r	Lag	Range
Entire water column									
SWF ↓	-0.44	9	8-12	x	x	x	-0.54	14	14-14
NAC ↑	0.56	10	3-26	x	x	x	0.65	11	8-12
NBR ↓	-0.39	5	2-7	x	x	x	x	x	x
NFB	x	x	x	x	x	x	x	x	x
entire	0.47	-3	-6-4	x	x	x			
Subtropical water ($\sigma_\theta < 27.68\,\mathrm{kg/m^3}$)									
SWF ↓	-0.43	8	9-13	x	x	x			
NAC ↑	0.56	10	2-27	x	x	x			
NBR ↓	-0.46	11	0-6	x	x	x			
NFB	0.38	54	54-54	x	x	x			
entire	0.38	32	31-33	x	x	x			

between the NAO index and the southward flowing SWF. The simulated SWF is also anti-correlated with the NAO index, but at a shorter lag time and for the entire model time period from 1960 to 2008. The southward flowing NBR and the NFB are not correlated with the NAO index in the observations, but the NBR is

anti-correlated with the NAO index in the simulation. Considering the subtropical part of the simulated water column, even the NFB is found to be correlated with the NAO index, but with a longer lag time of 54 months. All the other simulated flows, except for the entire section, are correlated to the NAO index within the range of 2 to 26 months.

The NAO not only influences the velocity and transport along the NAC pathway but also temperature and salinity (e.g *Eden and Willebrand*, 2001; *Bersch et al.*, 2007; *Frankignoul et al.*, 2009; *Reverdin*, 2010). Along the 47°N section in the Newfoundland basin temperature and salinity are variously correlated with the NAO index (Table 4.2). The temperature and salinity of the northward flowing NAC and the southward flowing NBR are significantly correlated with the NAO

Table 4.2.: Same as Table 4.1 but for the cross-correlation between the NAO index and simulated temperature and salinity time series from 1960 to 2008 along the 47°N section.

Properties at 47°N	Entire water column			Subtropical water ($\sigma_\theta < 27.68\,\mathrm{kg/m^3}$)		
	max. r	Lag	Range	max. r	Lag	Range
Temperature						
SWF ↓	0.34	49	49-49	x	x	x
NAC ↑	0.42	19	18-20	0.53	20	8-28
NBR ↓	0.35	11	11-11	0.51	13	7-27
NFB	x	x	x	0.35	15	14-17
entire	x	x	x	x	x	x
Salinity						
SWF ↓	x	x	x	x	x	x
NAC ↑	-0.36	42	42-44	0.41	19	17-29
NBR ↓	0.36	11	11-11	0.48	15	8-30
NFB	x	x	x	x	x	x
entire	x	x	x	x	x	x

index, over the entire water column and in the subtropical ($\sigma_\theta < 27.68\,\mathrm{kg/m}^3$) part. The correlations of the NBR are within the range of 7 to 30 months. The correlation of the NAC is within the same range, except for the salinity over the entire water column. Here the anti-correlation is found at lag times of 42 to 44 months. The salinity across the other flows along the 47°N section are not significantly correlated with the NAO index. The temperature of the SWF over the entire water column and the subtropical temperature of the NFB are found to be significantly correlated to the NAO index. Overall, the transport, salinity and temperature of the NAC and the NBR are significantly influenced by the NAO in the simulation from 1960 to 2008.

The observed and simulated different transport time series across the MAR section are significantly cross-correlated with the NAO index when the NAO leads the transport by 2 to 16 months for different time periods (Table 4.3). Except for the simulated absolute transport time series from 1993 to 2008, which is found to be correlated within the range of -2 to 1 months. Not only the lags of the different transport time series are in the same range, but the maximum correlation coefficients and their corresponding lag time are similar as well. These are in agreement with findings of *Roessler et al.* (2015), which reported that the NAO leads the observed MAR section transport by 6 to 7 months, with a maximum significant correlation of $r = 0.5$ for the time period 1993 to 2015.

The simulated temperature across the MAR section is found to be not significantly correlated to the NAO index, but the simulated salinity time series is anti-correlated from 1993 to 2008 (Table 4.3). Further east in the eastern basin of the NA at the OVIDE section the simulated subtropical temperature over the entire section and of the WNAC are anti-correlated with the NAO index (Table 4.4). The corresponding salinities are not influenced by the NAO index, but the WNAC salinity over the entire water column is. In contrast to that the transport of the WNAC is independent of the NAO index. The subtropical transport of the entire section and the ENAC further south is found to be significantly correlated with the NAO index, but the corresponding temperature and salinity of the ENAC are not.

Overall, multiple studies showed that the NAO index influences different properties of the NA (e.g *Curry and McCartney*, 2001; *Eden and Willebrand*, 2001;

Table 4.3.: Same as Table 4.1 but for the cross-correlation between the NAO index and simulated properties (transport, temperature, salinity) and the observed transport time series at the MAR section.

Properties at MAR	Correlation 1960-2008			Correlation 1993-2008		
	max. r	Lag	Range	max. r	Lag	Range
Referenced to 3400 m depth						
Model absolute transport	0.49	7	4-15	0.63	-1	-2-1
Model baroclinic transport	0.55	8	3-16	0.60	7	7-7
Observed transport				0.74	6	2-16
Model temperature	x	x	x	x	x	x
Model salinity	x	x	x	-0.65	-2	-4-2
Subtropical water ($\sigma_\theta < 27.68$ kg/m^3)						
Model absolute transport	0.48	9	5-15	x	x	x
Model baroclinic transport	0.53	8	4-15	0.58	7	7-7
Model temperature	x	x	x	x	x	x
Model salinity	x	x	x	-0.67	-3	-5-1

Bersch et al., 2007; *Frankignoul et al.*, 2009; *Reverdin*, 2010; *Hauser et al.*, 2015; *Roessler et al.*, 2015). Here the transport, temperature and salinity time series at three different sections along the pathway of the NAC were correlated to the NAO index. Across the three sections the influence of the NAO depends on the choice of the time period and the maximum lag to compute the cross-correlation. However, the NAC transport from the 47°N section over the MAR section into the eastern basin at the OVIDE section is found to be correlated to the NAO index, lagging the NAO index within the range of 0 to 26 months. The temperature and salinity are found to be significantly influenced by the NAO at the inflow into the NA and in the eastern basin, but across the MAR section other variability dominates the temperature and salinity time series. In general, the cross-correlations show that the NAO influences the properties of the NAC and therefore, the direct influence

Table 4.4.: Same as Table 4.1 but for the cross-correlation between the NAO index and simulated properties (transport, temperature, salinity) of the ENAC and WNAC at the OVIDE section and the entire OVIDE section from 1960 to 2008.

Properties at OVIDE	Entire water column			Subtropical water ($\sigma_\theta < 27.68\,\text{kg/m}^3$)		
	max. r	Lag	Range	max. r	Lag	Range
WNAC transport	x	x	x	x	x	x
ENAC transport	x	x	x	0.40	1	0-5
entire transport	x	x	x	0.40	41	38-43
WNAC temperature	x	x	x	-0.34	5	3-7
ENAC temperature	x	x	x	x	x	x
entire temperature	-0.35	24	21-28	-0.35	16	10-22
WNAC salinity	-0.33	3	3-5	x	x	x
ENAC salinity	x	x	x	x	x	x
entire salinity	x	x	x	x	x	x

of the NAO is investigated by studying the difference between the five strongest and five weakest NAO years and the five strongest transitions from positive to negative or negative to positive NAO years in the next sections.

4.1. Influence of the five strongest positive and five strongest negative NAO years

To study the role of the NAO further, *Roessler et al.* (2015) investigated the composite of the five highest and five lowest NAO index events and found a significant higher mean transport at the PIES array at the MAR section during the five positive NAO years. This transport increase was mainly found in the southern subsection of the array. One of the highest and three of the lowest NAO event years are found by *Roessler et al.* (2015) in the years after 2008. Here the entire

model time period is taken into account. The five strongest positive CORE.v2 NAO events are found in the years 1989, 1990, 1992, 1994 and, 1995 and the five strongest negative NAO in the years 1963, 1964, 1969, 1977 and, 1996 (Figure 4.1). The five strongest positive NAO events are mainly in the 1990s and the negative NAO events in the 1960s, therefore the difference between the positive and the negative NAO composite might also be biased by other decadal variability. In the section 4.2 the direct feedback of the NAO is investigated by studying transitions from one NAO state to the other.

The velocity composites reveal stronger velocities and different pathways during positive NAO years in comparison to negative NAO years (Figure 4.2). At the NWC e.g. it is seen that during positive NAO years the NWC shifts farther north and is stronger than during negative NAO years (Figure 4.2). Overall the shape of the NWC seems to be modulated by the topography. The stronger velocities lead to higher transports across the 47°N section in the western subpolar NA. At this section the direction of the mean transport over the whole water column across the entire section even changes from northward flowing transport (0.35 Sv with a standard deviation of the mean of 0.03 Sv) during the positive NAO phase to southward flowing transport (-0.15 Sv with a standard deviation of the mean of 0.16 Sv) in the negative NAO phase. The subtropical water increases from 18.7 Sv (with a standard deviation of the mean of 0.5 Sv) to 19.3 Sv (with a standard deviation of the mean of 0.4 Sv) from negative to positive NAO years over the entire section. During positive NAO phase the maximum northward inflow of the subtropical NAC into the NA at the 47°N section is slightly further east than during negative NAO years (Figure 4.3). Furthermore, the northward directed subtropical NAC carries significantly higher transport (46.2 Sv with a standard deviation of the mean of 1.2 Sv) into the NA during positive NAO years compared to negative NAO years (42.2 Sv with a standard deviation of the mean of 1.7 Sv). This increase in transport during positive NAO years is also seen over the whole water column, where the transport increases from 135 Sv (with a standard deviation of the mean of 5 Sv) to 122 Sv (with a standard deviation of the mean of 6 Sv). Further east the southward flowing subtropical NBR (-24.6 Sv with a standard deviation of the mean of 1.2 Sv) is stronger and the maximum transport appears further east during positive NAO phases compared to negative NAO phases (-20.3 Sv with a standard deviation of the mean of 0.9 Sv). This increase is again seen over the entire water
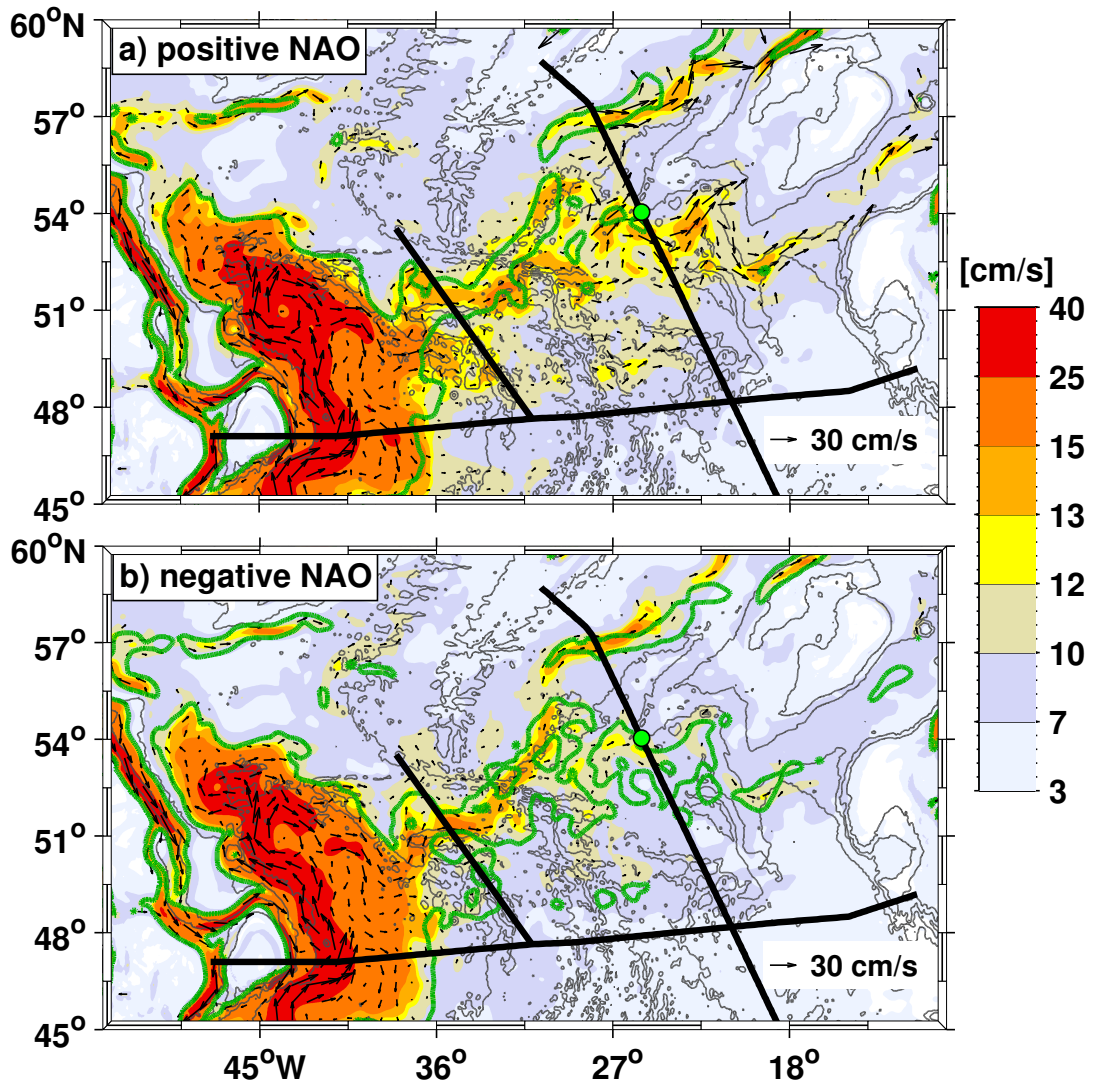
Figure 4.2.: Speed calculated from 1000 m depth to the surface from the model. The velocity time series at each grid point was detrended to eliminate possible decadal variability. Composites for the five strongest positive NAO phase (a) and the five strongest negative NAO phase (b). The green contour exhibits the 12 cm/s-isoline for the negative NAO state (a) and the positive NAO phase (b) for easier comparison. The black lines mark the 47°N, the MAR and the OVIDE sections.

column, here the transport increases from $-51\,\mathrm{Sv}$ (with a standard deviation of the mean of $3\,\mathrm{Sv}$) to $-65\,\mathrm{Sv}$ (with a standard deviation of the mean of $2\,\mathrm{Sv}$) for positive NAO years. In the eastern part of the 47°N section simulated southward
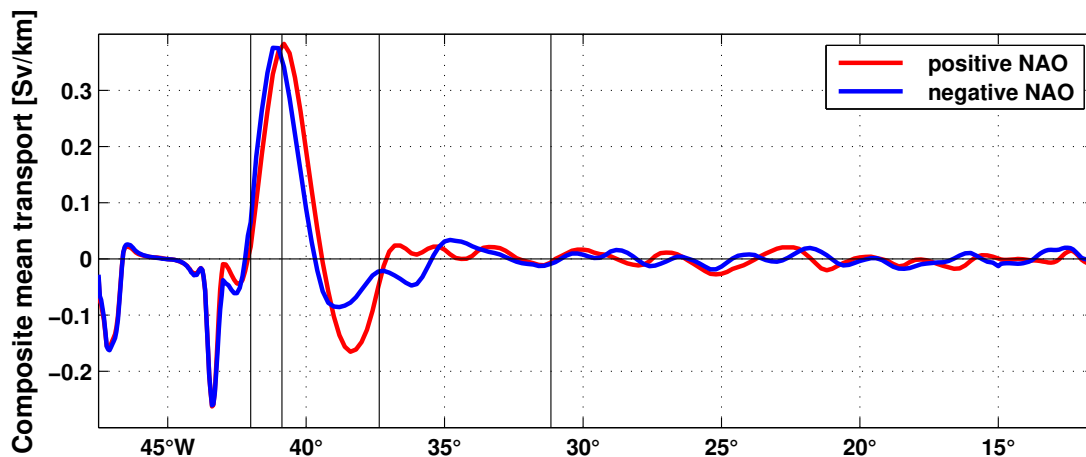
Figure 4.3.: Composites of simulated mean meridional transports along the 47°N section for positive NAO (red) and negative NAO (blue) phases, defined by the five strongest/weakest NAO years. The absolute transport is detrended and calculated from 1000 m depth to the surface, to display the subtropical water mass along the section. The vertical lines mark the PIES positions. The transport is given in Sv/km and the entire section is around 2710 km long.

and northward directed flow alternate and show different locations during different NAO phases.

In contrast to the simulated NAC and NBR described here and the observed transport at the MAR section (*Roessler et al.*, 2015) the observed northward top to bottom NAC and the southward directed top to bottom NBR at the 47°N section do not show significant differences for the five highest and five lowest NAO composites calculated as described by *Roessler et al.* (2015) for the years 1994, 1995, 2000, 2007, and 2012 (positive NAO) and the years 1996, 2001, 2010, 2011, and 2013 (negative NAO)[1].

Further downstream at the MAR section the composites reveal in agreement to observations (*Roessler et al.*, 2015) that the mean absolute transport across the PIES array (referenced to 3400 m) during the positive NAO phases (32.8 Sv with a standard deviation of the mean of 1.9 Sv) is significantly higher than during negative NAO phases (26.2 Sv with a standard deviation of the mean of 1.6 Sv). Under positive NAO conditions, the subtropical NAC transport (21.7 Sv with a

---

[1]A. Roessler, pers. com. 2017

standard deviation of the mean of 1.5 Sv) is in the entire section towards the east (Figure 4.4), with the highest values in the northern part (51°N – 52°30'N). During negative NAO phases, the transport (18.5 Sv with a standard deviation of the mean of 0.9 Sv) is much more unevenly distributed, with even westward transports in part of the central segment, and highest transports around 49°N, 51°N and 52°30'N (Figure 4.4).

In the eastern basin of the NA across the OVIDE section during positive NAO phases significant higher top to bottom transport (15.1 Sv with a standard deviation of the mean of 1.2 Sv) crosses the entire OVIDE section compared to negative NAO phases (13.6 Sv with a standard deviation of the mean of 0.4 Sv). The ENAC top to bottom mean transport is significantly higher during positive NAO phases (7.5 Sv with a standard deviation of the mean of 1.3 Sv) than during negative NAO phases (2.8 Sv with a standard deviation of the mean of 2.1 Sv). The corresponding subtropical transport behaves accordingly, with higher transports during positive NAO phases (9.9 Sv with a standard deviation of the mean of 0.9 Sv) compared to negative NAO phases (6.3 Sv with a standard deviation of the mean of 1.1 Sv). The subtropical transport across the entire OVIDE section is higher during positive NAO phases (16.3 Sv with a standard deviation of the mean of 0.7 Sv) compared to negative NAO phases (15.5 Sv with a standard deviation of the mean of 0.2 Sv) and alters differently during the two NAO phases between westward and eastward
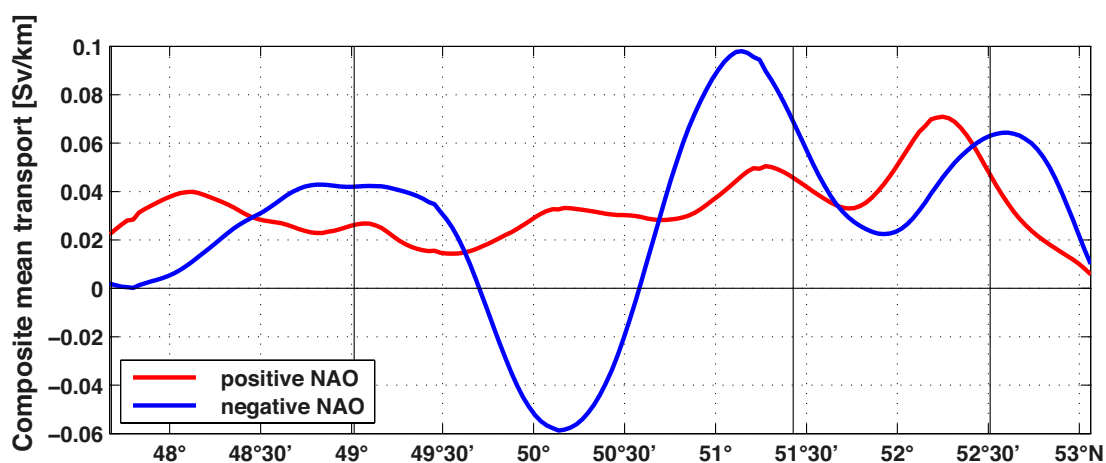
Figure 4.4.: Same as Figure 4.3 but for the northeastward transports along the MAR section. The entire section is around 755 km long.

directed flow (Figure 4.5). In the regime of the ENAC the transport during positive NAO years is mostly towards the east, except in the southern part. During negative NAO years however the westward and eastward directed flow alternates and therefore compensates each other regarding the mean transport. The WNAC is not correlated to the NAO index and therefore it is consistent that it does not show a significant difference between the transport during positive and negative NAO years.

Not only the transport and the velocity distributions are influenced by the NAO but the temperature (Figure 4.6) and salinity (Figure 4.7) of the NA as well (e.g *Eden and Willebrand*, 2001; *Bersch et al.*, 2007; *Frankignoul et al.*, 2009). Warmer and more saline water reaches further north during negative NAO phases in the VIKING20 model configuration. The $6\,°C$-isotherm during negative NAO phase e.g. reaches farther north in the NWC region, comes close to the $6\,°C$-isotherm during positive NAO phase, before the two isotherms separate west of the MAR and the isotherm of the negative NAO phase is found around 2 degrees further north along the path into the north (Figure 4.6). The different pathways of the negative and positive NAO phase isotherms increases with decreasing temperature, the $10\,°C$-isotherms e.g. show nearly the same pathway, where as the $5\,°C$-isotherms are only close to each other flowing north towards the NWC, where they separate
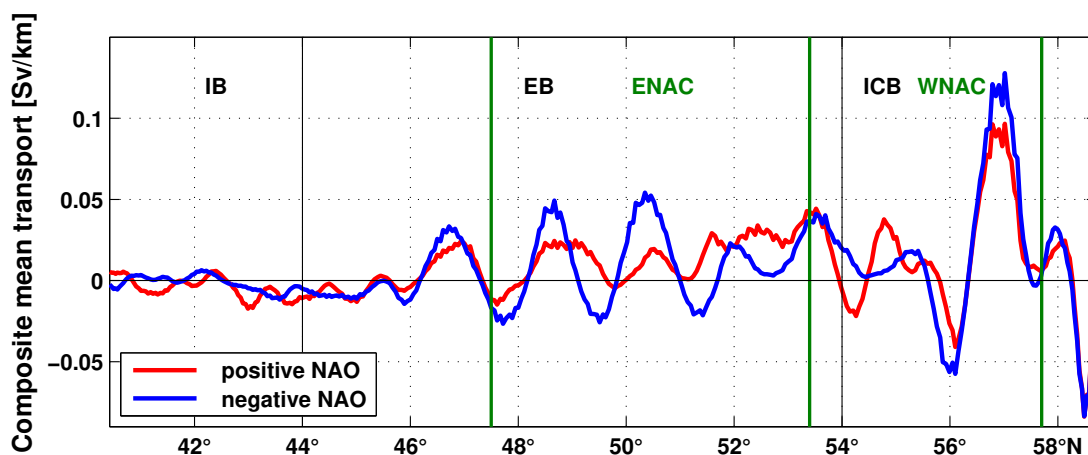
Figure 4.5.: Same as Figure 4.3 but along the OVIDE section. The entire section is around 2466 km long. The black lines mark the separation into the different basins and the green lines the separation into WNAC and ENAC.
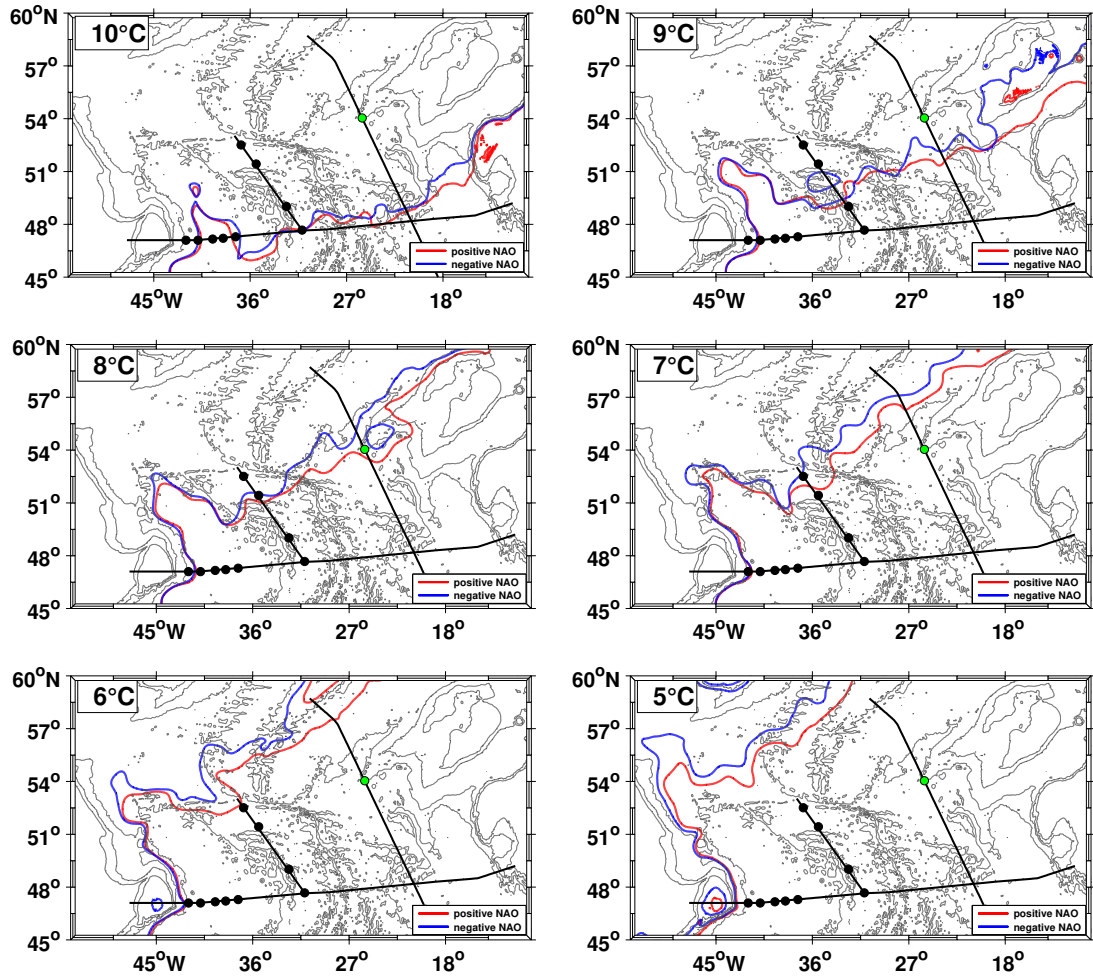
Figure 4.6.: Temperature composites for different temperatures for the five strongest positive NAO phase (red) and the five strongest negative NAO phase (blue) calculated from 1000 m depth to the surface. The temperature time series at each grid point was detrended to eliminate possible decadal variability. The black lines mark the three sections. The black dots indicate the PIES positions and the green dot shows the separation of the OVIDE line into Iceland and European basins after *Mercier et al.* (2015).

(Figure 4.6). The salinity distribution shows such a behavior as well (Figure 4.7), here e.g. the 35.4-isohalines are close to each other, where as the 35.05-isohalines are clearly separated after the NWC, where the negative NAO isohaline reaches again further north. Overall, in the western basin at the NWC the isotherms and isohalines seem to be steered by the topography like the velocity distribution.
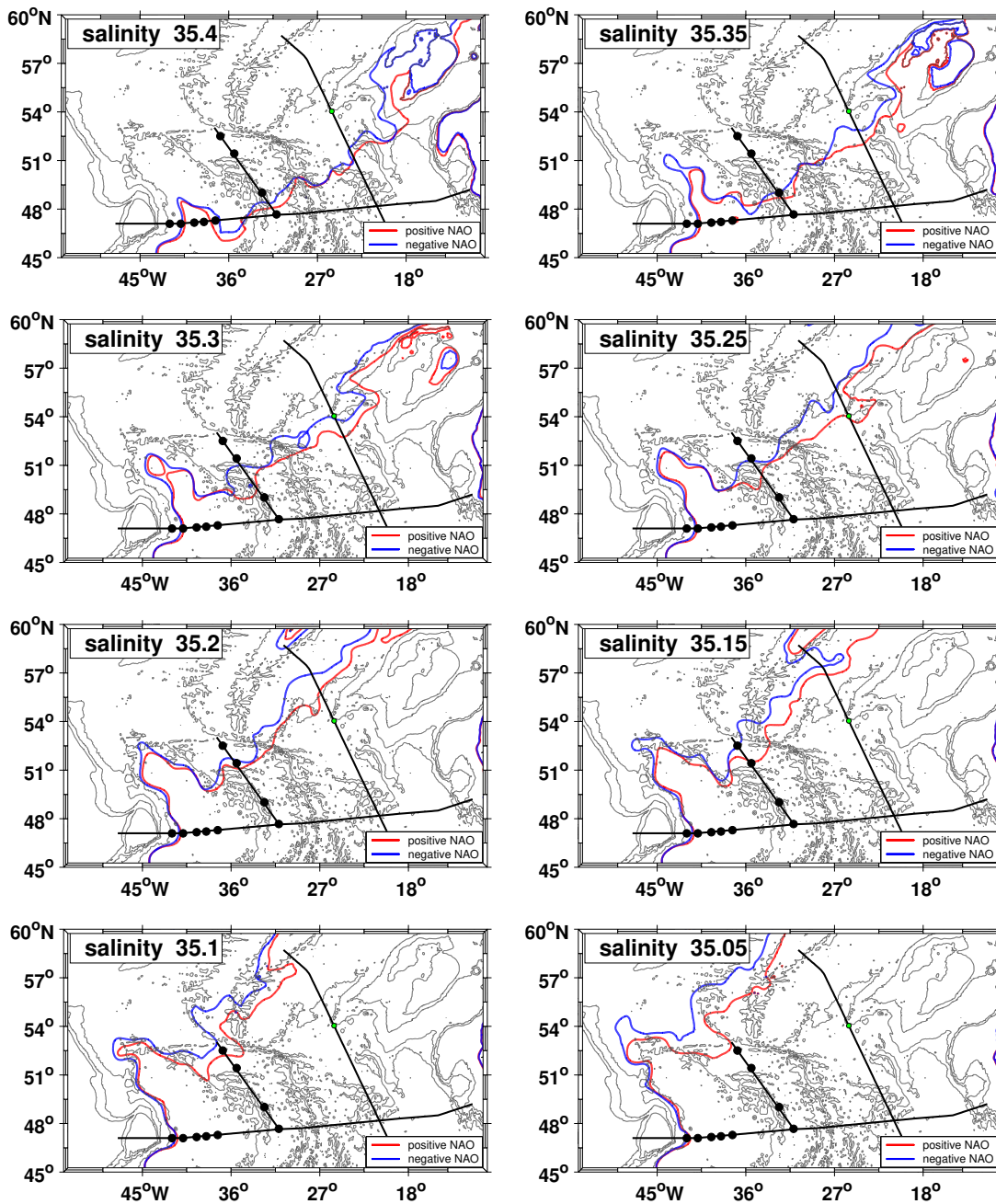
Figure 4.7.: Same as Figure 4.6 but for different salinites.

Furthermore, considering the 35.3-isohaline and the 8 °C-isotherm to represent the Subpolar Front (SF), the contraction and shift of the SF during negative NAO years is clearly observed. The largest differences between the positive and negative NAO years are seen north of the SF in the SPG regime.

Overall the NAC across the three sections along it's pathway is warmer and more saline during negative NAO years compared to positive NAO years in the subtropical water mass above the $\sigma_\theta = 27.68 \, \text{kg/m}^3$ isopycnal. Starting at the 47°N section in the subtropical northward flowing NAC higher mean salinity is found during negative NAO years (35.386 with a standard deviation of the mean of 0.008) compared to positive NAO years (35.368 with a standard deviation of the mean of 0.006). The corresponding temperature time series was found to be correlated to the NAO as well, but does not exhibit significant differences between the here considered positive and negative NAO years. West of the MAR the subtropical water mass across the entire section exhibits higher salinity (35.32 with a standard deviation of the mean of 0.01) and warmer temperature (9.7 °C with a standard deviation of the mean of 0.1 °C) during negative NAO years compared to positive NAO years (35.28 with a standard deviation of the mean of 0.01, 9.4 °C with a standard deviation of the mean of 0.1 °C, respectively). Further east at the OVIDE line the subtropical ENAC and WNAC show higher salinity (35.43 with a standard deviation of the mean of 0.01 (ENAC) and 35.26 with a standard deviation of the mean of 0.02 (WNAC)) and warmer temperature (9.8 °C with a standard deviation of the mean of 0.1 °C (ENAC) and 8.4 °C with a standard deviation of the mean of 0.2 °C (WNAC)) during negative NAO years compared to positive NAO years. For the latter years the ENAC exhibits a mean salinity of 35.409 with a standard deviation of the mean of 0.004 and mean temperature of 9.59 °C with a standard deviation of the mean of 0.03 °C and the WNAC shows mean salinity of 35.21 with a standard deviation of the mean of 0.01 and temperature of 7.9 °C with a standard deviation of the mean of 0.1 °C.

4.2. Influence of the NAO phase transitions

The influence of the positive and negative NAO years on the North Atlantic was investigated in the former section. The NAC transport was found to be higher during positive NAO years and warmer and more saline water reaches further north during negative NAO years. The investigation was based on composites calculated for the five highest and five lowest NAO years. The composites were based on the years 1989, 1990, 1992, 1994 and, 1995 for the positive NAO and on the years 1963, 1964, 1969, 1977 and, 1996 for the negative NAO. The five

strongest positive NAO events are mainly in the 1990s and the negative NAO events in the 1960s, therefor the difference between the positive and the negative NAO composite might also be biased by other decadal variability. In this chapter the direct feedback of the NAO on the North Atlantic is studied by investigating composite plots before and after a transition from one NAO state into another.

4.2.1. Positive to negative NAO phase transition

The direct feedback of the NAO on the NAC and the NA is investigated by velocity, transport, temperature and salinity composites calculated for the five strongest NAO transitions from positive to negative NAO phase (Figure 4.8). The years 1961, 1967, 1976, 1995, and 2000 are considered for the positive NAO composite and the following years, respectively for the negative NAO composite. These five transitions are more evenly distributed along the model time period as the five highest and five lowest NAO events.

It was found that the NAC transport along it's pathway increases during the five highest NAO index years compared to the five lowest NAO index years. These findings are partly confirmed from the five transitions considered here. The $12\,\mathrm{cm/s}$-isoline shows a similar behavior for the five transitions than for the five highest
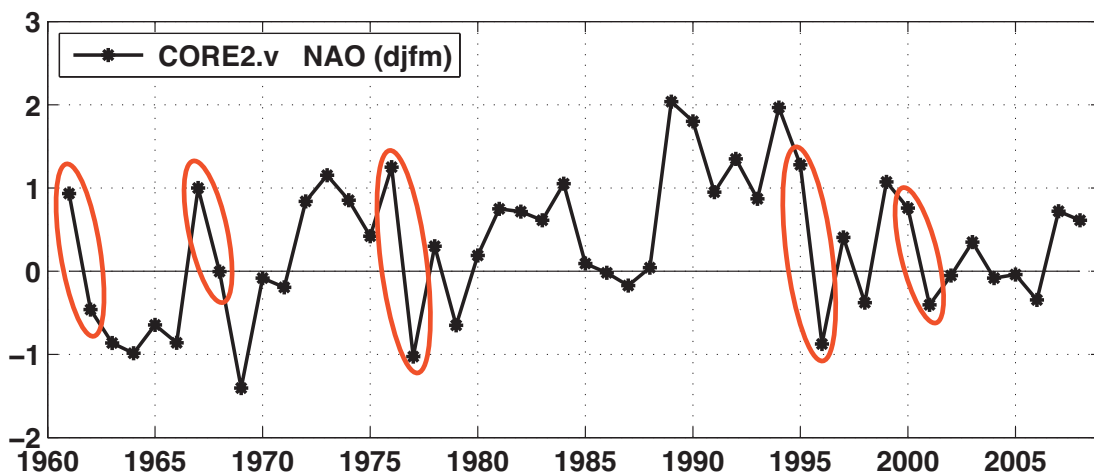
Figure 4.8.: Simulated NAO (djfm) time series with the five strongest NAO transitions from positive to negative NAO phase marked by the red circles.

and lowest NAO years (Figure 4.2 and Figure 4.9a). During positive NAO years the NWC reaches slightly further north and the velocity flows in a broader path across the MAR section. Further east a more distinct and localized pathway is found during negative NAO years.

The NAO influences the salinity and temperature of the NA and the NAC. It was found from the previous section that warmer and more saline water reaches further north during negative NAO years. This is partly seen by the here investigated transitions from positive to negative NAO index years (Figure 4.9b,c). Here in contrast to the former section the 6 °C-isotherms for the two composites do not separate so much after the NWC (Figure 4.9b). They even intersect each other, so that sometimes the negative NAO 6 °C-isotherm reaches further north and sometimes the positive NAO one. Overall the pathway of the 6 °C-isotherms follow the 6 °C-isotherm of the negative NAO state for the five lowest NAO years (Figure 4.6).

The salinity distribution over the NAO is exemplarily displayed by the 35.15-isohalines (Figure 4.9c). These isohalines are like the 6 °C-isotherms close to each
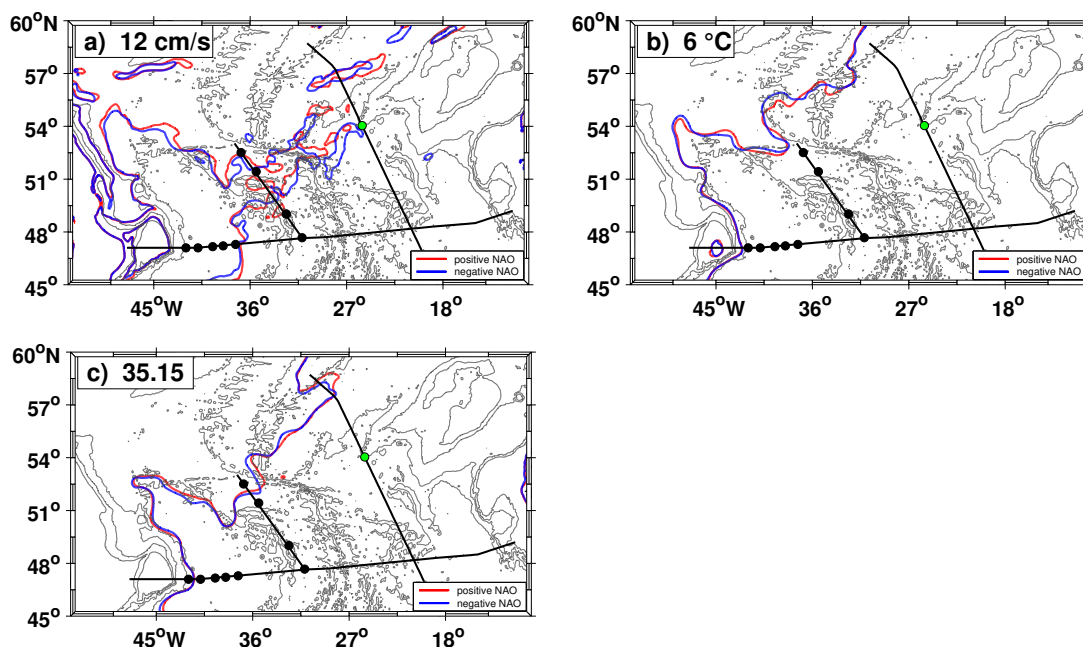
Figure 4.9.: Velocity a), temperature b), and salinity c) composites calculated for the five strongest positive (red) to negative (blue) NAO phase transitions from 1000 m depth to the surface.

other and intersect each other across the NA. In the NWC the isohaline for the negative NAO state reaches slightly further north. This is in agreement with the 35.15-isohalines calculated for the five highest and five lowest NAO years (Figure 4.7), the isohalines in this case are clearly separate from each other and do not intersect. The 35.15-isohalines calculated from the transitions follow mainly the 35.15-isohaline of the negative NAO state for the five lowest NAO years.

The top to bottom transport of the northward flowing NAC at 47°N is around 1.7 Sv lower during positive NAO years compared to negative NAO years, which is significantly different to the average 5-compound year to year difference of 0.6 Sv (based on 10^7 random realizations). Considering the subtropical transport the difference from positive to negative NAO years decreases to 0.2 Sv, which is not significantly different to the average 5-compound year to year difference of 0.2 Sv. The slight eastward shift of the maximum subtropical NAC flow during positive NAO years seen in the previous section (Figure 4.3) is smaller from the comparison of the transitions from positive to negative NAO years (Figure 4.10). The southward flowing NBR exhibit higher transport by 0.8 Sv during positive NAO years compared to negative NAO years (average 5-compound year to year difference of 0.5 Sv) over the whole water column. The difference increases taking
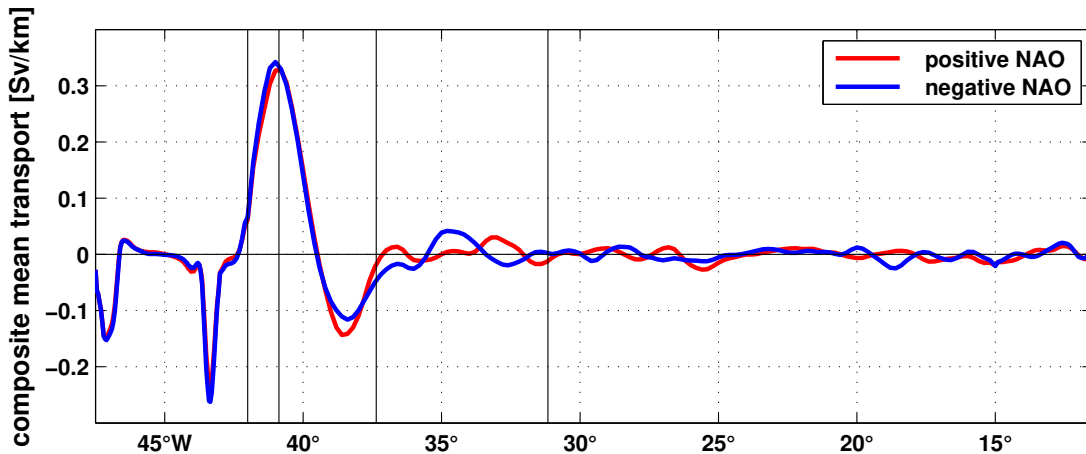
Figure 4.10.: Composites of meridional subtropical mean transports along the 47°N section calculated for positive (red) to negative (blue) NAO phase transitions. The vertical lines mark the PIES positions. The transport is given in Sv/km and the entire section is around 2710 km long.

only the subtropical transport into account to 3.3 Sv (average 5-compound year to year difference of 0.2 Sv). In the eastern part of the 47°N section the simulated southward and northward directed subtropical flow show different behavior and locations from the here investigated positive to negative NAO phase transition than for the five highest and five lowest NAO years (Figure 4.3).

The absolute transport across the MAR section referenced to 3400 m is around 1 Sv higher during positive NAO years compared to the negative NAO, which is significantly higher than the average 5-compound year to year difference of 0.1 Sv. Higher transport during positive NAO years are not seen in the subtropical part, where the difference decreases to 0.52 Sv (average 5-compound year to year difference of 0.03 Sv) and is higher during negative NAO years. In contrast to the composite for the five highest NAO years (Figure 4.4) the subtropical transport across the MAR for the positive NAO composite considered here is not only northeast directed but even southwest in the middle of the section (4.11). Furthermore, the amplitude is larger in the case of the positive to negative transition events. The amplitude for the positive NAO years is in the same range as the amplitude for the negative NAO years. The latter is nevertheless smaller than the corresponding transport amplitude across the MAR section calculated for the five weakest NAO years. But in both cases a southwestward flowing transport is found at
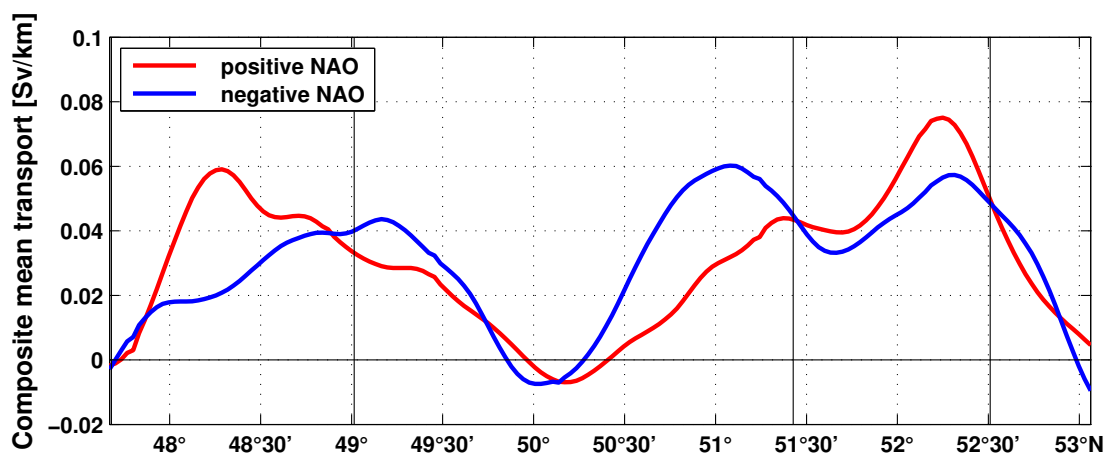
Figure 4.11.: Same as Figure 4.10 but for the mean northeastward transports along the MAR section. The vertical lines mark the PIES positions. The entire section is around 755 km long.

around 50°N. Similar amplitudes and alternating subtropical transport directions are found along the entire OVIDE section for the five highest/lowest NAO years composite (Figure 4.5) and the positive to negative NAO years transition composites (Figure 4.12). The subtropical transport across the entire OVIDE section is in contrast to the top to bottom transport (0.50 Sv lower during negative NAO years with average 5-compound year to year difference of 0.09 Sv) lower by 0.76 Sv (average 5-compound year to year difference of 0.02 Sv) during positive NAO years than during negative NAO years. The top to bottom (4.3 Sv with average 5-compound year to year difference of 0.1 Sv) and subtropical ENAC (1.93 Sv with average 5-compound year to year difference of 0.09 Sv) carry higher transport before the transition than afterwards. The WNAC, which was found to be not correlated with the NAO in the former sections, shows higher transports during negative NAO by 1.1 Sv (average 5-compound year to year difference of 0.1 Sv) over the entire water column and by 0.70 Sv (average 5-compound year to year difference of 0.06 Sv) for the subtropical water mass.

Overall the NAC across the three sections along it's pathway is warmer and more saline during negative NAO years compared to positive NAO years in the subtropical water mass above the $\sigma_\theta = 27.68 \, \text{kg/m}^3$ isopycnal. Starting at the 47°N
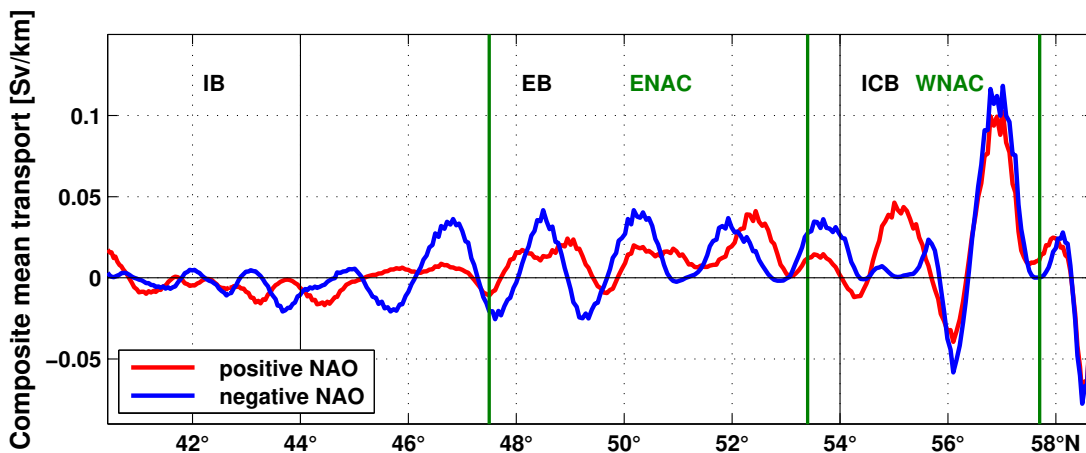
Figure 4.12.: Same as Figure 4.10 but along the OVIDE section. The black lines mark the separation into the different basins and the green lines the separation into WNAC and ENAC. The entire section is around 2477 km long.

the salinity of the subtropical NAC is around 0.013 (average 5-compound year to year difference of 0.0003) higher after the transition from positive to negative NAO years. The corresponding temperature is again not correlated with the NAO. At the MAR the subtropical water mass is warmer by 0.14 °C (average 5-compound year to year difference of 0.0001 °C) and more saline by 0.014 (average 5-compound year to year difference of 0.0004) after the phase transition. In the eastern basin of the NA across the OVIDE line the subtropical water mass of the ENAC exhibits higher salinity by 0.002 (average 5-compound year to year difference of 0.0002) and warmer temperature 0.02 °C (average 5-compound year to year difference of 0.002 °C) during negative NAO years. The further north located WNAC shows an increase in salinity of 0.002 (average 5-compound year to year difference of 0.0001) and a decrease in temperature by 0.02 °C (average 5-compound year to year difference of 0.004 °C) from positive to negative NAO years.

4.2.2. Negative to positive NAO phase transition

After investigating the influence of the NAO on the NA by using velocity, transport, temperature and salinity composites calculated for the five highest/lowest NAO index years and the five strongest transitions from positive to negative NAO phases here the composites for the strongest NAO transitions from negative to positive NAO phases are studied (Figure 4.13). The years 1966, 1977, 1996, 1998, and 2006 are considered for the negative NAO composite and the following years, respectively for the positive NAO composite. This five transitions are more evenly distributed along the model time period as the five highest and five lowest NAO events.

The horizontal velocity distribution composites investigated in the previous sections showed that the NWC reaches slightly further north and the velocity flow of the MAR section is in a broader path during positive NAO years (Figure 4.2 and Figure 4.9a). The velocity composites for the here considered NAO transition events show a similar behavior (4.14). From all three composites it is seen that the 12 cm/s-isoline behaves similar for the different composite calculations.

The salinity and temperature of the NA and the NAC was found to be influenced by the NAO, during negative NAO years warmer and more saline water
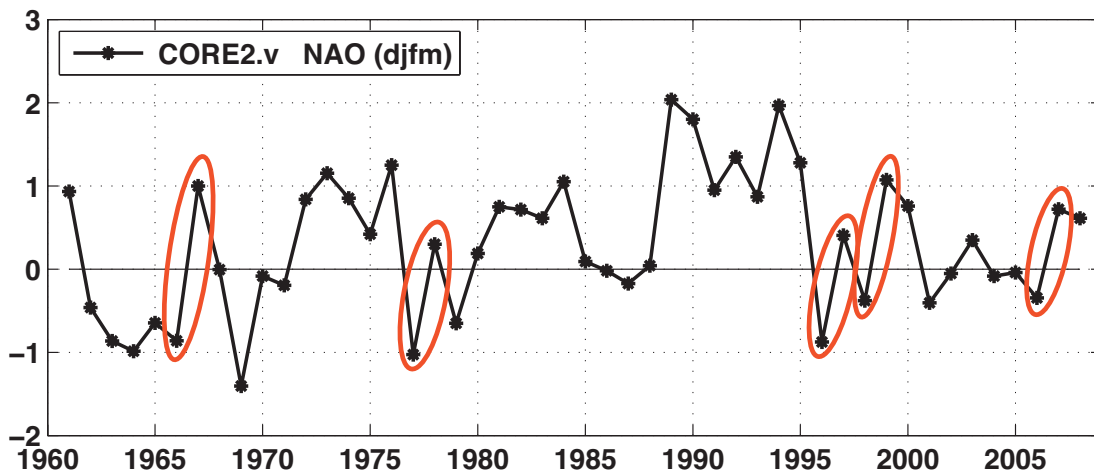
Figure 4.13.: Simulated NAO (djfm) time series with the five strongest NAO transitions from negative to positive NAO phase marked by the red circles.

reaches further north than during positive NAO years. This is partly seen by the here investigated transitions from negative to positive NAO index years (Figure 4.14b,c). In contrast to the 6 °C-isotherms calculated from the five highest and five lowest NAO events (Figure 4.6), but in agreement with the 6 °C-isotherms calculated for the transitions from positive to negative NAO years (Figure 4.9b) the here compared 6 °C-isotherms do not clearly separate from each other after the NWC. The here considered 6 °C-isotherms follow like the 6 °C-isotherms calculated for the positive to negative transition the 6 °C-isotherm of the five lowest NAO years (Figure 4.6). The salinity distribution over the NA is exemplarily displayed again by the 35.15-isohalines (Figure 4.14c). As already seen from the positive to negative NAO phase transitions the isohalines are again close to each other and intersect each other across the NA. The negative NAO isohaline reaches again slightly further north in the NWC, which is in agreement with the five highest/lowest and positive to negative NAO events (Figure 4.7 and Figure 4.9c). As in the other transition event the 35.15-isohalines considered here follow mainly the 35.15-isohaline of the five lowest NAO years.

The top to bottom transport of the northward flowing NAC at 47°N is around 7.1 Sv lower during positive NAO years compared to negative NAO years, which is significantly different to the average 5-compound year to year difference of 0.6 Sv (based on 10^7 random realizations). Considering the subtropical transport the dif-
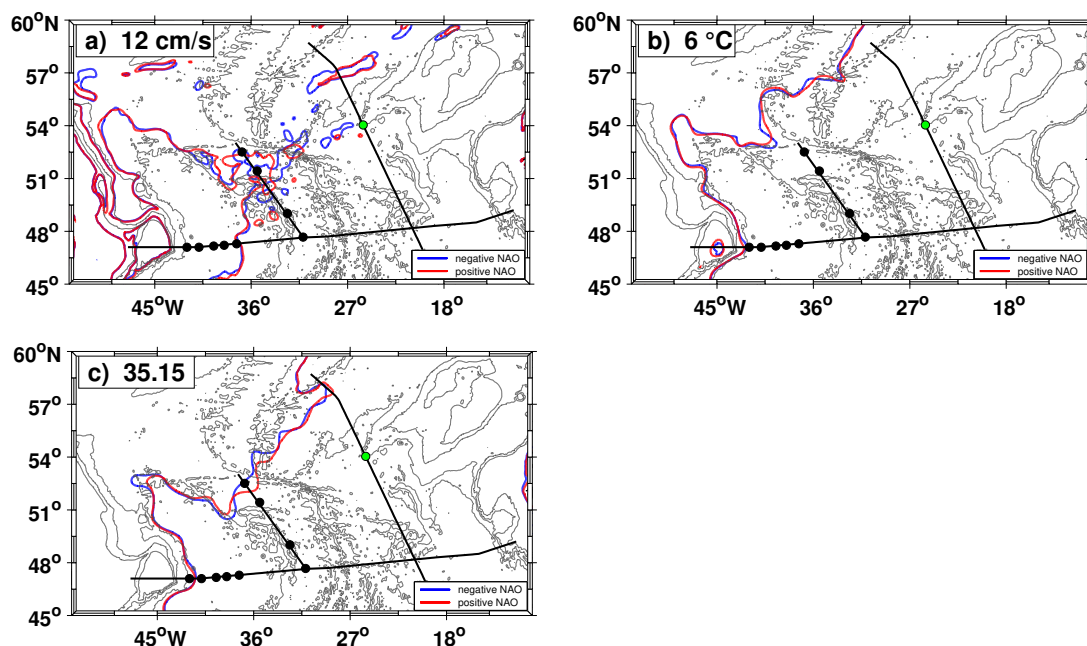
Figure 4.14.: Velocity a), temperature b), and salinity c) composites calculated for the five strongest negative (blue) to positive (red) NAO phase transitions from 1000 m depth to the surface.

ference decreases to 2.4 Sv (average 5-compound year to year difference of 0.2 Sv). These differences are larger than for the positive to negative NAO transition, where the subtropical transport did not show a significant difference. The slight eastward shift of the maximum subtropical NAC flow during positive NAO years is like for the transition from positive to negative NAO years smaller compared to the five strongest and five weakest NAO years (Figure 4.15). The southward flowing NBR exhibits higher transport by 3.6 Sv (average 5-compound year to year difference of 0.5 Sv) over the entire water column and by 1.4 Sv (average 5-compound year to year difference of 0.2 Sv) for the subtropical part during negative NAO years compared to positive NAO years. This is in contrast to the NBR for the positive to negative transitions, which exhibits higher transports during the positive NAO years. Across the MAR section the findings are in agreement with the positive to negative transition, here the transport referenced to 3400 m is around 0.7 Sv higher during positive NAO years (average 5-compound year to year difference of 0.5 Sv) and the subtropical transport is around 0.35 Sv higher during negative NAO years (average 5-compound year to year difference of 0.03 Sv). The distribu-
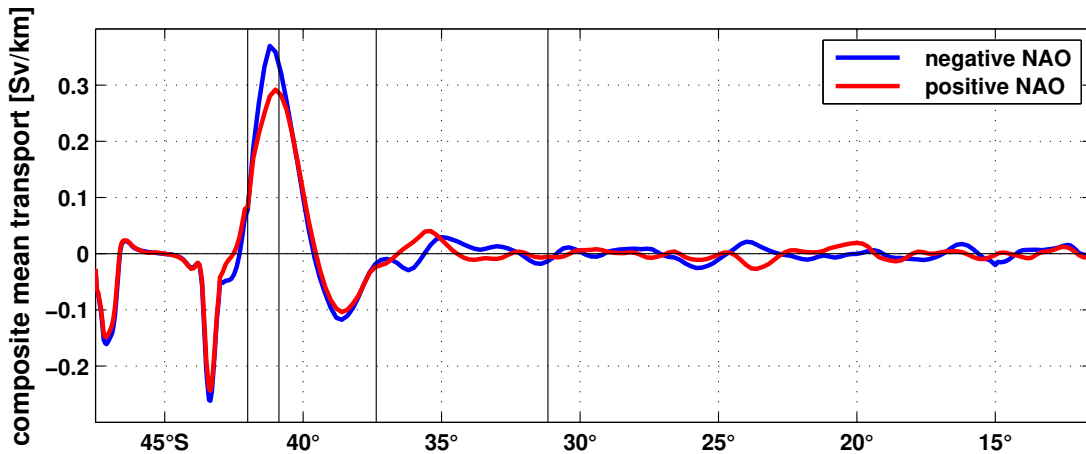
Figure 4.15.: Composites of mean meridional transports along the 47°N section calculated for negative (blue) to positive (red) NAO phase transitions. The absolute transport is detrended and calculated from 1000 m depth to the surface. The vertical lines mark the PIES positions. The transport is given in Sv/km and the entire section is around 2710 km long.

tions across the MAR section show again southwest directed subtropical transport in the middle of the section (Figure 4.16). In contrast to the composite of the five highest/lowest NAO years and for the positive to negative NAO transitions, the transport distribution for negative NAO shows in addition to the southward flow at around 50°N another southward directed area at around 51°30N. The amplitudes of the transport distributions are again similar for the positive and negative NAO phases.

Across the entire OVIDE section similar amplitudes from all three cases are found. But here the subtropical transport during negative NAO years (Figure 4.17) is found to be more northwestwards directed than for the other two NAO year composites (Figure 4.5 and Figure 4.12). The top to bottom transport difference across the entire OVIDE section is not found to be different than the 5-compound year to year difference of 0.1 Sv. The subtropical part however exhibits higher transports of 0.16 Sv (average 5-compound year to year difference of 0.02 Sv) during negative NAO years. For the negative to positive NAO transition the top to bottom (4.5 Sv with average 5-compound year to year difference of 0.1 Sv) and the subtropical (2.30 Sv with average 5-compound year to year difference of 0.08 Sv)
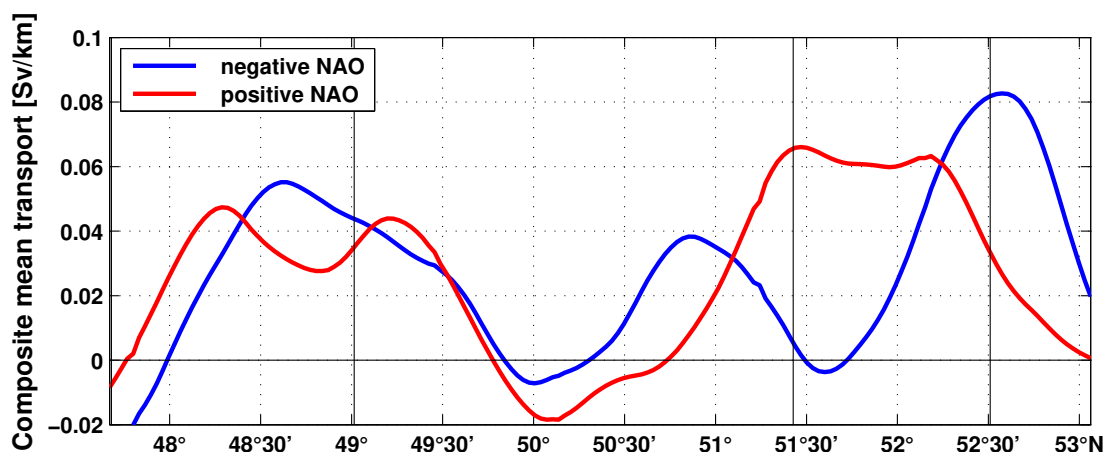
Figure 4.16.: Same as Figure 4.15 but for the mean northeastward transports along
the MAR section. The vertical lines mark the PIES positions. The
entire section is around 755 km long.

ENAC carry higher transport after the transition than before. These are in the
same order than the shift found from the positive to negative transition. The
WNAC was found not to be correlated with the NAO and in contrast to the positive
to negative transitions the influence of the negative to positive NAO transition is
not found to be different from the average 5-compound year to year difference of
0.1 Sv over the entire water column. The subtropical part however shows again
higher transport during negative NAO years by 0.29 Sv (average 5-compound year
to year difference of 0.06 Sv).

It was found from the two previous investigations that the salinity and temper-
ature of the NAC is overall influenced by the NAO and warmer and more saline
water reaches further north during negative NAO years in the subtropical water
mass above the $\sigma_\theta = 27.68\,\mathrm{kg/m^3}$ isopycnal. These findings are partly confirmed
from the here investigated transitions from negative to positive NAO years. Start-
ing at the 47°N section the salinity of the subtropical NAC is around 0.013 (average
5-compound year to year difference of 0.0003) higher before the transition from
negative to positive NAO years. As seen from the previous investigations the cor-
responding temperature is not correlated with the NAO. Against the expectation
the subtropical water mass at the MAR is colder by 0.05 °C (average 5-compound
year to year difference of 0.0001 °C), but as expected more saline by 0.006 (av-
erage 5-compound year to year difference of 0.0004) before the phase transition.
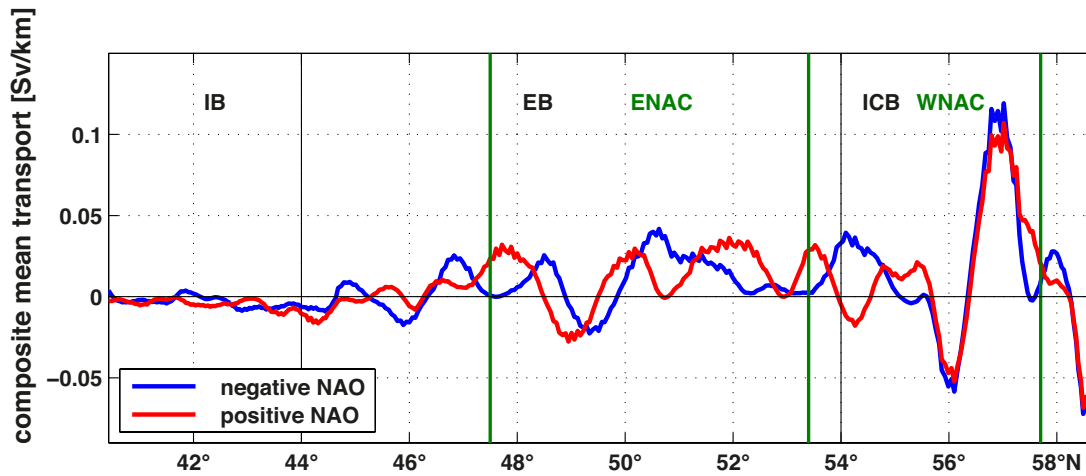
Figure 4.17.: Same as Figure 4.15 but along the OVIDE section. The black lines mark the separation into the different basins and the green lines the separation into WNAC and ENAC. The entire section is around 2466 km long.

In the eastern basin of the NA across the OVIDE line the subtropical water mass of the ENAC exhibits higher salinity by 0.003 (average 5-compound year to year difference of 0.0002) and unexpectedly cooler temperature by 0.05 °C (average 5-compound year to year difference of 0.002 °C) during negative NAO years. The further north located WNAC shows an decrease in salinity of 0.005 (average 5-compound year to year difference of 0.0001) and a decrease in temperature by 0.03 °C (average 5-compound year to year difference of 0.004 °C) from negative to positive NAO years.

5. Discussion and Conclusion

5.1. North Atlantic in model and observation

In this study the hydrography, flow field and transport time series at three sections along the pathway of the NAC and over the subpolar North Atlantic were investigated and compared using data from a high-resolution hindcast simulation and observations (PIES, CTD, lADCP and satellite altimetry measurements). The observational inflow into the NA at 47°N was studied from hydrographic snapshots taken during 14 cruises between 2003 and 2016 and a continuous transport time series calculated from a combination of PIES and satellite altimetry data from 1993 to 2008. Such a continuous transport time series and eight repeated CTD and lADCP sections between 2008 and 2016 were used to investigate the section at the western flank of the MAR. In the eastern basin of the NA at the OVIDE line, the observational investigation was based on five hydrographic snapshots taken every other year between 2002 and 2010 (*Mercier et al.*, 2015).

At the three sections along the NAC pathways the mean transports from the model and the observations agree within the standard deviations. However, the model underestimates the observed ENAC mean transport across the OVIDE line, which is based on five repeated hydrographic sections. This is not uncommon. The majority of eighteen models forced by CORE.v2 data exhibit lower transports than the in-situ measurements at the Rapid Climate Change program (RAPID) array along 26.5°N (*Danabasoglu et al.*, 2014).

In general, the modeled circulation at the MAR is shifted to the north compared to the observations by about half a degree, and in the eastern Atlantic, the more northward located WNAC carries the majority of the transport of the NAC, while in the observations, the ENAC is stronger. One reason for the northward shift

could be the more northward penetration of the NAC into the Labrador Sea, thus favoring the more northward pathways for the NAC to the eastern Atlantic. The strength of the SPG of the VIKING20 configuration (about 37 Sv) is comparable with other model configurations forced by CORE.v2 data (*Danabasoglu et al.*, 2014) and the observed southward transports at the exit of the Labrador Sea (53°N) of about 37-42 Sv (*Fischer et al.*, 2004, 2010; *Xu et al.*, 2013).

In contrast to the transport time series at the 47°N section from model and observations from 1993 to 2008, the transport time series at the MAR section are comparable and therefore discussed in detail. Despite the different geographical distribution of the flow, the annual mean modeled and observed transports at the MAR for the time period 1993-2004 are significantly correlated (correlation coefficient of 0.7). In the following years (2005-2008) the model shows weaker transports that are not correlated with the observations (Figure 3.14). During this time period the simulated SSH (Figure 5.1) calculated from the area between 15°-60°W and 48°-65°N (SPG SSH) diverges from the satellite altimetry SPG SSH (*Danabasoglu et al.*, 2016, their Figure 14), which could be one of the reasons for the discrepancies between modeled and observed transports. In models, the SPG SSH is correlated via geostrophy to the intensity of the SPG (*Böning et al.*, 2006; *Yeager and Danabasoglu*, 2014; *Danabasoglu et al.*, 2016), their correlation
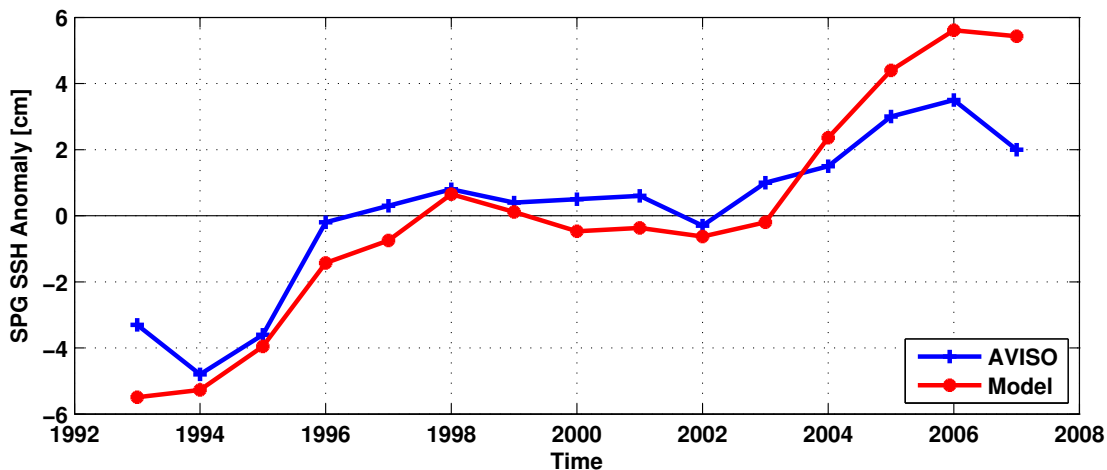
Figure 5.1.: SPG SSH anomaly calculated from the area between 15°-60°W and 48°-65°N from VIKING20 model configuration and AVISO data, taken from *Danabasoglu et al.* (2016) (their Figure 14).

coefficient in the VIKING20 model configuration is 0.8. The simulated transport across the MAR section is correlated with the wind stress curl over the SPG region and with the SPG SSH time series. *Lorbacher et al.* (2010) found from a global ocean-ice model experiment that the SSH variability pattern related to wind-driven variability of the AMOC depends critically on the time scales of interest.

Furthermore, in the years 2005-2007 the simulated transport at the MAR section is partly shifted towards the north, out of the section considered here in comparison to the observations (Figure 5.2). Taking this shift into account and calculating the maximum simulated annual transport for 2005-2007 the transport values approach the observed transports (Figure 3.14), but still show the transport minimum as expected from the simulated SPG SSH.

Although the 2006 transport is the most distinct minimum over the entire time period from 1960 to 2008, similar minima are found in the 1970s and 1980s in the model at the MAR section. The anomalously low transports ($< 20\,\text{Sv}$) affect the whole water column and last over several years, e.g. from 1984-1985 and 1987-88, and over 3 years from 2004 to 2006, making it unlikely that a meander or
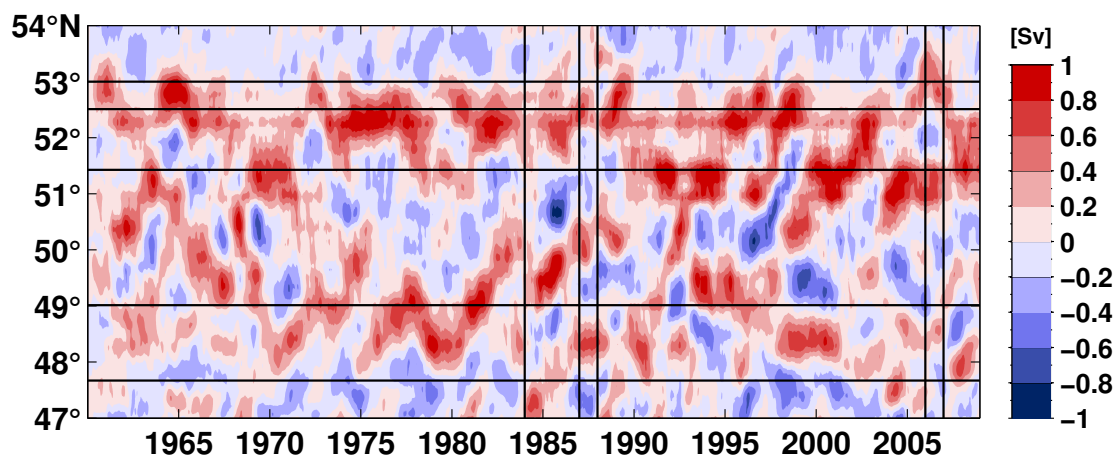
Figure 5.2.: Hovemöller diagram for absolute transport from $3400\,\text{m}$ to the surface along the MAR section. The section is extended towards the northwest and the southeast. The vertical lines mark the five weakest transport years and the horizontal lines the PIES positions and the horizontal line at 53°N marks the model extension into the north. The northeastern transport is displayed in red.

eddy is responsible (Figure 3.15). However the transport distributions within the segments show conspicuously reversed flows in some of the subsections. During the 1987 event, the central subsection and the northward extension exhibits a reversed flow, while in 2006, the flow in the northern segment is reversed. The velocity composite for the five weakest transport years (1984, 1987, 1988, 2006, 2007, Figure 5.3c) reveals that the main pathway across the MAR array is around 1° farther south than in the mean state of the circulation, it shifts from the northern segment to the central part of the section (Figure 5.3a). Overall, the minimum is found to be affecting the entire NAC and the flow across the MAR section occurs also outside the limit of the section used for the comparison with the observations. During the minimum periods the NAC exhibits weaker velocities across the entire NA compared to the velocity composite of the five strongest transport years (1962, 1974, 1977, 1992, 1995, Figure 5.3b). In the eastern Atlantic at the OVIDE line during the minimum transport years the weaker velocity of the WNAC is further influenced by a stronger recirculation than during the maximum transport years. The ENAC in the maximum state shifts slightly toward the west and crosses the OVIDE line in a broader pathway and further south than during the minimum transport years. At the 47°N section the maximum northward flow is more distinct and does not reach so far north at the NWC during minimum MAR transport years compared to the maximum and mean states.

During the extreme transport minima (1987, 2006) at the MAR section the NAO index is in a neutral state after several years of medium positive NAO (Figure 4.1). *Lohmann et al.* (2009) found from a model study forced by a persistent positive NAO phase that the subpolar gyre and thus the NAC transport weakens due to advection of warm water from the subtropical gyre.

One has to bear in mind that the observations do not show the transport minimum found in the model between 2004 and 2007, and so it is not surprising that the modeled trend of -8.6 Sv (1993-2008) of the NAC at the MAR section is not seen in the observations. The NAC trend over the entire model period from 1960 to 2008 is not significant (-0.3 Sv, Table 3.4). Neither the simulated nor the observed northward inflow into the NA at 47°N section show the strong minimum observed in the simulated MAR section transport, however both time series show a decrease from 1993 to 2008 (Table 3.2). Across the entire 47°N section the simulated transport increases slightly by 0.26 Sv from 1960 to 2008.
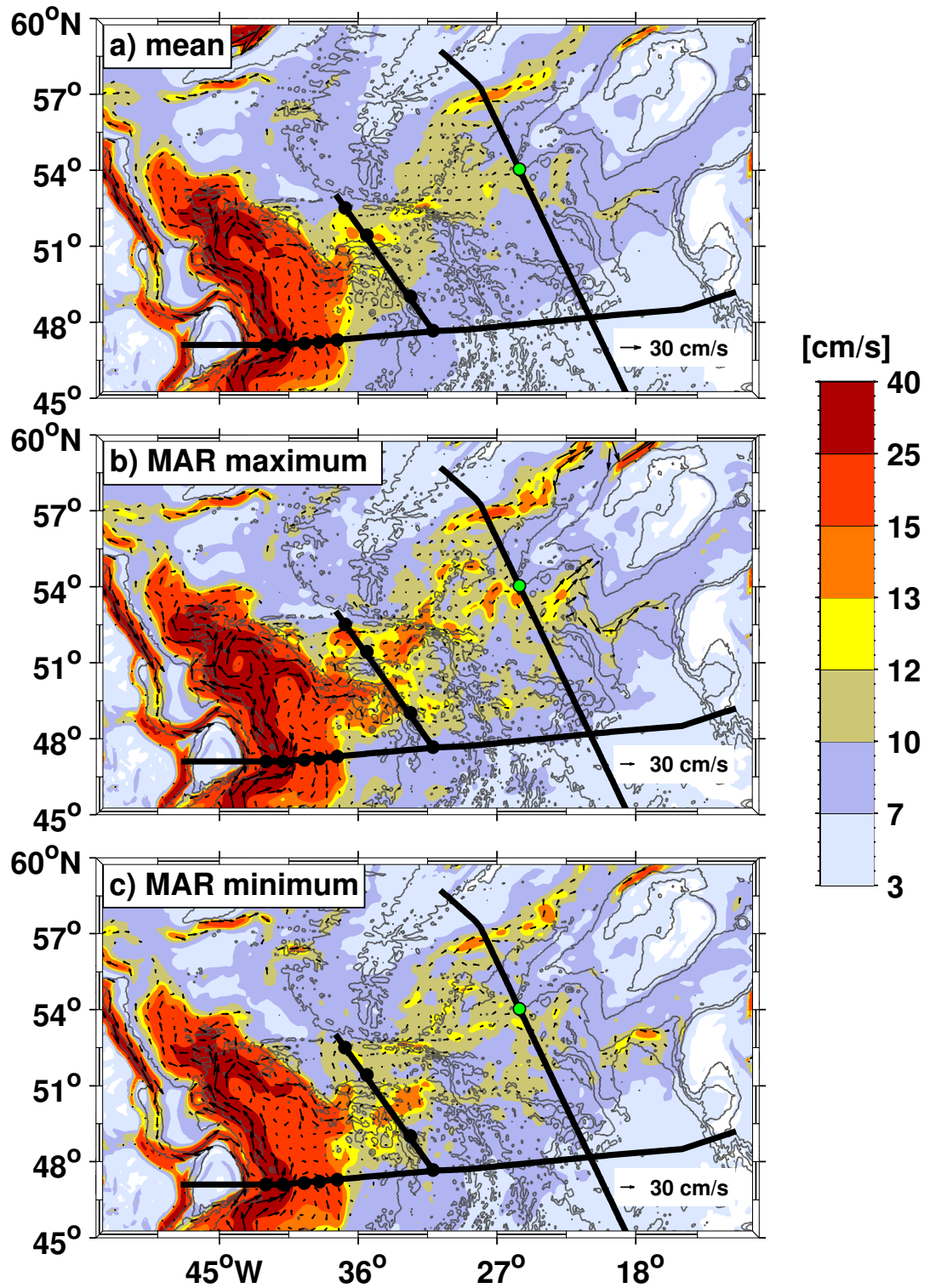
Figure 5.3.: Velocity composites for the mean, the five strongest and five weakest MAR transport years from 1000 m to the surface.

This is in contrast to the eddy-resolving simulation over 34 years slightly further north nominally along 48°N and between 10°W and 50°W across the World Ocean Circulation Experiment (WOCE) hydrographic section AR19, which does not show a systematic trend (*Xu et al.*, 2013). Further downstream of the NAC in the eastern basin, the modeled overall transports at the OVIDE line do not show the distinct minima found at the MAR, neither do the individual WNAC or ENAC branch transports (Figure 3.19). However, during 1960-2008, the modeled WNAC transport strengthened with a positive trend comparable to the increase of 5.6 Sv in the northern segment of the MAR section. Comparable significant positive trends of the AMOC at 26.5°N (1978-1998) and 45°N (1975-1995) are found from the multi model mean over twenty ocean-sea-ice coupled models forced by CORE.v2 (*Danabasoglu et al.*, 2016), the same atmospheric forcing dataset used in the VIKING20 model configuration. *Danabasoglu et al.* (2016) described negative significant trends at both locations from 1996 until 2007 and the rates are nearly double that of the strengthening period. The stronger flow is found to be associated with negative temperature anomalies in the Labrador Sea region, which leads to increased deep water formation, driven by NAO-related surface fluxes (*Yeager and Danabasoglu*, 2014; *Danabasoglu et al.*, 2016).

The simulated mean temperature at the three sections along the NAC pathway are partly comparable to the observations within the standard deviations from 1993 to 2008. At the three sections a warming trend is exhibited over the entire model time period. In the subtropical water mass the warming across the entire 47°N and OVIDE sections lie below the global upper ocean warming (surface to 75 m) from 1971 to 2010 by 0.11 °C per decade (*Rhein et al.*, 2013). It is reported that the anthropogenic influence on for example greenhouse gas concentrations leads to around half of the observed increase in global mean surface temperature (*IPCC*, 2013). The warming at the MAR exceeds the global one. However, individual parts of the sections show different trends. At all three sections the sharp warming since the mid-1990s described by e.g. *Desbruyères et al.* (2015) are found in the simulation. They furthermore described from their model study a cooling ocean in the 1960s and 1970s, which was followed by relatively minor changes. Such a behavior can be also seen from the northward flowing NAC subsection at the 47°N and the ENAC at the OVIDE section. The temperature at the MAR section and the WNAC exhibit different behaviors, a warmer ocean in the 1960s and 1970s is

followed by a colder ocean until the increase in the 1990s.

The simulation show in general higher mean salinity values than the observations and at the three sections a salinity increase over the entire model time period is simulated. The realism of the salinity trend in the VIKING20 model configuration has to be questioned since the simulation suffers from a spurious drift in the freshwater content of the subpolar North Atlantic of unknown origin [1]. However, the increase in the subtropical water over the entire 47°N section is one magnitude smaller than the strongest increase found in the upper 700 m in the area of the Gulf Stream (*Wang et al.*, 2010). Their trend of 0.06 per decade is calculated from the World Ocean Database, pentadal data for the periods 1955-1959 to 2002-2006 over a 1°x1° latitude-longitude grid (*Wang et al.*, 2010). Further north over the subpolar NA they found from the same data set a decrease in salinity of up to -0.02 per decade. The salinity trends might be caused by processes such as evaporation, ocean circulation, ice melting and precipitation (*Wang et al.*, 2010). In contrast to the decrease in the World Ocean Database data, the salinity over the entire MAR and OVIDE sections in the VIKING20 model increases comparable with the increase across the entire 47°N section over the entire model time period. *Boyer et al.* (2007) reported a salinity increase over the entire NA from the World Ocean Database data, but in agreement with *Wang et al.* (2010) a salinity decrease over the subpolar NA.

5.2. Comparison with other transport estimates

There are several programs aiming to measure and understand the NAC, starting with the Florida Current at the RAPID line at 26.5°N, where the mean top to bottom northward transport from up to 300 shipboard sections and 25 years of daily cable observations is around 32 Sv (e.g. *Larsen and Sanford*, 1985; *Cunningham et al.*, 2007; *Meinen et al.*, 2010; *Johns et al.*, 2011; *Meinen and Luther*, 2016). Recently, *Meinen and Luther* (2016) discussed in detail the evolution of the Gulf Stream transport from the Florida Strait to 42°N, describing the Gulf Stream at different locations as a stream within a channel, a freely meandering jet, and a bounded boundary current, so that here only a short summary of observed

---

[1] C. Böning, pers. com. 2017

transport calculations is given. The transport increases to about 65-94 Sv near Cape Hatteras at 73°W (e.g. *Richardson and Knauss*, 1971; *Halkin and Rossby*, 1985; *Leaman et al.*, 1989) and at 70°W to about 95 Sv (*Rossby et al.*, 2014). At 60°W, the Gulf Stream is about 5 times higher (150 Sv) than the Florida Current (*Hogg*, 1992). Further downstream at 50°W, around 80 Sv have been observed (*Clarke et al.*, 1980; *Schmitz and McCartney*, 1993), and most of the Gulf Stream turns northward and forms the NAC (*Clarke et al.*, 1980; *Rossby*, 1996). At 42°N, the northward transport including the inshore edge of the Mann Eddy is 146 Sv (*Meinen and Watts*, 2000; *Meinen*, 2001).

Across 47°N, *Mertens et al.* (2014) report from direct measurements that a transport of around 110 Sv flow northwards, with about 45 Sv of subtropical origin (above the $\sigma_\theta = 27.68 \, \mathrm{kg/m^3}$ isopycnal). Around 35 Sv of the subtropical water recirculates toward the south in the Newfoundland Basin (*Mertens et al.*, 2014). Their transport estimates are within the standard deviations of the here investigated observed and simulated mean transports from 1993 to 2008, even though the here used flow limits were different. Further downstream across the section at the MAR a mean transport of 18.2 Sv with a standard deviation of 4.7 Sv of subtropical water is found in the VIKING20 model configuration, compatible with the observed transport of about 16 Sv (*Roessler et al.*, 2015). The transport time series at the MAR section is correlated with the transport of the NAC branches WNAC and ENAC across the OVIDE line in the eastern basin. Here the mean transport of subtropical water in the model across both NAC branches of 18.7 Sv with a standard deviation of 4.6 Sv is similar to the mean transport crossing the MAR. *Daniault et al.* (2016a) compared the baroclinic mean transport (referenced to 3400 dbar) of 27 Sv along the MAR section taken from *Roessler et al.* (2015) to their OVIDE section transport calculations taken every other year between 2002 and 2012. They found - by referencing their transport to 3400 dbar and using limits defined by isolines of the surface absolute dynamic topography to match the position of the MAR section - a similar transport of 24 Sv. They concluded that the mean transport values calculated across the MAR and the OVIDE sections are highly influenced by the choice of the geographical limits of the sections. Furthermore, they argue that the MAR section does not include the southern NAC branch, which they found at the OVIDE section and the MAR section therefore misses parts of the 41.8 Sv NAC mean transport found at the OVIDE section. One

has to bear in mind, that the OVIDE section is basin wide and therefore encompasses the subtropical and subpolar gyres, whereas the deployment positions of the MAR section were chosen to measure only the transport of the subpolar gyre from the western into the eastern basin, based on the flow field inferred from drifters (*Rhein et al.*, 2011).

The simulated mean transport from the VIKING20 model configuration at the MAR section is within the standard deviation of the observed one. The observed section was extended towards the north in order to capture the entire northeastward flow at the MAR section in the model. An extension towards the south did not increase the simulated transport. The here considered comparison between the observations and the VIKING20 model configuration suggests that the simulation is reasonable and therefore the MAR section seems to capture the subpolar gyre flow into the eastern basin.

Further downstream across 59.5°N east of the crest of the Reykjanes Ridge *Sarafanov et al.* (2012) report from combined measurements between 2002 and 2008 a mean subtropical NAC transport of 15.5 ± 0.8 Sv. They separated the NAC subtropical water mass from the deep ocean with the $\sigma_\theta = 27.55$ kg/m^3, which lies above the $\sigma_\theta = 27.68$ kg/m^3 isopycnal that we used in our study at the MAR and the OVIDE line. Using the $\sigma_\theta = 27.55$ kg/m^3 isopycnal the modeled transport across the MAR section reduces to 16.3 Sv with a standard deviation of 4.1 Sv and across both branches of the NAC at the OVIDE line to 16.2 Sv with a standard deviation of 2.9 Sv. The similarity of the mean NAC transports at the MAR and in the eastern Atlantic at the OVIDE line suggest that the subtropical water that crosses 59.5°N entered the eastern basin of the NA via the MAR between 47°N and 53°N. This would mean that in the mean state, all or most of the subtropical water heading toward the Labrador Sea and the Nordic Seas crosses the MAR between 47°N and 53°N and that there is only a weak direct net transport from the subtropical gyre to SPG in the eastern NA. This could be different in a negative NAO state in which the gyres weaken, the polar front moves westward and open an enhanced northward access of the subtropical waters in the eastern boundary current (e.g *Bersch et al.*, 2007). Over the model time period from 1960 to 2008, the NAO is around two thirds of the time in a positive state and therefore the mean state is biased by the positive NAO pattern. To study the exchange of water between the two different gyres in the eastern NA is beyond the scope of this study

and is planned in further modeling and observational studies. For this purpose, moored instruments (current meters, PIES) were successfully deployed along the 47°N latitude in the eastern boundary current and in the eastern basin of the NA in May 2016. From the 16 Sv subtropical NAC, water flowing across the MAR into the eastern NA around 9 Sv cross the Greenland-Scotland Ridge further into the Nordic Seas[2], leaving about half of the inflow to remain in the SPG.

5.3. Influence of the North Atlantic Oscillation

The influence of the NAO on the NA and the NAC was investigated by using five year composites for different years. The composites were calculated for the five strongest positive and five strongest negative NAO years, and for the five strongest positive to negative or negative to positive NAO index year transitions, respectively. The transports across the three sections were found to be significantly correlated with the NAO index, lagging the NAO index within the range of 0 to 26 months. Across the 47°N section the northward flowing NAC transport from 1960 to 2008 exhibits a maximum correlation coefficient when the NAO leads the transport by 10 months (correlation range 3 to 26 months). The absolute and baroclinic transport time series at the MAR section from 1960 to 2008 are significantly correlated with the NAO index, with a correlation range from 3 to 16 months and the maximum correlation when the NAO leads the transports by 7 or 8 months. In the eastern basin the simulated warm subtropical water mass of the ENAC is significantly correlated with the NAO, with a maximum correlation coefficient when the NAO leads the transport by one month and exhibits a correlation range from 0 to 5 months. The short delay time is in correspondence with the findings of *Curry and McCartney* (2001), where the NAO index and the ocean gyre index, defined as the baroclinic pressure difference between the subtropical and subpolar gyre centers show similar temporal fluctuation structures. *Eden and Willebrand* (2001) also reported a fast, intraseasonal response to the NAO, which they found in their model study to be barotropic. A baroclinic oceanic response due to wind stress is described after 6-8 years (*Eden and Willebrand*, 2001).

During positive NAO years the NAC exhibits higher transports at the three

---

[2]B. Hansen, personal communication, 2016

sections investigated here and stronger velocities over the entire subpolar gyre. This intensification under positive NAO conditions is in agreement with other observations and model results (e.g. *Curry and McCartney*, 2001; *Häkkinen and Rhines*, 2004; *Bersch et al.*, 2007; *Häkkinen and Rhines*, 2009; *Lohmann et al.*, 2009; *Roessler et al.*, 2015), but the difference between the two composites for the five strongest and five weakest NAO years of 6.5 Sv for the absolute and 5.1 Sv for the baroclinic transport component in the model is about double the effect seen in the observations across the PIES array at the MAR (2.9 Sv) (*Roessler et al.*, 2015). This is probably owed to the different time periods chosen for the composites in model and observation.

Figure 5.4 illustrates the different flow fields in the eastern Atlantic for the five strongest and five weakest NAO years, integrated over the upper 1000 m. The more vigorous flow in the positive NAO state is clearly visible. In both cases the main pathway across the MAR is via the CGFZ. This is in agreement with observations, which found the northern branch of the NAC passing through this fracture zone (*Rossby*, 1996; *Bower et al.*, 2002; *Miller et al.*, 2013), although for the period 1993-2013, *Roessler et al.* (2015) reported the dominance of the flow
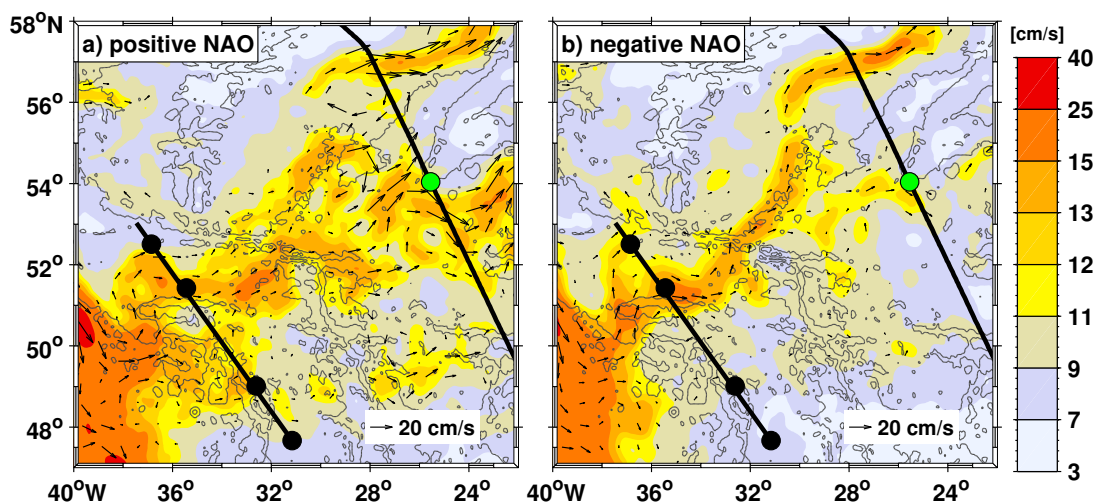
Figure 5.4.: Speed calculated as in Figure 4.2 but zoomed into the vicinity of the MAR section. The black dots indicate the PIES position and the green dot shows the separation of the OVIDE line into Iceland and European basins after *Mercier et al.* (2015).

through the FFZ. *Bower and von Appen* (2008) and *Walter and Mertens* (2013) describe single and double branch modes crossing the MAR via the CGFZ, FFZ and MFZ. East of the MAR the NAC splits into two pathways, the WNAC and the ENAC. During negative NAO phases these pathways are more focused and localized, and the ENAC mean transport is significantly lower by 4.7 Sv than during positive NAO events. This transport change is almost as high as at the MAR, meaning that the main NAO signal is focused on the ENAC. The WNAC transport is not significantly influenced by the NAO and therefore does not change with the NAO phases. Its pathway seems to be locked to the topography. The zonal location of the WNAC and ENAC across the OVIDE line does not change for the different NAO phases. This finding is unexpected and in contrast to other model and observational studies, reporting a zonal shift of the SPG during positive NAO years compared to negative NAO years (e.g. *Curry and McCartney*, 2001; *Chaudhuri et al.*, 2011; *Stendardo et al.*, 2015). However, the weakening of the ENAC transport during negative NAO years could be interpreted as the contraction of the SPG described by e.g. *Bersch* (2002).

The intensification of the flow under positive NAO conditions is also seen in the western subpolar NA, where the NWC shifts farther north and is stronger, and the recirculation in the Newfoundland basin shows higher velocities as well. The shift of the NWC is not strong, which is in agreement with the findings of *Stendardo et al.* (2016), who found from observed salinity gradient composites that the position of the NAC off the Grand Banks is slightly shifted westward during positive NAO years. They argue that the impact of the NAO on the ocean is stronger during persistent positive or negative NAO years as shown by *Lohmann et al.* (2009). During the predominantly negative NAO low period in the 1960s the NWC shifted northwestward in the Labrador Basin and an increased Newfoundland basin recirculation was observed by comparing hydrographic data from 1966 with climatology (*Bersch*, 2002).

The NAO not only influenced the transport and velocity distribution but the temperature and salinity of the NA as well (e.g *Eden and Willebrand*, 2001; *Bersch et al.*, 2007; *Frankignoul et al.*, 2009; *Herbaut and Houssais*, 2009; *Reverdin*, 2010). In agreement with the finding of *Flatau et al.* (2003) warmer water reaches further north during negative NAO phases in the VIKING20 model configuration. *Flatau et al.* (2003) investigated sea surface temperature data from the Advanced Very

High Resolution Radiometer (AVHRR) for the positive NAO winter 1994/95 and the negative NAO winter 1995/96 and showed this shift exemplarily for the 7 °C and 8 °C-isotherms. The change of the isotherms position was associated with the eastward displacement of the NAC during positive NAO phase described by *Bersch et al.* (1999). Furthermore, *Flatau et al.* (2003) found an overall increase in heat loss during positive NAO years and associated this with higher winds.

In addition to the warmer waters reaching farther north the isohalines during negative NAO years reach further north, bringing more saline water to the north, than during positive NAO years in the VIKING20 model configuration. This reduced northward salt transport during positive NAO phases is in agreement with the Ocean General Circulation Model (OGCM) hindcast study of *Frankignoul et al.* (2009), where increased precipitation was found during positive NAO years. *Eden and Willebrand* (2001) described from their model study during negative NAO years a warming and saltening at around 55°N and 30°W, which they associated with the Sverdrup response to the wind stress change. Observations show along 53°N an enhancement of the eastward transport of cold and less saline subarctic water from the Labrador Sea (*Bersch et al.*, 2007). At the NAC pathway between 33°W and 30°W the salinity at 300 dbar exhibits a broader latitudinal corridor and is shifted southward by about 1° during positive NAO phases in comparison to negative NAO years (*Stendardo et al.*, 2016).

Warm and saline water flowing into the NA during positive NAO years is confined and carried along by the strong northward flowing NAC. During negative NAO years the transport of the NAC weakens, leaving the warm and saline water reaching further north. Furthermore, the contraction of the SPG during negative NAO years leads to a preferred pathway of the NAC into the Iceland basin and not into the Rockall Trough (*Bersch*, 2002). This opens the way for the MOW towards the north into the Rockall Trough (*Lozier and Stewart*, 2008). The influence of the NAO on the NAC and NA are partly seen from all three different composite calculations, but are most apparent for the five highest and five lowest NAO year composite. For these years the NAO index is clearly separated from each other. Considering the transitions from one state of the NAO into the other the difference in the index value diminish and therefore the influence of the NAO might not be as clear as for the five highest and five lowest index years. However, from the transition analysis similar behavior and patterns are found and therefore

it can be concluded that the NAO influences the NAC such, that higher transport and velocity are observed during positive NAO years and warmer and more saline water reaches farther north during negative NAO years.

6. Summary and Outlook

Circulation, temperature and salinity distributions in the NA from $1/20\,^\circ$ hindcast model VIKING20 and observations were analyzed and compared. The comparison was done over the entire NA by using satellite altimetry and salinity fields from the World Ocean Atlas. Along the NAC pathway the comparison focused on three sections, the 47°N section monitoring the inflow into the NA, the MAR section at the western flank of the MAR capturing the flow from the western into the eastern basin, and across the OVIDE section in the eastern basin of the NA. Along these sections the hydrography, flow field and transport time series were analyzed and compared in more detail. The observations were obtained by lADCP, CTD, and PIES measurements along the sections. At the 47°N and MAR sections the PIES measurements provide, in combination with satellite altimetry data, a continuous transport time series from 1993 to 2008. The transport calculation at the OVIDE section was performed using data from five repeated cruises.

The mean transport values across the three sections are comparable in model and observations within the standard deviations. In general, the circulation at the MAR is shifted to the north in the model compared to the observations by about half a degree, and in the eastern Atlantic, the more northward located WNAC carries the majority of the transport of the NAC, while in the observations, the ENAC is stronger. Here, the observations are based on five repeated sections taken every other year between 2002 and 2010 (*Mercier et al.*, 2015). Neither the observed nor the simulated transport time series across the MAR array show an overall trend. However, due to a minimum in the simulated transport not present in the observed data between 2004 and 2007 the simulated transport decreases during the overlapping time period (1993-2008). This minimum is found to be a NA-wide phenomenon in the model, which leads to weaker velocities and different pathways of the NAC. This simulated minimum could be caused by different behavior of the

simulated and observed SPG SSH during those years.

The comparison between the model and observations showed, that the model simulates the observed transport (from lADCP and PIES measurements) crossing the 47°N, the MAR and the OVIDE sections within the standard deviations. Furthermore, the strength of the velocity field and the NAC are well simulated. However, the simulation puts the path of the NAC further north, including the NWC and has a preference for the CGFZ and the WNAC in the eastern NA and shows partly higher temperatures and salinities.

Due to the agreement between the observed and simulated transports of the NAC and the correspondence in the flow fields, the model is used to study the atmospheric influence of the NAO on the NA and the NAC. To do so, five year composites, calculated for the five strongest and five weakest NAO years and from the five strongest positive to negative or negative to positive NAO index years for transport, velocity, temperature, and salinity are used. The NA wide composites reveal stronger velocities, different pathways across the MAR area and a northward shift of the NWC during positive NAO years in comparison to negative NAO years. Warm and saline water flowing into the NA during positive NAO years are confined and carried along by the strong northward flowing NAC. The weaker velocities during negative NAO years lead to spread of warmer and more saline water, which therefore reaches farther north. Furthermore, the contraction of the SPG during negative NAO years leads to a preferred pathway of the NAC into the Iceland basin. These findings are in agreement with the simulated three sections along the NAC pathway exhibiting higher transports and colder and less saline waters crossing the sections during positive NAO years.

The focus of this study was the comparison of observational data with a high-resolution ocean model configuration and due to the confidence gain out of the comparison the analysis of the influence of the NAO on the NA and NAC. So far only mean pathways for the upper 1000 m and properties at three sections along the NAC pathway were investigated. A next step could be a closer look into the pathways between the sections to investigate the direction, depth, temperature, and salinity of and along different pathways. One could start at the MAR section to investigate where certain water masses which cross the section end up or were formed (Figure 6.1). The property changes along the pathways could give further
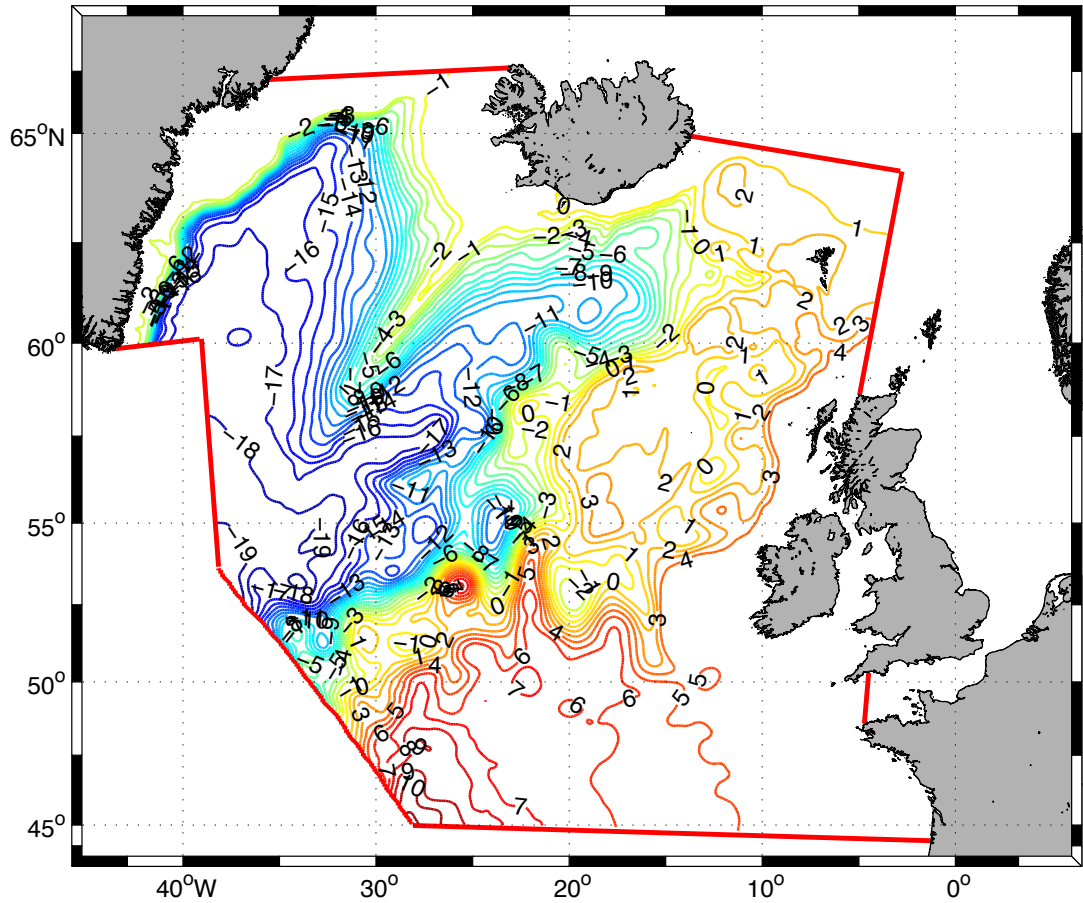
Figure 6.1.: Transport stream function calculated with the ARIANE tool in a 12°-resolution NA model configuration from 2002 to 2013 (the model was used and described for example by *Müller et al.* (2017)). 7001719 particles with a maximum transport per particle of 0.01 Sv were released along the MAR section over the entire water column for the first three years. This figure was produced in cooperation with Paul G. Myers at the University of Alberta.

insight into cooling, saltening and/or mixing processes. The investigation could be done by releasing particles over the entire water column or for a certain density or temperature range along the section and using the offline Lagrangian analysis tool ARIANE (*Blanke and Raynaud*, 1997; *Blanke et al.*, 1999). The tool calculates trajectories of numerical particles over time from simulated three-dimensional

velocity fields and can be used forward or backward in time. The Lagrangian analysis tool was for example used to distinguish between the subtropical and subpolar water flowing across the OVIDE section (*Desbruyères et al.*, 2015).

The comparison between the observations and the VIKING20 model configuration output revealed that the model simulates the observations in many aspects very well. However, due to higher salinities and therefore e.g. denser water in the deep ocean some features such as the ISOW are not correctly simulated. For future model projects it would be therefore important to be able to solve the salinity problem. Furthermore, the displacement of the NAC is an ongoing challenge for ocean and climate modeling. The horizontal resolution seems to be the dominant factor to influence the position of the NAC, hinting to the importance of the mesoscale current-topography interaction along the continental slope (e.g. *Böning et al.*, 2016). It is conceivable that the dynamics near the boundary are also affected by the parameterization of subgrid-scale mixing. To study these possible dependencies systematic model sensitivity experiments at high resolutions would be needed.

The overlap between the measurements used here and the VIKING20 model configuration is limited due to the availability of the here used atmospheric forcing (the CORE.v2 data set comprises the years 1948-2009) and observational data. Further long-term continuous measurements and simulations (updated to 2016) are needed to study longer-term fluctuations, to improve models by comparing them to observations. So far continuous measurements of the NAC transports away from the western boundary such as at the MAR section (*Roessler et al.*, 2015) are rare. The study of the exchange between the subpolar and the subtropical gyre in the eastern Atlantic is the aim of the moored boundary current meter array and several moored PIES deployed at the former WOCE line A2 at nominally 48°N in 2016, which is part of the German RACE (Regional Atlantic Circulation and Global Change) program (*www.marum.de/RACE.html*). The OSNAP (Overturning in the Subpolar North Atlantic Program) program, that started in 2014 and includes a number of existing and planned long-term observational efforts (*OSNAP*, 2016), will also produce important observations to better understand the large variability in transports, circulation and hydrography in the subpolar North Atlantic. There is also potential in combining satellite altimetry and Argo data to extend the well sampled Argo period starting in 2005 back to 1993 as was for instance done

by *Stendardo et al.* (2016) who constructed 20 years of high resolution salinity distributions in the upper 700 m. These efforts will provide longer overlapping periods of observations and simulations to further investigate the NA circulation and to understand e.g. the mechanisms behind the here analyzed feedback of the NA circulation to the NAO forcing.

A. Appendix

A.1. Observed individual hydrographic and velocity sections

The hydrographic and velocity distributions along the three sections, which were used to calculate the mean profiles in section 3.2 are shown here. Only profiles were taken into account, where CTD and lADCP data were available. The small tick marks above the figures mark the position where a profile was taken.

Individual hydrographic and velocity sections along 47°N

14 cruises along the 47°N section were used to calculate the mean profile of the section. The individual sections had different cruise tracks and started and ended at different locations. Overall, the warmest water is found in the upper ocean. The warm water above 9 Grad reaches till around 700 m depth. Above the Flemish Pass and Flemish Cap the coldest water is observed. This water is less saline than the warm surface water further east. The ISOW water mass between $\sigma_\theta = 27.80 \, \text{kg/m}^3$ and $\sigma_\theta = 27.88 \, \text{kg/m}^3$ is clearly visible in the M59/2, Subpolar, M82/2, M85/1, MSM28, and MSM53 profiles in the eastern basin between 2000 and 3000 m. The pathway of the NAC at around 40°N, the WBC, and NBR can be seen in each section which crossed these currents. Above the slope of the continental shelf, in the regime of the WBC a branch of the NAC flowing northward is observed in the individual profiles with varying strength. East of the NBR the northward flow is found to be exceptional strong during M59/2, MSM21/2, MSM53. The flow field in the eastern basin shows alternating north-south directed velocities with similar strength and surface intensified structures.
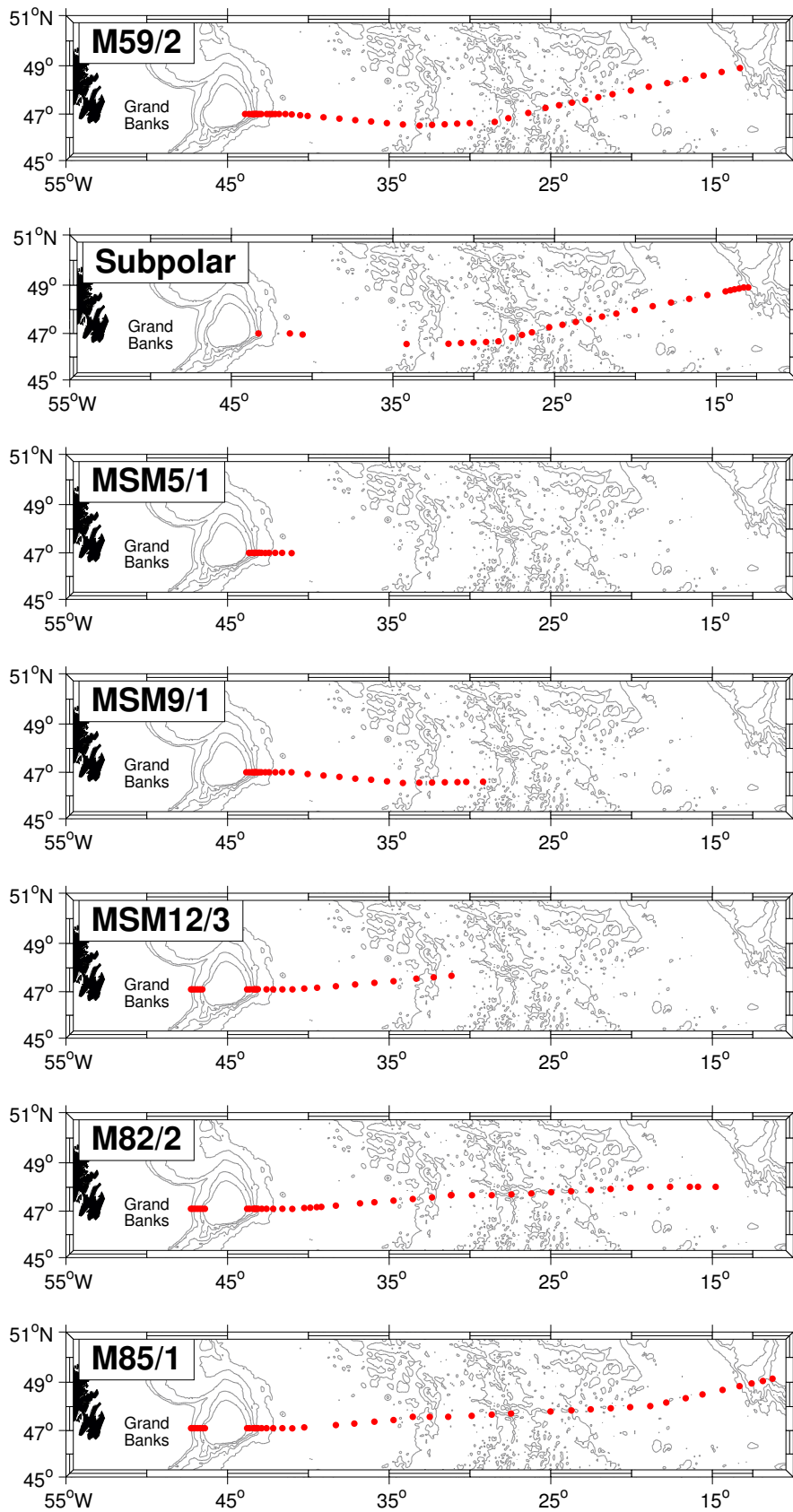
Figure A.1.: Station positions for individual cruises along the 47°N section for the years 2003-2011 (Table 2.2)
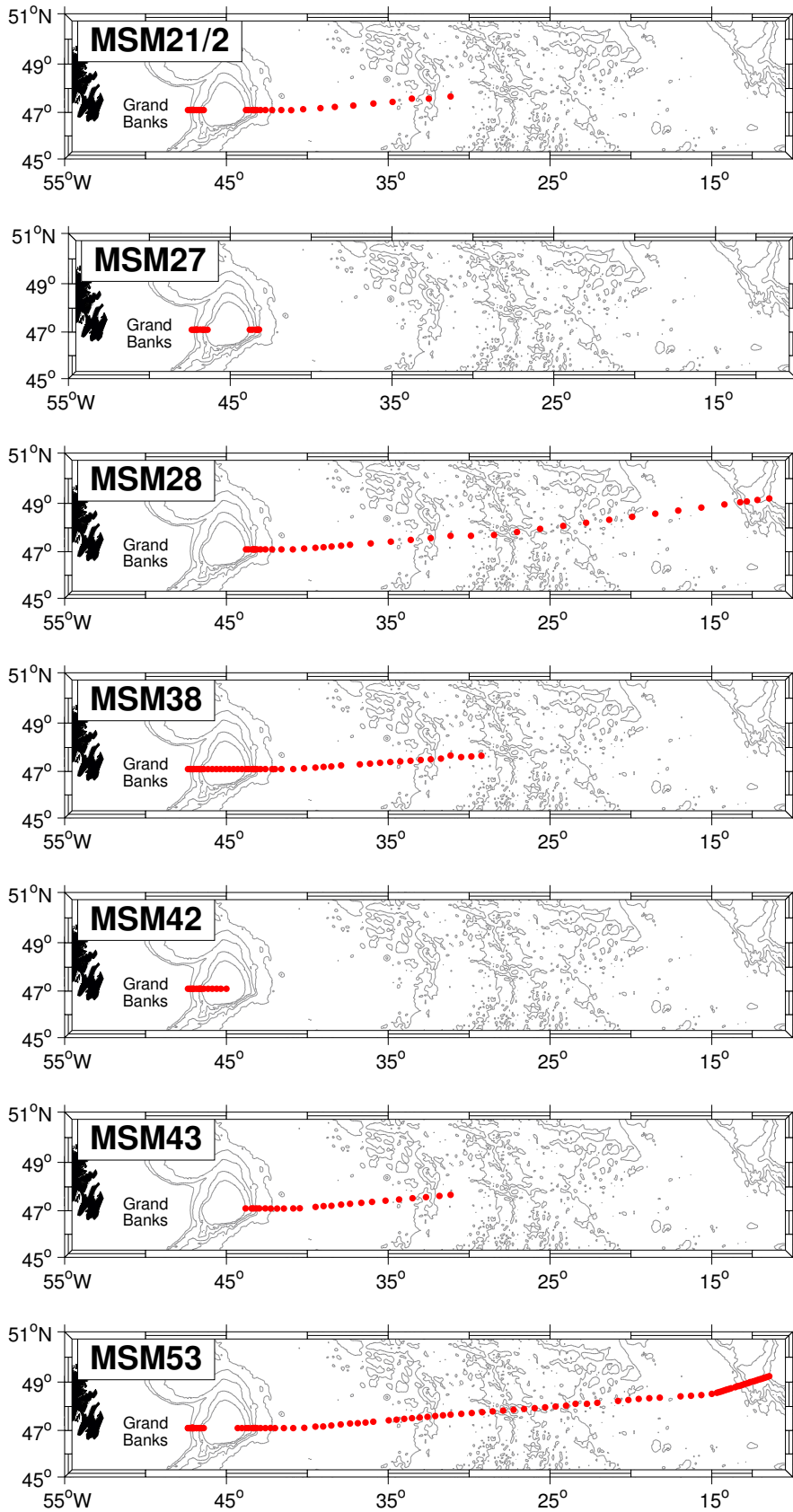
Figure A.2.: Station positions for individual cruises along the 47°N section for the years 2012-2016 (Table 2.2)
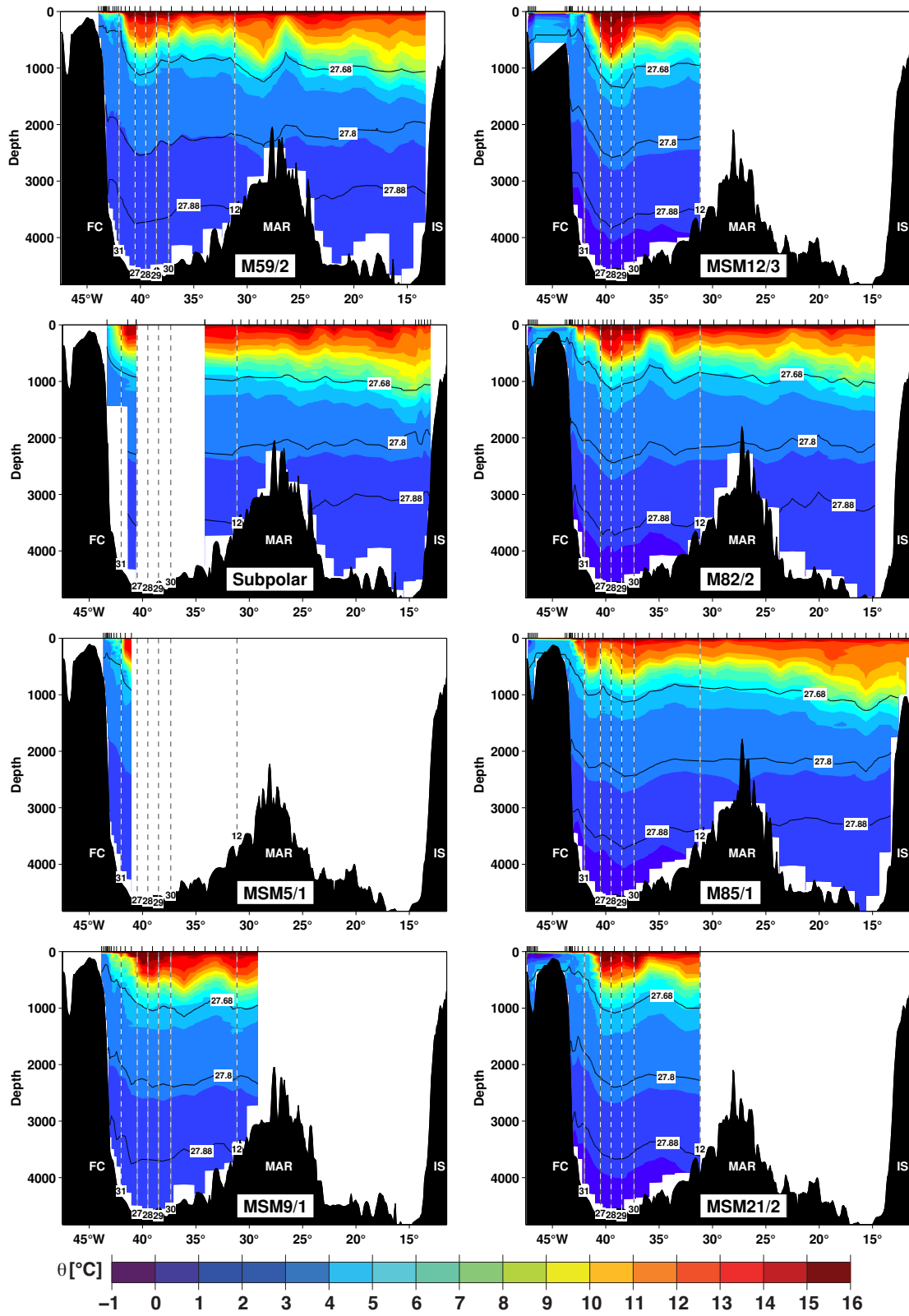
Figure A.3.: Potential temperature along the 47°N section for the years 2003-2012 (Table 2.2). Position and name of the PIES instruments are marked by the vertical lines (Table 2.5). Flemish Cap (FC), MAR and Irish Shelf (IS) are marked.
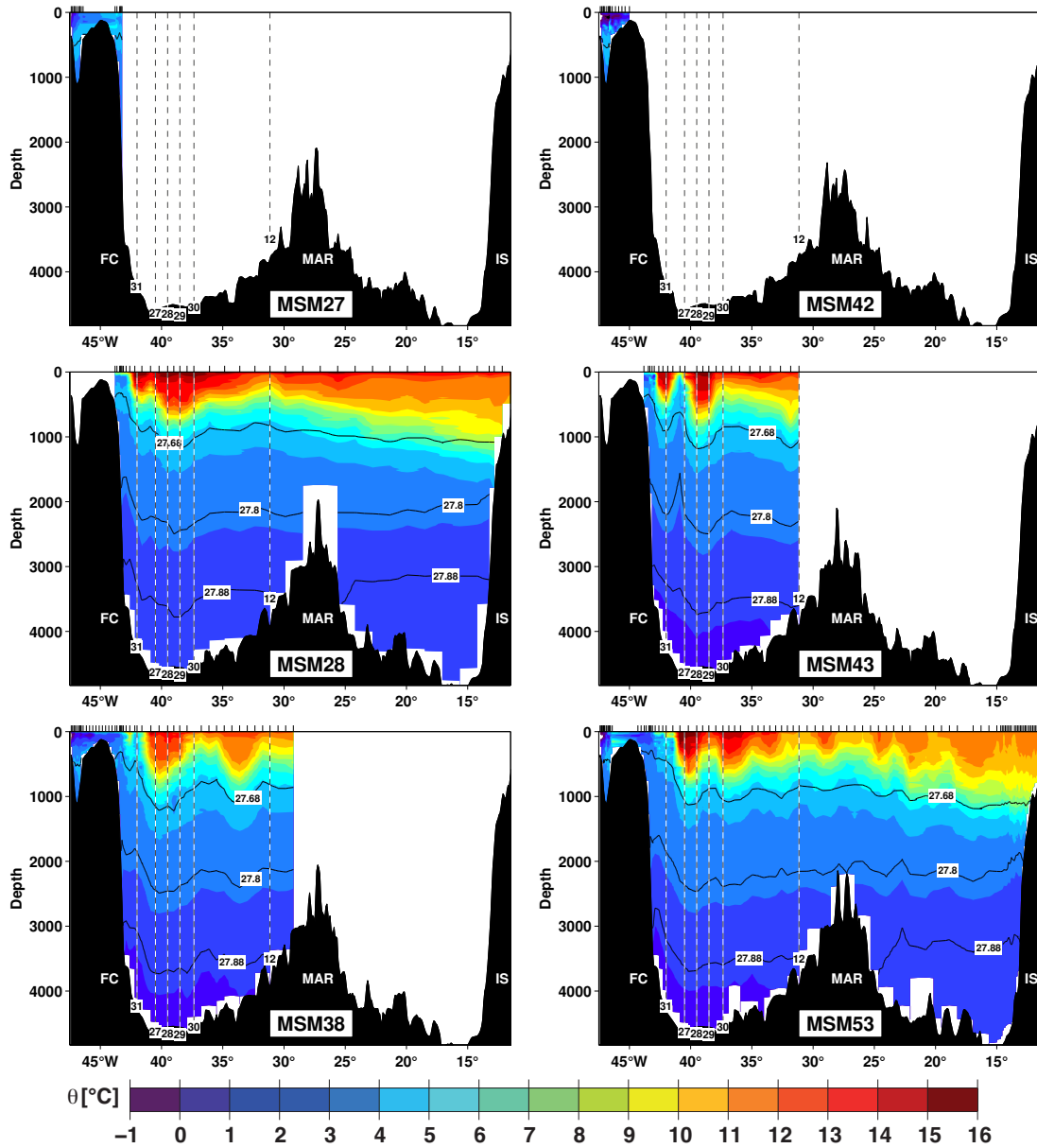
Figure A.4.: Potential temperature along the 47°N section for the years 2013-2016 (Table 2.2). Position and name of the PIES instruments are marked by the vertical lines (Table 2.5). Flemish Cap (FC), MAR and Irish Shelf (IS) are marked.
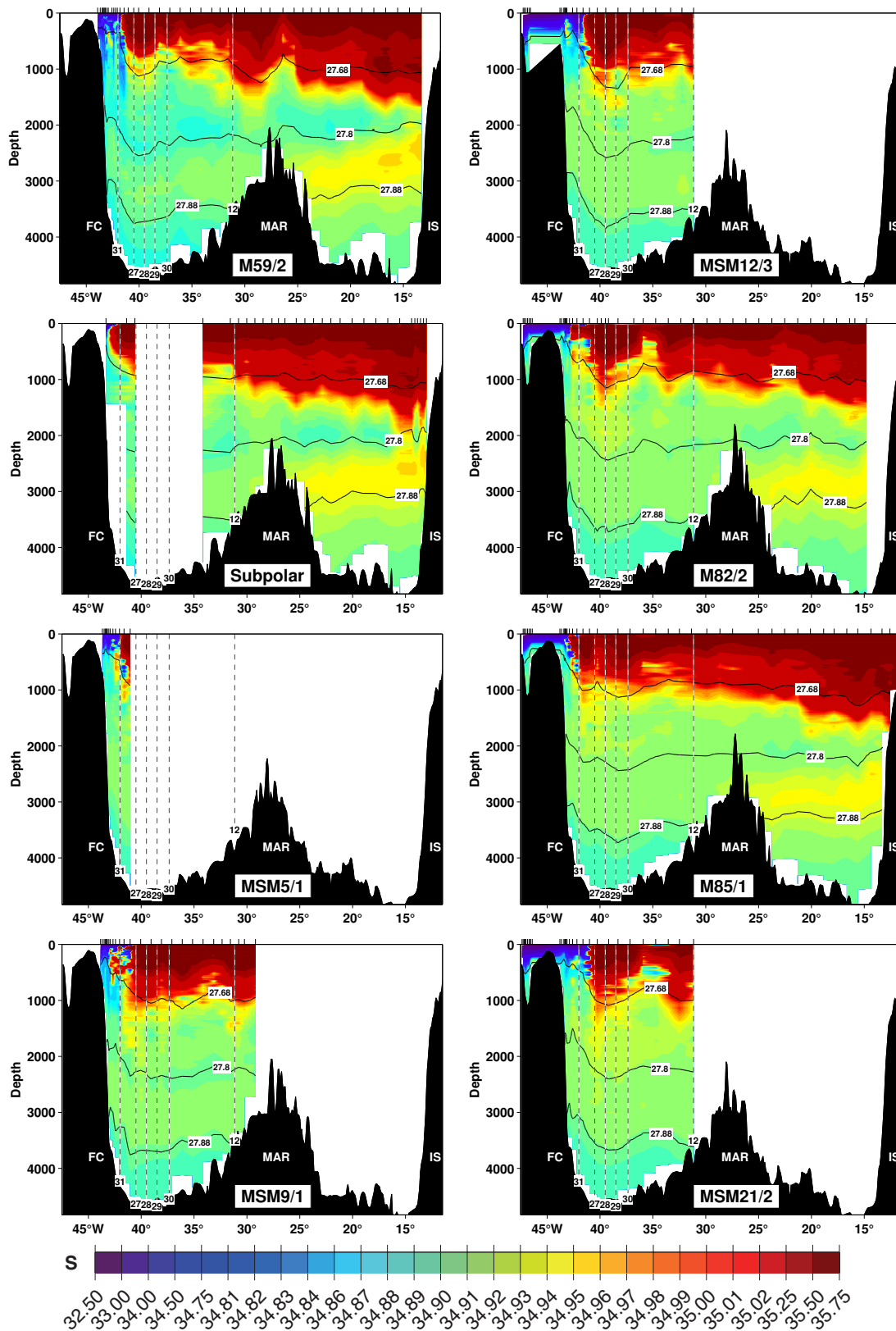
Figure A.5.: Salinity along the 47°N section for the years 2003-2012 (Table 2.2).Position and name of the PIES instruments are marked by the vertical lines (Table 2.5). Flemish Cap (FC), MAR and Irish Shelf (IS) are marked.
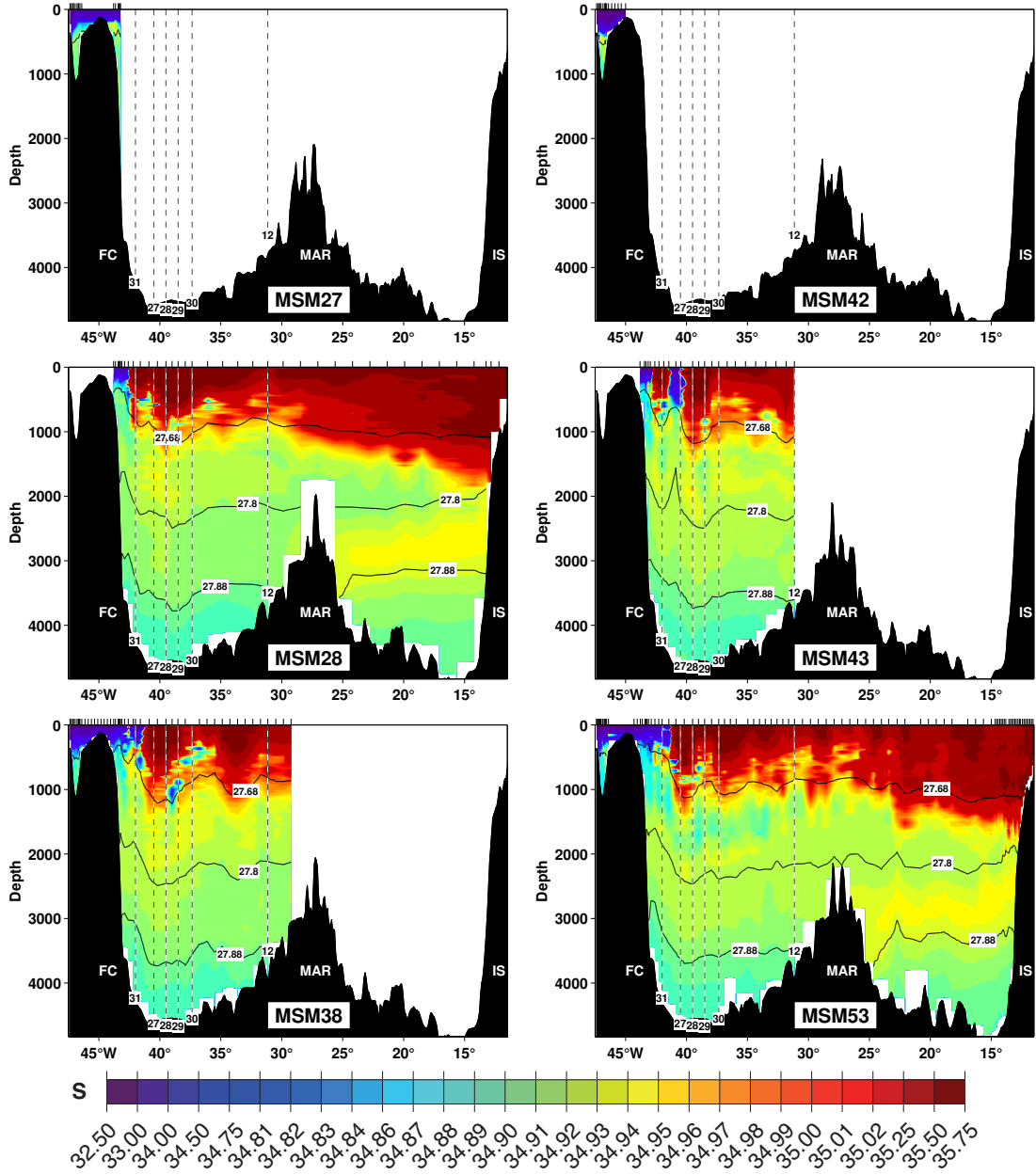
Figure A.6.: Salinity along the 47°N section for the years 2013-2016 (Table 2.2). Position and name of the PIES instruments are marked by the vertical lines (Table 2.5). Flemish Cap (FC), MAR and Irish Shelf (IS) are marked.
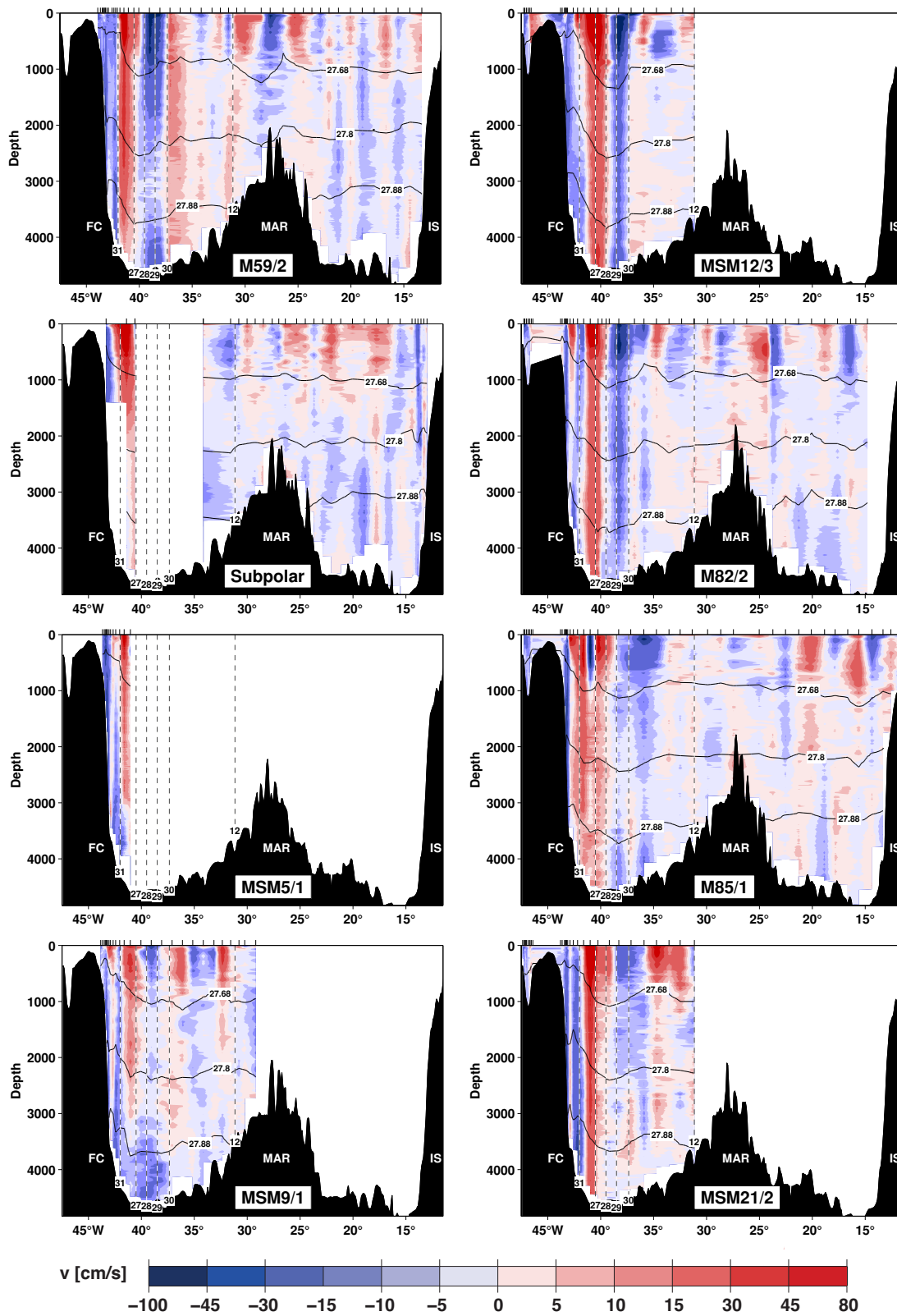
Figure A.7.: Velocity along the 47°N section for the years 2003-2012 (Table 2.2). Position and name of the PIES instruments are marked by the vertical lines (Table 2.5). Flemish Cap (FC), MAR and Irish Shelf (IS) are marked.
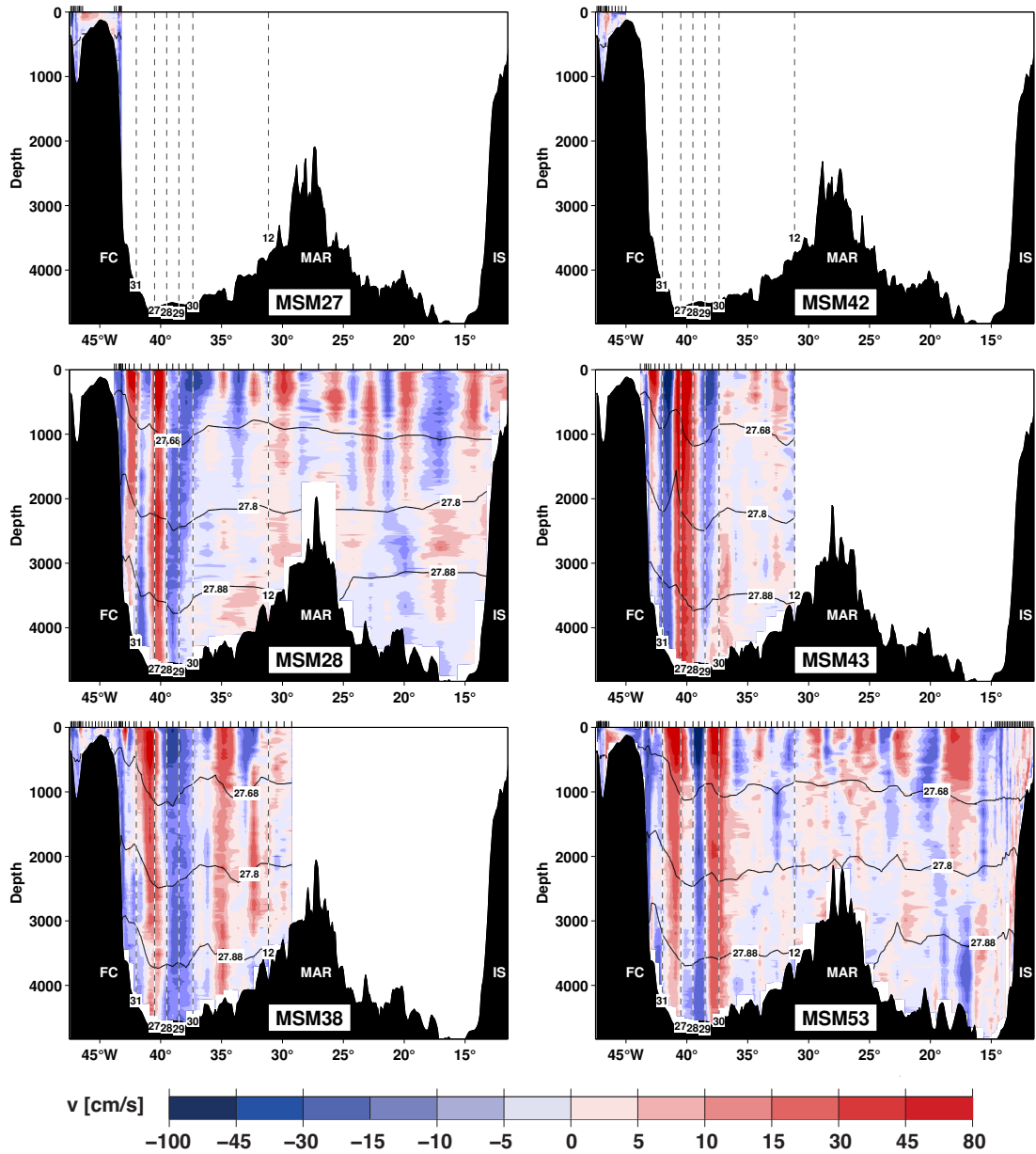
Figure A.8.: Velocity along the 47°N section for the years 2013-2016 (Table 2.2).Position and name of the PIES instruments are marked by the vertical lines (Table 2.5). Flemish Cap (FC), MAR and Irish Shelf (IS) are marked.

Individual hydrographic and velocity sections along MAR

Along the MAR section the individual cruise tracks are close to each other. Profiles used are between 17 and 22 per cruise. Over the entire time the fresh water at the surface in the northern part of the sections expands. The ISOW is strongest during the MSM28 cruise. The velocity distributions show single and double branching of the NAC crossing the MAR section towards the east as described for the MSM09/1 (2008), M82/2 (2010), and M85/1 cruises in *Walter and Mertens* (2013). In the years afterward branching of the NAC is still observed, e.g. during cruise MSM28 (2013) one branch is visible, which is similar to the branch during MSM09/1 in 2008. The strongest eastern flow was found during cruise MSM43 (2015), here two branches of the NAC are visible. The temperature distributions show that the surface water is getting colder from 2008 until 2016. Furthermore, the surface water also gets less saline in the southern part of the section. The minimum salinity at the surface in the northern part is found in each cruise but seems to be largest during the MSM43 cruise in 2015.
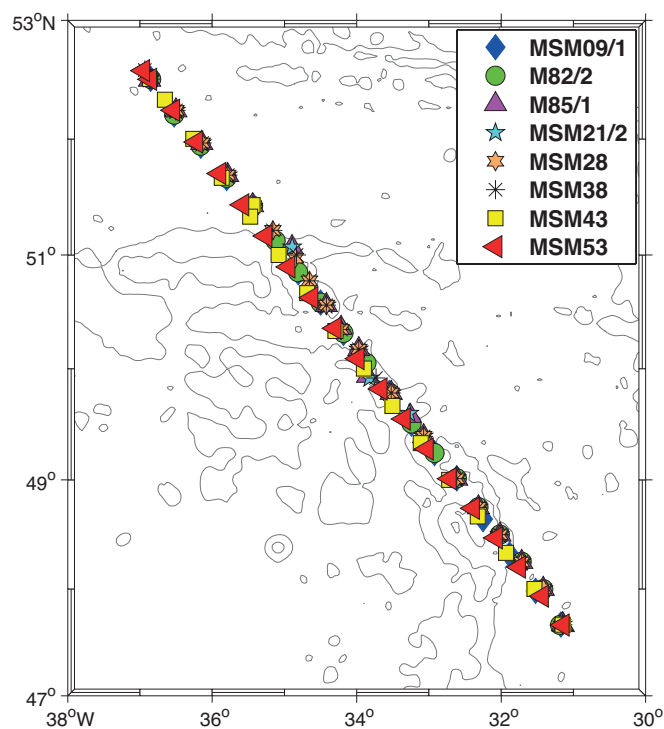
Figure A.9.: Cruise tracks along the MAR section from 2008 to 2016 (Table 2.1).
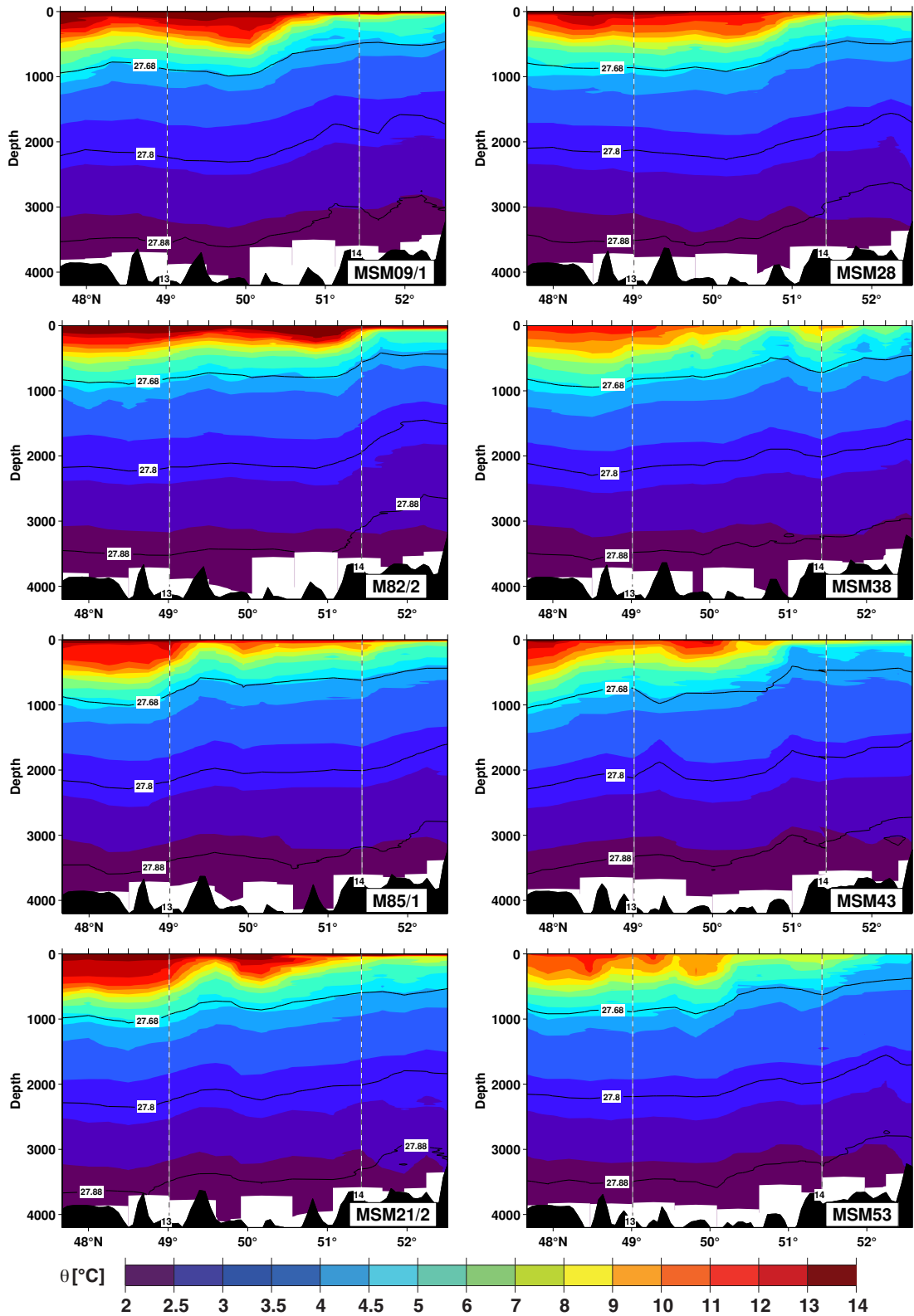
Figure A.10.: Potential temperature along the MAR section for the years 2008-2016 (Table 2.1). The position and names of PIES 13 and 14 are marked by the vertical lines (Table 2.4).
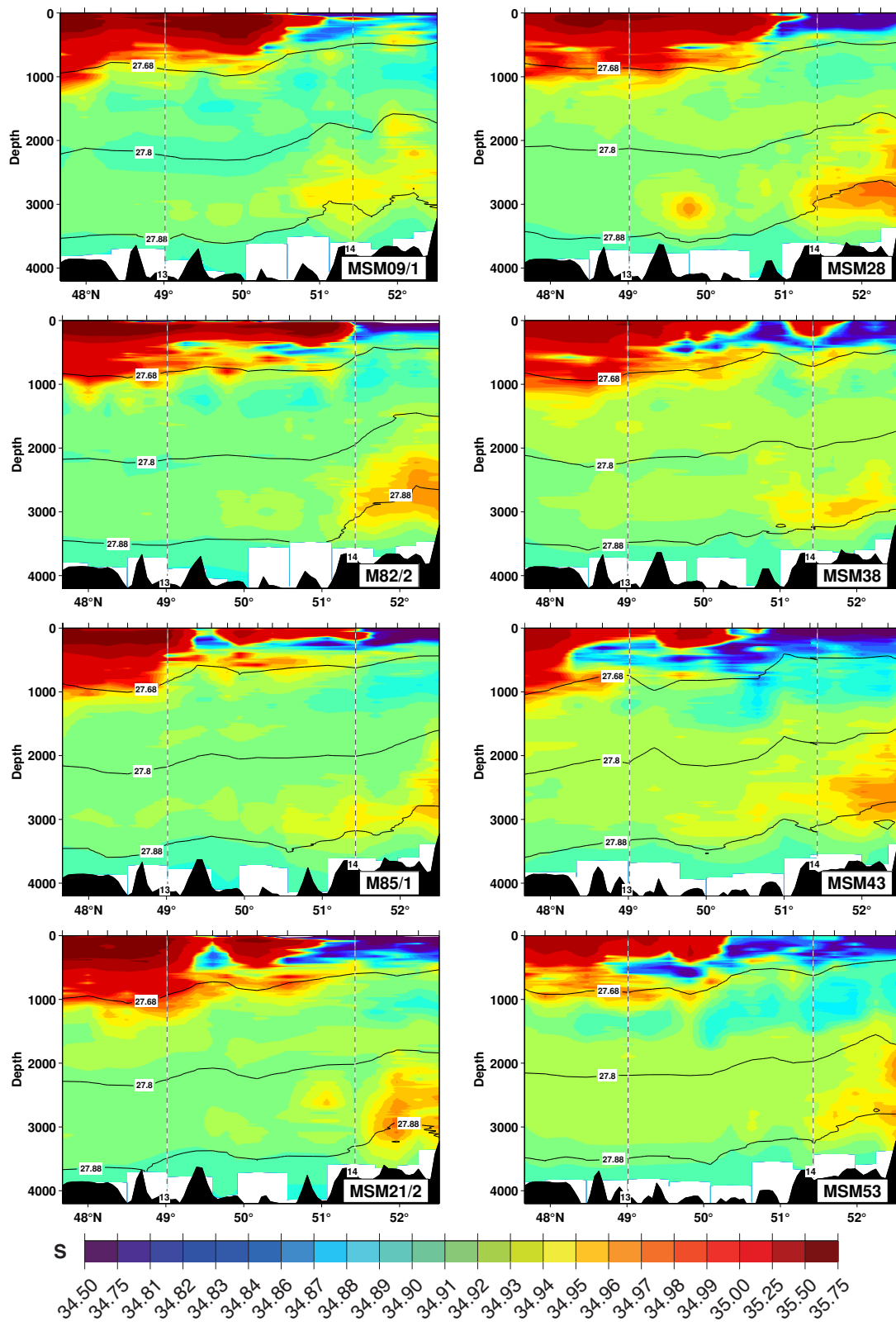
Figure A.11.: Salinity along the MAR section for the years 2008-2016 (Table 2.1)
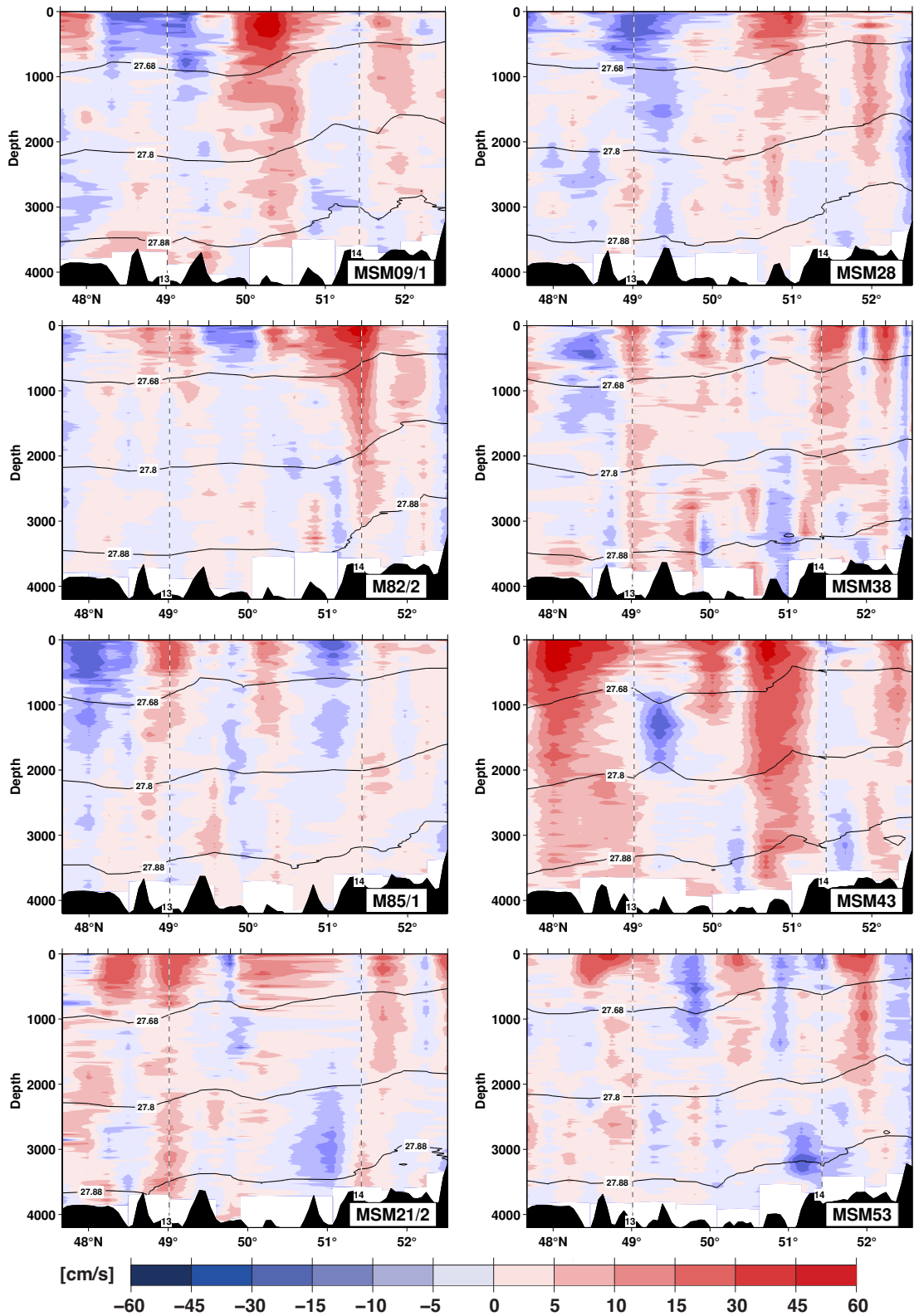
Figure A.12.: Zonal velocity along the MAR section for the years 2008-2016 (Table 2.1)

Individual hydrographic and velocity sections along OVIDE line

The OVIDE data used in this study to compute the mean distribution in section 3.2.3 are calculated from five cruises taken between 2002 and 2010[1]. In the southern part the surface is warmer and more saline than the deep ocean and partly the northern part of the section. Between 1000 and 2500 m a salinity minimum is observed through out the years, which is identified as LSW by *Lherminier et al.* (2010). The velocity distributions are dominated by a surface intensified flow and alternating velocity directions.
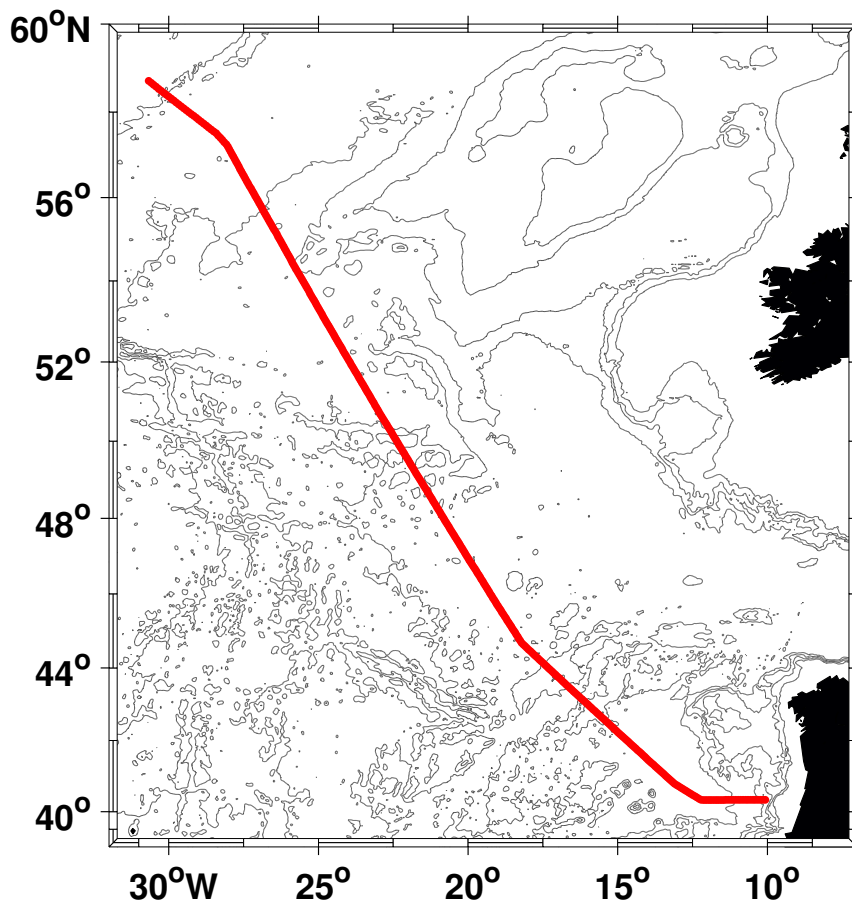
Figure A.13.: Cruise track along the OVIDE section for the years 2002-2010 (Table 2.3)

---

[1]Sections over entire OVIDE line (Portugal-Greenland) are found at `http://wwz.ifremer.fr/lpo_eng/Research/Projets-en-cours/OVIDE/Ovide-data/Hydrography-ADCP`
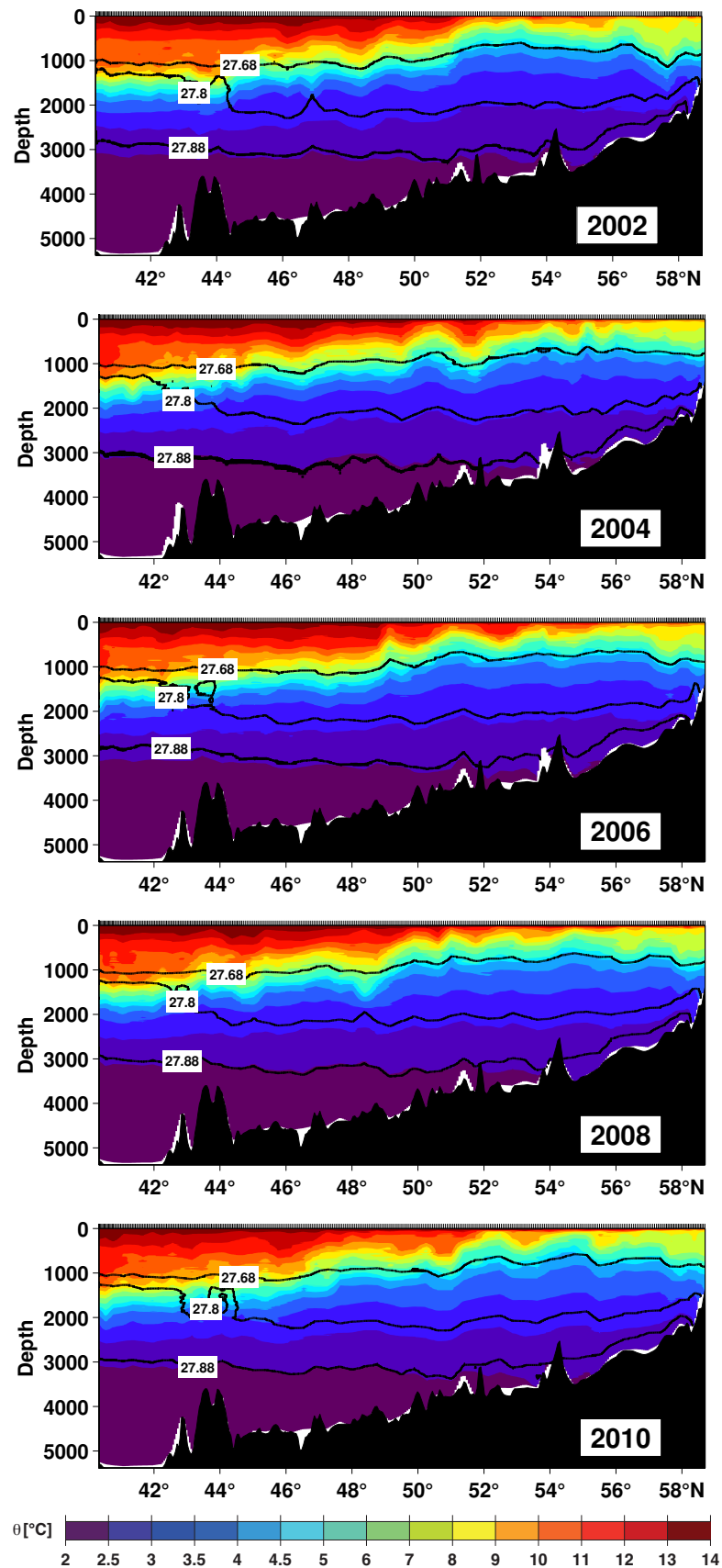
Figure A.14.: Potential temperature along the OVIDE line for the years 2002-2010 (Table 2.3)
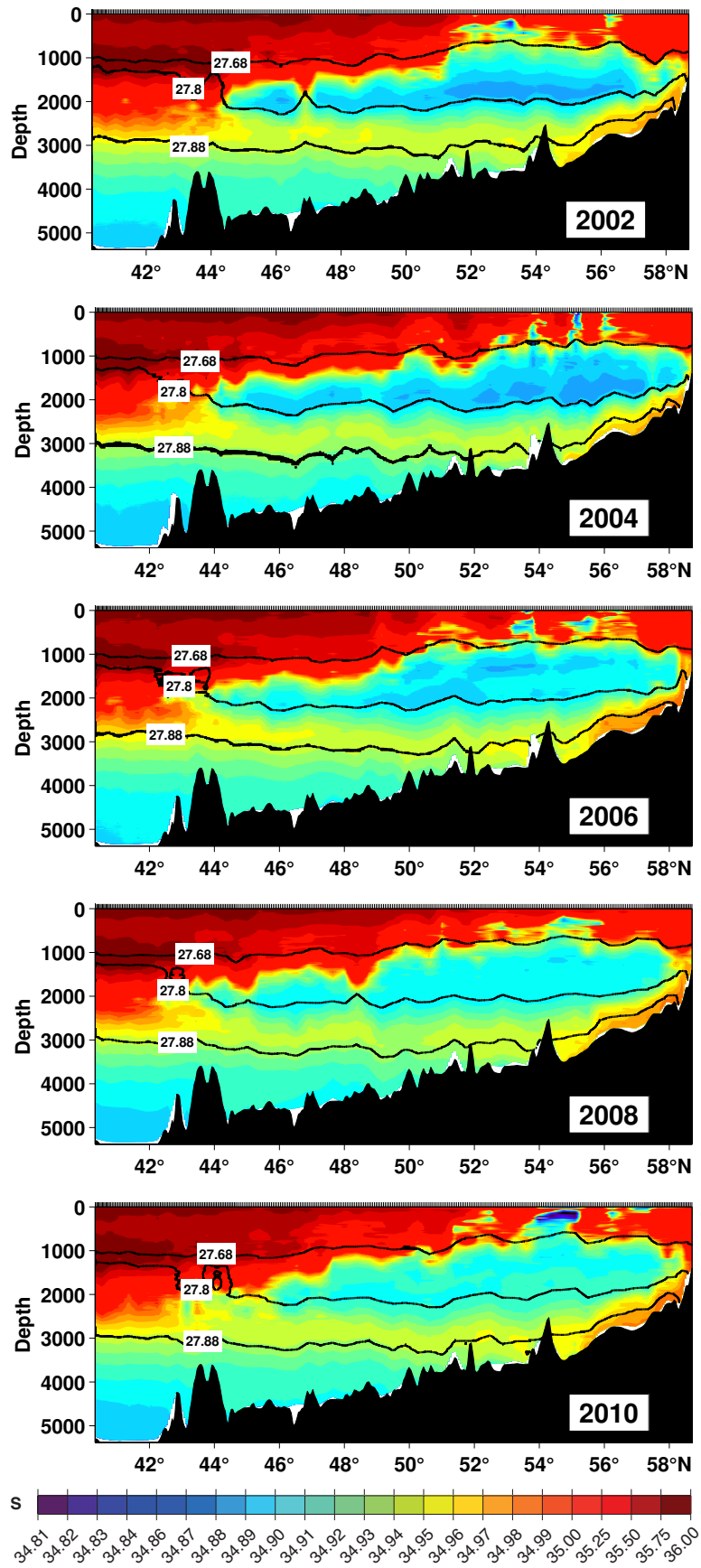
Figure A.15.: Salinity along the OVIDE line for the years 2002-2010 (Table 2.3)
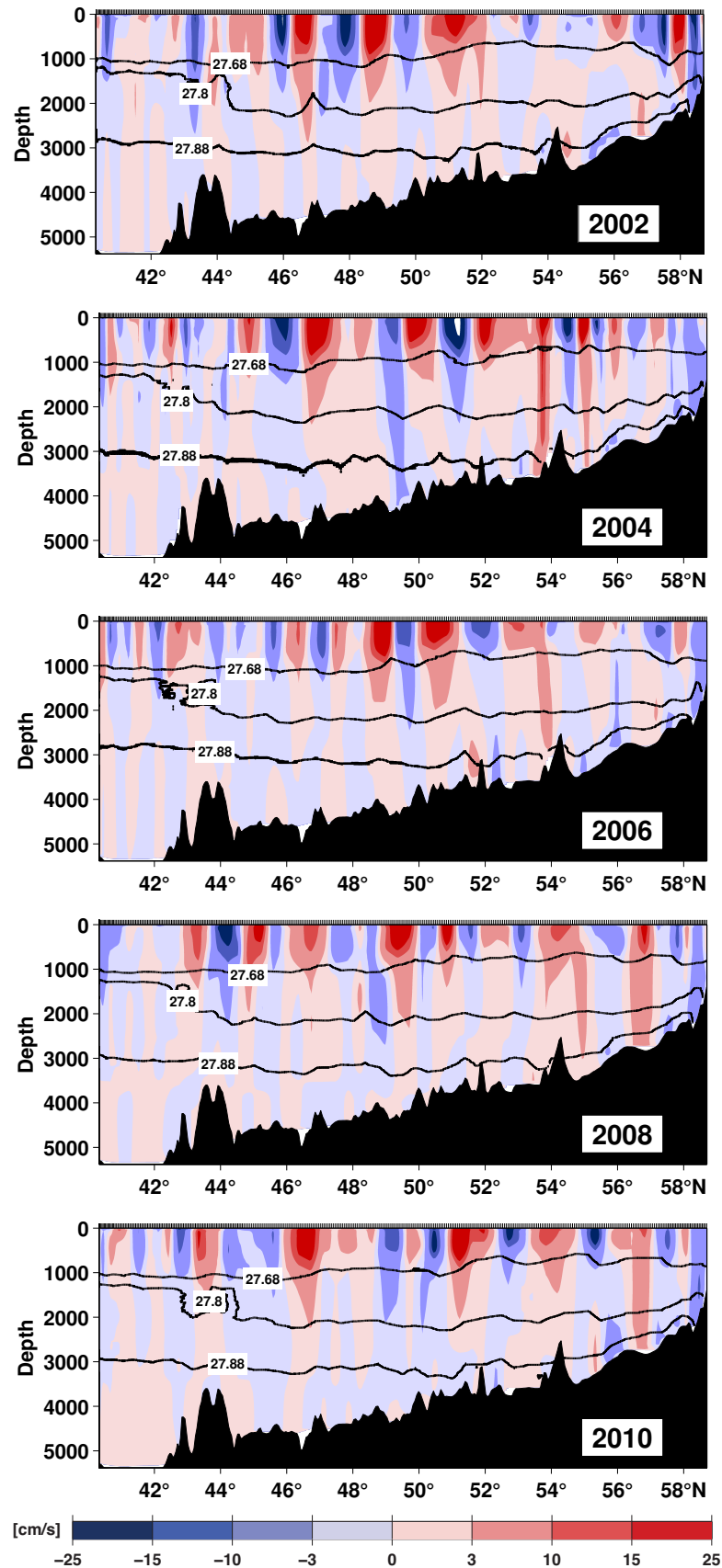
Figure A.16.: Velocity along the OVIDE line for the years 2002-2010 (Table 2.3)

A.2. Iceland-Scotland Overflow Water in the VIKING20 model
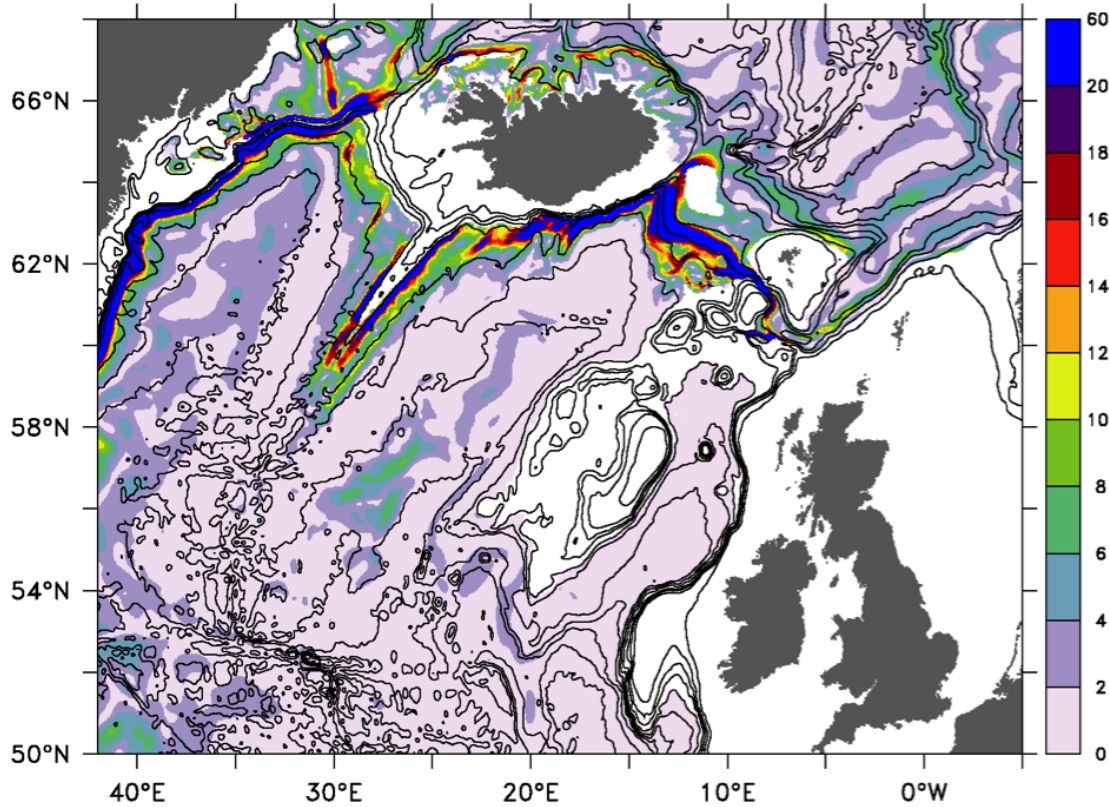
Figure A.17.: Mean velocity (cm/s) in the VIKING20 model on the $\sigma_\theta =$ 27.88 kg/m³ isopycnal as an indicator for Iceland-Scotland Overflow Water (ISOW). Bathymetry is displayed between 0 and 1000 m in 250 m interval and afterwards until 5000 m every thousand meter. Figure was provided by E. Behrens.

Bibliography

Acharya, T., and P.-S. Tsai (2007), Computational Foundations of Image Interpolation Algorithms, *ACM Ubiquity*, *8*.

Arakawa, A., and V. R. Lamb (1977), Computational design of the basic dynamical processes of the UCLA general circulation model, *Methods in computational physics*, *17*, 173–265.

Barnier, B., G. Madec, T. Penduff, J.-M. Molines, A.-M. Treguier, J. Le Sommer, A. Beckmann, A. Biastoch, C. Böning, J. Dengg, C. Derval, E. Durand, S. Gulev, E. Remy, C. Talandier, S. Theetten, M. Maltrud, J. McClean, and B. De Cuevas (2006), Impact of partial steps and momentum advection schemes in a global ocean circulation model at eddy-permitting resolution, *Ocean Dynamics*, *56*(5-6), 543–567, doi:10.1007/s10236-006-0082-1.

Behrens, E. (2013), The oceanic response to Greenland melting: the effect of increasing model resolution, Ph.D. thesis, University of Kiel, Germany, doi:urn:nbn:de:gbv:8-diss-136843.

Bersch, M. (2002), North Atlantic Oscillation–induced changes of the upper layer circulation in the northern North Atlantic Ocean, *Journal of Geophysical Research*, *107*(C10), 1–11, doi:10.1029/2001JC000901.

Bersch, M., J. Meincke, and A. Sy (1999), Interannual thermohaline changes in the northern North Atlantic 1991-1996, *Deep-Sea Research Part II: Topical Studies in Oceanography*, *46*(1-2), 55–75, doi:10.1016/S0967-0645(98)00114-3.

Bersch, M., I. Yashayaev, and K. P. Koltermann (2007), Recent changes of the thermohaline circulation in the subpolar North Atlantic, *Ocean Dynamics*, *57*(3), 223–235, doi:10.1007/s10236-007-0104-7.

Blanke, B., and S. Raynaud (1997), Kinematics of the Pacific Equatorial Undercurrent: An Eulerian and Lagrangian Approach from GCM Results, *Journal of Physical*

Oceanography, *27*(6), 1038–1053, doi:10.1175/1520-0485(1997)027<1038:KOTPEU>2.0.CO;2.

Blanke, B., M. Arhan, G. Madec, and S. Roche (1999), Warm Water Paths in the Equatorial Atlantic as Diagnosed with a General Circulation Model, *Journal of Physical Oceanography*, *29*(11), 2753–2768, doi:10.1175/1520-0485(1999)029<2753:WWPITE>2.0.CO;2.

Böning, C. W., M. Scheinert, J. Dengg, A. Biastoch, and A. Funk (2006), Decadal variability of subpolar gyre transport and its reverberation in the North Atlantic overturning, *Geophysical Research Letters*, *33*(21), doi:10.1029/2006GL026906.

Böning, C. W., E. Behrens, A. Biastoch, K. Getzlaff, and J. L. Bamber (2016), Emerging impact of Greenland meltwater on deepwater formation in the North Atlantic Ocean, *Nature Geoscience*, *9*(7), 523–527, doi:10.1038/ngeo2740.

Bower, A. S., and W.-J. von Appen (2008), Interannual Variability in the Pathways of the North Atlantic Current over the Mid-Atlantic Ridge and the Impact of Topography, *Journal of Physical Oceanography*, *38*(1), 104–120, doi:10.1175/2007JPO3686.1.

Bower, A. S., B. Le Cann, T. Rossby, W. Zenk, J. Gould, K. Speer, P. L. Richardson, M. D. Prater, and H.-M. Zhang (2002), Directly measured mid-depth circulation in the northeastern North Atlantic Ocean, *Nature*, *419*(6907), 603–607, doi:10.1038/nature01078.

Boyer, T., S. Levitus, J. Antonov, R. Locarnini, A. Mishonov, H. Garcia, and S. A. Josey (2007), Changes in freshwater content in the North Atlantic Ocean 1955-2006, *Geophysical Research Letters*, *34*(16), 1–5, doi:10.1029/2007GL030126.

Brambilla, E., and L. D. Talley (2006), Surface drifter exchange between the North Atlantic subtropical and subpolar gyres, *Journal of Geophysical Research*, *111*(C7), C07,026, doi:10.1029/2005JC003146.

Brambilla, E., and L. D. Talley (2008), Subpolar mode water in the northeastern Atlantic: 1. Averaged properties and mean circulation, *Journal of Geophysical Research: Oceans*, *113*(4), 1–18, doi:10.1029/2006JC004062.

Brauch, J. P., and R. Gerdes (2005), Response of the northern North Atlantic and Arctic oceans to a sudden change of the North Atlantic Oscillation, *Journal of Geophysical Research: Oceans*, *110*(C11018), 1–16, doi:10.1029/2004JC002436.

Breckenfelder, T., M. Rhein, A. Roessler, C. W. Böning, A. Biastoch, E. Behrens, and C. Mertens (2017), Flow paths and variability of the North Atlantic Current: A comparison of observations and a high-resolution model, *Journal of Geophysical Research: Oceans*, pp. 1–23, doi:10.1002/2016JC012444.

Burkholder, K. C., and M. S. Lozier (2011), Mid-depth Lagrangian pathways in the North Atlantic and their impact on the salinity of the eastern subpolar gyre, *Deep Sea Research Part I: Oceanographic Research Papers*, *58*(12), 1196–1204, doi:10.1016/j.dsr.2011.08.007.

Chafik, L., T. Rossby, and C. Schrum (2014), On the spatial structure and temporal variability of poleward transport between Scotland and Greenland, *Journal of Geophysical Research: Oceans*, *119*(2), 824–841, doi:10.1002/2013JC009287.

Chaplin, G., and D. Watts (1984), Inverted Echo Sounder Development, in *OCEANS 1984*, pp. 249–253, IEEE, doi:10.1109/OCEANS.1984.1152347.

Chaudhuri, A. H., A. Gangopadhyay, and J. J. Bisagni (2011), Contrasting Response of the Eastern and Western North Atlantic Circulation to an Episodic Climate Event, *Journal of Physical Oceanography*, *41*(9), 1630–1638, doi:10.1175/2011JPO4512.1.

Clarke, R. A., H. W. Hill, R. F. Reiniger, and B. A. Warren (1980), Current System South and East of the Grand Banks of Newfoundland, *Journal of Physical Oceanography*, *10*(1), 25–65, doi:10.1175/1520-0485(1980)010<0025:CSSAEO>2.0.CO;2.

Cunningham, S. A., T. Kanzow, D. Rayner, M. O. Baringer, W. E. Johns, J. Marotzke, H. R. Longworth, E. M. Grant, J. J.-M. Hirschi, L. M. Beal, C. S. Meinen, and H. L. Bryden (2007), Temporal Variability of the Atlantic Meridional Overturning Circulation at 26.5°N, *Science*, *317*(5840), 935–938, doi:10.1126/science.1141304.

Curry, R., and C. Mauritzen (2005), Dilution of the Northern North Atlantic Ocean in Recent Decades, *Science*, *308*(5729), 1772–1774, doi:10.1126/science.1109477.

Curry, R. G., and M. S. McCartney (2001), Ocean Gyre Circulation Changes Associated with the North Atlantic Oscillation, *Journal of Physical Oceanography*, *31*(12), 3374–3400, doi:10.1175/1520-0485(2001)031<3374:OGCCAW>2.0.CO;2.

Danabasoglu, G., S. G. Yeager, D. Bailey, E. Behrens, M. Bentsen, D. Bi, A. Biastoch, C. Böning, A. Bozec, V. M. Canuto, C. Cassou, E. Chassignet, A. C. Coward,

S. Danilov, N. Diansky, H. Drange, R. Farneti, E. Fernandez, P. G. Fogli, G. Forget, Y. Fujii, S. M. Griffies, A. Gusev, P. Heimbach, A. Howard, T. Jung, M. Kelley, W. G. Large, A. Leboissetier, J. Lu, G. Madec, S. J. Marsland, S. Masina, A. Navarra, a. J. George Nurser, A. Pirani, D. S. y Mélia, B. L. Samuels, M. Scheinert, D. Sidorenko, A. M. Treguier, H. Tsujino, P. Uotila, S. Valcke, A. Voldoire, and Q. Wang (2014), North Atlantic simulations in Coordinated Ocean-ice Reference Experiments phase II (CORE-II). Part I: Mean states, *Ocean Modelling*, *73*, 76–107, doi:10.1016/j.ocemod.2013.10.005.

Danabasoglu, G., S. G. Yeager, W. M. Kim, E. Behrens, M. Bentsen, D. Bi, A. Biastoch, R. Bleck, C. Böning, A. Bozec, V. M. Canuto, C. Cassou, E. Chassignet, A. C. Coward, S. Danilov, N. Diansky, H. Drange, R. Farneti, E. Fernandez, P. G. Fogli, G. Forget, Y. Fujii, S. M. Griffies, A. Gusev, P. Heimbach, A. Howard, M. Ilicak, T. Jung, A. R. Karspeck, M. Kelley, W. G. Large, A. Leboissetier, J. Lu, G. Madec, S. J. Marsland, S. Masina, A. Navarra, A. J. G. Nurser, A. Pirani, A. Romanou, S. y. M. David, B. L. Samuels, M. Scheinert, D. Sidorenko, S. Sun, A. M. Treguier, H. Tsujino, P. Uotila, S. Valcke, A. Voldoire, Q. Wang, and I. Yashayaev (2016), North Atlantic simulations in Coordinated Ocean-ice Reference Experiments phase II (CORE-II). Part II: Interannual to decadal variability, *Ocean Modelling*, *97*, 65–90, doi:10.1016/j.ocemod.2015. 11.007.

Daniault, N., H. Mercier, P. Lherminier, A. Sarafanov, A. Falina, P. Zunino, F. F. Pérez, A. F. Ríos, B. Ferron, T. Huck, V. Thierry, and S. Gladyshev (2016a), The northern North Atlantic Ocean mean circulation in the early 21st Century, *Progress in Oceanography*, *146* (July), 142–158, doi:10.1016/j.pocean.2016.06.007.

Daniault, N., H. Mercier, and P. Lherminier (2016b), Gridded property and transport data of the biennial Greenland-Portugal A25 OVIDE line, *SEANOE*, doi:10.17882/ 46446.

Debreu, L., C. Vouland, and E. Blayo (2008), AGRIF: Adaptive grid refinement in Fortran, *Computers and Geosciences*, *34* (1), 8–13, doi:10.1016/j.cageo.2007.01.009.

Delworth, T. L., and F. Zeng (2016), The impact of the North Atlantic Oscillation on climate through its influence on the Atlantic Meridional Overturning Circulation, *Journal of Climate*, *29* (3), 941–962, doi:10.1175/JCLI-D-15-0396.1.

Desbruyères, D., H. Mercier, and V. Thierry (2015), On the mechanisms behind decadal heat content changes in the eastern subpolar gyre, *Progress in Oceanography*, *132*, 262–272, doi:10.1016/j.pocean.2014.02.005.

Dickson, R. R., and J. Brown (1994), The production of North Atlantic Deep Water: Sources, rates, and pathways, *Journal of Geophysical Research: Oceans*, *99*(C6), 12,319–12,341, doi:10.1029/94JC00530.

DRAKKAR (2007), Eddy-permitting ocean circulation hindcasts of past decades, *Clivar Exchanges No. 42, 12(3)*, 8–10.

Eden, C., and J. Willebrand (2001), Mechanisms of interannual to decadal variability of the North Atlantic Circulation, *J. Clim.*, *14*(1994), 2266–2280, doi:10.1175/1520-0442(2001)014<2266:MOITDV>2.0.CO;2.

Egbert, G. D., and S. Y. Erofeeva (2002), Efficient inverse modeling of barotropic ocean tides, *Journal of Atmospheric and Oceanic Technology*, *19*(2), 183–204, doi:10.1175/1520-0426(2002)019<0183:EIMOBO>2.0.CO;2.

Etopo2 (2001), Global Gridded 2-minute Database.

Fichefet, T., and M. A. M. Maqueda (1997), Sensitivity of a global sea ice model to the treatment of ice thermodynamics and dynamics, *Journal of Geophysical Research*, *102*(C6), 12,609–12,646, doi:10.1029/97JC00480.

Fischer, J., F. A. Schott, and M. Dengler (2004), Boundary Circulation at the Exit of the Labrador Sea, *Journal of Physical Oceanography*, *34*(7), 1548–1570, doi:10.1175/1520-0485(2004)034<1548:BCATEO>2.0.CO;2.

Fischer, J., M. Visbeck, R. Zantopp, and N. Nunes (2010), Interannual to decadal variability of outflow from the Labrador Sea, *Geophysical Research Letters*, *37*(24), doi:10.1029/2010GL045321.

Fischer, J., J. Karstensen, R. Zantopp, M. Visbeck, A. Biastoch, E. Behrens, C. W. Böning, D. Quadfasel, K. Jochumsen, H. Valdimarsson, S. Jónsson, S. Bacon, N. P. Holliday, S. Dye, M. Rhein, and C. Mertens (2014), Intra-seasonal variability of the DWBC in the western subpolar North Atlantic, *Progress in Oceanography*, *132*(0), 233–249, doi:10.1016/j.pocean.2014.04.002.

Flatau, M. K., L. Talley, and P. P. Niiler (2003), The North Atlantic Oscillation, surface current velocities, and SST changes in the subpolar North Atlantic, *Journal of Climate*, *16*(14), 2355–2369, doi:10.1175/2787.1.

Fleischmann, U., H. Hildebrandt, A. Putzka, and R. Bayer (2001), Transport of newly ventilated deep water from the Iceland Basin to the Westeuropean Basin,

Deep-Sea Research Part I: Oceanographic Research Papers, *48*(8), 1793–1819, doi: 10.1016/S0967-0637(00)00107-2.

Frankignoul, C., J. Deshayes, and R. Curry (2009), The role of salinity in the decadal variability of the North Atlantic meridional overturning circulation, *Climate Dynamics*, *33*(6), 777–793, doi:10.1007/s00382-008-0523-2.

Fratantoni, D. M. (2001), North Atlantic surface circulation during the 1990's observed with satellite-tracked drifters, *Journal of Geophysical Research: Oceans*, *106*(C10), 22,067–22,093, doi:10.1029/2000JC000730.

García-Ibáñez, M. I., P. C. Pardo, L. I. Carracedo, H. Mercier, P. Lherminier, A. F. Ríos, and F. F. Pérez (2015), Structure, transports and transformations of the water masses in the Atlantic Subpolar Gyre, *Progress in Oceanography*, *135*, 18–36, doi: 10.1016/j.pocean.2015.03.009.

Gourcuff, C., P. Lherminier, H. Mercier, and P. Y. Le Traon (2011), Altimetry combined with hydrography for ocean transport estimation, *Journal of Atmospheric and Oceanic Technology*, *28*(10), 1324–1337, doi:10.1175/2011JTECHO818.1.

Guinehut, S., P. Y. Le Traon, and G. Larnicol (2006), What can we learn from Global Altimetry/Hydrography comparisons?, *Geophysical Research Letters*, *33*(10), 1–5, doi: 10.1029/2005GL025551.

Häkkinen, S., and P. B. Rhines (2004), Decline of subpolar North Atlantic circulation during the 1990s., *Science (New York, N.Y.)*, *304*(5670), 555–559, doi:10.1126/science. 1094917.

Häkkinen, S., and P. B. Rhines (2009), Shifting surface currents in the northern North Atlantic Ocean, *Journal of Geophysical Research: Oceans*, *114*(4), 1–12, doi:10.1029/ 2008JC004883.

Halkin, D., and T. Rossby (1985), The Structure and Transport of the Gulf Stream at 73°W, *Journal of Physical Oceanography*, *15*(11), 1439–1452, doi:10.1175/ 1520-0485(1985)015<1439:TSATOT>2.0.CO;2.

Hauser, T., E. Demirov, J. Zhu, and I. Yashayaev (2015), North Atlantic atmospheric and ocean inter-annual variability over the past fifty years – Dominant patterns and decadal shifts, *Progress in Oceanography*, *132*, 197–219, doi:10.1016/j.pocean.2014.10.008.

Herbaut, C., and M.-N. Houssais (2009), Response of the eastern North Atlantic subpolar gyre to the North Atlantic Oscillation, *Geophysical Research Letters*, *36*(17), L17,607, doi:10.1029/2009GL039090.

Hogg, N. G. (1992), On the transport of the gulf stream between cape hatteras and the grand banks, *Deep Sea Research Part A. Oceanographic Research Papers*, *39*(7-8), 1231–1246, doi:10.1016/0198-0149(92)90066-3.

Hurrell, J. W. (1995), Decadal trends in the North Atlantic Oscillation: regional temperatures and precipitation., *Science (New York, N.Y.)*, *269*(5224), 676–679, doi:10.1126/science.269.5224.676.

Hurrell, J. W., and C. Deser (2009), North Atlantic climate variability: The role of the North Atlantic Oscillation, *Journal of Marine Systems*, *78*(1), 28–41, doi:10.1016/j.jmarsys.2008.11.026.

IPCC (2013), Summary for Policymakers, in *Climate Change 2013: The Physical Science Basis. Contribution of Working Group I to the Fifth Assessment Report of the Intergovernmental Panel on Climate Change*, [Stocker, T.F., D. Qin, G.-K. Plattner, M. Tignor, S.K. Allen, J. Boschung, A. Nauels, Y. Xia, V. Bex and P.M. Midgley (eds.)]. Cambridge University Press, Cambridge, United Kingdom and New York, NY, USA, doi:10.1017/CBO9781107415324.004.

Johns, W. E., M. O. Baringer, L. M. Beal, S. A. Cunningham, T. Kanzow, H. L. Bryden, J. J. M. Hirschi, J. Marotzke, C. S. Meinen, B. Shaw, and R. Curry (2011), Continuous, array-based estimates of atlantic ocean heat transport at 26.5°N, *Journal of Climate*, *24*(10), 2429–2449, doi:10.1175/2010JCLI3997.1.

Kieke, D., and I. Yashayaev (2015), Studies of Labrador Sea Water formation and variability in the subpolar North Atlantic in the light of international partnership and collaboration, *Progress in Oceanography*, *132*, 220–232, doi:10.1016/j.pocean.2014.12.010.

Kieke, D., M. Rhein, L. Stramma, W. M. Smethie, J. L. Bullister, and D. A. LeBel (2007), Changes in the pool of Labrador Sea Water in the subpolar North Atlantic, *Geophysical Research Letters*, *34*(6), L06,605, doi:10.1029/2006GL028959.

Large, W. G., and S. G. Yeager (2009), The global climatology of an interannually varying air - sea flux data set, *Climate Dynamics*, *33*(2-3), 341–364, doi:10.1007/s00382-008-0441-3.

Bibliography

Larsen, J., and T. Sanford (1985), Florida Current volume transports from voltage measurements, *Science*, *227*, 302–304.

Lavender, K. L., R. E. Davis, and W. B. Owens (2000), Mid-depth recirculation observed in the interior Labrador and Irminger seas by direct velocity measurements, *Nature*, *407*(6800), 66–69, doi:10.1038/35024048.

Leaman, K. D., E. Johns, and T. Rossby (1989), The average distribution of volume transport and potential vorticity with temperature at three sections accross the Gulf Stream.

Levitus (1998), World Ocean Database 1998, vol. 1, Introduction, NOAA Atlas NESDIS 18, *US Government Printing Office, Washington, DC*.

Lherminier, P., H. Mercier, C. Gourcuff, M. Alvarez, S. Bacon, and C. Kermabon (2007), Transports across the 2002 Greenland-Portugal Ovide section and comparison with 1997, *Journal of Geophysical Research: Oceans*, *112*(7), 1–20, doi: 10.1029/2006JC003716.

Lherminier, P., H. Mercier, T. Huck, C. Gourcuff, F. F. Perez, P. Morin, A. Sarafanov, and A. Falina (2010), The Atlantic Meridional Overturning Circulation and the subpolar gyre observed at the A25-OVIDE section in June 2002 and 2004, *Deep Sea Research Part I: Oceanographic Research Papers*, *57*(11), 1374–1391, doi:10.1016/j.dsr.2010.07. 009.

Lohmann, K., H. Drange, and M. Bentsen (2009), Response of the North Atlantic subpolar gyre to persistent North Atlantic oscillation like forcing, *Climate Dynamics*, *32*(2-3), 273–285, doi:10.1007/s00382-008-0467-6.

Lorbacher, K., J. Dengg, C. W. Böning, and A. Biastoch (2010), Regional patterns of sea level change related to interannual variability and multidecadal trends in the Atlantic meridional overturning circulation, *Journal of Climate*, *23*(15), 4243–4254, doi:10.1175/2010JCLI3341.1.

Lozier, M. S., and N. M. Stewart (2008), On the Temporally Varying Northward Penetration of Mediterranean Overflow Water and Eastward Penetration of Labrador Sea Water, *Journal of Physical Oceanography*, *38*(9), 2097–2103, doi:10.1175/2008JPO3908.1.

Madec, G. (2008), NEMO ocean engine, *Note du Pòle demod? e- lisation, Inst. Pierre-Simon Laplace, Paris, France.*

Marzocchi, A., J. J.-M. Hirschi, N. P. Holliday, S. A. Cunningham, A. T. Blaker, and A. C. Coward (2015), The North Atlantic subpolar circulation in an eddy-resolving global ocean model, *Journal of Marine Systems*, *142*(0), 126–143, doi:http://dx.doi.org/10.1016/j.jmarsys.2014.10.007.

McCartney, M. S., and L. D. Talley (1982), The Subpolar Mode Water of the North Atlantic Ocean, *Journal of Physical Oceanography*, *12*(11), 1169–1188, doi:10.1175/1520-0485(1982)012<1169:TSMWOT>2.0.CO;2.

Meijers, A. J. S., N. L. Bindoff, and S. R. Rintoul (2011), Estimating the four-dimensional structure of the southern ocean using satellite altimetry, *Journal of Atmospheric and Oceanic Technology*, *28*(4), 548–568, doi:10.1175/2010JTECHO790.1.

Meinen, C. S. (2001), Structure of the North Atlantic current in stream-coordinates and the circulation in the Newfoundland basin, *Deep Sea Research Part I: Oceanographic Research Papers*, *48*(7), 1553–1580, doi:10.1016/S0967-0637(00)00103-5.

Meinen, C. S., and D. S. Luther (2016), Structure, transport, and vertical coherence of the Gulf Stream from the Straits of Florida to the Southeast Newfoundland Ridge, *Deep Sea Research Part I: Oceanographic Research Papers*, *112*, 137–154, doi:10.1016/j.dsr.2016.03.002.

Meinen, C. S., and D. R. Watts (2000), Vertical structure and transport on a transect across the North Atlantic Current near 42°N: Time series and mean, *Journal of Geophysical Research: Oceans*, *105*(C9), 21,869–21,891, doi:10.1029/2000JC900097.

Meinen, C. S., M. O. Baringer, and R. F. Garcia (2010), Florida Current transport variability: An analysis of annual and longer-period signals, *Deep Sea Research Part I: Oceanographic Research Papers*, *57*(7), 835–846, doi:10.1016/j.dsr.2010.04.001.

Mercier, H., P. Lherminier, A. Sarafanov, F. Gaillard, N. Daniault, D. Desbruyères, A. Falina, B. Ferron, C. Gourcuff, T. Huck, and V. Thierry (2015), Variability of the meridional overturning circulation at the Greenland–Portugal OVIDE section from 1993 to 2010, *Progress in Oceanography*, *132*, 250–261, doi:10.1016/j.pocean.2013.11.001.

Mercier, H., P. Lherminier, and F. F. Perez (2016), The Greenland-Portugal Go-Ship A25 OVIDE CTDO2 hydrographic data, *SEANOE*, doi:10.17882/46448.

Bibliography

Mertens, C., M. Rhein, M. Walter, C. W. Böning, E. Behrens, D. Kieke, R. Steinfeldt, U. Stöber, C. W. Boning, E. Behrens, D. Kieke, R. Steinfeldt, and U. Stober (2014), Circulation and transports in the Newfoundland Basin, western subpolar North Atlantic, *Journal of Geophysical Research: Oceans*, *119*, 7772–7793, doi: 10.1002/2014JC010019.

Miller, P. I., J. F. Read, and A. C. Dale (2013), Thermal front variability along the North Atlantic Current observed using microwave and infrared satellite data, *Deep Sea Research Part II: Topical Studies in Oceanography*, *98, Part B*(0), 244–256, doi: http://dx.doi.org/10.1016/j.dsr2.2013.08.014.

Müller, V., D. Kieke, P. G. Myers, C. Pennelly, and C. Mertens (2017), Temperature flux carried by individual eddies across 47°N in the Atlantic Ocean, *Journal of Geophysical Research: Oceans*, *119*(3), 2017–2033, doi:10.1002/2016JC012175.

National Geophysical Data Center (1988), Data Announcement 88-MGG-02, Digital relief of the Surface of the Earth, *NOAA*.

Nolting, W. (2011), *Grundkurs Theoretische Physik 1*, 361 pp., Springer-Verlag Berlin, Heidelberg.

OSNAP (2016), Overturning in the Subpolar North Atlantic Program (OSNAP).

Pérez-Brunius, P., T. Rossby, and D. R. Watts (2004), Absolute Transports of Mass and Temperature for the North Atlantic Current– Subpolar Front System, *Journal of Physical Oceanography*, *34*(8), 1870–1883, doi:10.1175/1520-0485(2004)034<1870: ATOMAT>2.0.CO;2.

Pond, S., and G. L. Pickard (1989), *Introductory Dynamical Oceanography (Second Edition)*, Pergamon Press, Oxford, New York, Beijing, Frankfurt, Sao Paulo, Sydney, Tokyo, Toronto.

Reverdin, G. (2010), North Atlantic subpolar Gyre surface variability (1895-2009), *Journal of Climate*, *23*(17), 4571–4584, doi:10.1175/2010JCLI3493.1.

Reverdin, G., P. P. Niiler, and H. Valdimarsson (2003), North Atlantic Ocean surface currents, *Journal of Geophysical Research: Oceans*, *108*(C1), 2–21, doi:10.1029/2001JC001020.

Rhein, M., D. Kieke, S. Hüttl-Kabus, A. Roessler, C. Mertens, R. Meissner, B. Klein, C. W. Böning, and I. Yashayaev (2011), Deep water formation, the subpolar gyre,

and the meridional overturning circulation in the subpolar North Atlantic, *Deep Sea Research Part II: Topical Studies in Oceanography*, *58*(17-18), 1819–1832, doi:10.1016/j.dsr2.2010.10.061.

Rhein, M., S. R. Rintoul, S. Aoki, E. Campos, D. Chambers, R. A. Feely, S. Gulev, G. Johnson, S. A. Josey, A. Kostianoy, C. Mauritzen, D. Roemmich, L. D. Talley, and F. Wang (2013), Observations: Ocean Pages, in *Climate Change 2013 - The Physical Science Basis*, edited by Intergovernmental Panel on Climate Change, pp. 255–316, Cambridge University Press, Cambridge, doi:10.1017/CBO9781107415324.010.

Richardson, P. L., and J. A. Knauss (1971), Gulf stream and Western boundary undercurrent observations at Cape Hatteras, *Deep-Sea Research and Oceanographic Abstracts*, *18*(11), 1089–1109, doi:10.1016/0011-7471(71)90095-7.

Roessler, A., M. Rhein, D. Kieke, and C. Mertens (2015), Long-term observations of North Atlantic Current transport at the gateway between western and eastern Atlantic, *Journal of Geophysical Research: Oceans*, *120*(6), 4003–4027, doi:10.1002/2014JC010662.

Rossby, T. (1996), The North Atlantic Current and surrounding waters: At the crossroads, *Reviews of Geophysics*, *34*(4), 463–481, doi:10.1029/96RG02214.

Rossby, T., C. N. Flagg, K. Donohue, A. Sanchez-Franks, and J. Lillibridge (2014), On the long-term stability of Gulf Stream transport based on 20 years of direct measurements, *Geophysical Research Letters*, *41*(1), 114–120, doi:10.1002/2013GL058636.

Sarafanov, A., A. Falina, H. Mercier, A. Sokov, P. Lherminier, C. Gourcuff, S. Gladyshev, F. Gaillard, and N. Daniault (2012), Mean full-depth summer circulation and transports at the northern periphery of the Atlantic Ocean in the 2000s, *Journal of Geophysical Research: Oceans*, *117*(1), 1–22, doi:10.1029/2011JC007572.

Saunders, P. M. (1994), The flux of overflow water through the Charlie-Gibbs Fracture Zone, *Journal of Geophysical Research*, *99*(C6), 12,343–12,355, doi:10.1029/94JC00527.

Schmitz, W. J., and M. S. McCartney (1993), On the North Atlantic Circulation, *Reviews of Geophysics*, *31*(1), 29–49, doi:10.1029/92RG02583.

Schneider, L., D. Kieke, K. Jochumsen, E. Colbourne, I. Yashayaev, R. Steinfeldt, E. Varotsou, N. Serra, and M. Rhein (2015), Variability of Labrador Sea Water trans-

ported through Flemish Pass during 1993–2013, *Journal of Geophysical Research : Oceans*, *120*, 5514–5533, doi:10.1002/2014JC010472.Received.

Scholz, P., D. Kieke, G. Lohmann, M. Ionita, and M. Rhein (2014), Evaluation of Labrador Sea Water formation in a global Finite-Element Sea-Ice Ocean Model setup, based on a comparison with observational data, *Journal of Geophysical Research: Oceans*, *119*(3), 1644–1667, doi:10.1002/2013JC009232.

Sea-Bird Electronics (2016), *SBE 911plus CTD*, june 2016 ed., 10–11 pp.

Smith, R. D., M. E. Maltrud, F. O. Bryan, and M. W. Hecht (2000), Numerical Simulation of the North Atlantic Ocean at 1 / 10°, *Journal of Physical Oceanography*, *30*, 1532–1561, doi:10.1175/1520-0485(2000)030<1532:NSOTNA>2.0.CO;2.

Stendardo, I. (2011), Interannual to decadal variability and trends of the oceanic oxygen content in the North Atlantic, Ph.D. thesis, ETH Zürich, Switzerland.

Stendardo, I., D. Kieke, M. Rhein, N. Gruber, and R. Steinfeldt (2015), Interannual to decadal oxygen variability in the mid-depth water masses of the eastern North Atlantic, *Deep Sea Research Part I: Oceanographic Research Papers*, *95*, 85–98, doi:10.1016/j.dsr.2014.10.009.

Stendardo, I., M. Rhein, and R. Hollmann (2016), A high resolution salinity time series 1993-2012 in the North Atlantic from Argo and Altimeter data, *Journal of Geophysical Research: Oceans*, *121*(4), 2523–2551, doi:10.1002/2015JC011439.

Stramma, L., D. Kieke, M. Rhein, F. Schott, I. Yashayaev, and K. P. Koltermann (2004), Deep water changes at the western boundary of the subpolar North Atlantic during 1996 to 2001, *Deep Sea Research Part I: Oceanographic Research Papers*, *51*(8), 1033–1056, doi:10.1016/j.dsr.2004.04.001.

Sy, A. (1988), Investigation of large-scale circulation patterns in the central North Atlantic: the North Atlantic current, the Azores current, and the Mediterranean Water plume in the area of the Mid-Atlantic Ridge, *Deep Sea Research Part A, Oceanographic Research Papers*, *35*(3), 383–413, doi:10.1016/0198-0149(88)90017-9.

Talley, L. D., and M. S. McCartney (1982), Distribution and Circulation of Labrador Sea Water, *Journal of Physical Oceanography*, *12*(11), 1189–1205, doi:10.1175/1520-0485(1982)012<1189:DACOLS>2.0.CO;2.

Talley, L. D., G. L. Pickard, W. Emery, and J. H. Swift (2011), *Descriptive Physical Oceanography, An Introduction*, 6 ed., Elsevier Ltd.

University of Rhode Island (2015), *Inverted Echo Sounder User ' s Manual IES Model 6.2C*, june 2015 ed., Graduate School of Oceanography, Univserity of Rhode Island, Narragansett, RI, USA.

Våge, K., R. S. Pickart, A. Sarafanov, Ø. Knutsen, H. Mercier, P. Lherminier, H. M. van Aken, J. Meincke, D. Quadfasel, and S. Bacon (2011), The Irminger Gyre: Circulation, convection, and interannual variability, *Deep-Sea Research Part I: Oceanographic Research Papers*, *58*(5), 590–614, doi:10.1016/j.dsr.2011.03.001.

Visbeck, M. (2002), Deep velocity profiling using lowered acoustic Doppler current profilers: Bottom track and inverse solutions, *Journal of Atmospheric and Oceanic Technology*, *19*(5), 794–807, doi:10.1175/1520-0426(2002)019<0794:DVPULA>2.0.CO;2.

Visbeck, M., E. P. Chassignet, R. G. Curry, T. L. Delworth, R. R. Dickson, and G. Krahmann (2003), The ocean's response to North Atlantic Oscillation variability, *Geophysical Monograph Series*, *134*, 113–145, doi:10.1029/134GM06.

Walter, M., and C. Mertens (2013), Mid-depth mixing linked to North Atlantic Current variability, *Geophysical Research Letters*, *40*(18), 4869–4875, doi:10.1002/grl.50936.

Wang, C., S. Dong, and E. Munoz (2010), Seawater density variations in the North Atlantic and the Atlantic meridional overturning circulation, *Climate Dynamics*, *34*(7-8), 953–968, doi:10.1007/s00382-009-0560-5.

Watts, D. R., and H. T. Rossby (1977), Measuring Dynamic Heights with Inverted Echo Sounders: Results from MODE, *Journal of Physical Oceanography*, *7*(3), 345–358, doi:10.1175/1520-0485(1977)007<0345:MDHWIE>2.0.CO;2.

Xu, X., H. E. Hurlburt, W. J. Schmitz, R. Zantopp, J. Fischer, and P. J. Hogan (2013), On the currents and transports connected with the atlantic meridional overturning circulation in the subpolar North Atlantic, *Journal of Geophysical Research: Oceans*, *118*(1), 502–516, doi:10.1002/jgrc.20065.

Yeager, S., and G. Danabasoglu (2014), The Origins of Late-Twentieth-Century Variations in the Large-Scale North Atlantic Circulation, *Journal of Climate*, *27*(9), 3222–3247, doi:10.1175/JCLI-D-13-00125.1.

Zweng, M., J.R. Reagan, J.I. Antonov, R.A. Locarnini, A.V. Mishonov, T.P. Boyer, H.E. Garcia, O.K. Baranova, D.R. Johnson, D. Seidov, M. M. Biddle, M. Zweng, J. Reagan, J. Antonov, R. Locarnini, A. Mishonov, T. Boyer, H. Garcia, O. Baranova, D. Johnson, D.Seidov, and M. M. Biddle (2013), World Ocean Atlas 2013, Volume 2: Salinity, *S. Levitus, E d . ; A. Mishonov , Technical Ed. ; NOAA Atlas NESDIS 74, 39 pp.*

List of Figures

List of Tables

Publications

Parts of the results of this study are published in a paper:

Breckenfelder, T., M. Rhein, A. Roessler, C. W. Böning, A. Biastoch, E. Behrens, and C. Mertens (2017), Flow paths and variability of the North Atlantic Current: A comparison of observations and a high-resolution model, *Journal of Geophysical Research: Oceans*, doi:10.1002/2016JC012444

I presented preliminary results of this work on the following international conferences, workshops and in seminars as first author:

Breckenfelder, T. , M. Rhein, A. Roessler, E. Behrens, C.W. Böning, A. Biastoch *Variability of the North Atlantic Current: high resolution model data versus in situ measurements* in the Institute of Environmental Physics seminar "Ocean, Ice, and Atmosphere" at the University of Bremen, Germany. January 2014, talk

Breckenfelder, T., M. Rhein, A. Roessler, E. Behrens, C.W. Böning, A. Biastoch *Variability of the North Atlantic Current: High resolution model data versus in situ measurements* at the AGU Ocean Sciences Meeting in Honolulu, USA. February 2014, poster

Breckenfelder, T., M. Rhein, A. Roessler, E. Behrens, C Böning, A. Biastoch und C. Mertens *Variability of the North Atlantic Current: high resolution model data versus in situ measurements* at the European Geosciences Union General Assembly in Vienna, Austria. April 2015, talk

Breckenfelder, T., M. Rhein, A. Roessler, E. Behrens, C. Böning, A. Biastoch und C. Mertens *The North Atlantic Current at the Mid-Atlantic Ridge in model and observations* at the second ArcTrain Annual Meeting in Montreal, Canada, August 2015, talk

Breckenfelder, T., M. Rhein, A. Roessler, P. G. Myers, E. Behrens, C. Böning, A. Biastoch und C. Mertens *The North Atlantic Current at the Mid-Atlantic Ridge in model and observations* at the 3rd Annual VITALS Science Meeting in Halifax, Canada, October 2015, talk

Breckenfelder, T., M. Rhein, A. Roessler, P. Myers, E. Behrens, C. Böning, A. Biastoch und C. Mertens *The North Atlantic Current at the Mid-Atlantic Ridge in model and observations* in the IGR Symposium at the University of Alberta in Edmonton, Canada, October 2015, talk

Breckenfelder, T., M. Rhein, A. Roessler, E. Behrens, C. Böning, A. Biastoch und C. Mertens *The upper branch of the AMOC in the subpolar North Atlantic in model and observation* at the Ocean Sciences Meeting in New Orleans,USA, February 2016, poster

Breckenfelder, T., M. Rhein, P. G. Myers, A. Roessler, E. Behrens, C. Böning, A. Biastoch, C. Pennelly and X. Hu *Variability of the North Atlantic Current in model and observation* at the European Geosciences Union General Assembly in Vienna, Austria. April 2016, poster

Breckenfelder, T. *Gulf Stream in model and observations* at the third ArcTrain Annual Meeting in Banff, Canada. September 2016, talk

Acknowledgment

First of all, I am heartily thankful to my supervisor Prof. Dr. Monika Rhein for her encouragement, guidance, support, and trust in me from the very beginning to the final state of this thesis. She always had an open door for discussions and questions and supported me in every possible way. Thank you very much!

My sincere thanks also goes to my second supervisor Paul G. Myers, who not only supported my work as a member of my thesis committee but also gave me a warm welcome to his working group at the Department of Earth and Atmospheric Sciences at the University of Alberta, Edmonton, Canada. Furthermore, I am grateful that he even comes all the way from Canada to Bremen to attend my PhD defense.

A special thanks goes to Achim Roessler, who always had an open ear, provided the PIES data, and answered all my countless questions.

I would like to thank Dagmar Kieke to be a member of my thesis committee and for her constant support in numerous ways along the thesis journey.

It was a privilege to be part of ArcTrain, which gave me the opportunity to attend conferences, workshops, summer schools, the Floating University onboard RV Polarstern and to visit Paul G. Myers in Edmonton for a research stay. Furthermore, being part of ArcTrain gave me the opportunity to get to know my fellow ArcTrain PhD students in Germany and Canada, which was a unique opportunity to build up a great scientific interdisciplinary network and find new friends. I would like to thank all ArcTrain PhD students and PIs for the experiences we shared together.

A special thanks goes to my fellow PhD students Andrea Klus, Henriette Kolling, Annegret Krandick, Kerstin Kretschmer, and Rike Völpel for all the much appreci-

163